Fabrication of three-dimensional carbon microelectrodes for electrochemical sensing

Hemanth, Suhith

Publication date:
2017

Document Version
Publisher's PDF, also known as Version of record

Technical University
of Denmark

Fabrication of three-dimensional carbon microelectrodes for electrochemical sensing

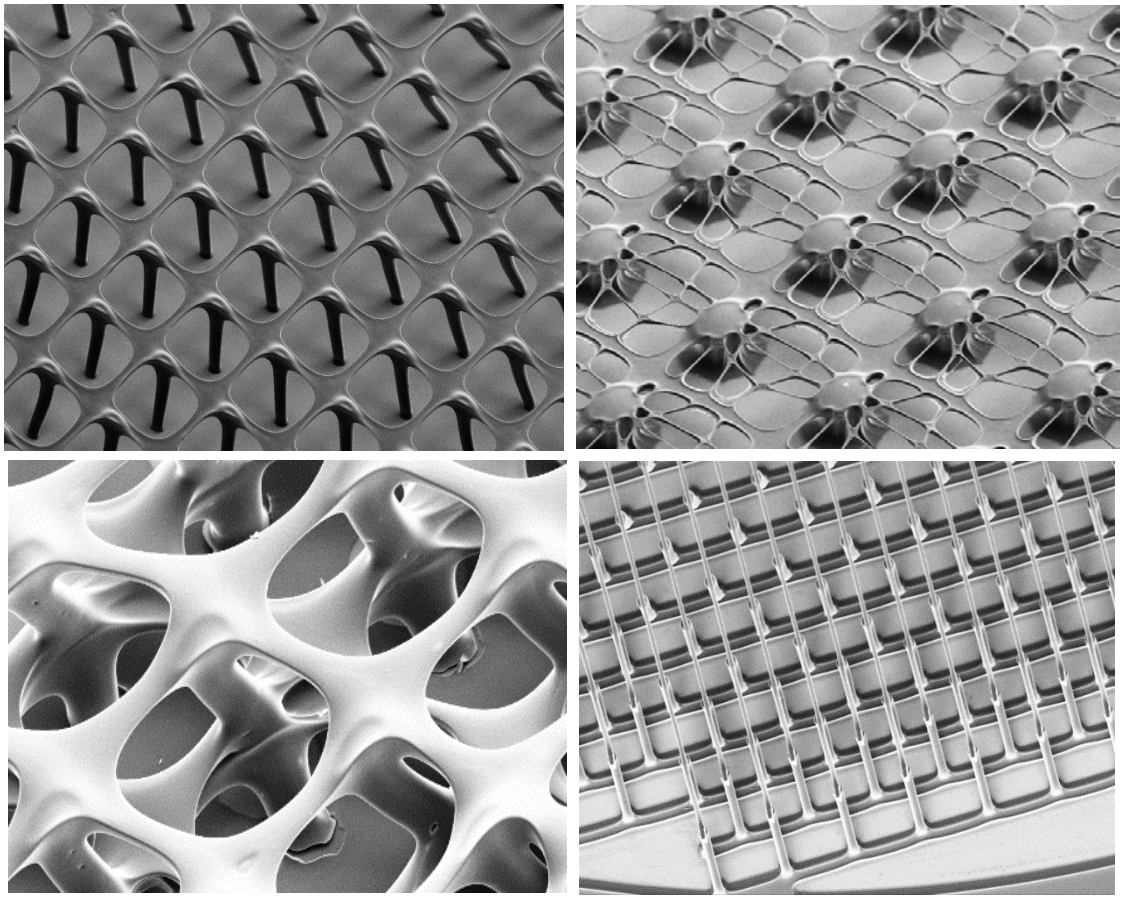

Suhith Hemanth

PhD Thesis, October 2017

DTU Nanotech
Department of Micro- and Nanotechnology

Fabrication of three-dimensional carbon microelectrodes for electrochemical sensing

By

Suhith Hemanth

DISSERTATION

Submitted in partial fulfillment of the requirements for the degree of Doctor of Philosophy in Electronics, Communication and Space Science in the department of Micro and Nanotechnology of Technological University of Denmark

October 2017

Supervised by:

Associate Professor Stephan S. Keller

Postdoc Claudia Caviglia

Acknowledgments

This project has been a mixed experience of fun and challenge, which has provided me the opportunity to work and learn in the field that fascinates me the most. I would like to express my sincere gratitude to my supervisors Stephan S. Keller and Claudia Caviglia for their high inspirational guidance, support and professional advice throughout my PhD project. Their profound knowledge of cleanroom fabrication, bioelectrochemistry techniques, and great overall perspective were invaluable for completing this thesis.

I would like to express my deepest gratitude to Danchip staff for their invaluable support in all times of need. Since the major part of my work was carried out in cleanroom facility, Danchip staff has played an important role in completing this project successfully. In particularly, I would like to thank Conny Hougaard, Mikkel D. Mar, Pernille V. Larsen and Thomas A. Anhøj for their special attention towards my project.

I greatly appreciate the strong support from the dynamic and highly international BioMic group for creating such a friendly and active atmosphere, especially the long-term members of the group (Nina R. Pedersen, Ritika S. Petersen, Afia A, Ioannis Mantis, Quang L. Nguyen, Yasmin M. Hassan and Zarmeena Abid). I would also like to appreciate Nanoprobe group for their support and making me feel one among them.

Finally I would like to thank the pillars of my life, friends and family. I want to thank my friends (Kuldeep, Nina, Soumy, Melta, Kristian, Julie, Silvia, Onur, Kaiyu, Lidia, Murat, Anil, Rokon, Abhay, Hitesh, Sanjukta, Spoorthy, Rashmi, Garmia, Ada, and Chantal) for supporting and inspiring me in all my ups and down. Last, but not the least, I thank my family my parents, brother and all cousins.

Suhith Hemanth

Abstract

Carbon microelectrodes have a wide range of applications because of their unique material properties and biocompatibility. The aim of the research work carried out in this thesis was to develop three-dimensional (3D) carbon microelectrodes for electrochemical applications. Three different fabrication processes were established for fabrication of 3D carbon microelectrodes using UV photolithography followed by pyrolysis. UV exposure at three different wavelengths 365 nm, 313 nm and 405 nm was optimized to fabricate suspended 3D epoxy polymer templates. The polymer template was pyrolysed at high temperature to obtain the corresponding carbon microelectrodes. The fabricated microelectrodes are characterized for their physical, electrical and electrochemical properties. The pyrolysis process was optimized for low electrical resistance and high mechanical stability. To explore the application of carbon microelectrodes four different model systems (Glucose sensing, Yeast analysis, Dopamine detection in human stem cell and bone cell monitoring) were tested. In all the model systems 3D carbon microelectrodes showed a 2-3 folds higher sensing signal when compared to 2D carbon electrodes.

Key words – 3D carbon microelectrodes, UV photolithography, pyrolysis, electrochemistry

Resumé

Mikroelektroder i karbon kan på grund af deres unikke egenskaber og biokompatibilitet anvendes indenfor en række forskellige områder. Målet for arbejdet bag denne afhandling var at udvikle tredimensionelle (3D) karbon mikroelektroder til anvendelser indenfor elektrokemien. Tre forskellige processer til fremstilling af 3D karbon mikroelektroder blev udviklet med brug af UV fotolitografi og efterfølgende pyrolyse. UV belysning ved tre forskellige bølgelængder 365 nm, 313 nm og 405 nm blev optimeret til at fremstille 3D skabeloner i epoxy polymer. Polymer skabelonen blev efterfølgende pyrolyseret ved høj temperatur for at fremstille den tilsvarende karbon mikroelektrode. De fysiske, elektriske og elektrokemiske egenskaber for de fremstillede mikroelektroder blev karakteriseret og pyrolyse processen blev optimeret til lav elektrisk modstand og høj mekanisk stabilitet. For at undersøge anvendelserne af karbon mikroelektroderne blev fire forskellige modelsystemer (Glucose måling, analyse af gær, detektion af dopamin i humane stamceller og monitorering af knogleceller) testet. I alle modelsystemerne viste karbon mikroelektroderne et 2-3 gange kraftigere signal sammenlignet med 2D karbon elektroder.

Nøgleord – 3D karbon mikroelektroder, UV fotolitografi, pyrolyse, elektrokemi

Table of Contents

List of publications and manuscripts

Paper I. Pyrolytic 3D Carbon Microelectrodes for Electrochemistry
S.Hemanth, C.Caviglia, L. Amato, T. A. Anhøj, A.Heiskanen, J. Emnéus, and S. S. Keller, *ECS Transactions*, 72 (2016), 117–124.

Paper II. Suspended 3D pyrolytic carbon microelectrodes for electrochemistry
S.Hemanth, C.Caviglia and S.S.Keller, *Carbon*, 121 (2017), 226–234.

Paper III. Suspended microstructures of epoxy based photoresist fabricated with UV Photolithograhy
S. Hemanth, T. A. Anhøj, C.Caviglia and S. S. Keller, *Microelectronic Engineering* 176 (2017) 40-44.

Paper IV. 3D suspended interdigitated carbon ultramicroelectrodes
I. Mantis, S.Hemanth, C. Caviglia and S.S.Keller (Manuscript)

Paper V. Bio-functionalized Graphene combined 3D Carbon Microelectrode as Ultra-sensitive Electrochemical Biosensor
S.Hemanth, A.Halder, C. Caviglia, Q.Chi and S.S.Keller (Manuscript)

My Contribution to the papers

Paper I. I planned, designed, and performed all the experiments. I also evaluated the results and wrote the manuscript.

Paper II. I designed, planned and performed all the experiments. I also analyzed the results and wrote the manuscript. Caviglia.C had equal contribution in analyzing electrochemical results.

Paper III. S.S Keller, TA Anhoj, and I contributed equally in planning the experiments. I designed and performed the experiments. I also analyzed the results and wrote the manuscript.

Paper IV. I designed and planned the experiments. I also supervised the fabrication process and had a major role analyzing the results and manuscript writing.

Paper V. I designed and planned the experiments. I also fabricated the electrode chips and had a significant role in analyzing and writing the manuscript.

List of publications not included in this thesis

High temperature SU-8 pyrolysis for fabrication of carbon electrodes
Y.M.Hassan, C.Caviglia, S.Hemanth, D.M.A.Mackenzie, T.S.Alstrøma, D.H.Petersen, S.S.Keller, *Journal of Analytical and Applied Pyrolysis*, 125 (2017), 91-99.

Pyrolytic carbon microelectrodes for impedance based cell sensing.
Y.M.Hassan, C.Caviglia, S.Hemanth, D.M.A.Mackenzie, D.H.Petersen, S.S.Keller, *ECS Transactions*, 72, (2016), 35-44.

A General Chemical Route Enabling High-loading of Enzymes in Biocompatible Graphene Matrix for Development of Flexible Biosensing Devices
A.Halder, S.Han, R.S. Dey, S.Hemanth, S.S.Keller, N.Zhu, and Q.Chi (Manuscript)

Chapter 1

Introduction

1.1 Motivation

Due to industrialization and globalization, the complex mix of pollutants threatening the Earth's regulatory mechanisms is constantly increasing [1]. There are various pollutants causing the degradation of the environment, the most common pollutants being heavy metals, pesticides, mould and fungal toxins, industrial chemicals, and volatile organic compounds [2–6]. The most common technique used to study the toxic effects of pollutants on cells is fluorescent microscopy which enables the observation of cell morphology, migration and proliferation [7]. However, microscopy techniques require expensive equipment and tedious sample preparation such as fluorescent cell staining. Furthermore, after each test the samples is destroyed and it is not possible to monitor the same cell population over time. The toxic effects of these pollutants can also be studied electrochemically by growing cells on the electrodes [8]. The use of electrochemical techniques to study cells can provide a label-free, real-time, fast, long term, minimally invasive measurements and the possibility for fully automated systems [9–12]. However these methods do not provide the same insight in cellular behavior as microscopic techniques. Therefore combining the microscopic readout and electrochemical measurements, could offer a complete approach.

In bioelectrochemistry cells are cultured on electrodes and electrochemical methods such as electrochemical impedance spectroscopy (EIS) or voltammetry are used to detect changes in cell populations, e.g. cell morphology, cell membrane integrity, receptor-ligand interactions or chemical compounds released in response to external stimuli, respectively [13–17]. Typically, thin flat (2D) metal microelectrodes have been used for monitoring of cell culture changes. The major limitation is that state-of-the-art metal microelectrodes are primarily restricted to 2D since the fabrication of 3D metal electrodes quickly turns expensive and relatively complicated. As a consequence, cells have commonly

been incubated on a 2D substrate that is different from their natural 3D environment. Although most biological assays still are performed in the 2D format the trend goes towards the 3D format, since it could contribute to more realistic results in toxicological testing and biological performance all together[18–23]. For *in vitro* cells studies, a large number of polymeric 3D scaffolds have been developed and the cell cultures are analyzed using microscopy techniques [24]. Recently, a 3D scaffold was placed on 2D Au electrodes and electrochemical monitoring of the cell response to toxins was demonstrated [25]. However, the sensitivity for detection of events in the "bulk" of the cell scaffold was found to decrease with increasing distance from the electrode surface and the actual characterization was limited to the cells in proximity of the 2D electrode. For this purpose, a 2D electrode (Figure 1.A) can be replaced by an intelligent three-dimensional (3D) electrode (Figure 1.B) which can act both as a substrate (scaffold) and as a sensing or transducer element [26–31]. Furthermore, the 3D nature of the electrodes better mimics the natural environment of cells, which is relevant for applications in tissue engineering and bioelectrochemistry [32]. The 3D nature of the microelectrodes can also increase the possibility of adhering/trapping the cells on the electrodes, which is very important for non-adherent cells in cell biology [8,33]. Finally, 3D microelectrodes could potentially be very efficient in mechanical trapping, sorting and aligning cells in various cell analysis systems [34–37].

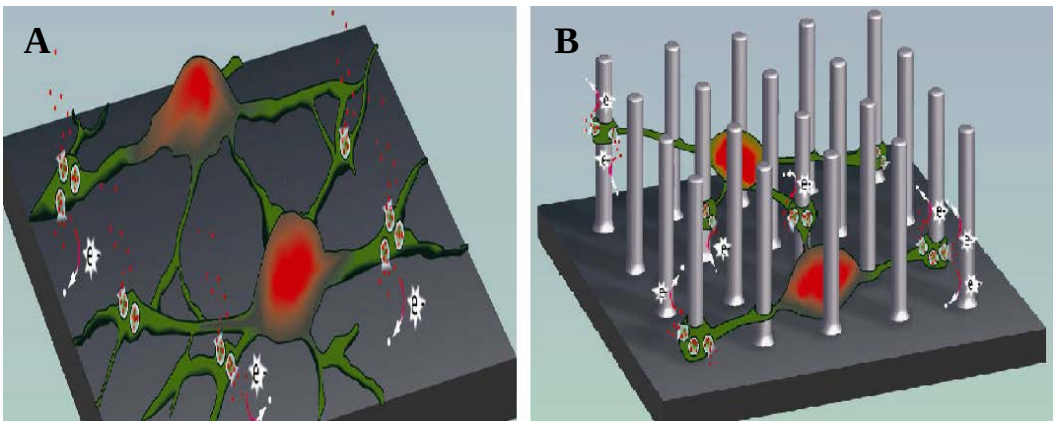

Figure 1 : (A) 2D carbon electrode (B) 3D carbon electrode [38]

1.2 3D microelectrode fabrication

Conducting substrates and scaffolds based on metal [39], conducting polymer [40] and carbon [41] can be used as electrodes for real-time monitoring of cell dynamics [13]. Several microfabrication techniques have been processed for the fabrication of 2D and 3D microelectrode. However fabrication techniques like electroplating [42–44], sputtering or evaporation [45], injection molding [46], microsolidics [47] and screen printing [48,49] are limited due to their lack of resolution, reproducibility, and throughput which are important for fundamental and applied research [50]. The more advanced processes like electrodeless electroplating [51] and metal ion implantation [52] are limited by their process cost and complexity [53]. Additionally the use of noble metals limits the electrochemical potential window [54,55] and electrodes are prone to fouling [56,57]. For these reasons carbonaceous materials such as graphene [58], CNTs, diamond-like carbon [59] and pyrolytic carbon have been emerging as electrode materials for electrochemistry in last few decades.

A simple and cost-effective process to fabricate microelectrodes is carbon MEMS (C-MEMS). C-MEMS is a process where a polymer template is pyrolyzed at high temperature (~ 1000ºC) in an inert atmosphere to obtain the corresponding pyrolytic carbon structure (Figure 2) [60]. This process enables fabrication of 2D and 3D electrodes with possibility for tailoring ad-hoc designs and unique sensitivities of microelectrodes for specific applications. Additionally carbon has various advantages as material for microelectrodes such as its wide electrochemical potential window [54,61], high chemical stability [62], ease of surface modification [63–65] and biocompatibility [66]. Due to this, pyrolytic carbon is becoming increasingly attractive for numerous applications, such as biosensors [67,68], microbatteries [69,70], tissue engineering [71,72] and chemical sensing [73].

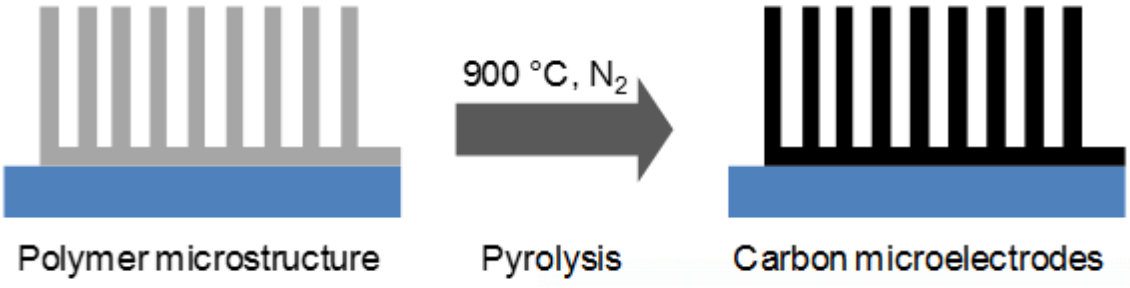

Figure 2: Fabrication of 3D carbon microelectrode by pyrolysis of a polymer microstructure

Figure 3 shows the 3D carbon electrodes fabricated from complex C-MEMS microfabrication processes. The most complex process in C-MEMS is to have a stable polymer template for pyrolysis. SU-8, a negative tone epoxy based photoresist is the most widely used polymer precursors for C-MEMS [74]. Different microfabrication processes have been reported for the fabrication of 3D SU-8 structures for pyrolysis. Fabrication techniques such as e-beam [75], two-photon [76] and X-ray [77] lithography have been employed for fabrication of 3D polymer templates for pyrolysis. The limiting factors for these techniques is the low throughput compared to standard UV photolithography. Different fabrication processes with UV photolithography have been proposed to fabricate 3D suspended layers such as using a polymerization stop layer or using SU-8 foil or a lower UV exposure for fabricating 3D polymer template [78–80]. But a simple and higher control of lateral resolution of the suspended layers is still lacking. The degree of freedom in UV photolithography followed by pyrolysis process provides possibility for mass production facilitating novel tailored electrode designs with unique properties for electrochemical application.

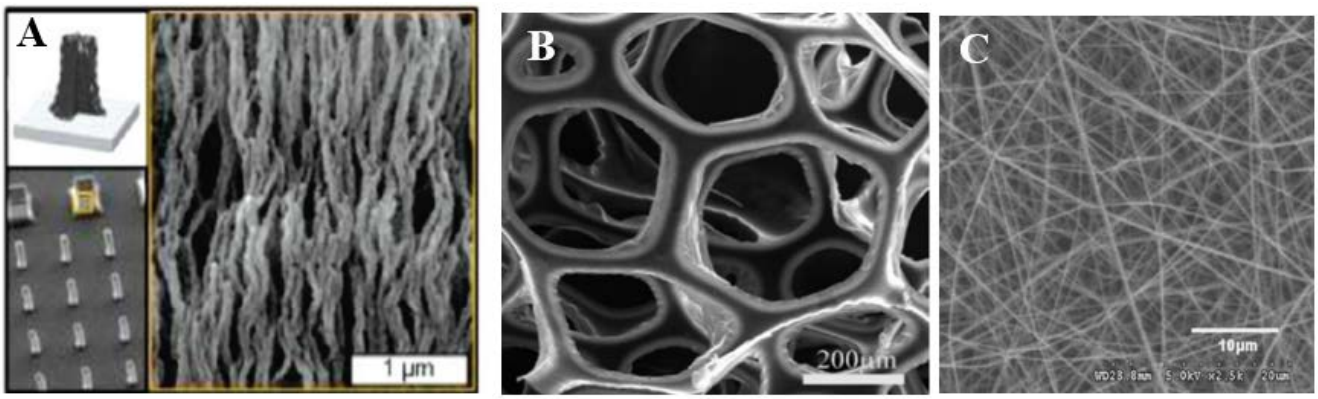

Figure 3: (A)3D carbon driven pyrolysis of polymer treated with plasma [81] (B) nanostructures sponge electrode [82] (C) 3D carbon electrode driven from pyrolysis of electrospun fiber [83]

1.3 Overall project goal

This project is a part of Young Investigator Program funded by the Villum Found. The overall goal of the project was to develop intelligent 3D carbon scaffolds for bioelectrochemistry. The 3D carbon scaffold is ideal for cell growth and provides possibility for in situ electro analysis of a 3D cell culture.

The project team included two PhD students (me and Y.M. Hassan) and one Postdoc (C.Caviglia). The main goals of this project were:

G1. Material science: Investigation of the influence of polymer template material on the properties of pyrolytic carbon microelectrode

G2. Microfabrication: Fabrication of 3D polymer templates and conversion to carbon microelectrodes by pyrolysis

G3. Bioelectrochemistry: *In vitro* model for toxicity studies or/and bioelectrochemical cell for removal of pollutants (biomediation).

1.4 Goal of PhD project

The main goals of this PhD project were to address G2 and advance the state of the art in fabrication of 3D electrodes and to fabricate 3D/2D carbon microelectrode chips for bioelectrochemistry (Figure 4.A and B). Figure 4.C illustrates potential 3D carbon microelectrode structures on the working electrode. The previous work done in the group by Letizia et.al. was used a starting point of this project [26,84]. The project is divided into following activities.

1. Polymer microfabrication – UV photolithography will be explored to fabricate 3D suspended polymer templates for pyrolysis. The technology will be explored to achieve high resolution (~10µm), 3D suspended microstructures, and 3D multilayers with reasonable throughput.

2. Pyrolysis process – Testing pyrolysis at different conditions (maximum temperature, different ramp rate, different process steps) to optimize the electrode performance/behavior.

3. 3D Microelectrode – Design and fabrication of a microelectrode chip. In this activity different microfabrication process flow will be established for fabricating working electrode (WE), reference electrode (RE),counter electrode (CE), passivation layer or interdigitated electrode on a single chip.

4. Microfluidic/Microelectrode chip design and setup – A microfluidic system will be built for the in-situ measurements. This activity includes building microfluidic channels, microfluidic interconnects, electrical interconnects and readout systems.

5. Bioelectrochemical characterization/testing – This activity includes the establishments of experimental proof of concept for bioelectrochemistry on 3D carbon microelectrodes. Some of the electrochemical techniques which will be used for measurements are Cyclic Voltammetry (CV), amperometry and impedance.

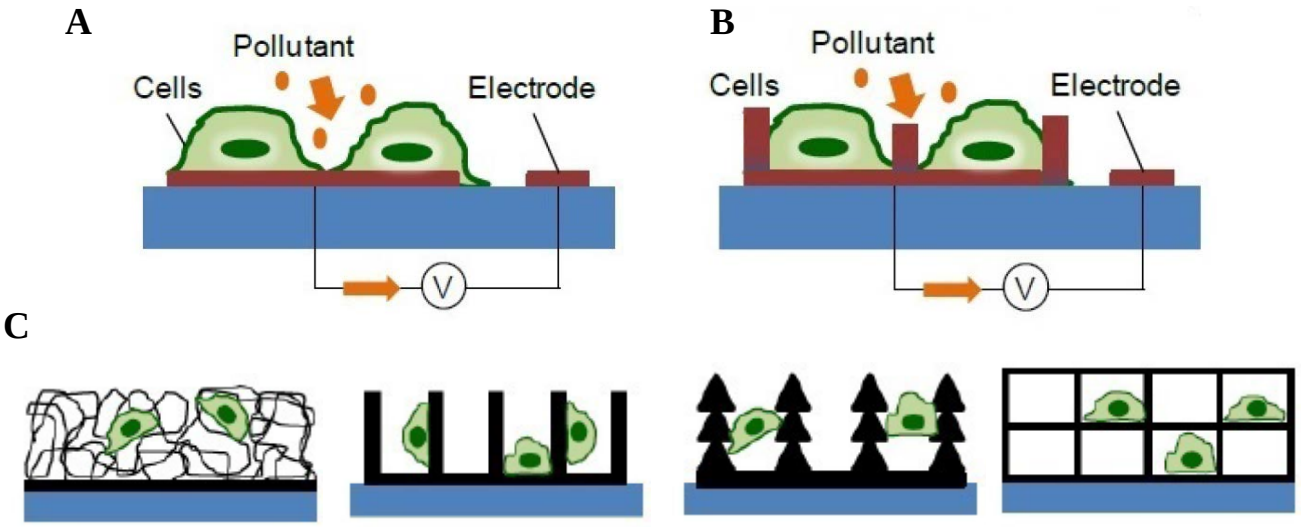

Figure 4: (A) – (B) 2D and 3D microelectrode for bioelectrochemistry and (C) Different shapes of carbon microelectrodes tailored for specific application

1.5 Structure of the thesis

Aim of this work was to develop pyrolytic carbon microelectrode (Carbon4Bio (C4B)) chip for bioelectrochemical applications. Figure 6 shows the evolution of C4B chips in this thesis. A planar, three electrode electrochemical chip was designed and fabricated with carbon as WE (2D C4B). In the second generation of C4B chips, 3D carbon microelectrodes were fabricated on the WE (3D C4B). Finally, the optimized process was used to fabricate 3D interdigitated microelectrodes (3D C4B IDE). The fabricated carbon microelectrodes acted as a scaffold and transducer for electrochemical monitoring of cell culture.

Chapter 2: This chapter gives a brief theoretical background on the materials and techniques used in this thesis.

Chapter 3: This chapter explains the microfluidic setup (MagClamp system) used to integrate 2D/3D carbon microelectrodes for testing in different condition such as, static and dynamic (flow). Three different microfluidic systems were simulated in a finite element software (COMSOL) and only the optimized flow system was fabricated (Figure 5).

Figure 5: Process flow for the development of microfluidic system in this thesis

Chapter 4: This chapter gives a detailed description of the optimization of 2D C4B chips. The initial work is focused on developing a three electrode chip with 2D pyrolytic carbon as working electrode. The 2D C4B chip was characterized electrochemically with CV and EIS. Further, pyrolytic carbon was tested as contact leads for 2D electrodes.

Chapter 5: In this chapter, the 3D suspended carbon layer design, fabrication, and characterization is explained in detail. A three electrode chip with 3D pyrolytic carbon as working electrode was fabricated (Paper I/Paper II). UV-photolithography with different exposure wavelengths were explored for fabrication of 3D suspended SU-8 microstructures which were pyrolyzed to get corresponding carbon structures (Paper III). The fabricated chips were characterized with SEM, Raman spectroscopy, XPS and electrochemically (CV and EIS).

Chapter 6: This chapter summarizes a small study of the pyrolysis process parameters to improve for electrical and mechanical stability of 3D carbon microelectrodes. Different parameters such as temperature ramp, pyrolysis temperature and number of heating steps were investigated for least electrical resistance and minimal stress.

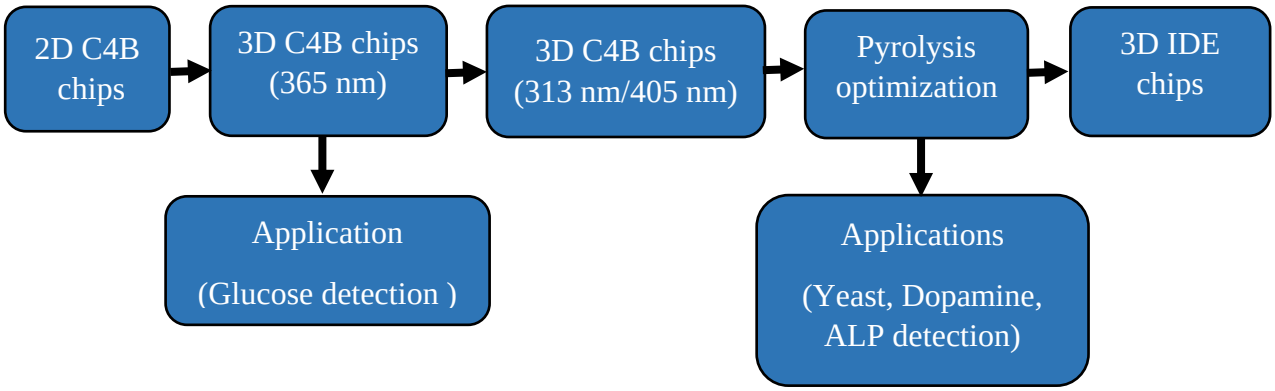

Figure 6: Flowchart of evolution of 3D carbon microelectrode in this thesis

Chapter 7: This chapter provides an overview of the different bioelectrochemical applications which are explored using 3D carbon microelectrode during this PhD project, i.e. glucose sensing (Paper IV), yeast cell seeding analysis, exocytosis of dopamine from human stem cells derived neurons and bone cell analysis.

Chapter 8: This chapter gives an overview of the main conclusions and the outlook.

Chapter 2

Theory on materials and methods

This chapter gives a brief theoretical introduction to the electrode material (glassy carbon) followed by the explanation of microfabrication techniques used in this thesis. The final part of this chapter has explanation of characterization techniques used in this work.

2.1 Carbon (materials) and structures

Carbon is the chemical element with the symbol C and exists in different allotropes such as graphite, diamond, graphene, fullerene and glass-like carbon [85,86]. The graphite structure consists of infinite graphene sheets which are planarly arranged carbon atoms, stacked together with a weak Van der Waals forces (Figure 7.A). Graphene has a polycrystalline structure characterized by the atomically ordered hexagonal surface. The carbon atoms in graphite are sp^2 hybridized, with an intra-planar C-C bond length of 141.5 pm and inter-planar spacing of 340 pm. The conductivity of graphite is $2 - 4 \times 10^5$ S/m [87]. Graphite is a good electric conductor, opaque, black, and soft. Diamond has a tetrahedral crystal structure. The carbon atoms in diamond are sp^3 hybridized with C-C bond length of 134 pm (Figure 7.B). Diamond is generally known as a good electrical insulator (1×10^{-18} S/m), transparent, and one of the strongest materials [88]. Carbon nanotubes (CNTs) are the fullerenes most commonly used for electrode material. CNTs are single or multiple rolled up graphene layers forming single-walled or multi-walled CNTs respectively (Figure 7.D). CNTs exhibit good electrical and heat conducting properties. Glassy carbon (GC) is obtained by heat treatment of organic polymer in an inert atmosphere [89]. This procedure is knows as carbonization or pyrolysis where polymer precursors (e.g. polyacrylonitrile (PAN) or phenol/formaldehyde) are treated at high temperatures (1000 ºC – 3000 ºC) [89] in an inert atmosphere. The GC comprises a mixture of sp^2 (graphitic region) and sp^3 (disordered region) carbon hybridization [90,91]. GC has a high temperature resistance, low electrical resistance, and a good chemical stability. GC

exhibits excellent electrochemical properties which has attracted its use in various applications. Initially GC was considered to have a ribbon-like geometry with entangled graphitic planes (Figure 7.E) [92].

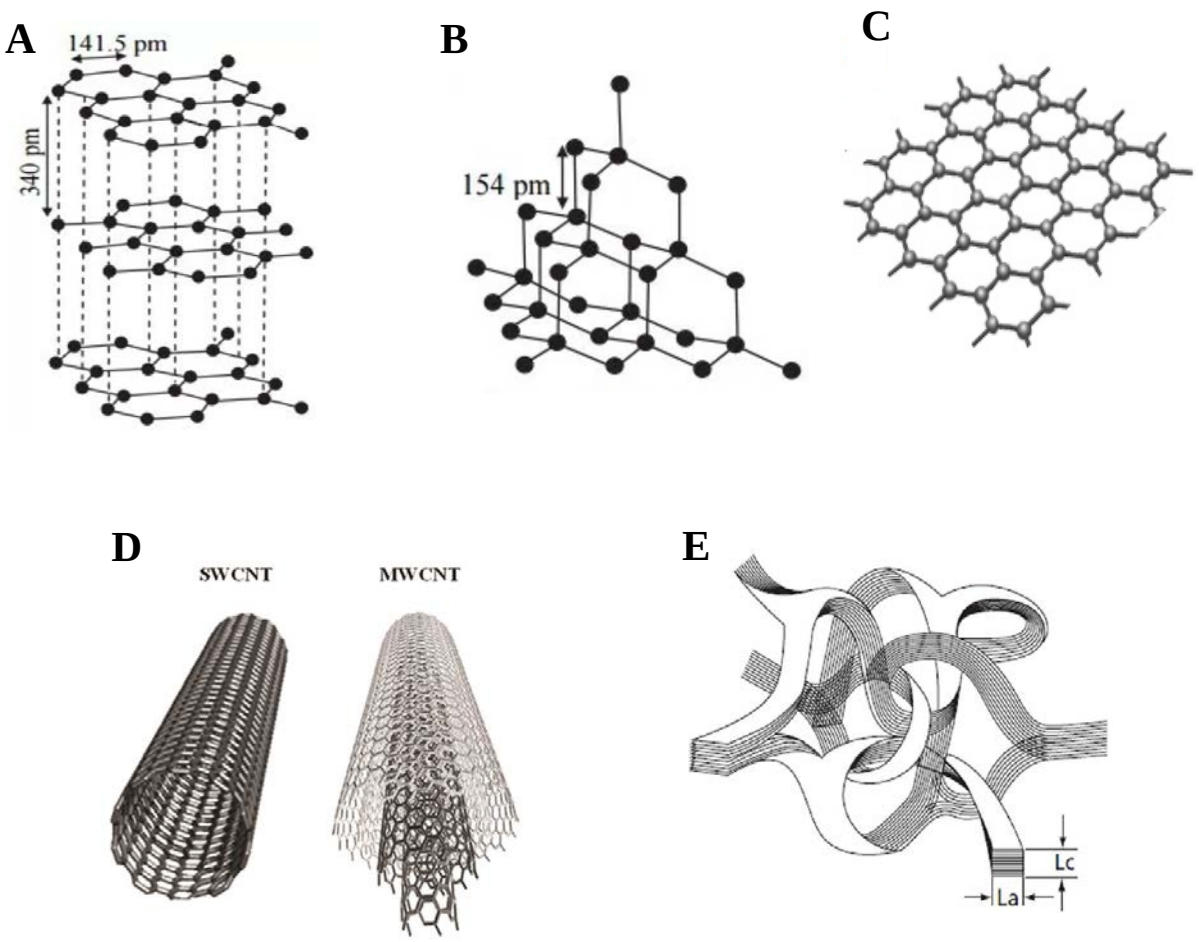

Figure 7 : Structural models of (A) Graphite [93],(B) Diamond [93], (C) Graphene, (D) Rolled up SWCNT and MWCNT [94] and (E) Glassy carbon [95]

Further research on GC by Harris [96] showed some isolated crystals of graphite. This is because the C-C bonds of the polymer precursor do not break and the graphitic region are unable to fully develop into graphene sheets. Based on this observation, Harris suggested that GC consists of sp^2 hybridized carbons forming six-membered rings as well as five and seven membered rings. According to this, GC prepared at different temperatures results in a different amount of dispersed graphene sheets (Figure 8). In this

thesis GC is obtained from the pyrolysis of epoxy resin (SU-8) at high temperatures. The GC is used as the working and counter electrodes for bioelectrochemical applications.

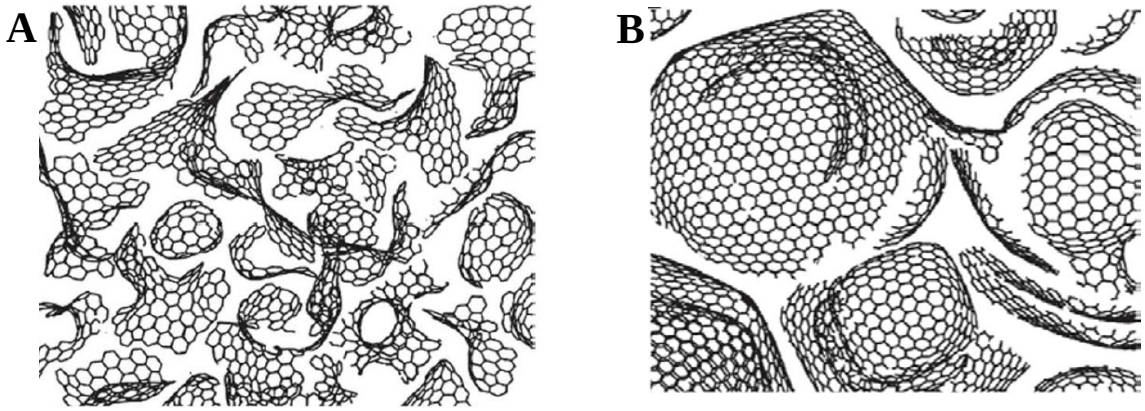

Figure 8 : Glassy carbon at (A) low temperature and (B) high temperature [96]

2.2 Microfabrication processes

2.2.1 UV- photolithography

UV- photolithography is the central part of C-MEMS [74]. UV-photolithography is the most common technique used to pattern the polymer template, which is pyrolyzed to get pyrolytic carbon. Photolithography is a process of transferring a pattern from mask to a light sensitive photoresist by the use of light at a specific wavelength [97,98]. Photolithography is generally performed in five steps.

Figure 9 shows the UV-photolithography process steps to pattern an epoxy based negative photoresist (SU-8). Negative photoresists are the once whereby the parts exposed to UV become cross-linked, while the remainder of the film remains soluble and can be washed away during development. Whereas the positive photoresists are the inverse of the negative photoresists. First, a layer of SU-8 is spin coated on the Si substrate and soft baked (SB) for removal of solvents (Figure 9.A). Next step is to expose the substrate with the SU-8 to UV light through a patterned mask (Figure 9.B) followed by an optional baking (PEB) step (Figure 9.C). The fourth step is the development, where the SU-8 is patterned. Finally, a hard bake step can be introduced to harden the polymer (Figure 9.D).

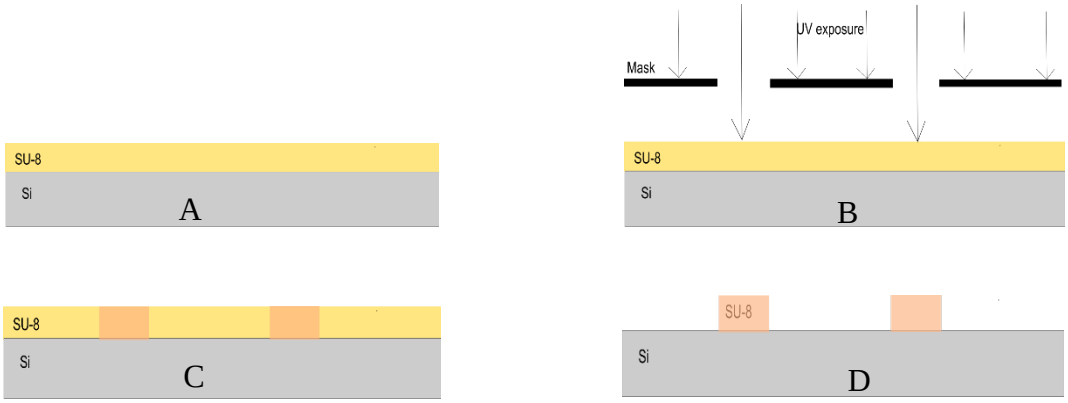

Figure 9: UV-photolithography process steps (A) spin-coating and SB (B) UV exposure (C) PEB and (D) Development followed by hard bake

Three different types of photolithography are present based on the distance of the mask from the substrate.

- `Contact printing' where the mask is in contact with the substrate. This results in high resolution but risks substrate deformation and increases the stiction between mask and substrate.
- `Proximate printing' where the mask is placed at a defined distance from the substrate (< 10 µm). The resolution is less good but the mask and substrate is preserved. In this project all the UV exposures were carried out at proximity.
- `Projection printing' where the light is focused by the use of optics (lenses). Here structures with very high resolution can be produced. The resolution of the projection printing depends on the optics used (numerical aperture). The photolithographic resolution *b* of the contact and proximate printing can be derived as equation 2.1 [99].

$$2b = 3\sqrt{\lambda\left(s + \frac{1}{2}d\right)} \qquad \textbf{2.1}$$

where λ - exposure wavelength, *s* - proximate distance (10 µm typical), *d* - Resist thickness. Figure 10 shows the side view of proximate printing lithography.

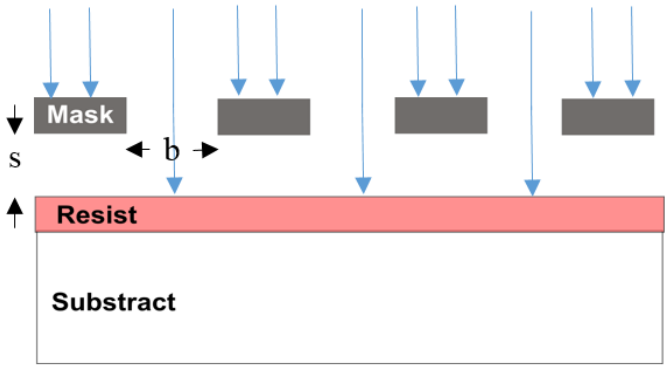

Figure 10 : Proximate photolithography setup

The most typical UV photolithography processes use i-line (365 nm) to transfer the pattern onto the resist. The UV exposure is equipped with an i-line filter, which filters out all the other wavelengths. Most of the photoresist are also designed to be sensitive at 365 nm. The optical properties of SU-8 is shown in Figure 11 [100]. SU-8 is highly absorbing below 350 nm wavelength and highly transmitting above 400 nm. This property is exploited in the fabrication of suspended SU-8 microstructures for 3D carbon microelectrodes.

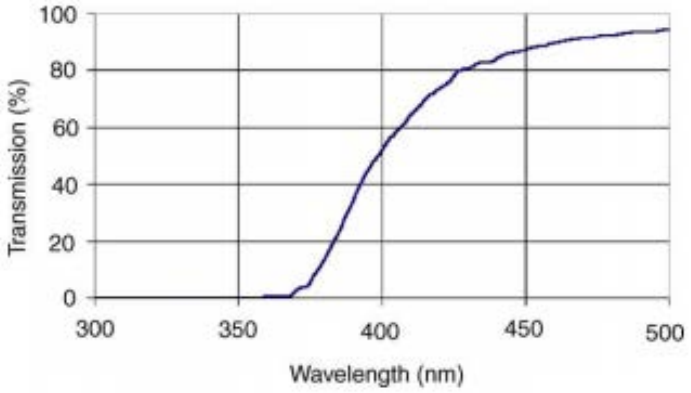

Figure 11: UV transmission of 1 mm SU-8 8100 [101]

2.2.2 Electron beam evaporation

Electron beam (e-beam) evaporation is a form of physical vapor deposition in which a target material at the anode is bombarded with an electron beam in high vacuum conditions. The electron beam causes atoms from the target material to transform into the gaseous phase. These atoms then precipitate into solid form on the substrate [102]. Figure 12 shows the e-beam evaporation set-up, where a tungsten filament

is used to generate the electron beam. The advantages of this deposition technique is that it has a high material utilization efficiency and provides high structural and morphological control of deposited films. The disadvantage of this process is that the filament degradation in the electron gun results in non-uniform evaporation rate and that it is difficult to coat inner surface of complex geometries [103,104]. In the context of this thesis e-beam was used for the deposition of metal contacts.

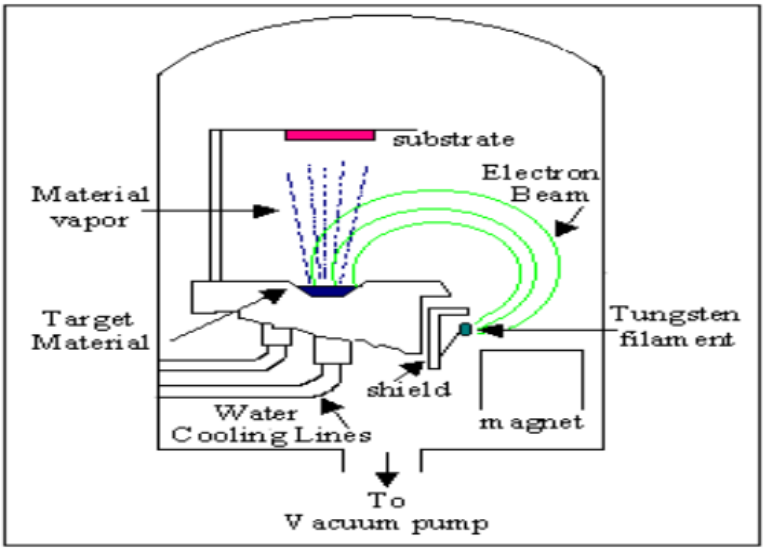

Figure 12 : Experimental set up of electron beam evaporation method [104]

2.3 Pyrolysis

Pyrolysis or carbonization is a thermochemical decomposition of an organic material at high temperatures in an inert atmosphere. Pyrolysis can happen at different temperatures, atmospheres (e.g. nitrogen, forming gas, argon) and pressures (e.g. ambient or vacuum). Depending on the initial kind of polymer template, polymer can change to liquid state [105], be eliminated as gas [89] or remain intact [106–108] during the pyrolysis. Pyrolysis can be divided into three steps for thermosetting resins (e.g. SU-8) as shown in Figure 13 [85]. In the pre-carbonation step below 300 ºC, unreacted monomers and solvent molecules are eliminated. In the first step of carbonization, halogens and heteroatoms like oxygen are eliminated between 300 ºC – 500 ºC. This also results in a rapid mass loss for the polymer precursor. During the second step of carbonization, hydrogen, oxygen, and nitrogen atoms attached to carbon are removed and the aromatic network is formed. At the end of this step the density, hardness, and electrical

conductivity increases. The third and final step is for temperatures above 1200 ºC where annealing occurs and the remaining impurities are removed. The degree of carbonization, which determines the conductivity of the carbon depends on the final process temperature. The inert atmosphere leads to an oxygen deprived surface.

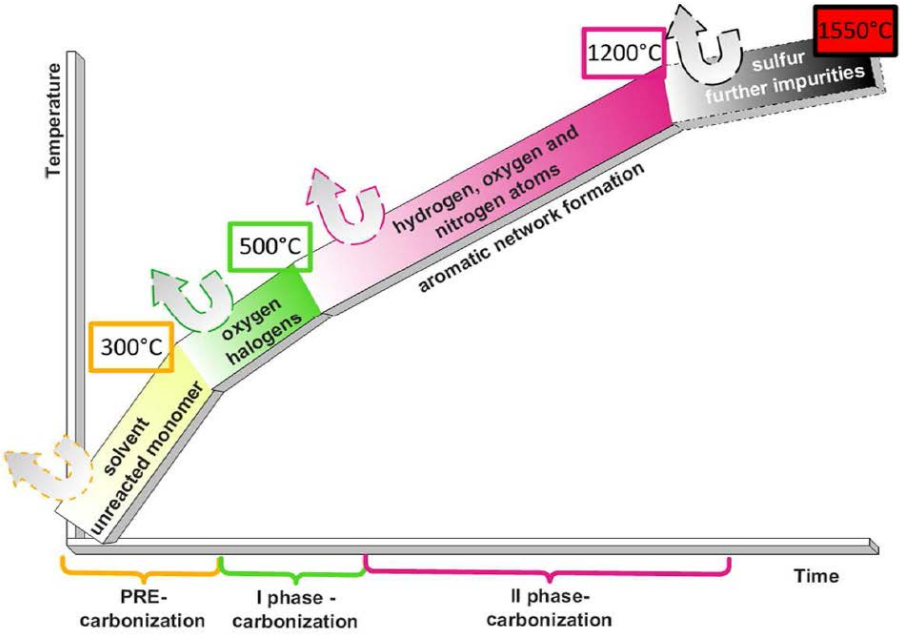

Figure 13 : Different phases in a pyrolysis of organic compound [38]

The selection of the polymer precursor is an important factor in obtaining glass-like carbon structures after pyrolysis. Different polymers like epoxy resins [110–112], polyimides [113,114], phenolic resins [115], furfuryl alcohol resins [116], polystyrene-block-poly (2-vinylpyridine) [117], polyvinyl chloride [118,119], polyvinylidene [120], etc. have been used in the past. Furthermore polymer precursor have been doped with CNTs [121] or beats [70] to increase the mechanical stability and electrical conductivity (Figure 14.A and B). Different polymer template results in various surface topologies and carbon content as shown in Figure 14. C and D. The other important factor affecting the properties of the pyrolytic carbon is the pyrolysis temperature. Higher pyrolysis temperature results in higher conductivity and better electrochemical behavior [122]. This is because at higher temperatures more graphitic regions are formed thereby increasing the conductivity

of the glass-like carbon [63]. However at higher temperatures more stress is observed which increases the probability of jeopardizing the electrode structures [123,124]. One of the main advantages of pyrolysis is that the high flexibility of the polymer template fabrication provides an attractive approach to tailor carbon structures. The pyrolysis process is a simple process with high reproducibility, high yield and additionally it is cost effective compared to metal electrodes. In this thesis the SU-8 polymer precursor is pyrolyzed at high temperatures (≤ 900 ºC) in N_2 atmosphere to get corresponding carbon electrodes.

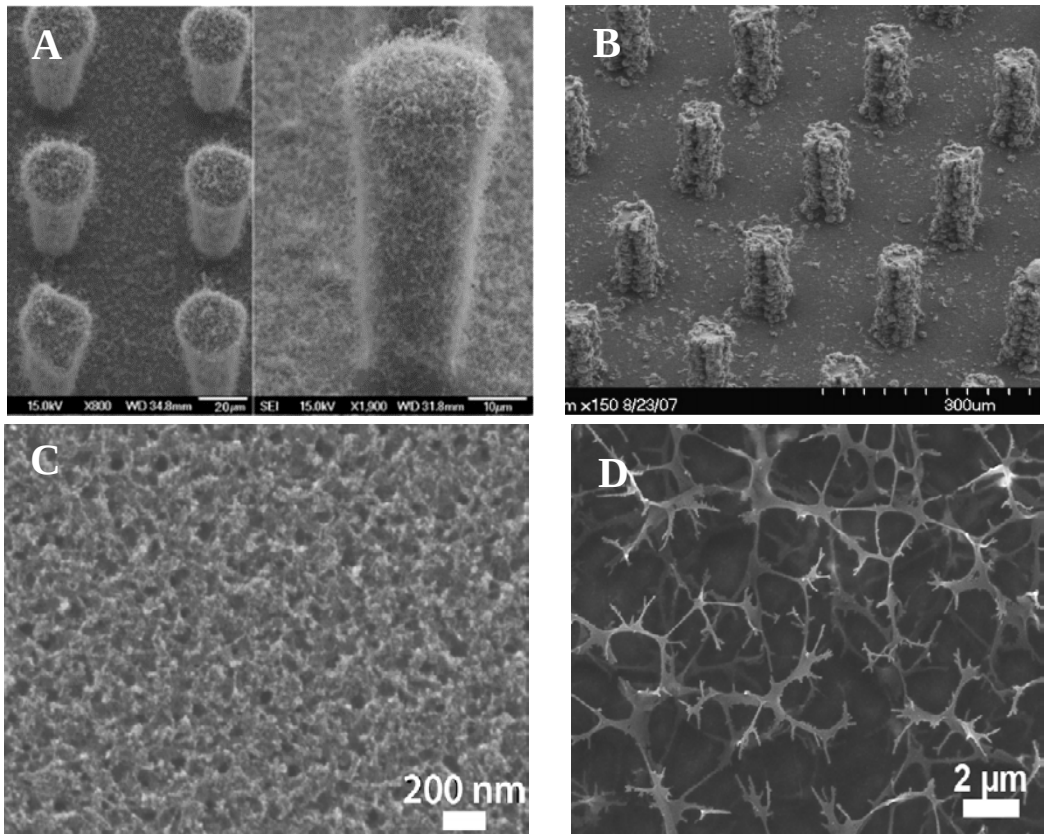

Figure 14 : (A) Pyrolytic carbon with CNTs [121] and (B) Pyrolytic carbon with meso-carbon micro-beads [70] (C) pyrolytic carbon derived from PS[125] (D) pyrolytic carbon derived from PS- PDMS [125]

2.4 Material characterization techniques

2.4.1 Scanning electron microscopy (SEM)

Scanning electron microscopy (SEM) is a traditional electron microscopy technique widely used for structure characterization in materials science, chemistry, biology, and polymer science [126]. By taking

advantage of the short wavelengths of electrons, focused by electromagnetic lenses, the SEM can achieve high-resolution imaging [127]. When a high-energy electron beam is incident on a specimen in a high vacuum SEM chamber, the electrons lose energy by repeated random scattering and absorption within the volume of the specimen. The interaction volume can vary from few nm to mm from the specimen surface depending on factors like electron energy, atomic number of the specimen and the specimen density. Scattering of the beam results in secondary electron (SE), back-scattered electrons (BSE), X-Rays, cathode luminescence and transmitted electrons which all provide details like surface topology and composition [128]. Figure 15 shows the interaction volume and the region from which SE, BSE and X-rays can be detected.

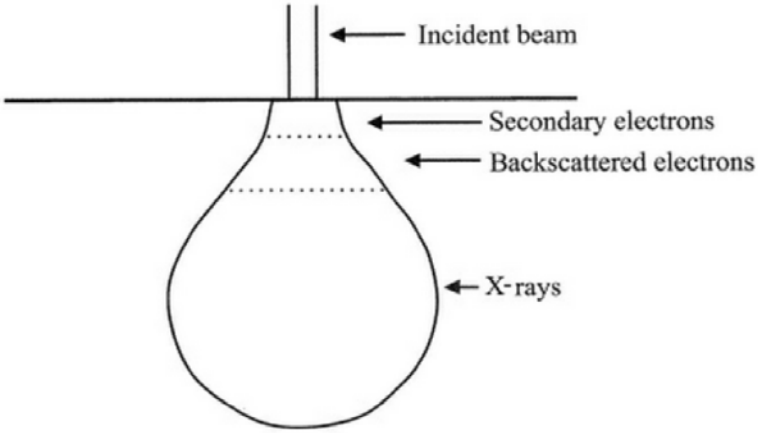

Figure 15 : The interaction volume and the region from which the secondary electrons, the backscattered electrons and the X-rays can be detected [128]

The conventional high vacuum SEM avoids that the gas molecules scatter and absorb the electron beam which results in charging in a non-conducting materials. Hence microstructure characterization within a polymer and surface studies of non-conductive materials remains a challenge. The development of SE detectors and the use of pressure limiting apertures with differential pumping in the path of the electron beam have facilitated the imaging of biological samples, wet samples, insulators, and polymers. Variable pressure scanning electron microscopy (VP-SEM) is one of the most promising and upcoming techniques for polymer analysis [129,130]. Two of the most important aspects of this instrument are its ability to image insulating and poorly conducting materials because of the presence of gas in the microscope [131] and the development of a charge contrast imaging technique, which has unique benefits for the study of the inhomogeneous chemistry of complex materials [132]. In a VP-SEM a positively charged detector electrode

is placed at the base of the objective lens above the sample chamber. An electric field is therefore established between the anode and the specimen. As the primary electron beam hits the sample surface, secondary electron emitted from the sample are attracted to the positive electrode, undergoing acceleration through the electric field between the grounded specimen stage and the positively biased anode. As they travel through the gaseous environment, collisions occur between electrons and the gas particles, producing more electrons and leading to ionization of the gas molecules [128]. This event effectively amplifies the original secondary electron signal (electron cascade). Any electrons on the surface are neutralized rapidly by reaction with positive ions formed by the interaction of the primary beam with the gas molecules led into the microscope. This enables the electrons to be carried away from the surface of the sample, preventing the unwanted charge buildup [128]. Hence this technique is widely used to analyze bio-samples, polymers and wet samples. In this thesis, VP-SEM is used to characterize the SU-8 microstructures. Figure 16 shows the less charging due to VP-SEM.

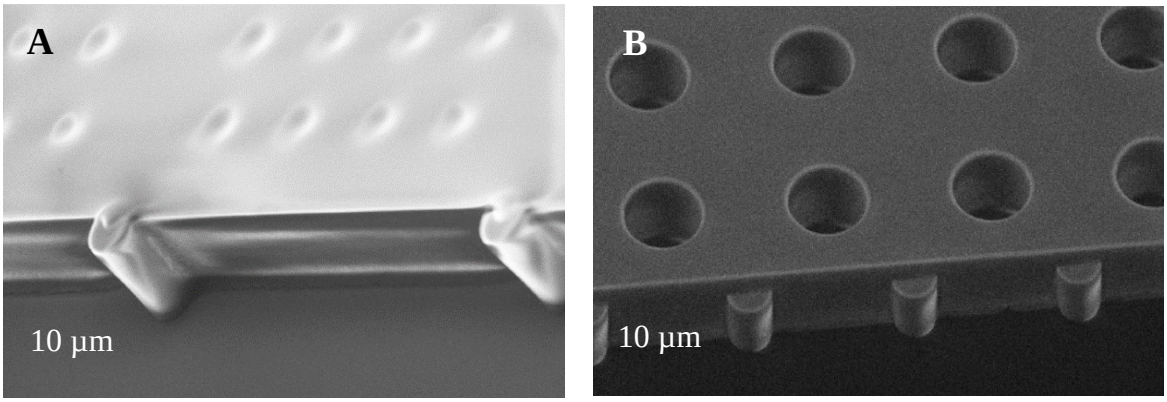

Figure 16: SU-8 images with (A) high pressure and (B) variable pressure

2.4.2 Raman Spectroscopy

Raman spectroscopy can be used to observe vibrational, rotational, and other low-frequency modes in a system [133]. Raman spectroscopy gives a structural footprint which can be used to identify the molecule. [134,135]. Molecules are excited to a higher energy state by a form of energy (light) and during relaxation light is emitted which is known as scattering. When light of frequency v_0 interacts with the molecule of interest, these are excited to an intermediate state called “virtual state”. During relaxation the molecules emit photons via scattering (Figure 17).

For elastic scattering, also known as Rayleigh scattering, the scattered photon is at the same frequency as the incident photon. Rayleigh scattering has the highest probability of occurring. For inelastic scattering also known as Raman scattering, the scattered photon has a different frequency than the incident photon. Here, the total energy is conserved by a change in vibrational energy. There are two types of Raman scattering depending on whether the frequency is up shifted or down shifted. If the vibrational state of the molecule is higher than the initial state, then the emitted photon will be shifted to a lower frequency to ensure that the total energy is conserved (Stokes scattering). Similarly, if the vibrational state of a molecule is less energetic than the initial state, the emitted photon has a higher frequency (anti-Stokes scattering). The wavelength close to the Rayleigh scattering is filtered out and the remaining wavelengths are recorded by a detector for analysis.

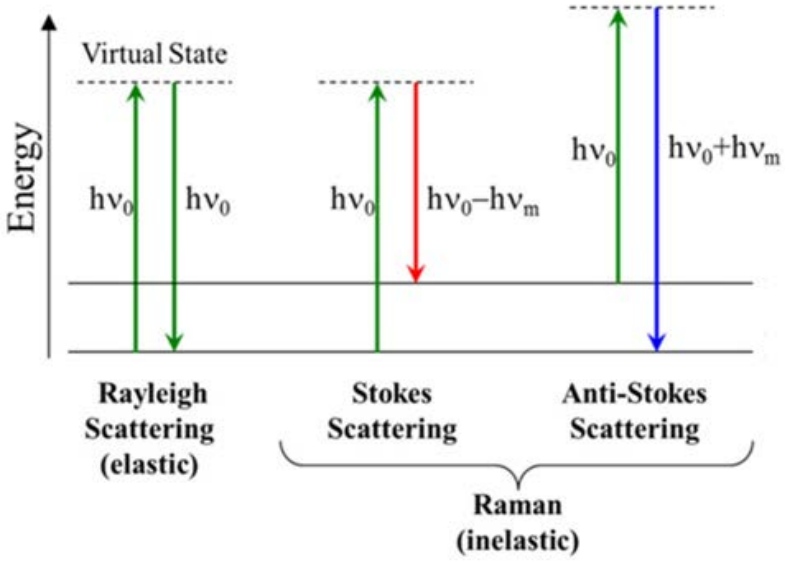

Figure 17 : Quantum Energy Transitions for Rayleigh and Raman Scattering

In this thesis, Raman spectroscopy is used to get information about the degree of disorder of pyrolytic carbon. In pyrolytic carbon, the E_{2g} vibrational mode at 1580 cm^{-1} (also present in graphite) and the A_{1g} vibrational mode at 1360 cm^{-1} are Raman active. Figure 18 shows the Raman spectra of pyrolytic carbon derived from SU-8 photoresist where both D and G peaks are identified, which means that both amorphous and graphitic regions are present as reported previously for pyrolytic carbon [84].

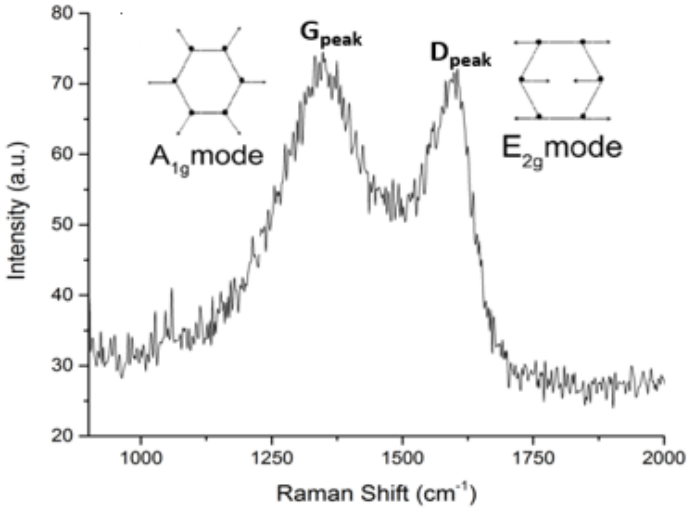

Figure 18: Raman spectra of pyrolytic carbon film

2.4.3 X-ray photoelectron spectroscopy (XPS)

X-ray photoelectron spectroscopy (XPS) is a surface-sensitive quantitative spectroscopic method, which can measure surface elemental configuration, empirical formula, chemical state, and electronic state of elements [136]. The XPS spectra is derived from the binding energies of the electrons in atoms [137]. When an X-ray is projected on the sample, the core electron of the atom has the highest probability to match the X-ray energy. Hence the electrons gain sufficient energy to be ejected from the surface of the sample. Figure 19. A shows the photoelectron generated from the sample after illuminated with X-ray source and Figure 19.B shows the example of the oxygen atom. The energy of the electron (core electron) is characteristic for the particular element. The emitted photoelectron has a kinetic energy proportional to the radiation energy given by equation 2.2.

$$KE = h\nu - E_b - \varphi \qquad 2.2$$

where KE is the kinetic energy of the electron, $h\nu$ is the photon energy (h is the Planck's constant and ν is the frequency of incident radiation), E_b is binding energy and φ is the work function. By calculating the kinetic energy of the emitted photoelectrons, their binding energies in atomic orbitals can be evaluated and plotted as spectrum which determines the relative concentration of atomic elements in the sample. It can also be used to get information on the functional group on the surface [138].

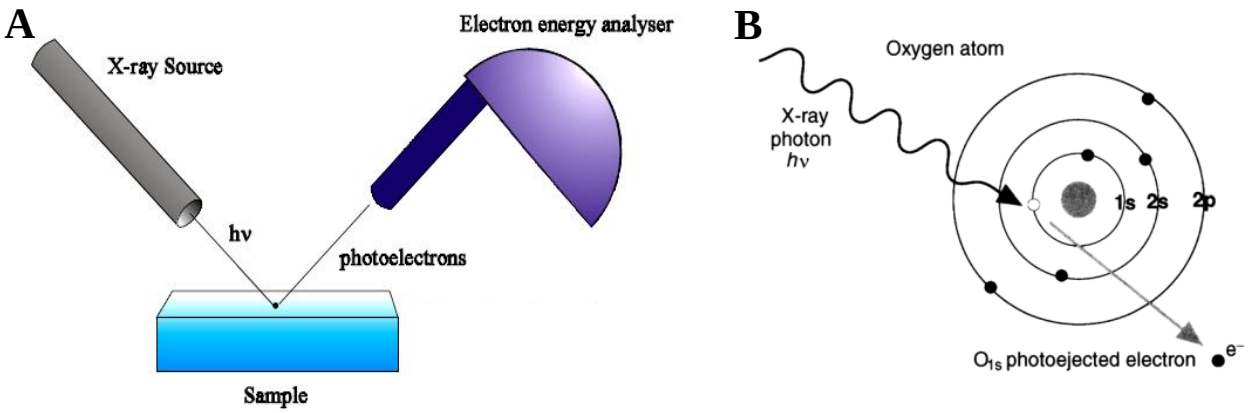

Figure 19 : (A) Photoelectron emitted from the sample due to X-ray illumination and (B) Photoelectron emitted from an oxygen atom [139]

In this thesis, XPS survey spectra were used to evaluate the atomic percentage composition of pyrolytic carbon electrode. The analysis showed carbon (C_{1s}) and oxygen (O_{1s}) peaks between 280 eV -290 eV and 525 eV – 540 eV respectively (Figure 20) which is in accordance with previously reported results for pyrolytic carbon [140]. The carbon microelectrodes consists of 94.3 % of carbon and 5.7 % oxygen.

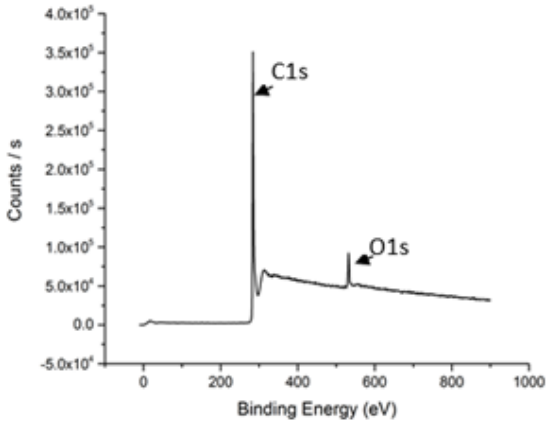

Figure 20: Shows the XPS spectra of pyrolytic carbon film

2.4.4 Four point probe (4PP)

A four point probe (4PP) setup can be used to investigate the electrical properties of a material [141]. A current *I* is applied between the outer two probes and the voltage drop *V* across the inner two probes is measured (Figure 21). The resistance R is calculated by Ohms law (equation 2.3).

$$R = \frac{V}{I}\ [\Omega] \qquad \textbf{2.3}$$

For a thin homogeneous sheet, the sheet resistance (R_s) can be calculated by considering a correction factor (k) which is dependent on the geometry of the sample and the probe. In equation 2.4 the sheet resistance is expressed in ohm per square.

$$R_s = k \times \frac{V}{I}\ [\Omega/\square] \qquad \textbf{2.4}$$

For a known thickness of the layer (t), the resistivity (ρ) of the material can be calculated as shown in equation 2.5. The 4pp was used in measuring the sheet resistance of the carbon electrodes after each pyrolysis step.

$$\rho = R_s \times t \qquad \textbf{2.5}$$

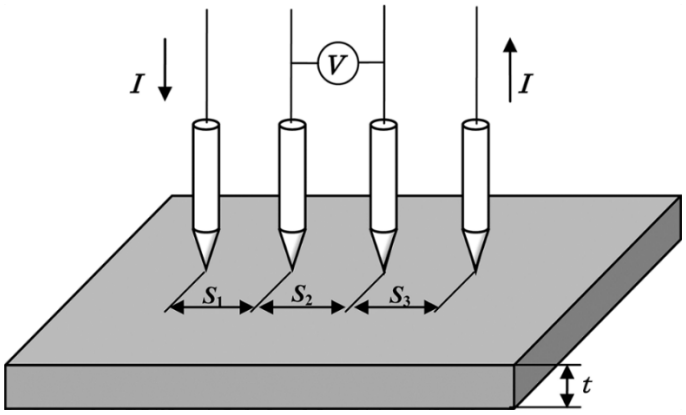

Figure 21 : Experimental setup for 4 point probe [142]

2.5 Electrochemistry

2.5.1 Electrochemical cell

An electrochemical cell consists of two half-cells, one anode and one cathode electrically connected with an electrolyte. Reduction always takes place at the cathode and oxidation at the anode [143]. The basic three electrode electrochemical cell consists of WE, CE and RF. The WE works as the cathode, the CE

as the anode and the RE measures the electrode potential of the cathode. When no current is flowing through the electrochemical cell, an equilibrium is reached. The thermodynamic cell potential or Nernst potential (E_{Nernst}) at this stage is called open circuit potential (OCP) which is given by equation 2.6.

$$E_{Nernst} = E_c \times E_a \qquad \textbf{2.6}$$

where E_c is the electrode potential for the cathode reaction and E_a is the electrode potential for the anodic reaction. E_{Nernst} is the theoretically calculated cell potential necessary to drive the electrochemical cell. For a half-cell reaction it is possible to write the Nernst equation, which relates the electrode potential and the concentration of the electroactive species as shown in equation 2.7.

$$E_M = E_M^0 - \frac{RT}{nF} \, ln \frac{1}{M^{n+}} \qquad \textbf{2.7}$$

where E_M^0 is the standard electrode potential at standard condition, *n* is the number of electrodes, *R* is the gas constant, *F* the Faraday's constant , *T* the absolute temperature and M^{n+} the concentration of the electroactive species in the solution [143].

2.5.2 Electrochemical redox reaction

At equilibrium condition without any current flowing in an electrochemical cell in the presence of a redox couple the Nernst equation can be written as shown in equation 2.8.

$$E = E^{0'} + \frac{0.059}{n} \, log \frac{[Ox]}{[Red]} \qquad \textbf{2.8}$$

where $E^{0'}$ is the electrode potential, [*Ox*] the concentration of oxidized and [*Red*] the concentration of reduced species. When a potential deviating from the Nernst potential is applied across the electrodes, electrons transfer between the electrode and electroactive species in the electrolyte solution occurs, leading to the flow of current in an electrochemical cell.

The potential at the electrode shifts the energy levels of the free electrons, resulting in electron transfer between the conducting material (electrode) and the redox species. By applying a negative potential, the energy of the electrons in the electrode material increases, resulting in a flow of the electrons to the Lowest Unoccupied Molecular Orbital (LUMO) of the electroactive species in the electrolyte.

Consequently, reduction of the oxidized species (Ox) takes place ($Ox + e^- \rightarrow Red$). Similarly, the electron energy level decreases upon applying a positive potential and electrons flow from the Highest Occupied Molecular Orbital (HOMO) to the electrode (Figure 23). Consequently, oxidation of the reduced species in the electrolyte occurs ($Red \rightarrow Ox + e^-$).

For an electrochemical reaction to take place at the electrode surface a potential should be applied deviating from the formal potential $E^{0'}$. The applied positive or negative potential difference with respect to $E^{0'}$ is called overpotential η, which is the driving force for electrochemical reaction. When a potential is applied to the electrode a stagnant layer is formed called the Nernst diffusion layer. During the electrochemical reaction the redox species are replenished through this layer by diffusion, regardless of the overall mass transfer in the bulk solution. The anodic or cathodic current measured is related to the applied potential. Until the limiting current is reached it is given by equation 2.9 (assuming the diffusion of redox species is equal).

$$\eta = \frac{RT}{nF} ln \frac{i_{cl} - i}{i - i_{al}} \qquad \textbf{2.9}$$

where i is the measured current, i_{cl} the cathode limiting current for reduction of oxidized species and i_{ca} the anode limiting current for oxidation of reduced species.

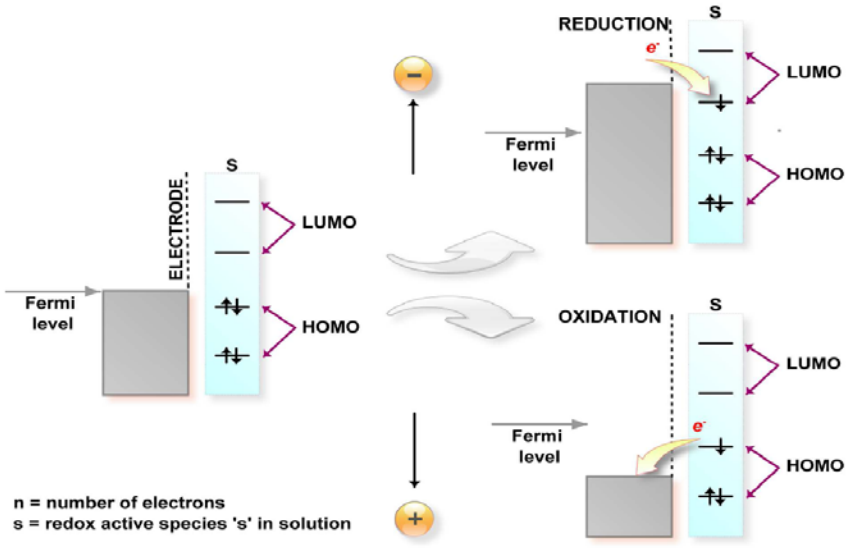

Figure 22 : Energy level at equilibrium and when applying a positive or negative potential to the WE resulting in oxidation or reduction, respectively [38]

2.5.3 Cyclic voltammetry (CV)

Cyclic voltammetry (CV) is a electrochemical measurement technique, where the current at the working electrode (WE) is measured as the potential is ramped linearly with time [143]. CV can be used to study a variety of redox processes, electron transfer kinetics [144], the presence of intermediates in redox systems[145] and reversibly of a reaction [146]. The potential is applied with respect to a stable reference electrode (RE) and the current is measured between the WE and a counter electrode (CE).

In CV, the applied potential is swept forward from an initial potential ($E_{\lambda 1}$) to a final potential ($E_{\lambda 2}$) and then swept back to initial potential in a triangular waveform (Figure 23.A). CV probes the study of electroactive species on the electrodes. During the forward scan the current increases as the potential approaches the oxidation potential of the analyte. As the concentration of the analyte is depleted near the electrode/anode surface the potential drops again (Figure 23.B). The resulting peak current is known as the oxidation peak current or anodic peak current (i_{pa}). When the applied potential is reversed, it will reach a potential at which the reduction of the products formed during the forward scan starts. A current of reverse polarity from the forward scan is recorded and the peak current at the reverse bias is called the reduction peak current or cathodic peak current (i_{pc}). The peak current for a reversible system is described by Randles-Sevcik equation 2.10 [145].

$$i = 2.69 \times 10^5 A n^{3/2} D^{1/2} \nu^{1/2} C \qquad \textbf{2.10}$$

where A is the area of the electrode, ν the scan rate, n the number of electron transferred per reaction, C the concentration of the species and D is the diffusion coefficient.

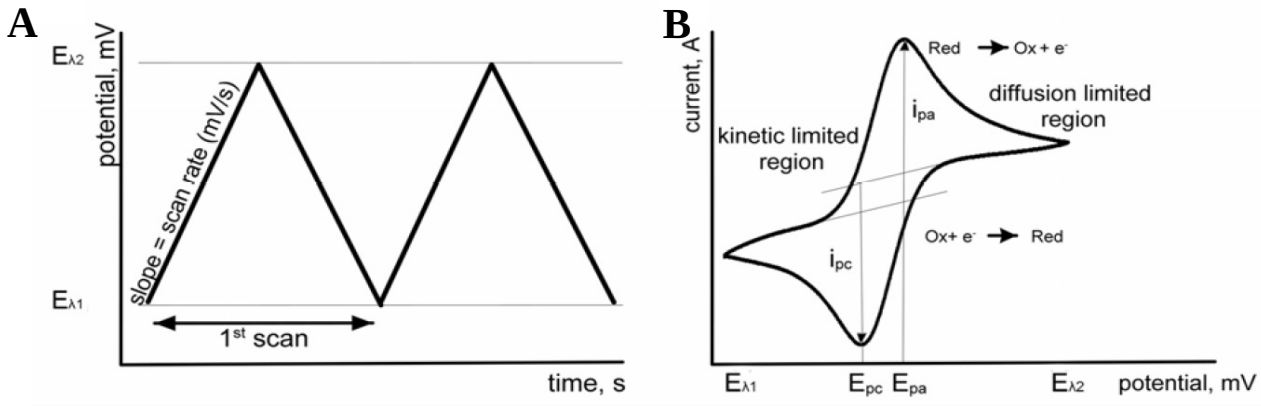

Figure 23 : Cyclic voltammetry (A) Applied potential (B) Resulting voltammogram

For a reversible electron transfer process, the oxidation peak current is equal to the reduction peak current. The potential difference between the oxidation and reduction peaks (E_{pa} - E_{pc}) is theoretically 59/n mV at 25 ºC with n the number of electrons transferred per reactant [147]. Another important parameter is the ratio of peak currents (i_{pa}/i_{pc}) which is always a unity for a Nernstian system. CV can also be used to evaluate the kinetic parameters of redox reaction at the electrode surface which is very useful for electrode surface characterization [145]. In this thesis, CV was used for characterization of the carbon electrodes in potassium ferri-ferrocyanide redox probe.

2.5.4 Amperometry

Amperometry in an electrochemical technique where ions in a solution can be detected based on electric current or changes in electric current for an applied constant potential. The constant potential to be applied can be determined by CV based on the anodic and cathodic peak current. The overpotential at which the desired electrochemical reaction is driven must be high enough to ensure rapid depletion of electroactive species at the electrode surface. The working electrode potential is stepped from a value at which no faradaic reaction happens to a potential at which the surface concentration of electroactive species is zero. Instantly after the step, a large current is identified which decreases exponentially with time due to the depletion of electroactive species close to the electrode surface [148]. The mass transport is only driven by diffusion. The current–time curve reveals the change in concentration gradient in the vicinity of the electrode surface. The Cottrell equation defines the dependence of current response on time for planar diffusion (equation 2.11).

$$i\,(t) = \frac{nFAD_i^{1/2}C_i^*}{\pi^{1/2}t^{1/2}} \qquad \textbf{2.11}$$

where n is the number of electrons involved, F is Faradays constant (C mol^{-1}), A is the electrode area (cm^2), D_i is the diffusion coefficient of electroactive specie i (cm^2 s^{-1}), C_i^* is the bulk concentration of the component i of a redox probe (mol cm^{-3}) and t the time (s). In this thesis, amperometry is used for glucose and dopamine detection.

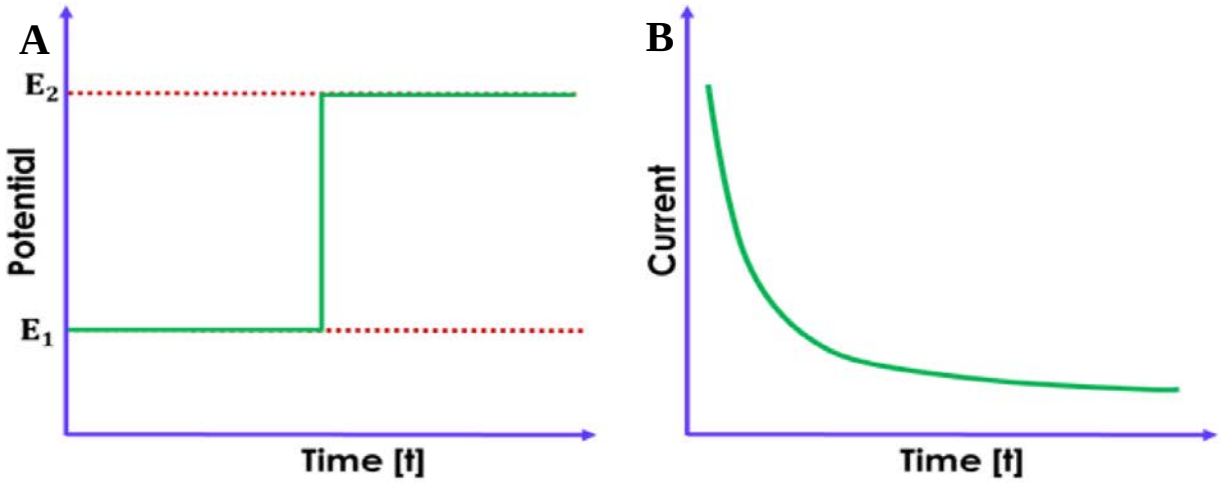

Figure 24: Chronoamperometry. (A) Change in applied potential and (B) Corresponding current response

2.5.5 Squarewave voltammetry (SWV)

The squarewave voltammetry is a sensitive form of linear potential sweep voltammetry technique where the electrochemical cell current is measured as a function of time and as a function of the potential between the working electrode and the reference electrode. The potential waveform can be viewed as a superposition of a regular squarewave onto an underlying staircase waveform (Figure 25.A). The current is measured at the end of each half-wave, just prior to the potential change (Figure 25.B) [149,150]. The magnitude of the peak current (i) is given by [143]:

$$i = \frac{nFAD_0^{1/2}C_0^*}{(\pi t_p)^{1/2}}\,\Delta\varphi \qquad \textbf{2.12}$$

where A is the surface area of the electrode, C_0^* the concentration of the species, D_0 is the diffusion parameter of the species, t_p is the pulse width, and $\Delta\varphi$ is a dimensionless parameter which gauges the peak height in SWV relative to the limiting response in normal pulse voltammetry. In this thesis SWV was used for dopamine and bone cell monitoring.

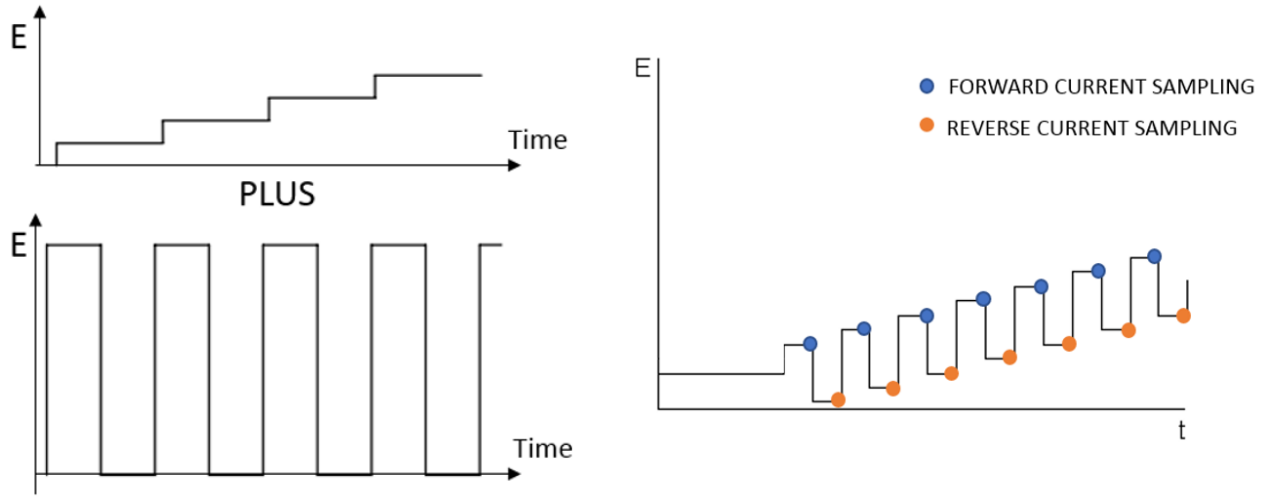

Figure 25: (A) superposition of regular squarewave onto an underlying staircase waveform [150] (B) Schematic representation of the current sampling in SWV [150]

2.5.6 Electrochemical impedance spectroscopy (EIS)

Electrochemical impedance spectroscopy (EIS) is a powerful technique to characterize an electrochemical system [151]. It is used in investigating the complex electrical resistance of the electrode surface and the bulk [152]. In general two electrode (WE and CE) configuration is used to measure the impedance of the system. The impedance *Z* of a system is determined by applying a sinusoidal potential *V* and detecting the current *I* between WE and CE. The applied potential can be expressed as a function of time t as shown in equation 2.13.

$$V\ (t) = V_0\ sin(2\pi f t) = \ V_0 sin(\omega t) \qquad \textbf{2.13}$$

with V_0 the maximum voltage and ω the angular frequency. The maximum voltage V_0 is generally small. Therefore, the current response can be considered as pseudo-linear. Equation 2.14 shows the current response *I*, which is of the same frequency *f* but shifted in phase ∅ and has an amplitude I_0. This shift is due to the capacitive and resistive behavior of the system. A shift of 0° indicates a purely resistive and a shift of -90° indicates a purely capacitive system.

$$I\ (t) = I_0 sin(\omega t + \emptyset) \qquad \textbf{2.14}$$

According to Ohm's law, the impedance is the ratio of voltage time function *V(t)* and the resulting current time function *I(t)* (equation 2.15).

$$Z\ (\omega) = \frac{V(t)}{I(t)} = \frac{V_0 sin(\omega t)}{I_0 sin(\omega t + \emptyset)} \qquad \textbf{2.15}$$

The impedance is a complex value and can be expressed as a modulus $|Z|$ and the phase shift $\emptyset$ or by the real Z_R and imaginary Z_I parts. Using Euler's relationship

$$e^{j\emptyset} = cos(\emptyset) + j\ sin(\emptyset) \qquad \textbf{2.16}$$

The impedance Z can be expressed as

$$Z\ (\omega) = \frac{V}{I} = \frac{V_0 e^{j\omega t}}{I_0 e^{j\omega t - \emptyset}} = \ |Z| e^{j\emptyset} \qquad \textbf{2.17}$$

$$|Z| e^{j\emptyset} = \ |Z|\ cos(\emptyset) + j\ sin(\emptyset) = Z_R(\omega) + Z_I(\omega) \qquad \textbf{2.18}$$

where $\emptyset = arctan\ (Z_I/Z_R)$ and $|Z|^2 = |Z_R|^2 + |Z_I|^2$. $Z_R\ (\omega)$ and $Z_I\ (\omega)$ represents the restrictive and capacitive components of the system respectively.

When the electrode is immersed in an electrolyte solution and a potential is applied, a double layer is formed between the electrode surface and the electrolyte. The model used to describe the charge distribution at the electrode –electrolyte interface at atomic level is called electrical double layer (EDL). Figure 26 illustrates the different layers at the electrode- electrolyte interface. The layer closest to the electrode is called "inner Helmholtz layer" and consists of solvent molecules and adsorbed ions. The inner Helmholtz plane (IHP) contains specifically adsorbed ions. The next layer is the outer Helmholtz layer that covers the transition of ions from electrode surface to the bulk solution. In this layer the ions are not adsorbed on the electrodes since they are shielded by an IHP. The ions interact with the electrode through a weak long-range electrostatic forces. The outer Helmholtz plane (OHP) contains the nearest solvent ions. The nonspecifically adsorbed ions are distributed in the region that extends from OHP into the bulk of the solution called the diffusion layer.

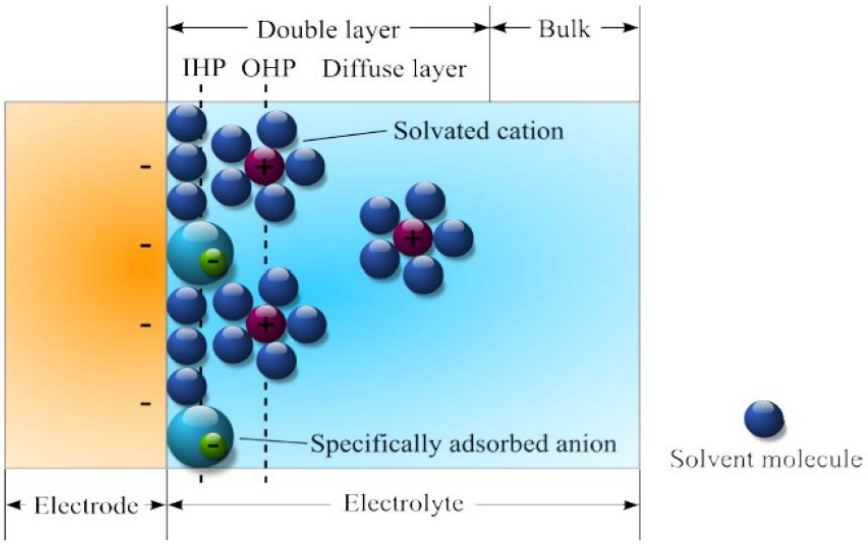

Figure 26 : Illustration of charge distributions within at the electrode-electrolyte interface [153].

2.5.7 Impedance contribution in EIS

In an electrochemical system, impedance measurements are usually carried out with a two electrode configuration. The sensing electrode as the working electrode (WE) and a counter electrode (CE). When performing an impedance measurement, the recorded impedance consists of the sum of the different contributions (Figure 27). There is the contribution of the electrode/electrolyte interface on the WE, the impedance of the solution and the electrode/electrolyte interface of the CE. These contributions depend on the electrode material, the electrolyte, and the geometry of the system. In addition, parasitics from connecting wires and stray capacitance, will influence the measured impedance.

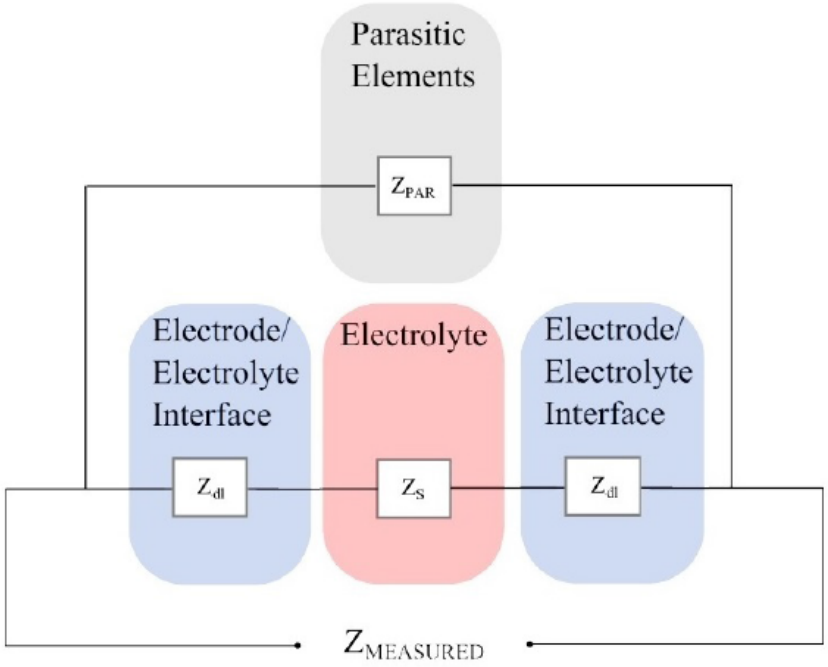

Figure 27: Illustration of the different contributions for impedance measurements [153]

The overall electrochemical system can be represented by electrical circuit models, which explains the physical phenomena that contribute to the measured impedance. The behavior of the electrode-electrolyte interface resembles the behavior of a capacitor. When a potential is applied across the electrode – electrolyte interface, charges accumulate in close proximity of the interface and form an EDL. This current is called charging or capacitive current. The total electrochemical system can be expressed as the electrode – electrolyte interface, described by a double layer capacitor C_{dl} and the resistance of the solution as resistor R_s (Figure 28.A). The impedance can be expressed as in equation 2.19.

$$Z_{E-E\ interface} = \frac{1}{j\omega C_{dl}} + R_s \qquad \textbf{2.19}$$

At lower frequencies the capacitive contributions dominate and the impedance is determined by the charged interface. At higher frequencies the capacitance is short-circuited, the resistive contributions are dominating and impedance is dependent on the bulk solution. To include surface factors such as roughness or absorption the capacitor is replaced by a constant phase element (CPE) as shown in Figure 28.B. The impedance of CPE is described by equation 2.20.

$$Z_{CPE} = \frac{1}{C(j\omega)^n} \qquad \textbf{2.20}$$

where *C* is the capacitance and *n* is a number between 0 and 1, which indicates the degree of capacitive (n=1) or resistivity (n=0) properties.

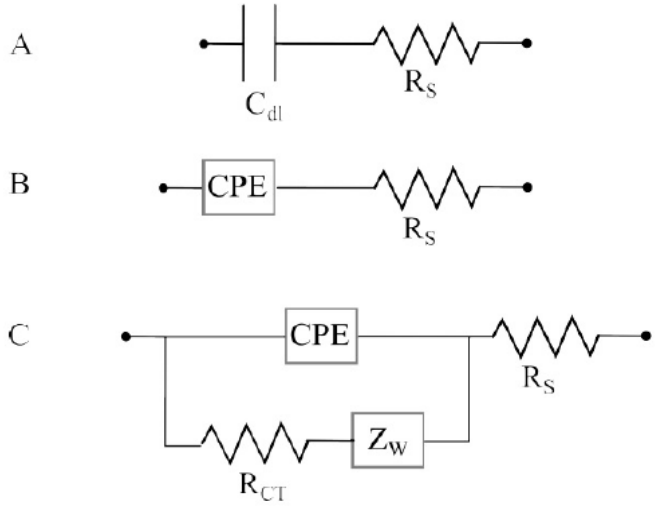

Figure 28 : General equivalent circuit models for electrode-electrolyte interfaces (A) simple (ideal) electrode, (B) including CPE to include the surface characteristics and (C) in the presence of a redox probe

If the electrolyte contains a redox couple, the occurring redox reaction results in mass and charge transfer which effects the electrochemical behavior of the system. This results in adding two components in parallel to the interface capacitance (Figure 28.C). The Warburg impedance Z_W models the influence of diffusion on the electron transfer rate. The charge transfer resistance R_{CT} controls the kinetics of electrochemical reaction which can be given as shown in equation 2.21 [143].

$$R_{CT} = \frac{RT}{C`n^2F^2Ak^0} \qquad \textbf{2.21}$$

where *R* is the molar gas constant, *T* the absolute temperature, *C`* the equal concentration of the redox probe, *n* the number of electrons involved in the redox process, *F* the Faraday constant, *A* the electrode area available for the reaction and k^o the apparent standard rate constant.

The impedance can be plotted in two different ways namely as Bode plot and Nyquist plot. Both give a clear visualization of system characteristics. The Nyquist plot typically consists of a semicircle and a linear region as shown in Figure 29. The semicircle diameter in the plot represents the charge-transfer resistance (R_{CT}), which defines the electron transfer limitation. The highest point of the semicircle can

be used to derive the electrical double layer capacitance C_{dl}. The intercept of the semicircle at the real axis is related to the sum of the solution and external resistance (R_{tot}). The linear portion at low frequencies characterizes the diffusion-limited process. In this thesis impedance is measured to characterize the electrode and also in yeast analysis.

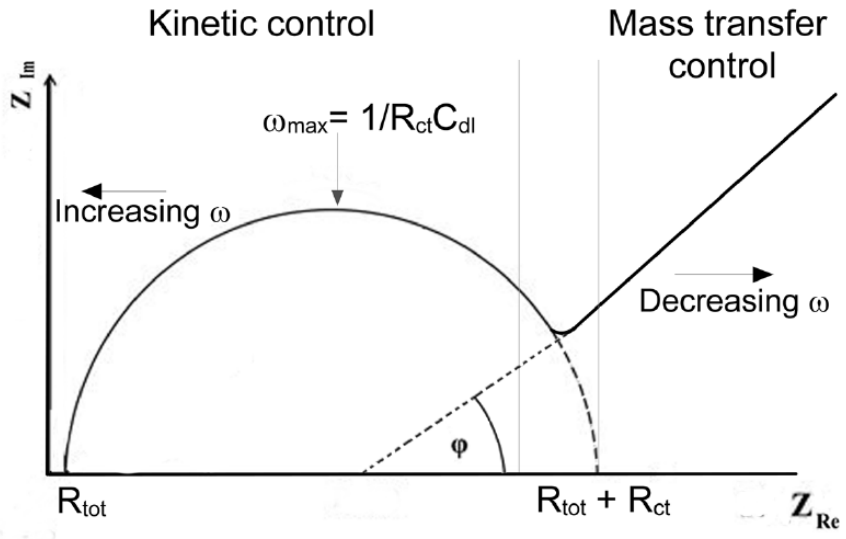

Figure 29: Illustration of Nyquist plot resulting in an electrolyte containing a redox-probe.

Chapter 3

Microfluidic systems (MagClamp)

Microfluidics can be defined as the science and technology of systems that process or manipulate small amounts of fluids, using channels with dimensions of tens to hundreds of micrometers [154–156]. Microfluidic devices provide numerous advantages such as, the ability to use very small quantities of samples and reagents, carry out separations and detections with high resolution and sensitivity, short times for analysis, and small footprints for the analytical devices [157–161]. In this thesis, two microfluidic devices with magnetic clamping were developed for characterization of carbon electrodes in static and flow conditions. The design of the microfluidic systems was optimized in a finite element software (COMSOL).

3.1 Batch systems

To characterize the carbon electrodes in static condition the MagClamp batch system was developed. The fabrication process of the batch systems is illustrated in Figure 30 and described in more detail in paper I. The batch system was fabricated by laser micromachining of poly-methyl-methacrylate (PMMA) of different thickness and bonded together with pressure sensitive adhesive (PSA). Figure 31 shows the C4B chip integrated in the MagClamp batch system. The batch system was used to hold a defined quantity of liquid (300 µL) on the carbon electrode for electrochemical characterization.

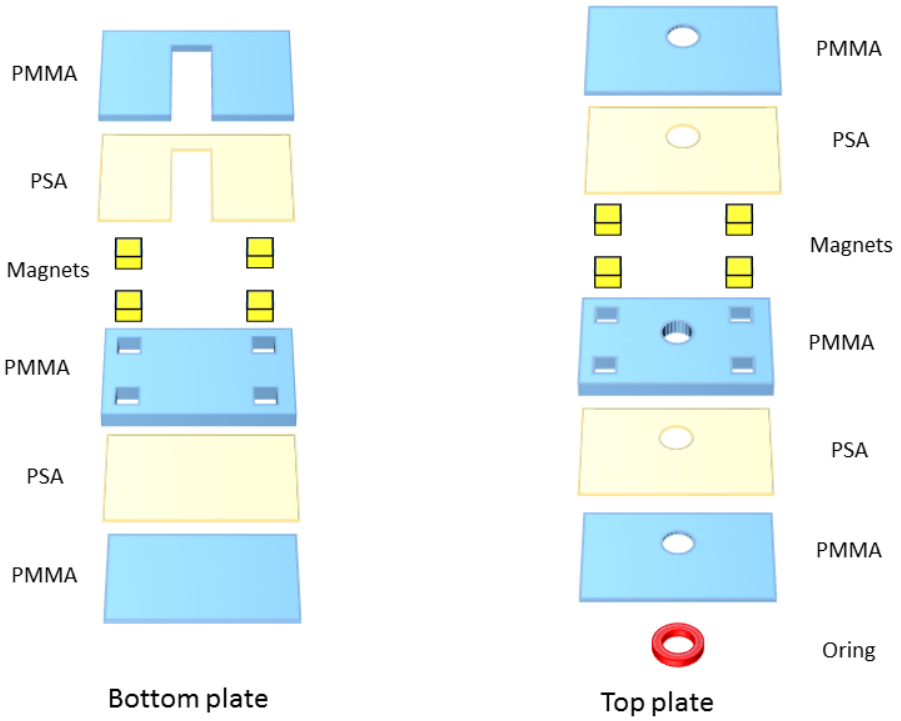

Figure 30: Different components in the magnetically clamped batch system[162]

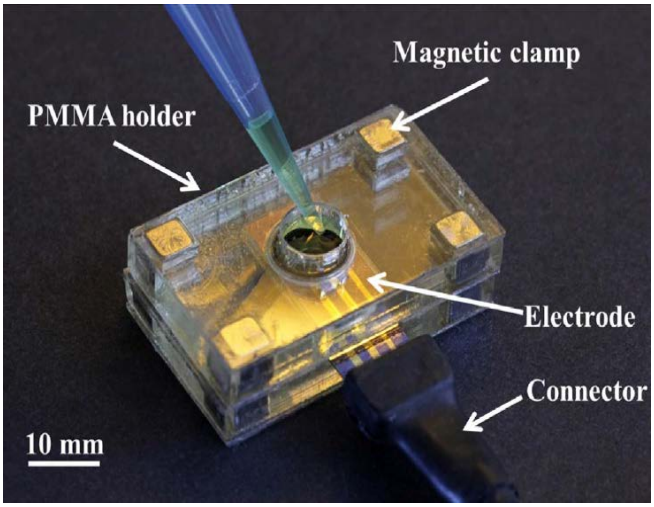

Figure 31: Experimental setup with C4B chips integrated in MagClamp system

3.2 Microfluidic systems

The batch systems can be used to characterize the electrodes in static condition but it's very difficult to achieve to fast response, continuous nutrient feed, waste removal etc. In this thesis, microfluidic systems were developed to analysis non adherent cells (yeast cells) on the electrodes. The systems were optimized for minimal shear stress on the electrode and smallest response time to reach maximum concentration upon exchange of liquid or introduction of external stimuli. The microfluidic systems was used to provide nutrients to yeast cells without drastically distributing the cells.

3.2.1 COMSOL simulations

Three different types of microfluidic systems were studied by finite element simulation in COMSOL for integrating carbon electrodes in a microfluidic system. The carbon electrodes were assumed to be at the bottom of the microfluidic chamber similar to the batch system. Figure 32 shows the design of the three systems selected for investigation. The flow systems were considered because they offer minimal shear stress on the electrodes, since the analyte transport is mainly diffusion controlled. The wall-jet system offer a higher stress but provide a fast response time, which is significant in cell biology. Flow-thought systems was also investigated, since they offer a minimal response time.

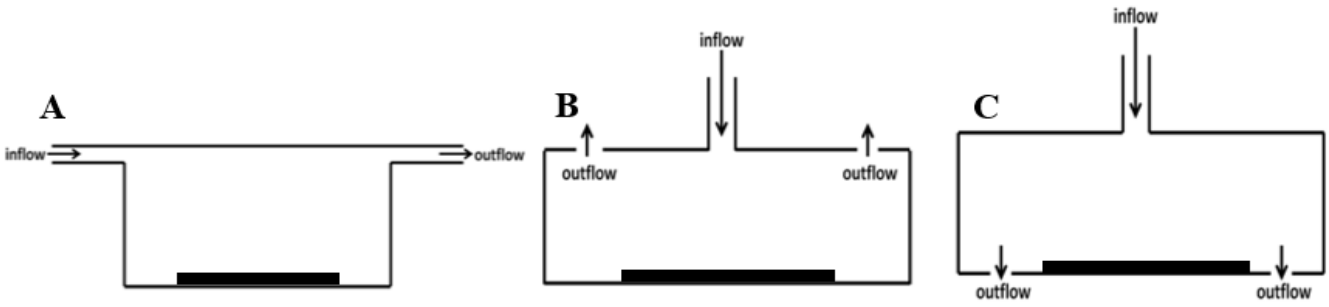

Figure 32 : (A) Flow system (B) wall-jet system and (C) flow-through system (▬ electrode area)

The microfluidic systems were represented as 2D models as shown in Figure 33. The working electrode was 4 mm in diameter and 2 µm in thickness. For initial simulations the height of the chamber was set to 1.5 mm. The diameter of the inlet and the outlet were set to 800 µm [163]. The width of the chamber was 8mm. For the initial tests to determine the best systems for cell based applications, a laminar flow Multiphysics was selected in COMSOL 5.2.a. The module assumes a laminar flow across the channels

and the chamber when there is no drastic change in material geometry, media, pressure, or temperature. The chamber was assumed to be filled with PBS. The constant flow rate and concentration of a media (glucose) were constant at the inlets and were set as 20 µL/min and 10 mM/m^3 respectively. This experimental setup will mimic the media exchange on the electrode in ideal conditions. The glucose diffusion coefficient was set to be 0.6×10^{-9} m^2/s [164]. All the studies were conducted at room temperature and all other conditions are neglected. For finite element simulation a very fine mesh is established along the electrode. A time dependent study is performed to analyze the change in concentration and shear stress along the electrode.

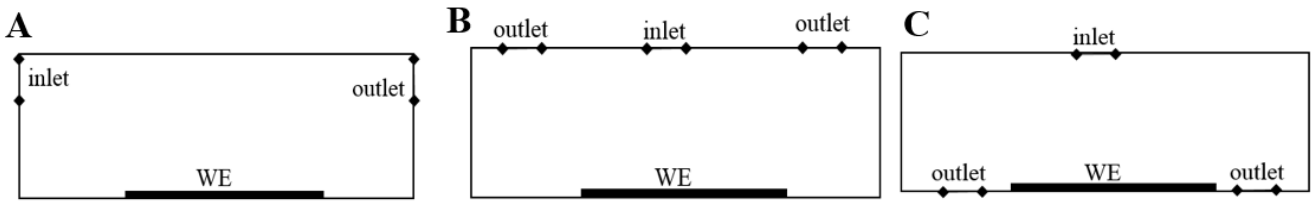

Figure 33: 2D models of (A) flow system (B) wall-jet system and (C) flow-through system

Table 1 summarizes the time required to reach the maximum concentration (response time) on the electrode (WE) surface and the average shear stress along the electrode at that time for the three designs. The flow system has a minimum shear stress but has the highest response time. The flow through system has the highest shear stress and the fastest response time. But the wall-jet system has a comparable response time with a lower shear stress when compared to flow through system. In this thesis wall-jet systems were selected for all further optimizations. Table 2 shows the concentration gradient at time T = 60 s and at the end of the experiment (i.e. when the maximum concentration is reached). Table 2 also shows the shear stress profile at the end of the experiment.

Table 1 : Average shear stress and response time to reach maximum concentration for different microfluidic systems

System	Shear $stress_{av}$ (µPa)	Response time (s)
Flow	0.00001	1091
Wall-jet	0.00724	261
Flow-through	0.00974	240

Table 2: Concentrations and shear stress at different time during the experimental

	Concentration at $T_{60\ s}$	Concentration T_{end}	Shear stress at T_{end}
Flow system	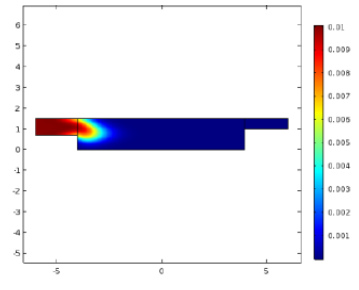	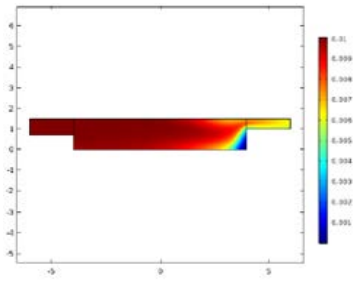	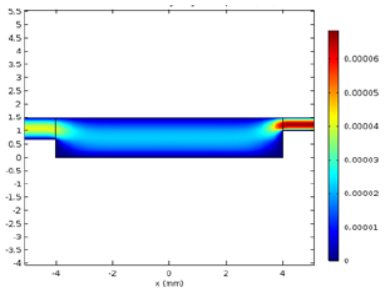
Wall-jet system	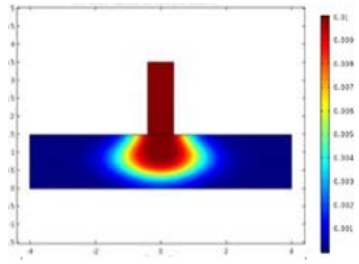	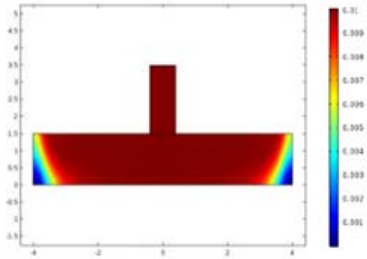	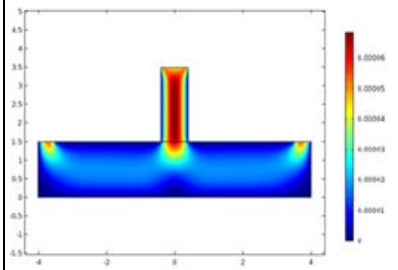
Flow-through system	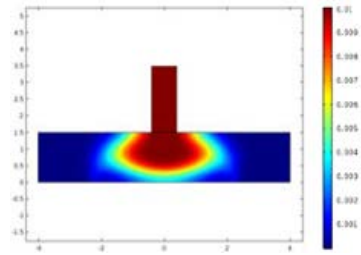	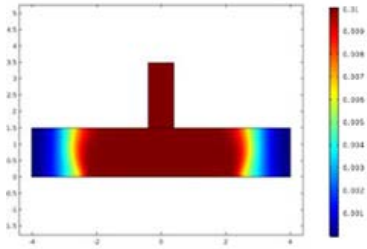	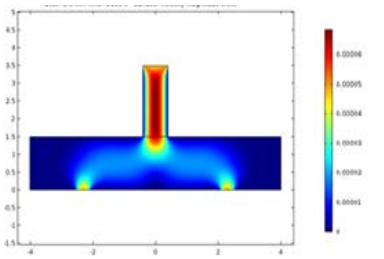

In the wall-jet system the height of the chamber and the position of the outlets are optimized to have a faster response time and minimum shear stress. To further reduce the shear stress on the WE, the flow rate was reduced to 10 µL/min in the following experiments. The system is symmetrical along the center hence an axial symmetry is added at the center. Figure 34.A shows the change in response time as the height of the chamber is varied. The smallest chamber height resulted in the fastest response because the glucose can reach the electrode surface faster. However, the smaller chamber height results in a higher shear stress (Figure 34.B). Hence a wall-jet system with a chamber height of 1.5 mm was selected. The second parameter is the factor k, i.e. the distance of the outlets from the center of the chamber. Figure 34.C and D show the concentration distribution of the glucose and shear stress on the electrode when the

position of the outlets is varied. As the position of the outlet is varied the distribution of glucose and shear stress remains constant at the center of the electrode and has a small variation at the edges. Hence the position of the outlet doesn't matter for the selected range of dimensions. The final optimized wall-jet system has a chamber height of 1.5 mm and outlets at 2 mm from center.

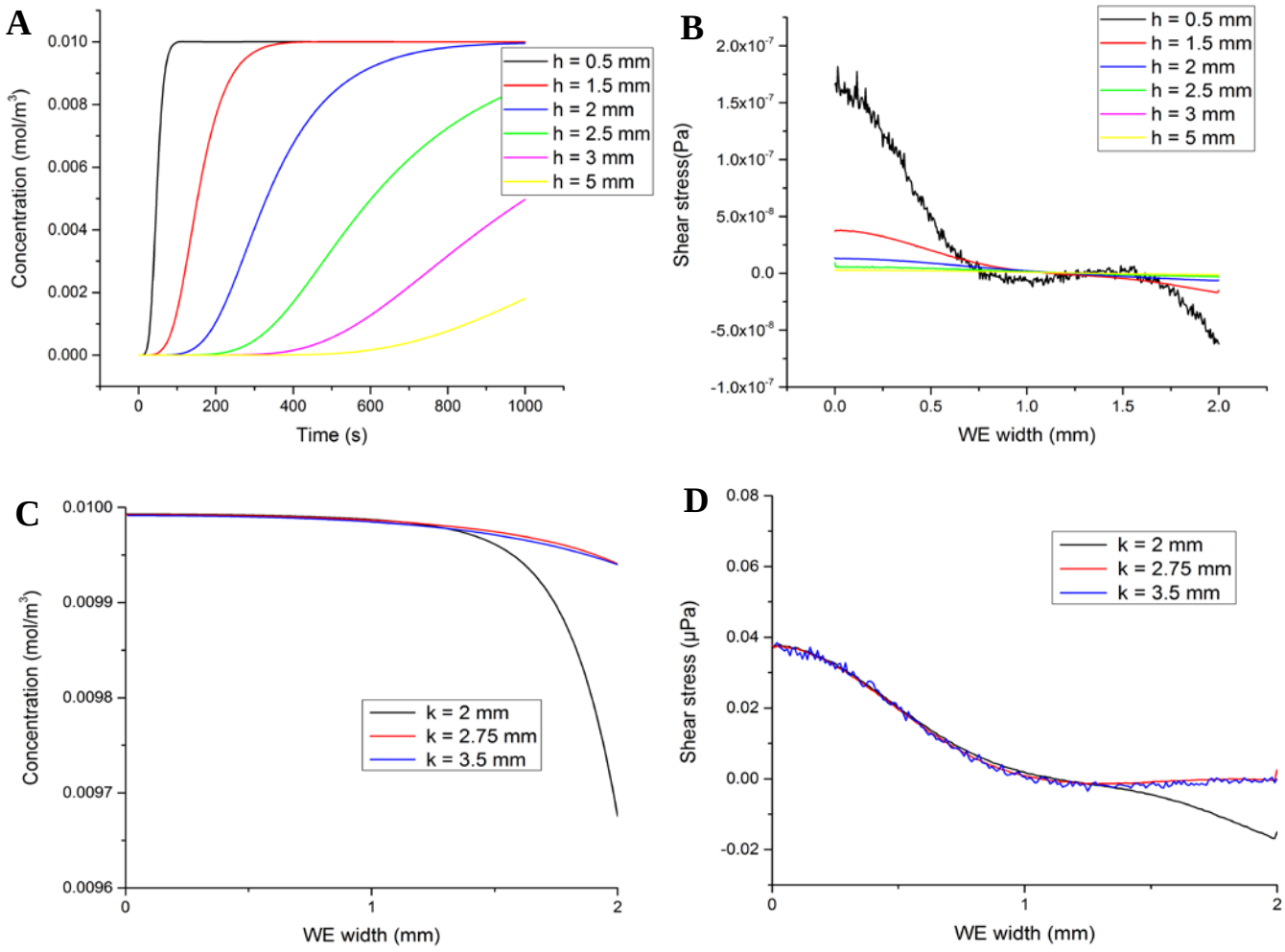

Figure 34: (A) concentration of glucose on the electrode with respect to time, (B) shear stress on the WE as the chamber height is changed (C) - (D) concentration profile and shear stress on the electrode as the outlets are moved

3.2.2 Fabrication of wall-jet system

The wall-jet system was fabricated by micro-milling PMMA sheets and bonding them together by PSA. Figure 35 shows the different layers in the system. The topmost part (1) consists of a magnet holder and an external connection port. The microfluidic channels were micro-milled on the third PMMA sheet (3)

1 mm and the channels were closed by another PMMA sheet (2) with a thickness of 0.5 mm on top. The fourth layer of PMMA (4) has a thickness of 1.5 mm includes a slot for the O-ring, which is very important to achieve a good sealing around the electrodes. This layer also defines the height of the microfluidic chamber. The fifth layer (t = 0.5 mm) has a slot for integrating the carbon chip. The sixth layer has the slots for the magnets and a seventh layer of PMMA (t = 0.5 mm) is used to seal the magnets in their respective slots.

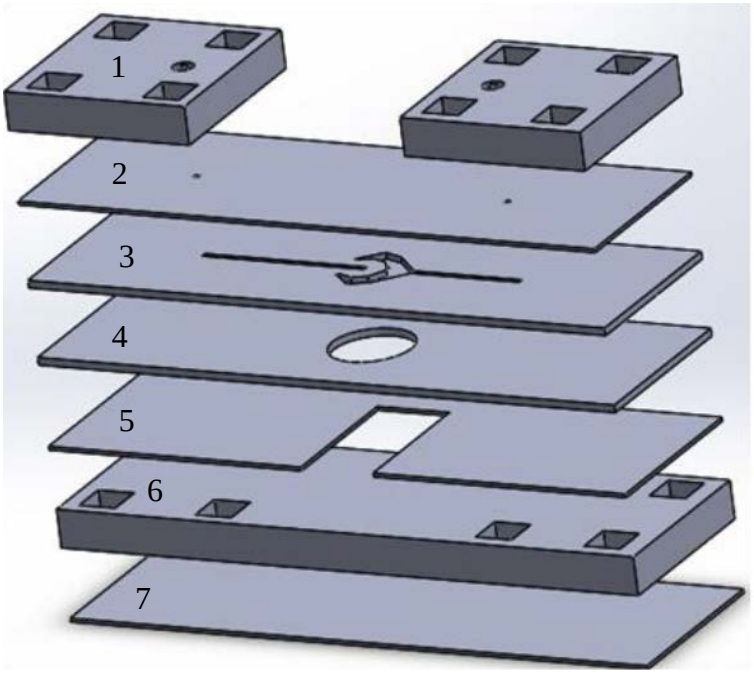

Figure 35: Different layers in a wall-jet system without PSA

The overall dimensions of the fabricated microfluidic chip is 7 cm × 2.5 cm (Figure 36). The magnets are used to seal the chamber. The fabricated systems provides a simple and fast integration of carbon electrodes into a microfluidic set-up. In addition the system is low cost, allows easy interfacing and is compact.

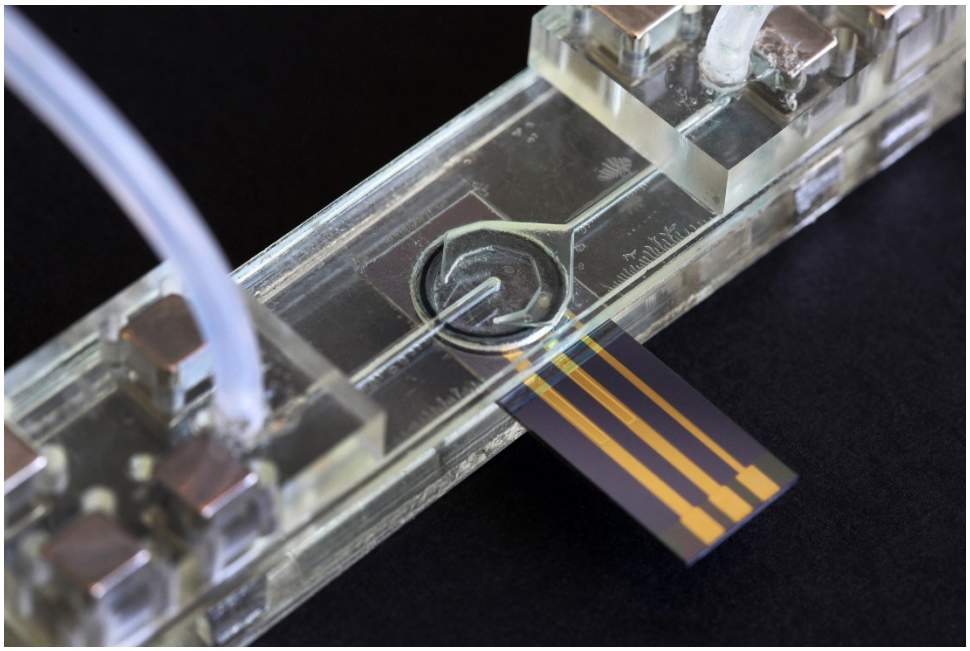

Figure 36: Carbon electrode integrated in a wall-jet system

3.3 Conclusion

Easy, fast, low cost and compact microfluidic systems were developed for testing carbon microelectrodes in static and dynamic conditions. The batch system was used for characterization of carbon electrodes in static conditions (paper I, paper II, paper V). To integrate the carbon electrodes in flow, a microfluidic device (wall-jet) was optimized in a finite element software (COMSOL). Wall-jet systems with a chamber height of 1.5 mm and outlets at 2 mm from the center was found to be optimal for the planned cell based applications. The optimized microfluidic system was fabricated with micro-milling and bonding. In the context of this thesis, the wall-jet system will be used in yeast analysis.

Chapter 4

2D carbon electrode (Carbon4Bio chips)

In this chapter a carbon4bio (C4B) chip was designed with 2D pyrolytic carbon as working electrode. 2D pyrolytic carbon as contact leads was fabricated and characterized for minimal loss. The C4B chip was also optimized with different electrode thicknesses.

4.1 Chip design (C4B)

A three electrode chip for electrochemical measurements with pyrolytic carbon as WE (diameter = 4 mm) was designed. The CE was also designed to be pyrolytic carbon. The dimension of the CE was 1.25 times bigger then WE electrode, so that the CE doesn't limit the kinetics of the electrochemical process under investigation. A pseudo Au reference was selected to complete the three electrode system. The overall chip dimension was 1cm × 3cm. The dimensions were selected to be in sync with the commercially available Dropsens electrodes which would help in further interfacing the electrode with the potentiostat.

4.2 Fabrication of 2D carbon electrode

A three electrode electrochemical chip was designed and fabricated with the 2D pyrolytic carbon as the working and counter electrode. Figure 37 shows the schematic of the process flow for fabricating 2D C4B chips. A negative epoxy resin (SU-8) is patterned on Si/SiO_2 substrate with UV- photolithography and pyrolysed at 900 ºC or 1 h in nitrogen atmosphere to obtain 2D pyrolytic carbon electrodes (Figure 38.A). The fabrication process of 2D carbon is explained in detail in Paper I [122]. The Gold (Au) contacts and pseudo reference is added by e-beam evaporation through a shadow mask (Figure 38.B). The

passivation layer of SU-8 is added to define the working electrode region (Figure 38.C). Figure 38.D shows the fabricated electrochemical 2D chips.

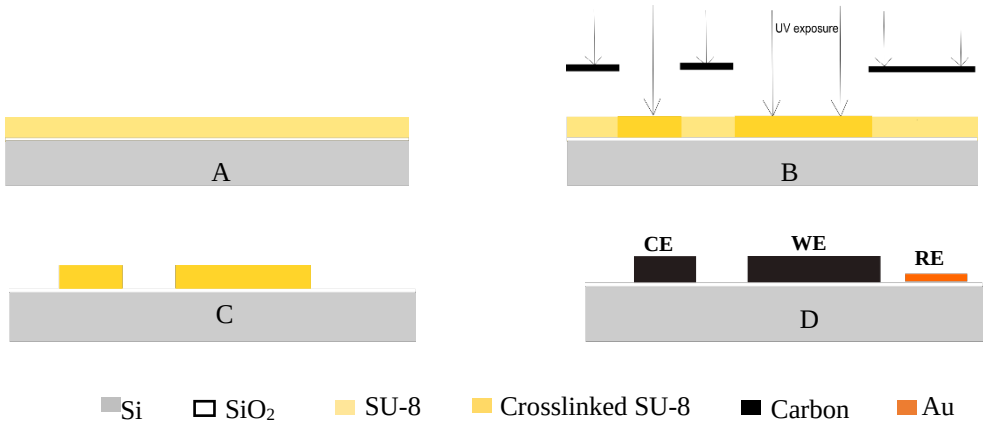

Figure 37: Schematic process flow for fabrication C4B chips (A) Spincoating SU-8 and SB, (B) UV exposure and PEB, (C) Development and hard bake and (D) pyrolysis and Au deposition

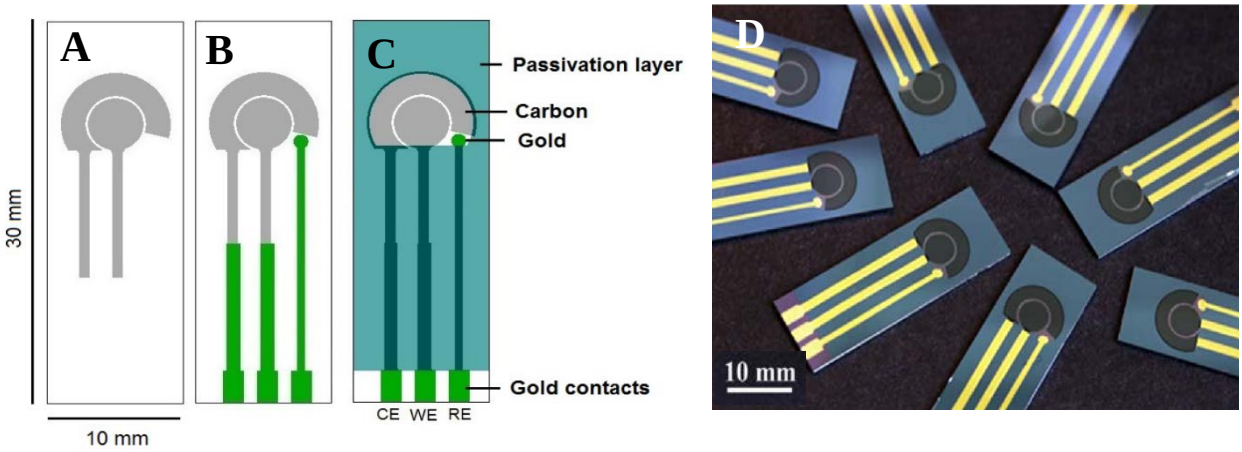

Figure 38 : (A) 2D carbon electrodes (WE and CE) and contact leads (B) Au contact and reference deposited on carbon (C) SU-8 passivation and (D) Fabricated C4B chips

4.3 Electrochemical characterization of C4B chips

The 2D carbon electrodes are characterized electrochemically for high signal or minimal lose. The electrochemical characterization of C4B chips provides information of the electron transfer process and the interaction between the electrode surface and the electrolyte. Two electrochemical techniques were used, CV and EIS. Peak current (I_p) and peak potential difference (ΔE_p) were obtained from CVs. For an ideal electrochemical behavior a higher I_p and lower ΔE_p is desired. All the electrochemical experiments (CV and EIS) were carried out with a standard 10 mM potassium ferri-ferrocyanide ($[Fe(CN)_6]^{4-}$/$[[Fe(CN)_6]^{3-}$) redox probe in phosphate buffer in the batch system. The C4B chips were placed in the bottom plate of the batch system and sealing was achieved with the O-ring of the top plate. 300 µL of redox probe were pipetted on the electrode for each measurement. CV was conducted with a three electrode configuration and a scan rate of 100 mV/s in a potential range of -1.2 V to 1.2 V. EIS was performed using a two-electrode configuration (WE and CE) acquiring data in the frequency range of 0.1 Hz – 10^6 Hz at 10 points/decade while applying a sinusoidal potential of 10 mV.

4.4 Surface treatment of electrode

The electrode chips were pretreated in oxygen (O_2) plasma at 50 W for 60 seconds at a pressure of 0.4 bar before the electrochemical measurements. Plasma treatment is one of the most effective, rapid, and versatile surface treatment for carbon electrode. This method can used to introduce a wide range of functional groups by varying the parameters such as power, gas, pressure, and treatment time [84,165]. The excited species strongly interact with the carbon surface and influence the physical and chemical properties. In this work, O_2 plasma was used to increase the surface wettability of the electrode and as a physical cleaning process [38,166]. Plasma treatment plays an important role in obtaining distinct redox peaks during CV (Figure 39). The carbon electrode thickness in those experiments was 0.7 µm. The CV recorded with the carbon electrodes before plasma treatment displayed no distinct peaks compared to the electrodes after plasma where a distinct redox peak at 0.6 V and -0.55 V was recorded respectively. Hence for all the electrochemical characterization in this thesis carbon electrodes were pre-treated with O_2 plasma.

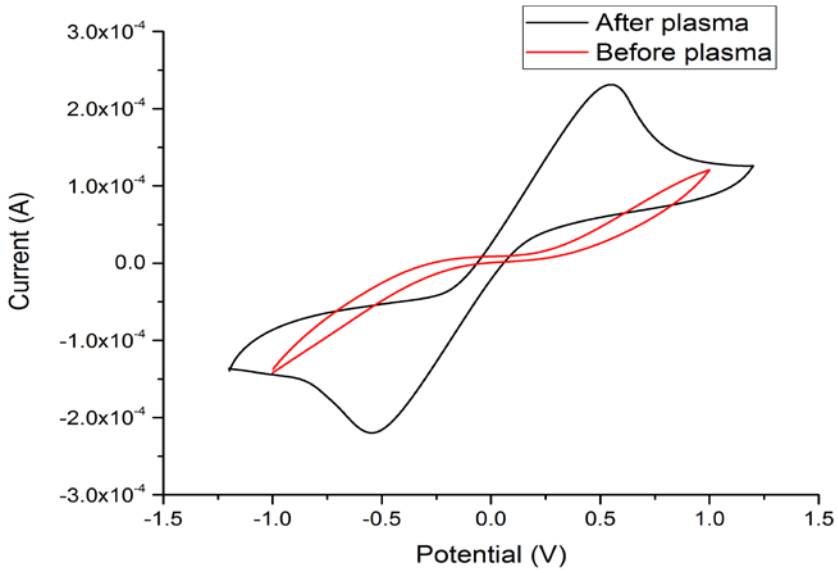

Figure 39: CV of 2D carbon electrode before and after plasma treatment

4.5 Optimization of 2D C4B chip

4.5.1 Contact leads width optimization

To reduce the overall cost and increase the fabrication yield of the chip, pyrolytic carbon as contact leads was tested. In the first series of experiments, the influence of contact leads on the electrochemical performance of the chip was investigated. Initially only carbon as contact leads and contact pads was fabricated. These chips failed to produce any electrochemical signal, since interfacing with the potentiostat was not possible, without damaging the carbon contact pads. Carbon contact leads with different widths were fabricated with Au contact pads. As shown in Figure 38.B the electrochemical chip has the contact leads fabricated with pyrolytic carbon and Au. Au was added for the contact pads to ease the connection to potentiostat. Chips with four different contact leads widths (700 µm, 500 µm, 250 µm and 100 µm) were fabricated and characterized electrochemically with CV and EIS (Figure 40). The thickness of the carbon electrodes was 0.7 µm. Figure 40.A shows the voltammograms for different contact lead widths in 10 mM $[Fe(CN)_6]^{4-}$/$[[Fe(CN)_6]^{3-}$ in PBS. The peak current was extracted. The second parameter considered in this study was ΔE_p, which is 59 mV for a reversible redox reaction. Hence an ideal electrochemical behavior corresponds to a high peak current and low ΔE_p. According to

the Randles-Sevcik equation the peak current varies with the electrode area, diffusion coefficient, redox species, concentration or the potential scan rate [143]. In our experiments, peak current is a direct indicator of overall resistance or minimal loss of the signal since all the other parameters were kept constant. Table 3 shows the anodic peak, cathodic peak and ΔE_p. It can be seen that there is an increase in peak current and decrease in ΔE_p as the width of the contact leads is increased from 250 µm to 700 µm. For a contact lead width of 100 µm, no current was detected. This can be explained by the high resistance offered by the carbon material compared to metals (such as Au). As the width of the contact leads was increased the overall resistance is decreased and hence a minimal loss is achieved.

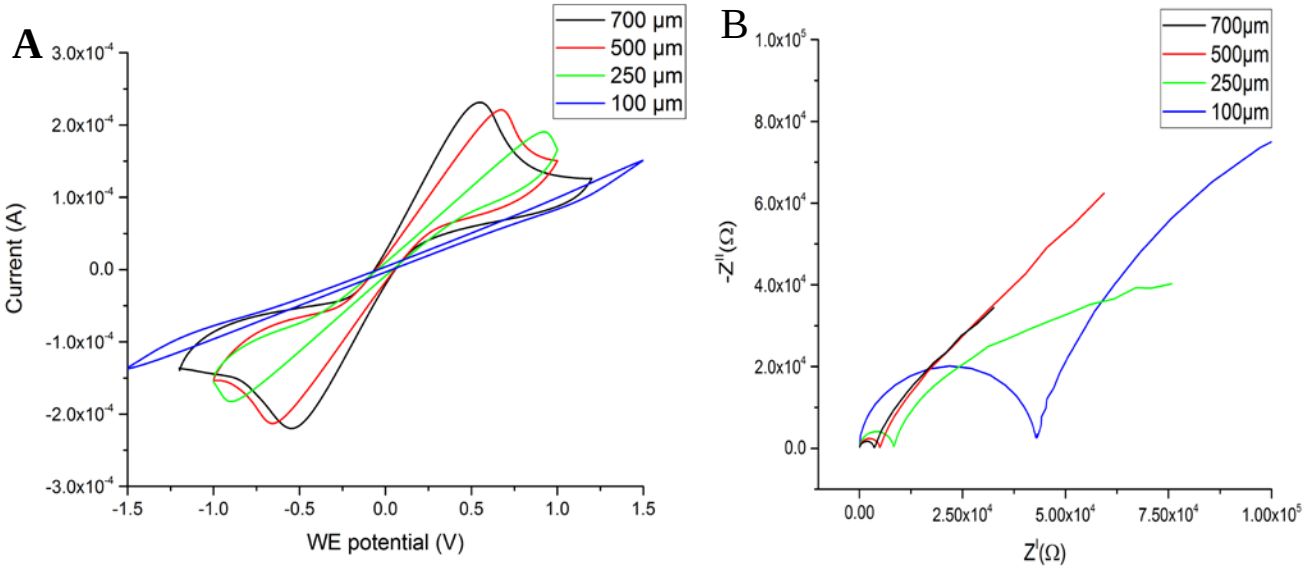

Figure 40: (A) CVs and (B) EIS of carbon electrodes with different contact lead widths

Table 3 : Values of I_p and ΔE_p for different contact lead widths (N=4)

Leads widths	Anodic peak current (µA)	Cathodic peak current (µA)	ΔE_p (V)
700 µm	187.3 ± 4.20	-185.3 ± 6.38	1.03± 0.002
500 µm	126.7 ± 1.82	-116.7 ± 8.25	1.29± 0.035
250 µm	19.90 ± 5.93	-19.10 ± 3.37	1.66 ± 0.069
100 µm	-	-	-

The decrease in the resistance as the width is increased can be seen in the EIS study (Figure 40.B). An equivalent circuit is fitted to derive the charge transfer resistance (R_{ct}) from the impedance spectra (Figure 41) [26,27,122]. The charge transfer resistance of carbon electrodes with contact widths of 700 µm, 500 µm 250 µm and 100 µm was 4.02 kΩ, 5.78 kΩ, 11.98 kΩ and 42.51 kΩ respectively.

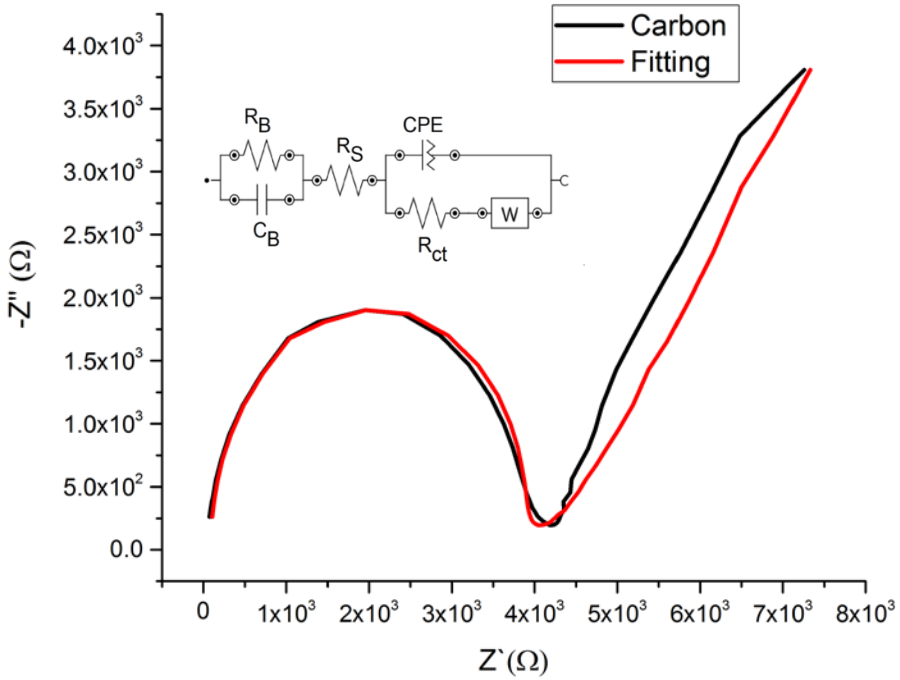

Figure 41 : Nyquist plot of carbon electrode with a contact width of 700 µm. Insert shows the equivalent circuit model.

4.5.2 Au vs. carbon leads

To improve the electrochemical performance and reduce losses in the contact leads, the carbon leads were partially replaced with the Au contact leads. Figure 42.B shows the modified chip design. The fabrication process is the same as outlined above and described in paper I, except for a different shadow mask for e-beam deposition. By replacing the carbon leads, the resistance at the contact leads is minimized and a higher signal (higher I_p = 28.3 mA and lower ΔE_p = 0.36 V) is achieved (Figure 43).

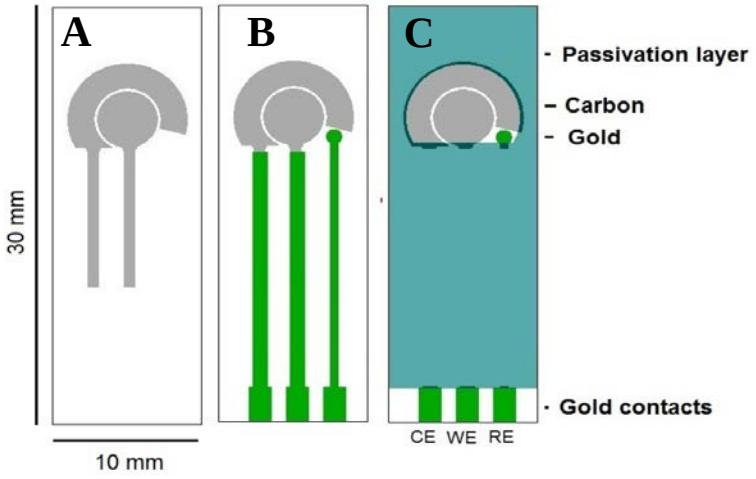

Figure 42: Optimized carbon electrode chip

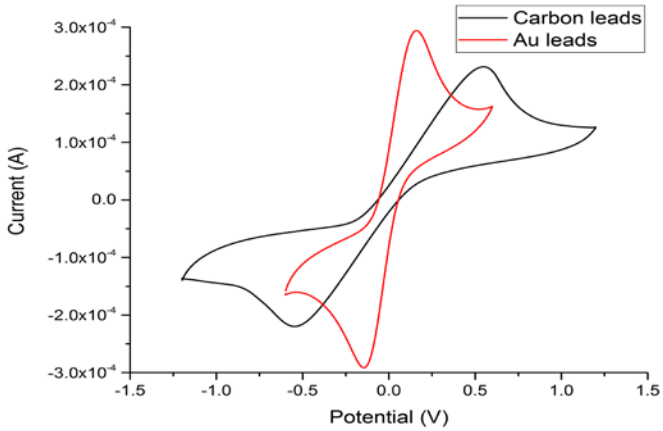

Figure 43 : CV of carbon electrodes with carbon and Au contact leads

An EIS study was carried out to compare the pyrolytic carbon microelectrode with carbon and Au contact leads with commercial screen printed carbon electrodes (from Dropsens). The area of the working electrode in all the three case was 12.56 mm^2. Figure 44 shows the EIS in PBS. The carbon electrodes with the Au leads have a lower impedance than the carbon leads. The screen printed electrode has the lowest impedance, which can be explained by a higher surface roughness and having a low resistance metal below the electrode area. In addition, the decrease of the phase in the high frequency range could indicate that the carbon lead and the resulting resistance were influencing the parasitic effect.

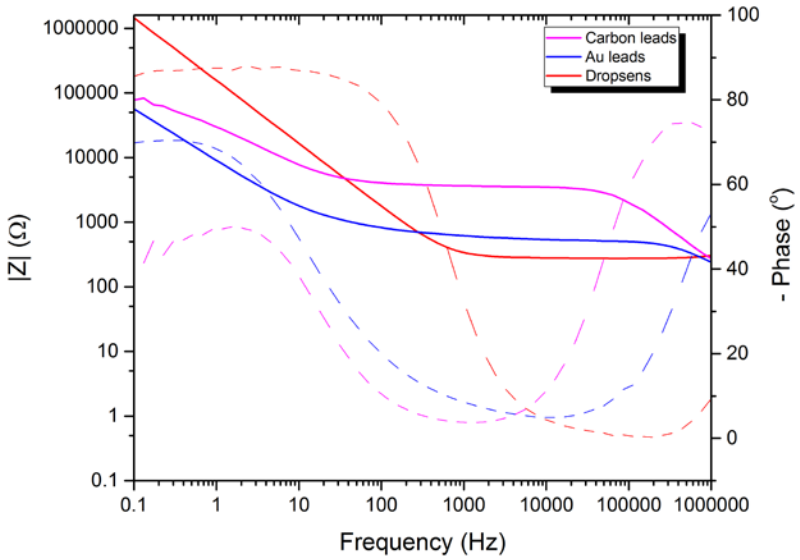

Figure 44 : Impedance spectra of carbon electrodes with carbon and Au contact leads compared with a screen printed commercial electrode

4.5.3 Electrode thickness optimization

To evaluate the effect of carbon WE thickness on the electrochemical analysis, three different thicknesses (0.7µm, 1.1 µm and 2.2 µm) were fabricated. The fabrication process is the same as explained above and in paper I. Three different thicknesses of SU-8 film were spin-coated which after pyrolysis resulted in carbon electrodes with three different thicknesses. Table 4 summarizes the thickness of SU-8 and the corresponding carbon thickness with the sheet resistance measured after pyrolysis. Figure 45 summarizes the CVs of the electrodes with different carbon thickness. By increasing the carbon thickness, the amount of electron transferred is increased which in turn increases I_p and decreases ΔE_p. This can be explained by the decrease in sheet resistance of the electrodes shown in Table 4.

Table 4 : Polymer template (SU-8) and corresponding carbon electrode (WE) heights and their sheet resistances

SU-8 height (µm)	Carbon height (µm)	Sheet resistance (Ω/sq)
5.7±0.3	0.70 ± 0.07	260 ± 7.6
9.2±0.2	1.12 ± 0.02	202 ± 21.1
17.1±0.4	2.25 ± 0.08	81.1± 7.9

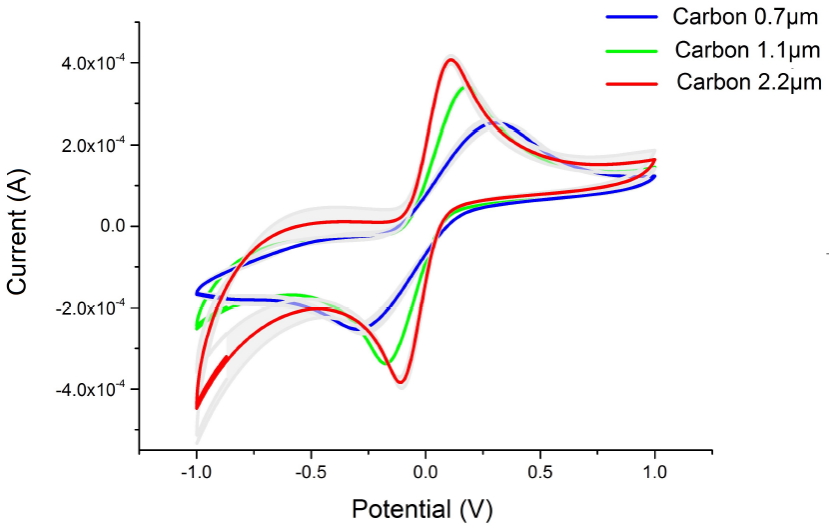

Figure 45: Voltammogram of different thickness of carbon WE with Au contact leads (N =4)

Figure 46 shows the measured impedance spectra of carbon WE with different thicknesses in PBS. The carbon electrodes with 1.1 µm and 2.2 µm carbon thickness show the same qualitative behavior as the 0.7 µm thick carbon electrode. By increasing the thickness of the carbon electrode, the impedance at high frequency is reduced. Additionally, the phase at the high frequencies decreases with an increase in the thickness of the carbon electrodes.

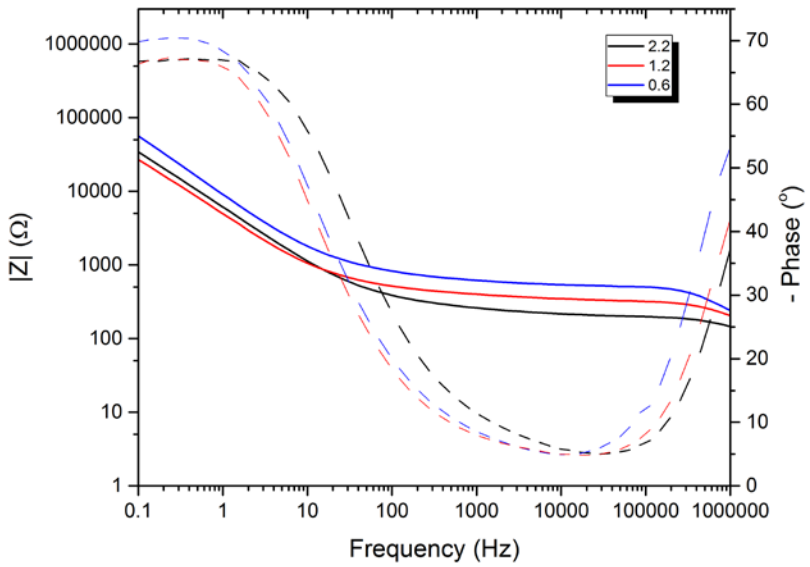

Figure 46: Impedance spectra of carbon electrodes with different WE thickness

4.6 Conclusion

The 2D carbon electrode chip (2D C4B) was successfully optimized to have a lower impedance at high frequency and reduced the resistive loss in the carbon contact leads. The maximum losses were due to the carbon contact leads, by covering the leads with Au the losses were reduced. To enhance the electron transfer at the electrode the WE electrode thickness was increased. The thicker WE resulted in a higher I_p and lower ΔE_p. The optimized 2D electrode will be used as a base for fabricating 3D carbon microelectrodes (chapter 5).

Chapter 5

3D carbon microelectrodes

In this chapter, C-MEMS fabrication process is used to fabricate 3D carbon microelectrodes for electrochemical sensing. The suspended 3D polymer template (SU-8) was fabricated with UV photolithography at three different wavelengths (313 nm, 365 nm and 405 nm). The fabrication techniques developed for fabricating polymer template is simple, reproducible, and cost effective when compared to the previously reported techniques (paper III)[78,79,167–169] . Three different fabrication processes are established for fabrication of 3D epoxy based suspended layer polymer template on the working electrode of an electrochemical chip described in Chapter 4. The polymer template is pyrolyzed at 900 ºC for 1 h to obtain a 3D pyrolytic carbon microelectrodes on the WE.

5.1 3D carbon microelectrodes with 365 nm partial UV exposure

5.1.1 Fabrication of 3D C4B chips

A three electrode electrochemical chip was fabricated with 3D pyrolytic carbon as working electrode. The fabrication process is illustrated in Figure 47 and explained in detail in paper II. Suspended SU-8 polymer template is fabricated with multiple UV exposure and pyrolyzed at 900 ºC for 1 h in N_2 atmosphere. The UV exposure was carried out at 365 nm wavelength. A partial exposure was optimized for fabricating suspended SU-8 structures.

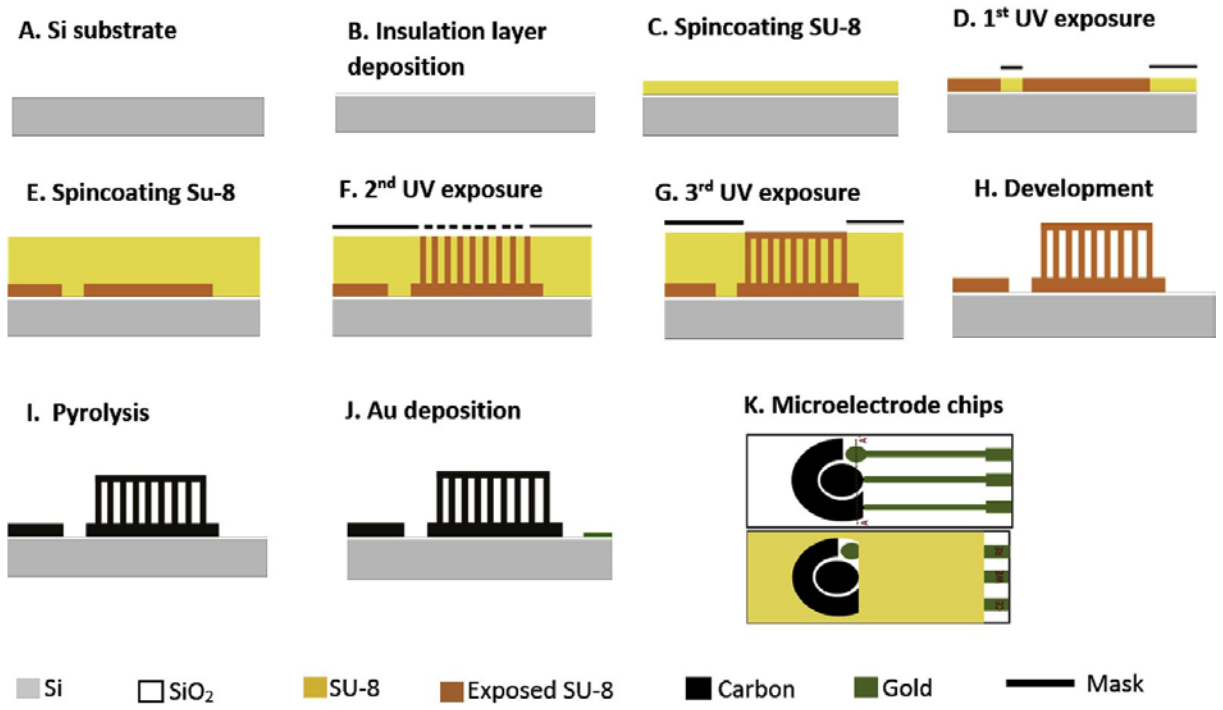

Figure 47 : Schematic of carbon microelectrode fabrication (A) Starting Si substrate (B) Thermal oxidation (C) SU-8 2035 is spin coated and soft baked (D) 1st UV exposure and post exposure bake (E) Second layer SU-8 2075 is spin coated and baked (F) 2nd UV exposure (G) short 3rd UV exposure and post exposure bake (H) Development in PGMEA (I) Pyrolysis at 900 ºC for 1 h (J) e-beam Au deposition through a shadow mask; (K) Top view of the microelectrode chip without and with passivation (SU-8 2005) layer [27]

5.1.2 Exposure dose optimization

The most important parameter in fabricating the 3D polymer template is the partial UV exposure. The optimization of the partial exposure dose is explained in Paper I. Figure 48 shows that a small variation in the optimized exposure dose of the partial exposure results in a complete crossing or no crosslinking at all.

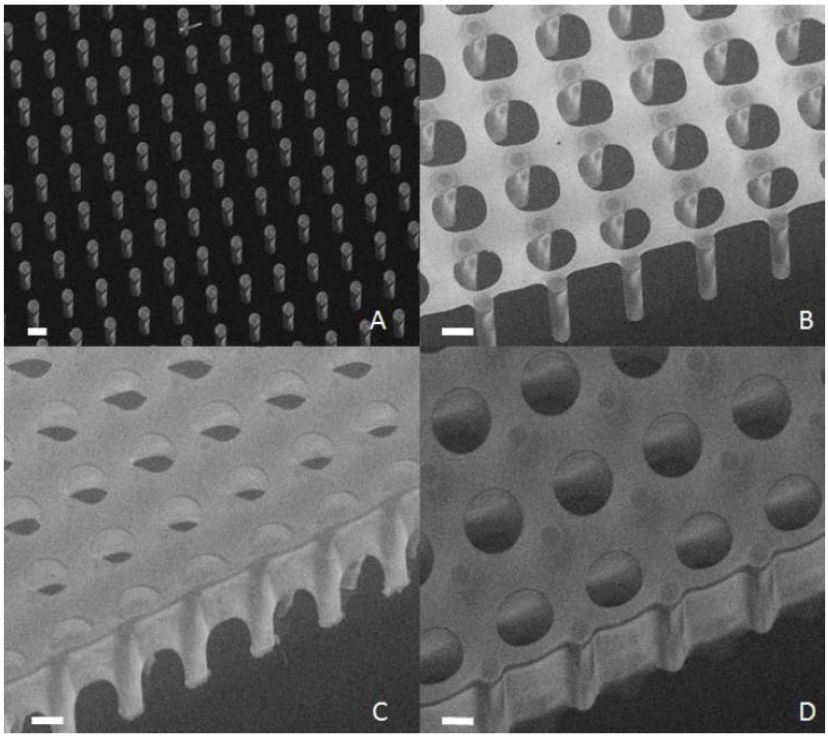

Figure 48: Optimization of partial UV exposure (D2) with different exposure dose: (A) 21 mJcm^{-2}; (B) 28 mJcm^{-2}; (C) 35 mJcm^{-2}; (D) 42 mJcm^{-2} (Scale bar – 25µm)

5.1.3 3D Electrode design optimization

The design of SU-8 polymer template for pyrolysis was also optimized. Some of the main design variables were SU-8 pillar diameters (d = 10–100 µm) with a varying pitch (a = 20–250 µm), hole diameter w and distribution of the holes defined in the suspended SU-8 layer (w = 10-200 µm). Figure 49 shows the resolution limit for the supporting pillars to obtain 3D suspended microstructures with multiple step of UV photolithography. Two different parameters, pillar diameter (d) and pillar pitch (a) evaluate the mechanically stable suspended layer. As d decreases and a increases, the suspended SU-8 layer shows a higher tendency to collapse due to lack of mechanical stability which results from the low partial exposure dose. Pillars with d = 10 µm can support a suspended layer for $a \leq 60$ µm (Figure 49.A and B) whereas a collapse is observed for $a \geq 100$ µm (Figure 49.C). However, for structures with $a \geq$ 100 µm a suspended layer can be fabricated by increasing the pillar diameter (Figure 49.D and E). Moreover, different designs of the suspended layer can be fabricated by changing the number and the diameter (w) of holes such as the one shown in Figure 49.F.

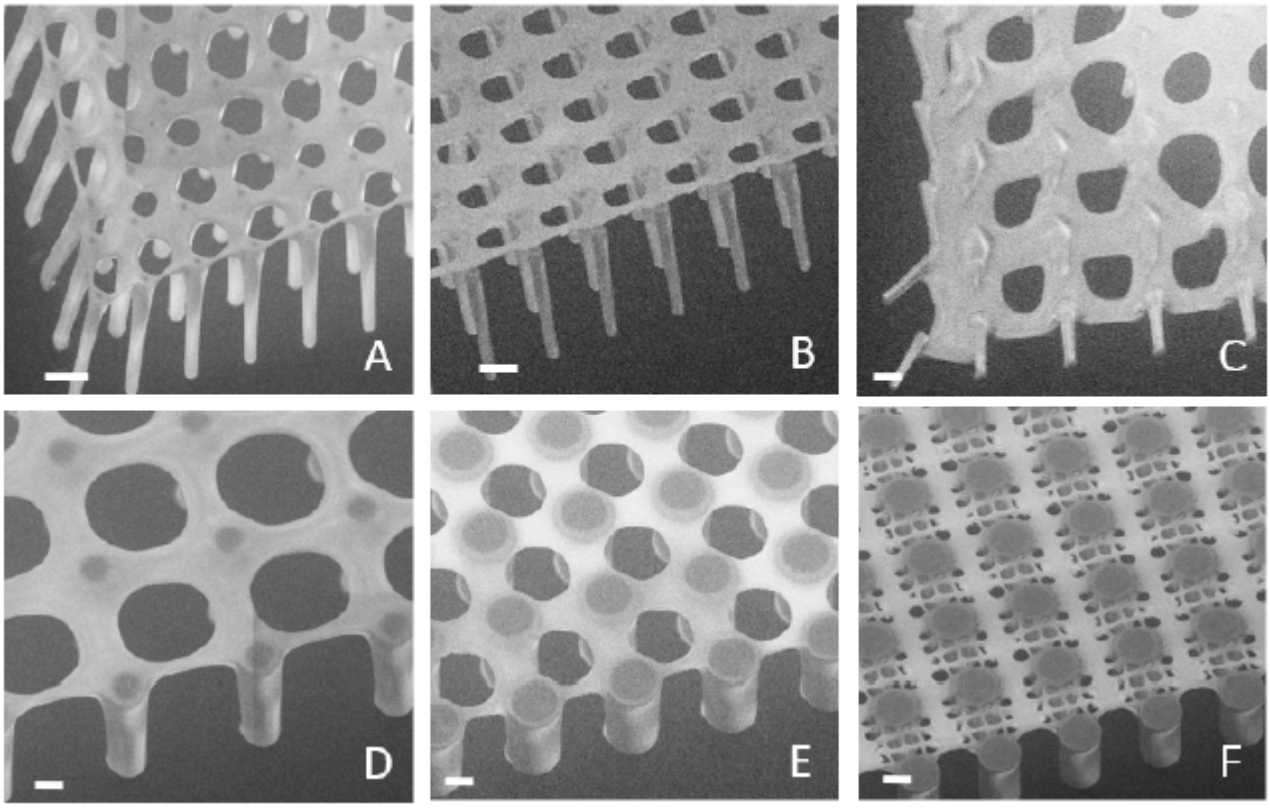

Figure 49: Comparison of different SU-8 templates with 3D suspended structures fabricated with two steps of UV exposure (A)-(C): d=10 µm, w=40 µm, a=30, 60 and 100 µm, (D)-(E): d=25 and 50 µm, w=40 µm, a=100 µm, (F): d=25 µm, w=20 µm, a=150 µm (Scale bar–25µm)

5.1.4 Characterization of the carbon microelectrodes

The polymer template fabricated with UV photolithography was pyrolysed to get the 3D carbon microelectrodes. Five designs of 3D microelectrodes were fabricated on the WE. The characterized of the different designs with Raman spectroscopy, XPS, and SEM is explained in paper II. The optimized design of the 3D carbon microelectrode chip was compared with the 2D electrode and 2D electrodes with micro pillars on top (Figure 50.A-E). The detailed characterization and comparison of these electrodes is described in Paper II. In summary, the 3D carbon microelectrode show a sensitivity two fold higher than the 2D electrodes due to approximately two times more surface area (Figure 50.F).

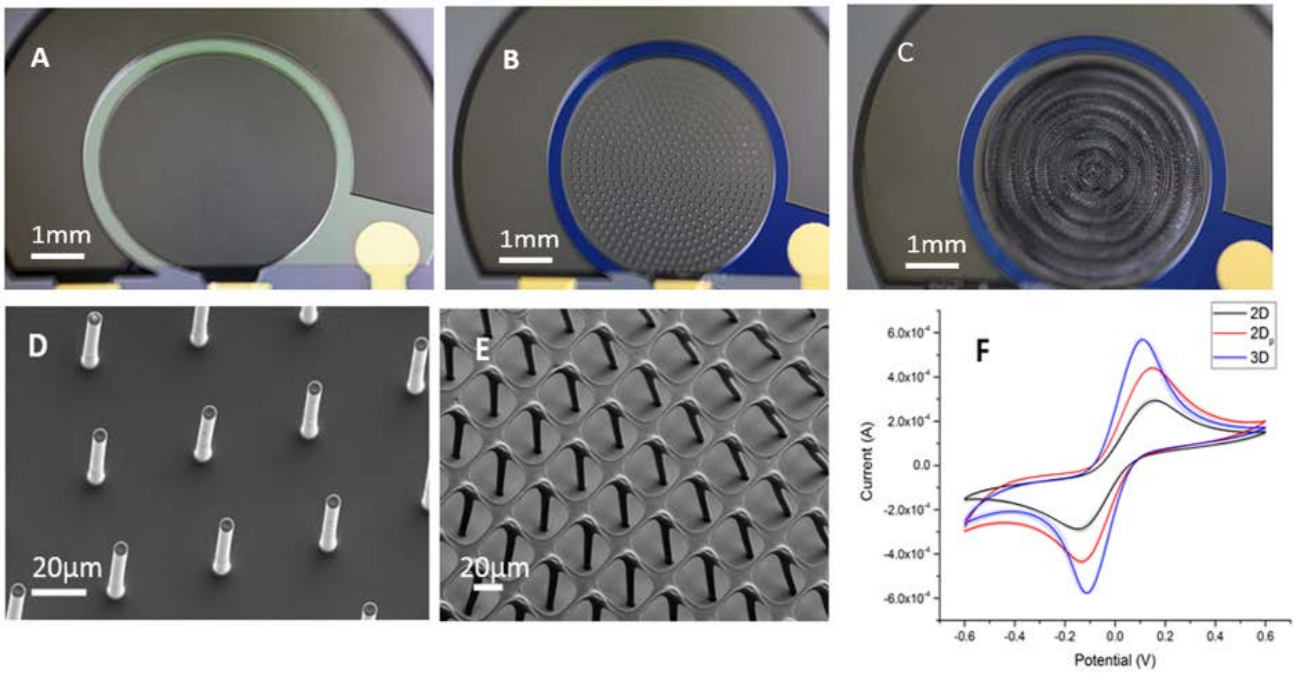

Figure 50: (A- B) Carbon microelectrodes : A- 2D, B- 2D$_p$ and C- 3D (design 1), (D-E) SEM image of working electrode of 2D$_p$ and 3D, (F) CV with 10mM $Fe(CN)_6^{3-/4-}$ (N = 4 chips)

5.2 3D carbon microelectrodes with UV exposure at different wavelengths

5.2.1 Fabrication of 3D polymer templates

The 3D carbon microelectrode developed with pyrolysis of SU-8 fabricated by a partial exposure at 365 nm wavelength has a very narrow process window (5±1 sec UV exposure) as explained in Figure 48. We observed that minor variations in parameters such as the baking temperature, humidity, and exposure dose results in cracks and difficulties to control the suspended layer thickness. Furthermore, instability of the features with a size smaller than 10 µm was seen (Paper III). Alternatively, the use of a lower wavelength (313 nm) to crosslink or pattern the suspended layer has been proposed [78]. At this wavelength, the absorption by SU-8 is increased, resulting in a lower penetration depth of the UV radiation. Figure 51 describes the fabrication process for fabricating 3D SU-8 polymer template with 313 nm wavelength UV exposure.

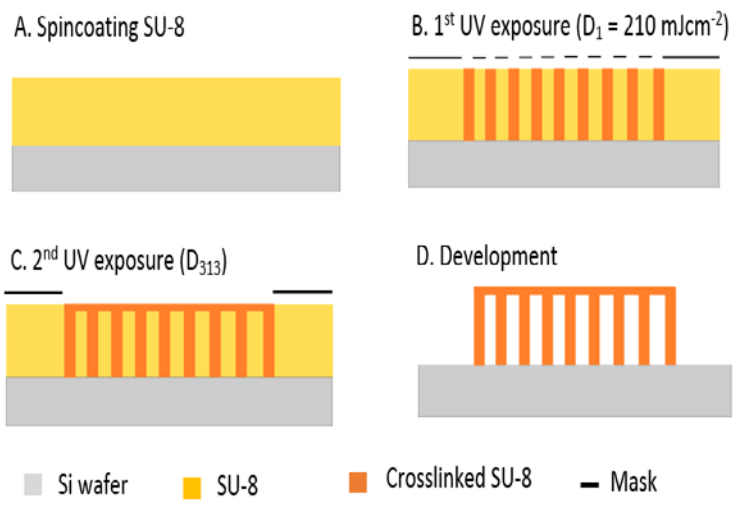

Figure 51: Schematic of the 313 nm UV lithography process: (A) SU-8 is spin coated on a Si/SiO2 substrate and soft-baked; (B) 1st UV exposure at 365 nm; (C) 2nd partial UV exposure at 313 nm and post-exposure bake; (D) Development in PGMEA[170]

In this work, we introduce a third approach for fabrication of suspended layers of epoxy based photoresists with UV photolithography using a higher wavelength of 405 nm. The combination of two different photoresists (SU-8 and mr-DWL) is exploited to fabricate suspended layers with a precise lateral and longitudinal resolution. This novel approach is compared with a process using partial exposure at wavelengths of 313 nm to crosslink the suspended layers. Compared to the earlier work, all the processes were carried out with a low temperature baking profile to minimize the thermal stress [171,172]. After optimization of the exposure dose, both fabrication processes resulted in a well-defined suspended layer in lateral direction. However, the fabrication process with 405 nm and mr-DWL provided a wider processing window and improved control of the thickness of the suspended layer. Figure 52 illustrates the fabrication process of fabricating 3D polymer template with 405 nm wavelength UV exposure.

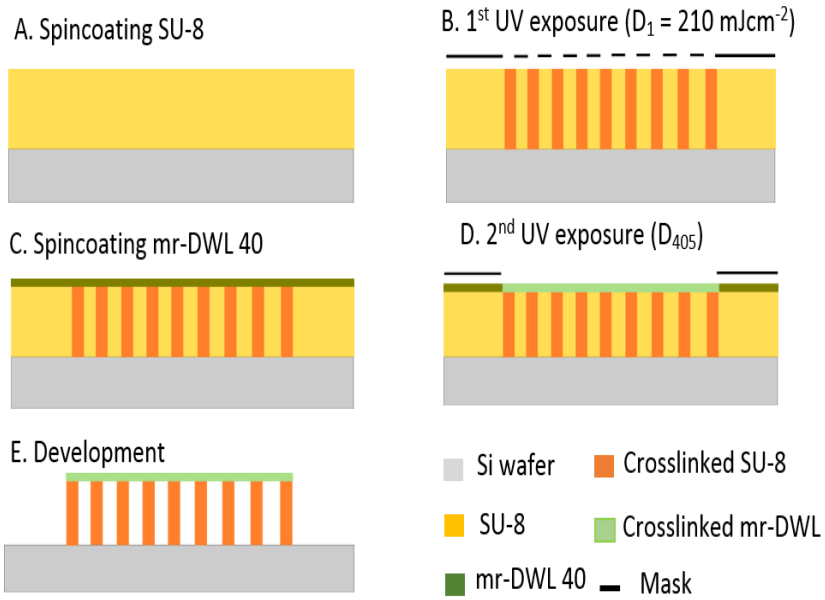

Figure 52: Schematic of 405 nm microfabrication process: (A) SU-8 is spin coated on a Si/SiO2 substrate and soft-baked; (B) 1st UV exposure at 365 nm; (C) mr- DWL 40 spin coating on SU-8; (D) 2nd UV exposure at 405 nm and post-exposure-bake; (E) Development in PGMEA [170]

5.2.2 Exposure dose optimization for 313 nm and 405 nm UV exposure

The fabrication and optimization of 3D SU-8 polymer template for pyrolysis is explained in detail in Paper III. The UV exposure at 313 nm limits the crosslinking to the top surface, due to the high absorption of SU-8. The optimized exposure dose for high lateral resolution was 3.15 $mJcm^{-2}$ (3 s of UV exposure). To improve the vertical resolution the 405 nm wavelength UV exposure process was developed, since the photo-initiator in SU-8 is not activated at 405 nm wavelength. The optimized exposure dose to pattern mr-DWL with thickness of 17 µm (suspended layer) on SU-8 is 31.50 $mJcm^{-2}$ (3 s of UV exposure).

5.2.3 3D carbon microelectrodes

The polymer templates fabricated with multiple UV exposures were pyrolyzed to obtain 3D carbon microelectrodes. The pyrolysis process was the same as for the 2D electrodes. The polymer template was hard baked at 95 ºC for 15 h before pyrolysis. The polymer was pyrolysed at 900 ºC for 1 h in N_2 atmosphere with a ramp of 2 ºC/min and an intermediate step at 200 ºC for 30 min. Figure 53 shows the polymer templates and their corresponding carbon microelectrodes.

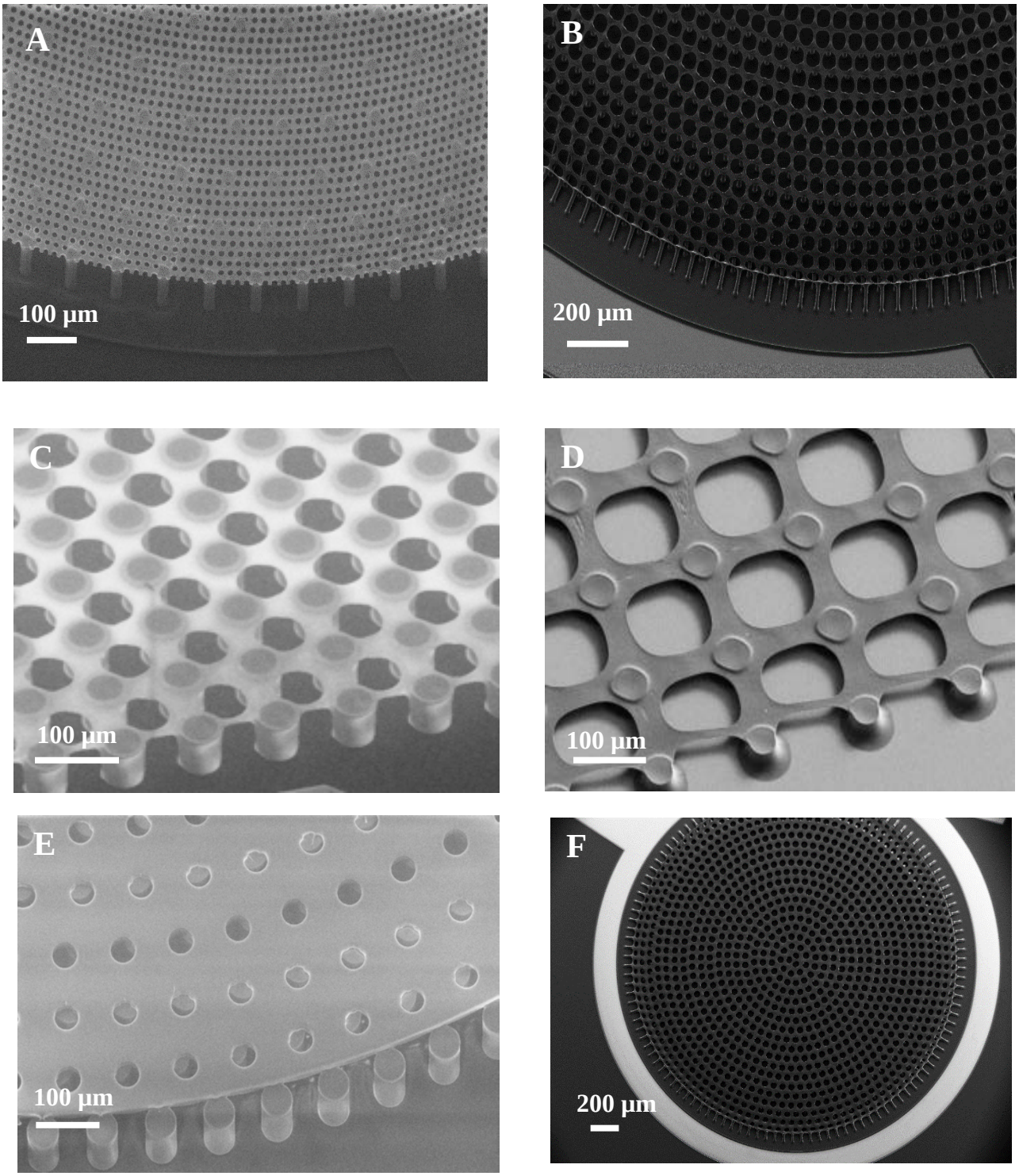

Figure 53: Polymer fabricated with (A) 313 nm (C) 365 nm and (E) 405 nm UV exposure and (B), (D) and (F) are corresponding 3D carbon structures respectively.

5.2.4 Shrinkage analysis

Shrinkage plays an important role in fabricating a 3D microelectrode with C-MEMS process. Figure 54 shows the SU-8 template and the corresponding carbon structures with shrinkage, detailed explanation is given in paper II. The overall height of the electrode, pillar diameter and suspended layer thickness shrink by 48.26%, 41.01% and 48.43% respectively.

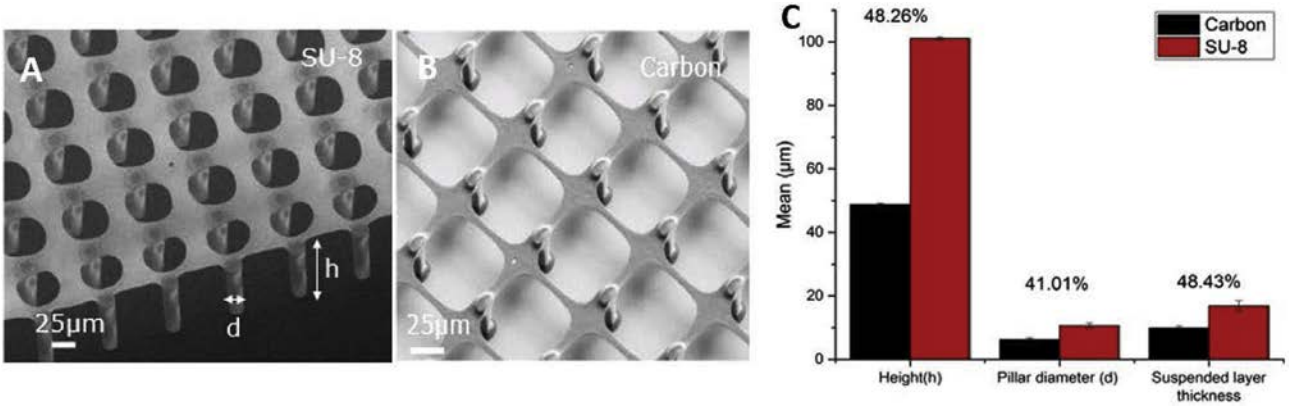

Figure 54: (A) SU-8 polymer microstructure template, (B) Corresponding carbon microstructures and (C) Percentage shrinkage analysis [27]

5.2.5 Electrochemical characterization of 3D carbon microelectrodes

The 3D carbon microelectrode fabricated by pyrolysis of SU-8 with 313 nm and 405 nm wavelength UV exposure were characterized with CV. The electrochemical experiments were carried out with a 10 mM $[Fe(CN)6]^{4-}$/$[[Fe(CN)_6]^{3-}$) redox probe in the batch system. 300 µL of redox probe were pipetted on the electrode for each measurements. CV were acquired with a three electrode configuration and a scan rate of 100 mV/s in a potential range of -0.6 V to 0.6 V. The voltammograms were compared to the 3D carbon electrodes fabricated with 365 nm UV exposure (Figure 55). All the three polymer templates were pyrolyzed at the same temperature (900 ºC) and displayed similar characteristics. The CVs from the 405 nm process showed a slightly higher signal. This can be explained by a higher surface area from the added layer of mr-DWL resist.

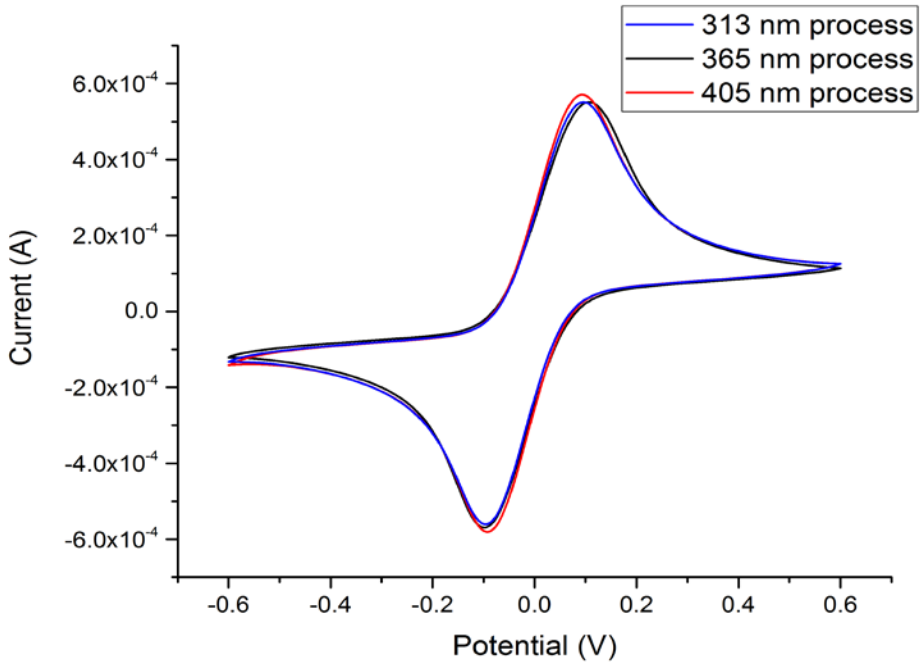

Figure 55: Cyclic voltammograms of 3D carbon microelectrodes fabricated with the three different processes

5.3 Conclusion

Three fabrication processes were optimized for the fabrication of SU-8 polymer templates. The suspended structures were pyrolyzed to obtain 3D carbon microelectrodes. The fabricated microelectrodes are characterized with Raman spectroscopy, XPS, SEM and electrochemical methods (CV and EIS). The fabrication process with 405 nm UV exposure has a higher process window for suspended layer fabrication. Hence only fabrication process with 405 nm UV exposure is used further optimization of 3D carbon microelectrodes during pyrolysis and in test applications (yeast analysis, dopamine detection and ALP detection).

Chapter 6

Pyrolysis process optimization

The pyrolysis process plays an important role in tailoring the electrode properties. Different parameters such as maximum temperature, dwell time, heating rate, gas composition, and number of steps can affect the electrode performance. The goal of this experiments described in this chapter was to increase the mechanical stability, decrease the electrode resistance and increase the electrochemical performance (higher I_p and lower ΔE_p). Figure 56 shows the pyrolysis profile with the important factors affecting the electrode properties. This work was based on the results from the other members in the team [122].

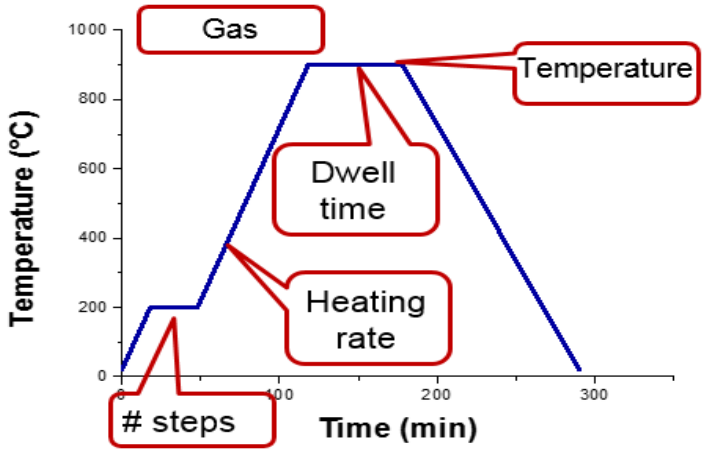

Figure 56: Pyrolysis profile with some important parameter

6.1 Pyrolysis with different temperatures, heating rates and steps

The SU-8 3D microstructures fabricated with 405 nm UV exposure were used as the polymer template for pyrolysis. To fabricate more conductive and mechanically stable 3D carbon microelectrodes three different parameters were varied: The maximum temperature (700 ºC, 900 ºC and 1100 ºC), the heating rate (1 ºC/min and 10 ºC/min) and the number of steps. The maximum temperature was limited the by

the furnace used. The preliminary experiments were conducted in a 3 week project and doesn't represent a full experimental study.

Table 5 shows the different pyrolysis parameters used and the corresponding sheet resistance measured immediately after the pyrolysis. All the processes had the same dwell time (60 min), gas flow (N_2), and cooling step i.e. natural cooling to room temperature. The process with the lowerst temperature (700 ºC) shows the maximum sheet resistance (14 kΩ/sq) because SU-8 is not completely carbonized. The pyrolysis with the highest temperature (1100 ºC) showed the least sheet resistance (22-29 Ω/sq) which is comparable to our previously reported values [122]. This is because higher temperature allows formation of more graphitic regions. The heating rate (1- 10 ºC/min) did not seem to have a large influence on electrode conductivity. An intermediate step of 30 min was introduced at 200 ºC and 600 ºC. Additional steps also seemed to not influence the electrode resistance. One of the most important factors for fabricating 3D electrodes is the mechanical stability after pyrolysis. Figure 57.A and B show the SU-8 polymer templates (Design 5 and 1 in paper II) which were pyrolyzed with all the conditions described in Table 5. All the designs survive the pyrolysis process and show high mechanical stability (Figure 57. C and D) except design 2 at 1100 ºC. The low gap between the pillars (10 µm) in design 2 results in a higher intrinsic stress at higher temperature and results in delamination of the electrode from the substrate (Figure 57.E and F).

Table 5: Pyrolysis process parameters and their corresponding sheet resistance

Steps	Ramp (ºC/min)	Temperature (ºC)	Sheet resistance (Ω/sq)
0	1	700	14k ± 270
0	1	900	55 ± 7.78
1 (200 ºC)	10	900	58 ± 3.3
2 (200 ºC and 600 ºC)	10	900	66 ± 5.2
0	1	1100	22 ± 2.87
0	10	1100	29 ± 6.98

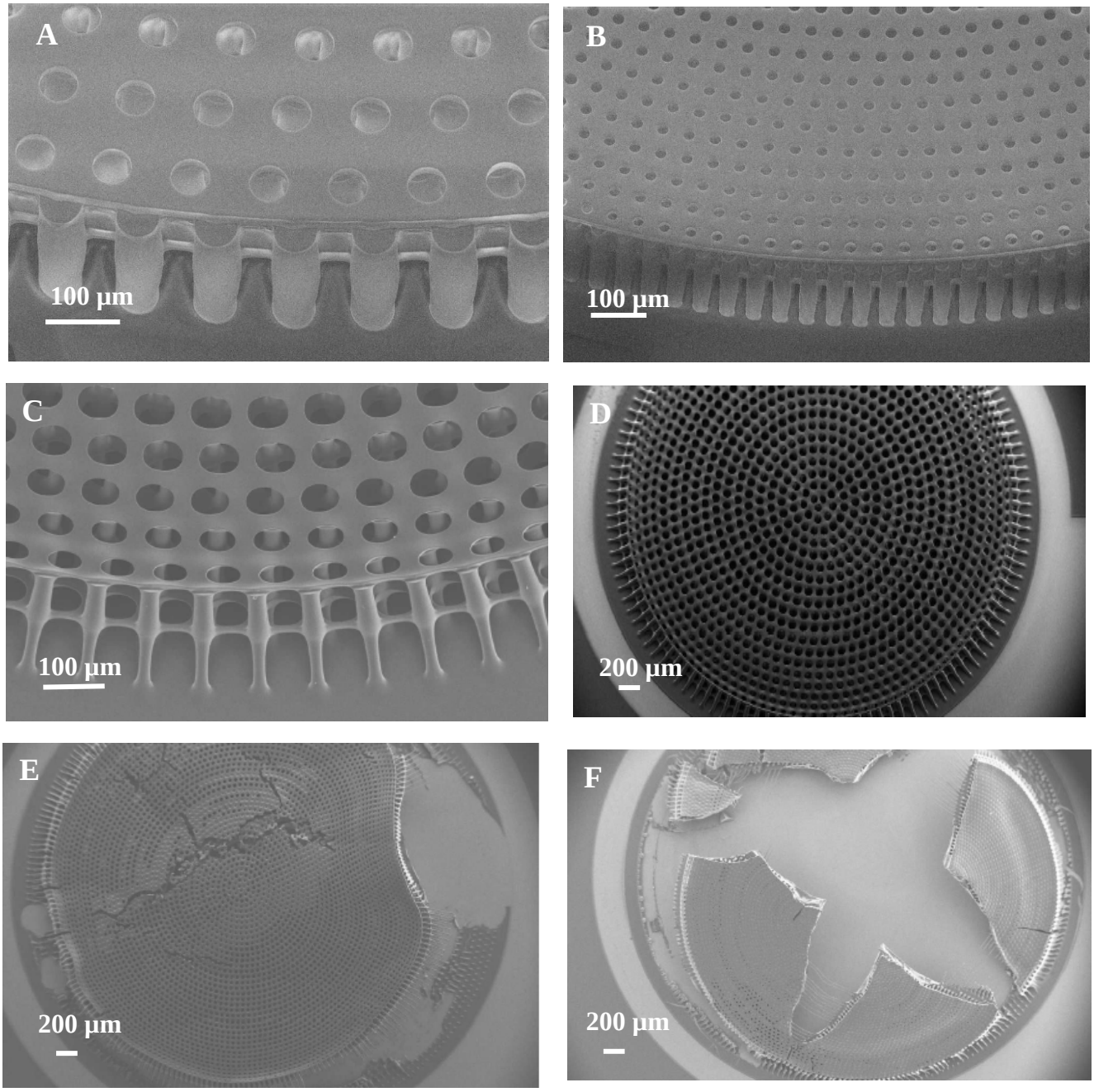

Figure 57: (A) - (B) SU-8 templates, (C) - (D) pyrolytic carbon electrodes and (E) – (F) damaged carbon electrodes

6.2 Electrochemical characterization

To test the electrochemical performance of the pyrolytic carbon 3D microelectrodes fabricated at high temperature (1100 ºC @ 10 ºC/min), CV was performed. CV was carried out with a 10 mM $[Fe(CN)_6]^{4-}$ /$[[Fe(CN)_6]^{3-}$ redox probe in the batch system. 300 µL of redox probe were pipetted on the electrode for each measurement. CVs were acquired with a three electrode configuration and a scan rate of 100 mV/s in a potential range of -0.6 V to 0.6 V. The voltammogram of carbon at higher temperature showed a higher peak current (0.63 mA) and smaller ΔE_p (0.21 V) (Figure 58).

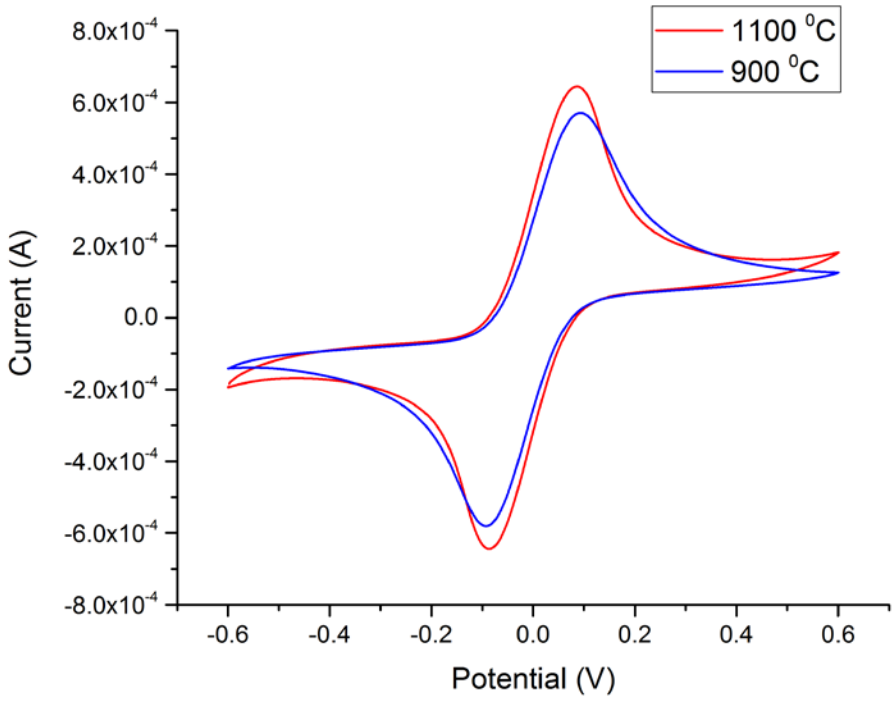

Figure 58: CV of 3D carbon electrodes fabricated at 1100 ºC and 900 ºC

6.3 IDE carbon electrodes

The optimized process of 405 nm UV exposure followed by pyrolysis at 1100 ºC was transferred to fabricate the 3D interdigitated electrodes (IDE) in an MSc project by Ioannis Mantis. The IDEs were also characterized electrochemically. Fabrication and characterisation is described in a manuscript draft (paper IV). Figure 59. A shows the 3D pyrolytic carbon IDE fabricated with multiple UV exposure

followed by pyrolysis at 1100 ºC for 1 h. Figure 59. B shows the CVs obtained with different concentration of $[Fe(CN)_6]^{4-}$/$[[Fe(CN)_6]^{3-}$ in PBS. More detailed analysis is described in paper IV.

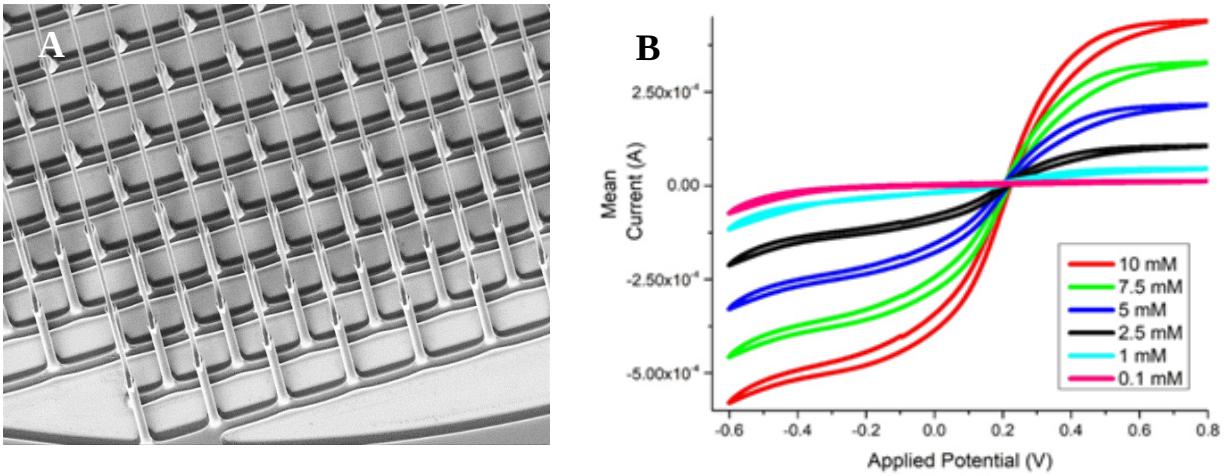

Figure 59: (A) Shows the 3D pyrolytic carbon IDE and (B) CVs at of 3D IDE (design 2) with different concentration of $[Fe(CN)_6]^{4-}$/$[[Fe(CN)_6]^{3-}$ in PBS

6.4 Conclusion

The pyrolysis process to fabricate the 3D carbon microelectrodes was optimized for increased conductivity and improved electrochemical performance (higher I_p and lower ΔE_p). The high temperature process (1100 ºC) combined with 405 nm UV exposure to fabricate the polymer template, a highly controlled process was developed to fabricate a 3D carbon microelectrode.

Chapter 7

Applications

This chapter gives an overview of the implementation of the highly sensitivity 3D carbon microelectrodes for several different applications such as (i) glucose biosensor, (ii) yeast analysis in a flow system, (iii) human stem cell differentiation and bone cell analysis. The developed 3D carbon based microelectrode is a more sensitive, enables easy surface functionalization, cost efficient, and provides a biocompatible platform for electrochemical application. The following application enhances the importance of 3D carbon microelectrodes compared to 2D carbon electrodes.

7.1 Glucose biosensor

Electrochemical biosensors are one of the most mature sensor technology in real-world applications [173–176]. Therefore, research and development of electrochemical biosensors is presently one of the most lively area for various important applications such as health care diagnostics [177], environmental monitoring [178], food quality control [179], security and defense etc [180]. The electrodes are the central part of all electrochemical applications and are used as transducer in electrochemical biosensing devices [181]. Therefore, design and optimization of electrodes is an integral part for advancement of electrochemical biosensors. In this thesis, amperometric glucose sensing was used as an example/model system for biosensing. The highly sensitive 3D carbon microelectrodes described in section 5.1 were functionalized using reduced graphene oxide (RGO) for electrochemical glucose sensing. The sensitivity and detection limit of 3D microelectrodes were compared to 2D electrodes functionalized with RGO. Figure 60 shows the current response obtained from amperometric glucose detection with different concentrations. The current response obtained with 3D carbon microelectrodes is higher than 2D electrodes, which shows the higher sensitivity (5 folds) of 3D microelectrodes. The 3D electrodes are also tested for selectivity and glucose detection in real blood serum. This work is done in collaboration with Arnab Halder, PhD

student at DTU Chemistry under the supervision of Associate Prof Qijin Chi. The results are discussed more in detail in paper V.

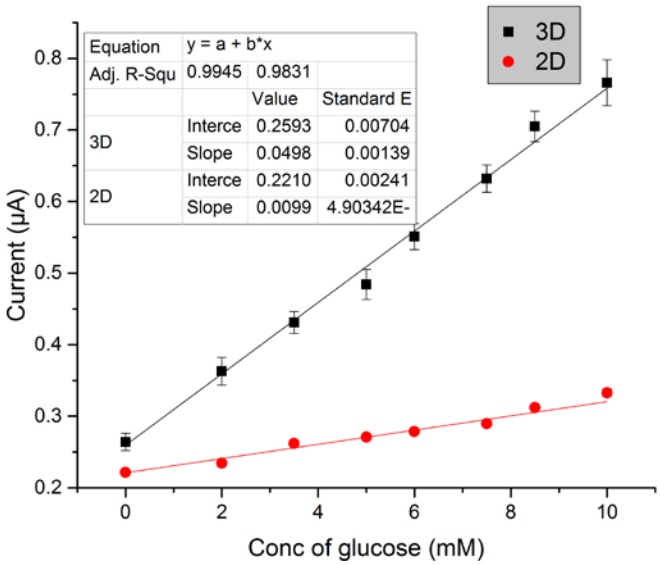

Figure 60: Current values obtained from amperometric measurement for glucose detection on 2D and 3D carbon electrodes with increasing concentration of glucose.

7.2 Yeast analysis

To evaluate the application of the 3D carbon microelectrodes for impedance measurements, preliminary experiments with yeast (Saccharomyces cerevisiae) cells were performed. Yeast is the most common microorganism used in baking, winemaking, and brewing [182]. Impedance is one of the most common method used to analysis yeast cell seeding [9]. The goal of the experiments was to correlate the cell concentration to the measured impedance. As the number of cells on the electrode surface increases the overall impedance also increases [153]. Yeast cells are non-adherent cells which influences the impedance measurements. The experimental set-up shown in Figure 31 was used for initial experiments. 100 µL of PBS were added on the 2D electrode chip and impedance was measured between working and counter electrode. A standard concentration of yeast cell of 6.9×10^5 cells/mL was added and a second impedance was measured (Y (0min)). The cells were allowed to settle at the bottom of the chamber for 30 min and impedance was measured again (Y (30min)). Then glucose solution of 1 M concentration

was added to initiate cell growth and impedance was measured (G (0h)). A final impedance value was measured after 2 h of glucose addition (G (2h)). Figure 61.A shows the EIS spectra at the five time points explained above and Figure 61.B shows the impedance sampled at 1 Hz for yeast and PBS on 2D carbon electrodes. The low frequency of 1 Hz was selected to monitor the yeast cells near the electrode surface [9]. The impedance at 1 Hz, shows an increase in the signal from 0.1 MΩ to 0.123 MΩ as the concentration of yeast cell is increasing on the WE. It has been mentioned that these results had large standard deviations. This may be explained by the movements of the non-adherent yeast cells when the media is added into the chamber. To minimize fluctuations on the WE during media exchange, the wall-jet system described in section 3.2 was used for yeast cell analysis. The wall-jet system could potentially also provide a more controlled method for cell seeding.

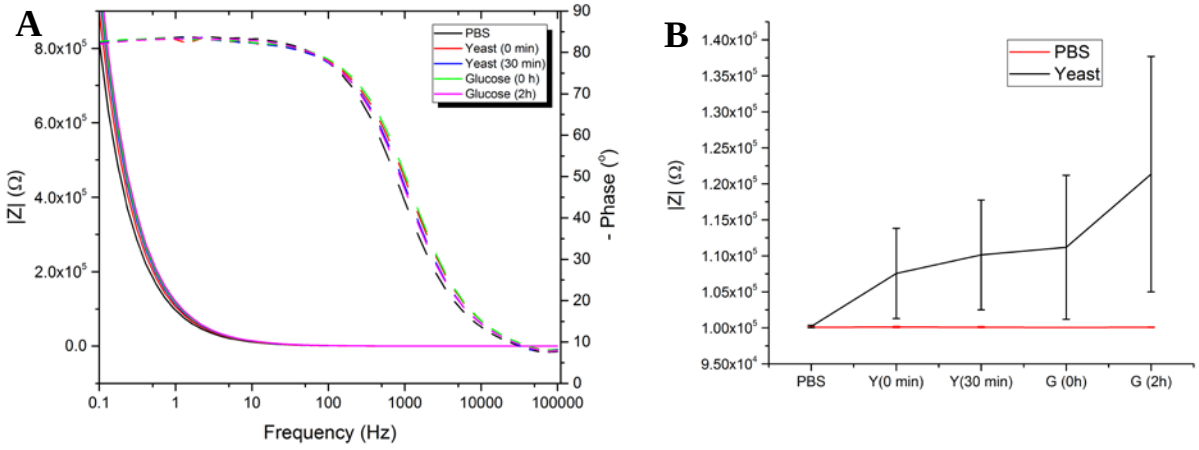

Figure 61: (A) EIS spectra of 2D carbon electrodes in static conditions and (B) Impedance sampled at 1 Hz for yeast and PBS on 2D carbon electrode (n = 3)

Microfluidic cell culture systems can provide a long term stable environment for cell culture, eliminate fluctuations in media and provide continuous supply nutrient and oxygen for a long time [183–185]. In this thesis the wall-jet system is used to have minimal shear stress on the cells on the WE and to have a uniform seeding of yeast cells. The wall-jet system shown in Figure 36 is used for this study. The chamber was filled with PBS and the impedance was measured between WE and CE. Yeast cells were seeded on the electrode with a flow of 10 µL/min and the impedance was measured as the cells reached the chamber (Y (0min)). After this, the flow was stopped and the yeast cells were allowed to settle down on the electrode (by sedimentation). The impedance was measured after 30 min (Y (30min)). A 1 M concentration glucose was pumped into the system at a flow rate of 10 µL/min and the impedance was

measured after 2 h. Figure 62.A and C shows the EIS spectra's of 2D and 3D carbon and Figure 62.B and D shows the impedance at 1 Hz.

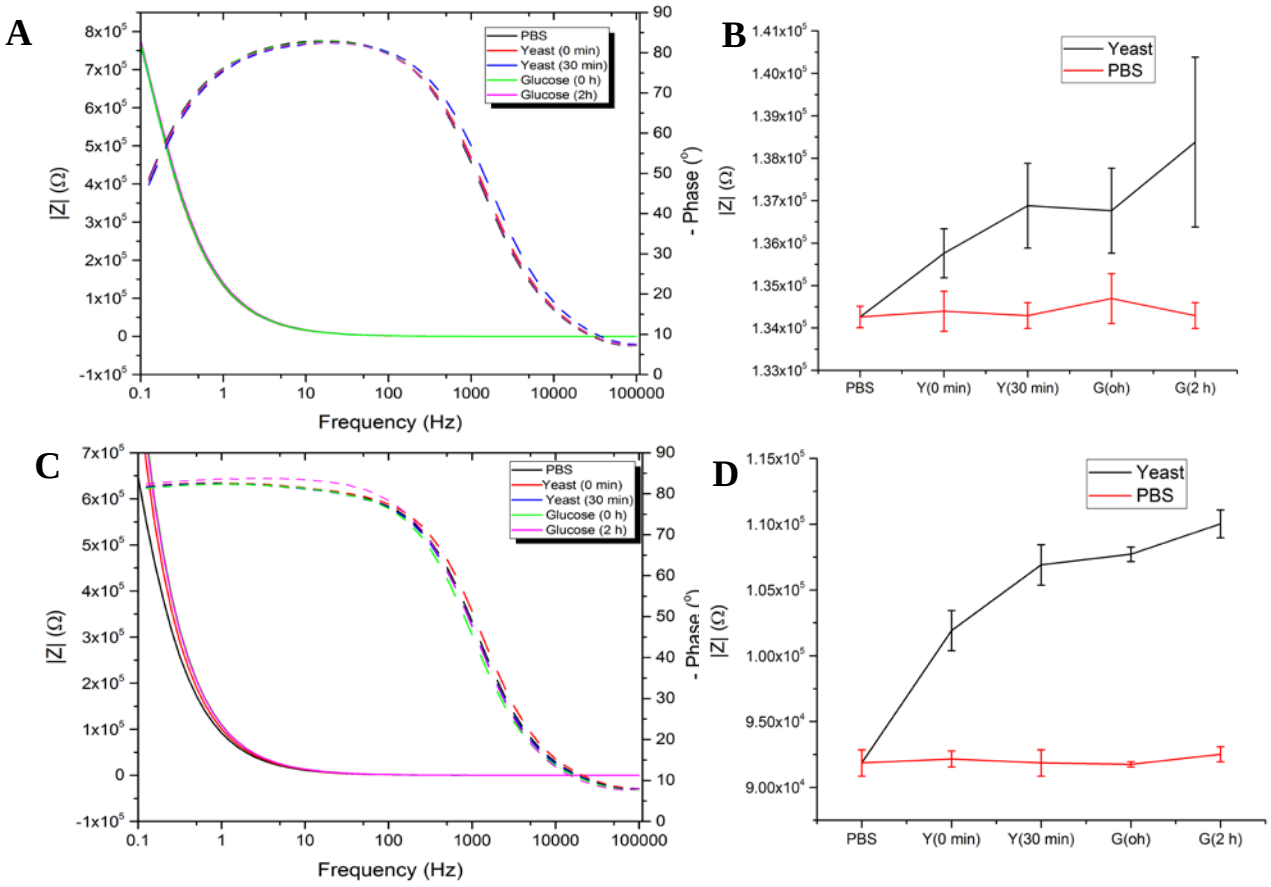

Figure 62: (A) and (C) shows the EIS spectra of 2D and 3D electrode respectively and (B) and (D) shows the impedance at 1 Hz for 2D and 3D electrode respectively (n = 3)

The impedance measurement on 2D electrode showed an increase in impedance from 0.134 MΩ to 0.136 MΩ for yeast seeding and further increased to 0.138 MΩ after yeast growth for 2 h. The impedance for 3D microelectrodes shows an increase from 0.09 MΩ to 0.106 MΩ after yeast seeding and further increased to 0.108 MΩ after yeast growth. The 3D microelectrode showed a higher change in impedance (18 kΩ) when compared to 2D electrodes (2 kΩ). Both 2D and 3D carbon electrode show an increase in impedance as the cell concentration is increased. Table 6 shows the yeast cells on the electrodes at various stages of experiments. The impedance measurement for yeast analysis, provide a simple model for testing the impedance response for carbon electrodes. The results shows a higher response (higher change in impedance) for 3D carbon microelectrodes when compared to 2D electrodes.

Table 6: Yeast cell on carbon electrodes at various stages of experiments

	2D	3D
PBS	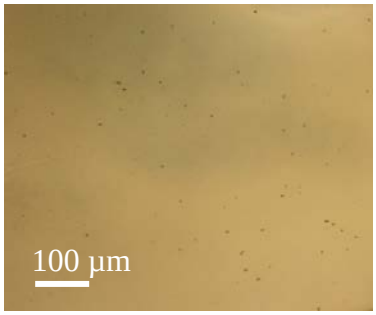	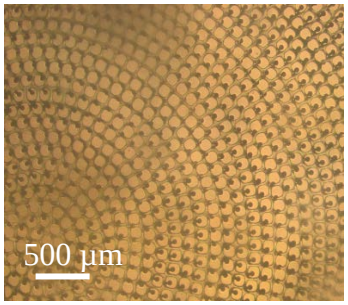
Yeast (0min)	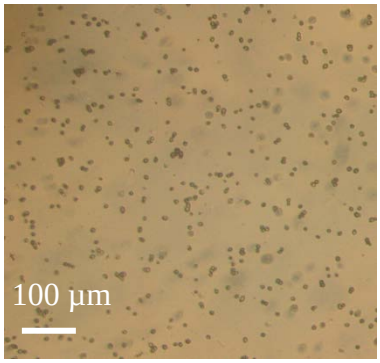	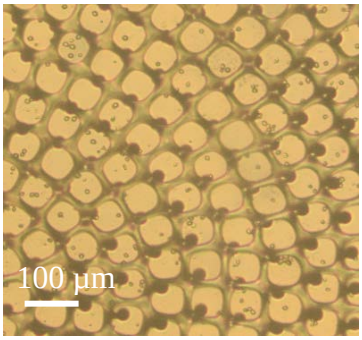
Glucose (2 h)	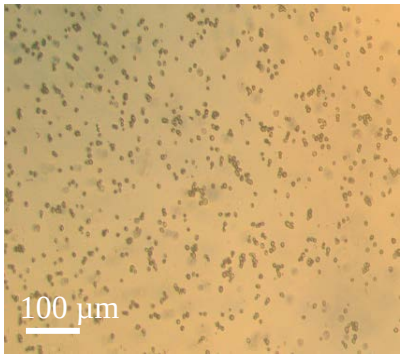	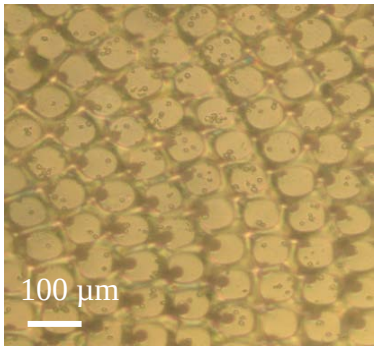

7.3 Neural stem cell differentiation

Dopamine released from human neural stem cells after differentiation into dopaminergic neurons is an important neurotransmitter in the central nervous system. Dopamine is a vital tool in modulating central nervous system functions, such as voluntary movements [186–188]. In Parkinson's disease the neurons releasing the dopamine are dying or dysfunctional which leads to impaired motor functions [189]. Hence monitoring the dopamine concentration plays an important role in Parkinson's disease. Electrochemical detection of dopamine on a pyrolytic carbon has been recently demonstrated [26]. In this thesis, 3D carbon microelectrode were used as a scaffold for growth of human neural stem cells (hNSCs) and an electrochemical detection of dopamine (preliminary experiments). 3D microelectrodes enable electrochemical detection of large fractions of dopamine compared to 2D electrodes [26,38]. This work is done in collaboration with Afia.Asif, PhD student at DTU, Nanotech supervised by Prof. Jenny Emnéus.

Human neural stem cells (hNSC) from the immortalized human ventral mesencephalic cell line overexpressing Bcl-XL (hVM-Bcl-XL) were cultured as described by E.T.Courtois et.al for ten days[190]. The carbon electrode (both 2D and 3D carbon electrodes) and the batch system were sterilized by immersion in 96% ethanol for 10min and 0.5 M NaOH for 30 min. This was followed by applying coating of poly L-Lysine (PLL) on the electrodes to promote cell adhesion. A cell density of 30,000 cells/cm^2 was seeded on the electrodes and the culture media was replaced by differentiation media after two days to initiate differentiation. The differentiation media was changed every other day for a duration of 10 days. The electrochemical experiments were carried out on the 11^{th} day. A high-k^+ buffer (10 mM HEPES, 5 mM glucose, 1.2 mM $MgCl_2$, 2 mM $CaCl_2$, 5 mM NaCl, and 450 mM KCl) was prepared to trigger the exocytosis in hNSC. The working electrode was set at a potential of 350 mV vs RE. After recording a baseline, 15 µL of high-k^+ was added to simulate the exocytosis. Figure 63.A and B shows the amperometric results of dopamine released from hNSC. The 3D carbon microelectrode detected a current response of 3.75 µA as compared to 2.9 nA recorded with 2D electrode. The higher current corresponds to the detection of larger amount of dopamine. Figure 63.C and D show the SEM images of hNSC cell distribution on 2D and 3D electrodes. Figure 63.E and F show confocal images with nuclei, cell body and dopaminergic neurons staining.

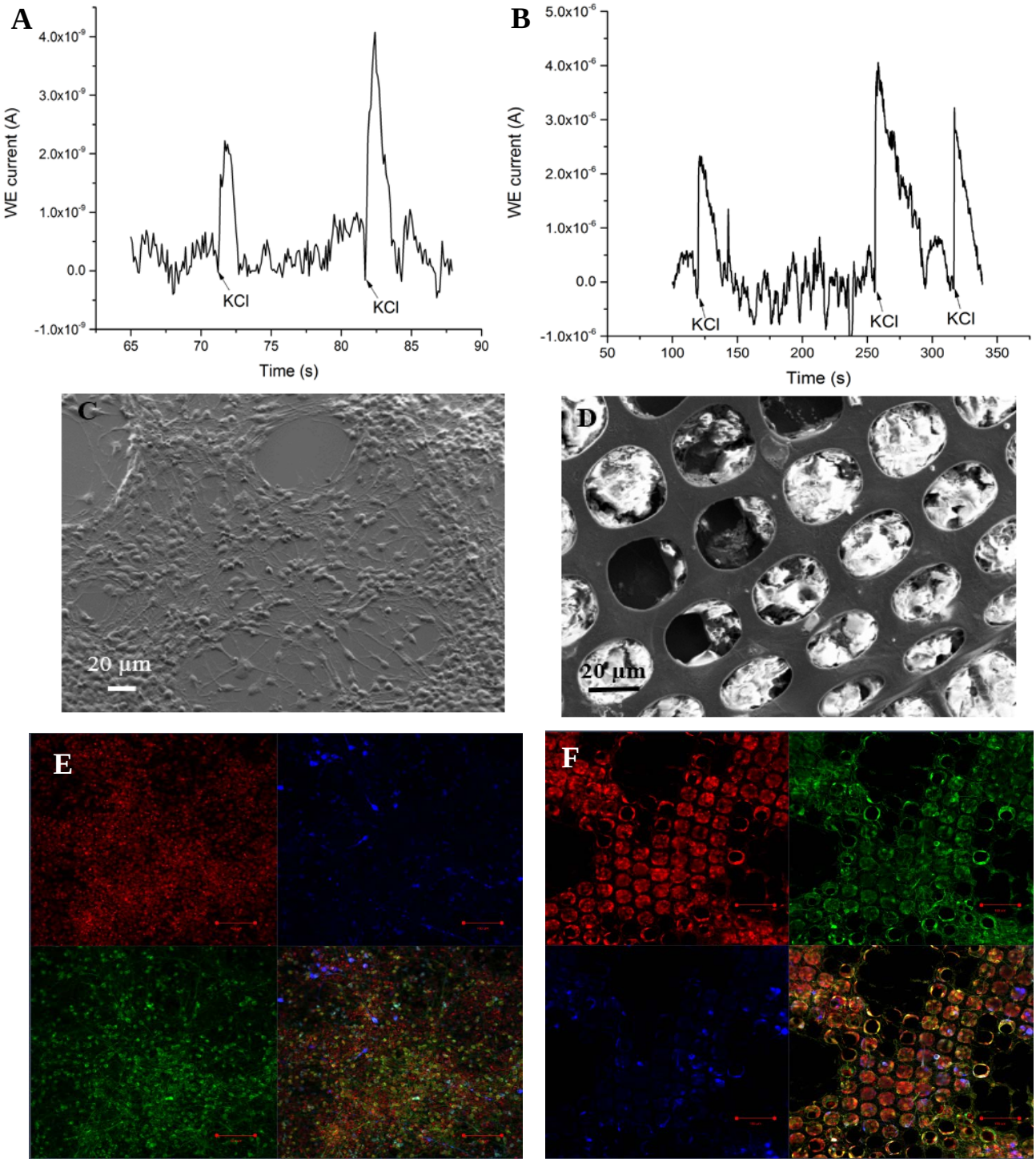

Figure 63: (A) – (B) Current- time trace recorded during amperometric detection of dopamine on 2D and 3D electrode respectively, (C) - (D) SEM images of hNSC distribution on 2D and 3D carbon respectively and (F) - (G) confocal image of 2D and 3D electrode with nuclei (red), cell body (green) and dopaminergic neurons(blue) staining.

7.4 Bone cells

A 3D *in vitro* model resembling the bone tissue for supporting bone diseases research and drug screening applications was developed by Claudia Caviglia Postdoc in the same group. Many techniques are available for detecting ALP activity based on specific ALP antibody, colorimetric assays, fluorometric assay and histochemical stains [191,192]. But these techniques are either labour insensitive or time consuming and expensive. Electrochemical technique for ALP detection is also present, which offers several advantages, making this ALP assay fast, economic and very sensitive [193]. The model system is used to monitor bone cell differentiation in real-time through the quantification of Alkaline Phosphatase (ALP) activity, a biomarker of bone cell differentiation, with 3D and 2D electrodes. First results indicates, the 3D electrode can be used to detect more ALP, which is not possible via 2D electrodes (Figure 64).

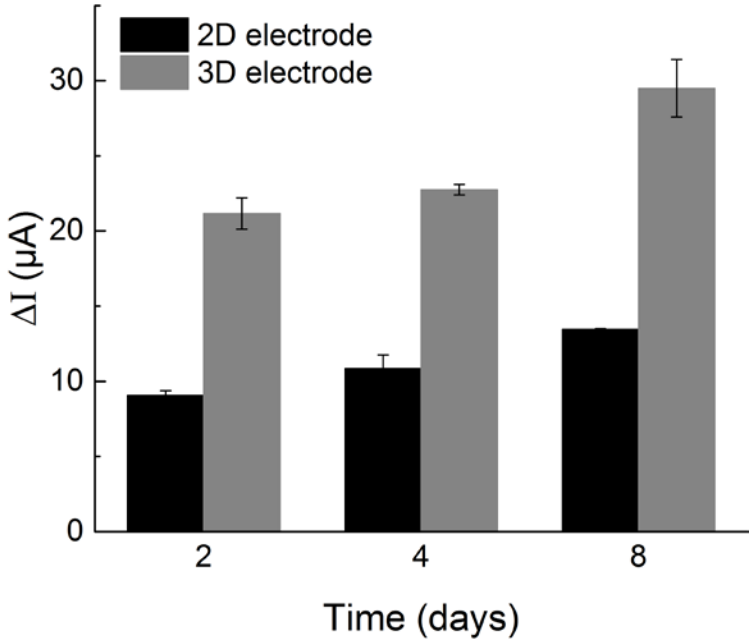

Figure 64: Current detected via SWV during ALP detection on 2D and 3D electrodes over 8 days (n = 3)

Chapter 8

Conclusion and outlook

Microelectrode chips with suspended 3D carbon microelectrodes for bioelectrochemistry were designed, fabricated and characterized. The developed electrochemical chip was also integrated in a microfluidic system and was used in several bioelectrochemical applications. Referring to chapter 1.4 the main goals achieved in this thesis are:

1. Polymer microfabrication – Three different UV photolithography processes with UV exposure at 313 nm, 365 nm and 405 nm were established for fabricating 3D suspended polymer templates in epoxy based resins. The most promising process for fabricating suspended layers was UV exposure at 405 nm. The process with UV exposure at 405 nm was used to fabricate high resolution (~ 5 µm), 3D suspended microstructures, and 3D multilayers with a reasonable high throughput.

2. Pyrolysis process – 3D suspended pyrolytic carbon microstructures were fabricated by pyrolysis at high temperatures for 1 h in N_2 atmosphere. Different parameters (such as maximum temperature, ramp rate and number of process steps) were examined for mechanical stability and electrical conductivity. The pyrolysis process with the highest temperature (1100 ºC) and ramp of 10 ºC/min was the most optimal parameters for fabricating 3D suspended microelectrodes with excellent electrochemical performance.

3. 3D Microelectrode – The three electrode chip (1 cm × 3cm) with pyrolytic carbon as the WE was fabricated successfully. Different 3D microstructures on the WE of the C4B chip were designed and tested for shrinkage, mechanical stability and electrochemical performance. The 3D carbon microelectrode with the pillar diameter of 6.7 µm, pitch of 50 µm and suspended layer thickness of 11 µm was the optimal design. The 3D carbon microelectrode showed two fold higher sensitivity when compared to 2D carbon electrodes.

4. Microfluidic/Microelectrode chip design and setup – Compact, easy self- aligning magnetic clamping systems (MagClamp) were developed for both static and dynamic testing. The wall-jet system was optimized in COMSOL and fabricated with micro-milling successfully. The wall-jet systems provided least shear stress and a reasonable response time when compared to other systems.

5. Bioelectrochemical characterisation/testing – The developed 3D carbon microelectrode was successfully used for four different applications. The glucose sensing and monitoring of hNSC elaborated the use of 3D C4B chips for amperometric detection. In both cases 3D C4B chips gave a higher response compared to 2D C4B chips (2 folds or higher). The yeast cells were used to measure the change in impedance. The 3D C4B chips showed a reasonable high change in impedance compared to 2D C4B chips. The final case study was the amperometric detection of ALP released by bone cells, in which 3D C4B gave two folds higher signal when compared to 2D electrodes.

Table 7: Summary of the C4B chips

Method	Electrode	Test system	Conclusion	Paper
CV and EIS	3D	$[Fe(CN)_6]^{4-}$/$[[Fe(CN)_6]^{3-}$	✓ 2x higher signal	[II]
SWV	3D	Dopamine and 4-AP	✓ 2.5x higher signal	[II] and [IV]
Amperometric	3D+RGO	Glucose	✓ 5x higher signal	[V]
EIS	3D	Yeast cell	• Not yet conclusive	-
Amperometric	3D	hNSC	✓ Work in progress	-
SWV	3D	Bone cell	✓ 2x higher signal	[manuscript]

In conclusion the 3D microelectrodes developed in the course of this PhD project have shown very promising results for bioelectrochemistry. Table 7 shows the summary of C4B chips used in this project. The 3D C4B chips could be used as an intelligent scaffold where the substrate can act as a sensing element at the same time. In the future more detailed bioelectrochemical studies can give more insights into actual advantages of 3D microelectrodes in bioelectrochemistry. Also the fabrication cost of 3D C4B chips are still relatively high with the present method. This can be reduced by replacing the Au with other metals (such as Ag), avoiding the passivation layer, reducing the overall size of the chips and further optimization of pyrolysis process.

Reference

1. European Environment Agency. *SOER 2010 — assessment of global megatrends — European Environment Agency*. (2010).

2. Landrigan, P. J., Schechter, C. B., Lipton, J. M., Fahs, M. C. & Schwartz, J. Environmental pollutants and disease in American children: estimates of morbidity, mortality, and costs for lead poisoning, asthma, cancer, and developmental disabilities. *Environ. Health Perspect.* 110, 721–8 (2002).

3. Henk, J. M. V., Cees, J. va. L. & Joop, L. M. H. Classifying environmental pollutants. *Chemosphere* 25, 471–491 (1992).

4. Brody, J. G. & Rudel, R. A. Environmental pollutants and breast cancer. *Environ. Health Perspect.* 111, 1007–19 (2003).

5. Kerstin, B. *et al.* German Environmental Survey 1998 (GerES III): environmental pollutants in blood of the German population. *Int. J. Hyg. Environ. Health* 205, 297–308 (2002).

6. Baeumner, A. J. Biosensors for environmental pollutants and food contaminants. *Anal. Bioanal. Chem.* 377, 434–445 (2003).

7. Shi, H. *et al.* Real-Time Monitoring of Cell Apoptosis and Drug Screening Using Fluorescent Light-Up Probe with Aggregation-Induced Emission Characteristics. *J. Am. Chem. Soc.* 134, 17972–17981 (2012).

8. El-Ali, J., Sorger, P. K. & Jensen, K. F. Cells on chips. *Nature* 442, 403–411 (2006).

9. Zór, K. *et al.* A compact multifunctional microfluidic platform for exploring cellular dynamics in real-time using electrochemical detection. *RSC Adv.* 4, 63761–63771 (2014).

10. Joachim, W., Charles, R. K. & Ivar, G. Electric Cell–Substrate Impedance Sensing (ECIS) as a Noninvasive Means to Monitor the Kinetics of Cell Spreading to Artificial Surfaces. *Exp. Cell Res.* 259, 158–166 (2000).

11. Shao, Y. *et al.* Graphene based electrochemical sensors and biosensors: A review. *Electroanalysis* 22, 1027–1036 (2010).

12. Grieshaber, D., MacKenzie, R., Vörös, J. & Reimhult, E. Electrochemical Biosensors - Sensor Principles and Architectures. *Sensors (Basel).* 8, 1400–1458 (2008).

13. Spegel, C., Heiskanen, A., Skjolding, L. H. D. & Emnéus, J. Chip Based Electroanalytical Systems for Cell Analysis. *Electroanalysis* 20, 680–702 (2008).

14. Hanrahan, G., Patil, D. G. & Wang, J. Electrochemical sensors for environmental monitoring: design, development and applications. *J. Environ. Monit.* 6, 657 (2004).

15. Caide Xiao, Bernard Lachance, Geoffrey Sunahara, and & Luong*, J. H. T. Assessment of

Cytotoxicity Using Electric Cell−Substrate Impedance Sensing: Concentration and Time Response Function Approach. (2002). doi:10.1021/AC025848F

16. Meissner, R., Eker, B., Kasi, H., Bertsch, A. & Renaud, P. Distinguishing drug-induced minor morphological changes from major cellular damage via label-free impedimetric toxicity screening. *Lab Chip* 11, 2352 (2011).

17. Chun-Min, L., Charles, R. K. & Ivar Giaever. pH Changes in Pulsed CO2 Incubators Cause Periodic Changes in Cell Morphology. *Exp. Cell Res.* 213, 391–397 (1994).

18. Chen, C. *et al.* Recent advances in electrochemical glucose biosensors: a review. *RSC Adv.* 3, 4473 (2013).

19. Schöning, M. J. *et al.* Recent advances in biologically sensitive field-effect transistors (BioFETs). *Analyst* 127, 1137–1151 (2002).

20. D'Orazio, P. Biosensors in clinical chemistry. *Clin. Chim. Acta.* 334, 41–69 (2003).

21. Mueller-Klieser, W. Three-dimensional cell cultures: from molecular mechanisms to clinical applications. *Am. J. Physiol.* 273, C1109-23 (1997).

22. Page, H., Flood, P. & Reynaud, E. G. Three-dimensional tissue cultures: current trends and beyond. *Cell Tissue Res.* 352, 123–131 (2013).

23. Kraehenbuehl, T. P., Langer, R. & Ferreira, L. S. Three-dimensional biomaterials for the study of human pluripotent stem cells. *Nat. Methods* 8, 731–736 (2011).

24. Lee, J., Lilly, G. D., Doty, R. C., Podsiadlo, P. & Kotov, N. A. In vitro Toxicity Testing of Nanoparticles in 3D Cell Culture. *Small* 5, NA-NA (2009).

25. Jeong, S. H., Lee, D. W., Kim, S., Kim, J. & Ku, B. A study of electrochemical biosensor for analysis of three-dimensional (3D) cell culture. *Biosens. Bioelectron.* 35, 128–133 (2012).

26. Amato, L. *et al.* Pyrolysed 3D-Carbon Scaffolds Induce Spontaneous Differentiation of Human Neural Stem Cells and Facilitate Real-Time Dopamine Detection. *Adv. Funct. Mater.* 24, 7042–7052 (2014).

27. Hemanth, S., Caviglia, C. & Keller, S. S. Suspended 3D pyrolytic carbon microelectrodes for electrochemistry. *Carbon N. Y.* 121, 226–234 (2017).

28. Chen, S. *et al.* Electrospun and solution blown three-dimensional carbon fiber nonwovens for application as electrodes in microbial fuel cells. *Energy Environ. Sci.* 4, 1417 (2011).

29. Gao, H. & Duan, H. 2D and 3D graphene materials: Preparation and bioelectrochemical applications. *Biosens. Bioelectron.* 65, 404–419 (2015).

30. Yi, W., Yang, Y., Hashemi, P. & Cheng, M. M.-C. 3D carbon nanofiber microelectrode arrays fabricated by plasma-assisted pyrolysis to enhance sensitivity and stability of real-time dopamine detection. *Biomed. Microdevices* 18, 112 (2016).

31. Kamath, R. R. & Madou, M. J. Three-Dimensional Carbon Interdigitated Electrode Arrays for

Redox-Amplification. *Anal. Chem.* 86, 2963–2971 (2014).

32. Santoro, F., Schnitker, J., Panaitov, G. & Offenhäusser, A. On Chip Guidance and Recording of Cardiomyocytes with 3D Mushroom-Shaped Electrodes. *Nano Lett.* 13, 5379–5384 (2013).

33. Müller, T. *et al.* A 3-D microelectrode system for handling and caging single cells and particles. *Biosens. Bioelectron.* 14, 247–256 (1999).

34. Jaramillo, M. del C., Torrents, E., Martínez-Duarte, R., Madou, M. J. & Juárez, A. On-line separation of bacterial cells by carbon-electrode dielectrophoresis. *Electrophoresis* 31, 2921–2928 (2010).

35. Martinez-Duarte, R., Gorkin III, R. A., Abi-Samra, K. & Madou, M. J. The integration of 3D carbon-electrode dielectrophoresis on a CD-like centrifugal microfluidic platform. *Lab Chip* 10, 1030 (2010).

36. Park, J. *et al.* An efficient cell separation system using 3D-asymmetric microelectrodes. *Lab Chip* 5, 1264 (2005).

37. Andersson, H. & van den Berg, A. Microfluidic devices for cellomics: a review. *Sensors Actuators B Chem.* 92, 315–325 (2003).

38. Amato Letizia. Pyrolysed carbon scaffolds for bioelectrochmistry in life science. (DTU, 2014).

39. Dvir, T. *et al.* Nanowired three-dimensional cardiac patches. *Nat. Nanotechnol.* 6, 720–725 (2011).

40. Ghasemi-Mobarakeh, L. *et al.* Application of conductive polymers, scaffolds and electrical stimulation for nerve tissue engineering. *J. Tissue Eng. Regen. Med.* 5, e17–e35 (2011).

41. Li, N. *et al.* Three-dimensional graphene foam as a biocompatible and conductive scaffold for neural stem cells. *Sci. Rep.* 3, 1604 (2013).

42. Joel Voldman, *, Martha L. Gray, †, Mehmet Toner, ‡ and & Schmidt, M. A. A Microfabrication-Based Dynamic Array Cytometer. (2002). doi:10.1021/AC0256235

43. Lee, S., Ahn, J., Seo, J.-M., Chung, H. & Cho, D.-I. Electrical Characterization of 3D Au Microelectrodes for Use in Retinal Prostheses. *Sensors* 15, 14345–14355 (2015).

44. Greiner, F. *et al.* Fabrication techniques for multiscale 3D-MEMS with vertical metal micro- and nanowire integration. *J. Micromechanics Microengineering* 23, 25018 (2013).

45. Rajaraman, S. *et al.* Microfabrication technologies for a coupled three-dimensional microelectrode, microfluidic array. *J. Micromechanics Microengineering* 17, 163–171 (2007).

46. Piotter, V., Benzler, T., Gietzelt, T., Ruprecht, R. & Haußelt, J. Micro Powder Injection Molding. *Adv. Eng. Mater.* 2, 639–642 (2000).

47. Siegel, A. C., Bruzewicz, D. A., Weibel, D. B. & Whitesides, G. M. Microsolidics: Fabrication of Three-Dimensional Metallic Microstructures in Poly(dimethylsiloxane). *Adv. Mater.* 19, 727–733 (2007).

48. Kim, S., Park, J., Kang, K., Park, C.-O. & Park, I. Direct metal micropatterning on needle-type structures towards bioimpedance and chemical sensing applications. *J. Micromechanics Microengineering* 25, 15002 (2015).

49. Wang, J., Tian, B., Nascimento, V. B. & Angnes, L. Performance of screen-printed carbon electrodes fabricated from different carbon inks. *Electrochim. Acta* 43, 3459–3465 (1998).

50. Patel, J. N., Gray, B. L., Kaminska, B. & Gates, B. D. Flexible three-dimensional electrochemical glucose sensor with improved sensitivity realized in hybrid polymer microelectromechanical systems technique. *J. Diabetes Sci. Technol.* 5, 1036–43 (2011).

51. Paiè, P. *et al.* Straightforward 3D hydrodynamic focusing in femtosecond laser fabricated microfluidic channels. *Lab Chip* 14, 1826–1833 (2014).

52. Choi, J.-W. *et al.* 3-dimensional electrode patterning within a microfluidic channel using metal ion implantation. *Lab Chip* 10, 783 (2010).

53. Martinez-Duarte, R. Microfabrication technologies in dielectrophoresis applications-A review. *Electrophoresis* 33, 3110–3132 (2012).

54. Chunlei Wang, Guangyao Jia, Taherabadi, L. H. & Madou, M. J. A novel method for the fabrication of high-aspect ratio C-MEMS structures. *J. Microelectromechanical Syst.* 14, 348–358 (2005).

55. Niwa, O. & Tabei, H. Voltammetric measurements of reversible and quasi-reversible redox species using carbon film based interdigitated array microelectrodes. *Anal. Chem.* 66, 285–289 (1994).

56. Baldwin, R. P. Electrochemical determination of carbohydrates: enzyme electrodes and amperometric detection in liquid chromatography and capillary electrophoresis. *J. Pharm. Biomed. Anal.* 19, 69–81 (1999).

57. Lane, R. F. & Hubbard, A. T. Differential double pulse voltammetry at chemically modified platinum electrodes for in vivo determination of catechol amines. *Anal. Chem.* 48, 1287–1293 (1976).

58. Chen, Z. *et al.* Three-dimensional flexible and conductive interconnected graphene networks grown by chemical vapour deposition. *Nat Mater* 10, 424–428 (2011).

59. G. Sreenivas, † *et al.* Fabrication and Characterization of Sputtered-Carbon Microelectrode Arrays. (1996). doi:10.1021/AC9508816

60. Madou, M. *et al.* Carbon micromachining (c-mems). in *Chemical and Biological Sensors and Analytical Electrochemical Methods: Proceedings of the Symposium on Chemical and Biological Sensors and Analytical Electrochemical Methods* 97, 1961 (The Electrochemical Society, 1997).

61. McCreery, R. L. Advanced Carbon Electrode Materials for Molecular Electrochemistry. *Chem. Rev.* 108, 2646–2687 (2008).

62. Cowlard, F. C. & Lewis, J. C. Vitreous carbon — A new form of carbon. *J. Mater. Sci.* 2, 507–

512 (1967).

63. Lyons, A. M. Photodefinable carbon films: Electrical properties. *J. Non. Cryst. Solids* 70, 99–109 (1985).

64. Park, B. Y., Taherabadi, L., Wang, C., Zoval, J. & Madou, M. J. Electrical Properties and Shrinkage of Carbonized Photoresist Films and the Implications for Carbon Microelectromechanical Systems Devices in Conductive Media. *J. Electrochem. Soc.* 152, J136 (2005).

65. Kawamura, K. & Jenkins, G. M. Mechanical properties of glassy carbon fibres derived from phenolic resin. *J. Mater. Sci.* 7, 1099–1112 (1972).

66. Teixidor, G. T. *et al.* Carbon microelectromechanical systems as a substratum for cell growth. *Biomed. Mater.* 3, 34116 (2008).

67. Kassegne, S., Wondimu, B., Majzoub, M. & Shin, J. High-efficiency microarray of 3-D carbon MEMS electrodes for pathogen detection systems. in (eds. Otani, Y. et al.) 7266, 726615 (International Society for Optics and Photonics, 2008).

68. Lee, J. A. *et al.* An electrochemical impedance biosensor with aptamer-modified pyrolyzed carbon electrode for label-free protein detection. *Sensors Actuators B* 129, 372–379 (2008).

69. Min, H.-S. *et al.* Fabrication and properties of a carbon/polypyrrole three-dimensional microbattery. *J. Power Sources* 178, 795–800 (2008).

70. Teixidor, G. T., Zaouk, R. B., Park, B. Y. & Madou, M. J. Fabrication and characterization of three-dimensional carbon electrodes for lithium-ion batteries. *J. Power Sources* 183, 730–740 (2008).

71. Mitra, J., Jain, S., Sharma, A. & Basu, B. Patterned growth and differentiation of neural cells on polymer derived carbon substrates with micro/ nano structures in vitro. *Carbon N. Y.* 65, 140–155 (2013).

72. Zhou, H., Zhou, J., Gupta, A. & Zou, T. Photoresist Derived Carbon for Growth and Differentiation of Neuronal Cells. *Int. J. Mol. Sci.* 8, 884–893 (2007).

73. Zachek, M. K., Takmakov, P., Moody, B., Wightman, R. M. & McCarty, G. S. Simultaneous decoupled detection of dopamine and oxygen using pyrolyzed carbon microarrays and fast-scan cyclic voltammetry. *Anal. Chem.* 81, 6258–65 (2009).

74. Martinez-Duarte, R. & Rodrigo. SU-8 Photolithography as a Toolbox for Carbon MEMS. *Micromachines* 5, 766–782 (2014).

75. Ma, Y. *et al.* Processing study of SU-8 pillar profiles with high aspect ratio by electron-beam lithography. *Microelectron. Eng.* 149, 141–144 (2016).

76. Ohlinger, K., Lin, Y., Poole, Z. & Chen, K. P. Undistorted 3D microstructures in SU8 formed through two-photon polymerization. *Appl. Phys. Lett* 1, 32163–32163 (2011).

77. Barber, R. L. *et al.* Optimisation of SU-8 processing parameters for deep X-ray lithography.

Microsyst. Technol. 11, 303–310 (2005).

78. Ceyssens, F. & Puers, R. Creating multi-layered structures with freestanding parts in SU-8. *J. Micromechanics Microengineering* 16, S19–S23 (2006).

79. Melai, J., Blanco Carballo, V. M., Salm, C. & Schmitz, J. Suspended membranes, cantilevers and beams using SU-8 foils. *Microelectron. Eng.* 87, 1274–1277 (2010).

80. Rammohan, A. *et al.* One-step maskless grayscale lithography for the fabrication of 3-dimensional structures in SU-8. *Sensors Actuators B Chem.* 153, 125–134 (2011).

81. De Volder, M. F. L. *et al.* Hierarchical Carbon Nanowire Microarchitectures Made by Plasma-Assisted Pyrolysis of Photoresist. *ACS Nano* 5, 6593–6600 (2011).

82. Chen, W. *et al.* High-Performance Nanostructured Supercapacitors on a Sponge. *Nano Lett.* 11, 5165–5172 (2011).

83. Clark, J. E. & Olesik, S. V. Electrospun glassy carbon ultra-thin layer chromatography devices. *J. Chromatogr. A* 1217, 4655–4662 (2010).

84. Amato, L. *et al.* Dense high-aspect ratio 3D carbon pillars on interdigitated microelectrode arrays. *Carbon N. Y.* 94, 792–803 (2015).

85. Falcao, E. H. & Wudl, F. Carbon allotropes: beyond graphite and diamond. *J. Chem. Technol. Biotechnol.* 82, 524–531 (2007).

86. Hirsch, A. The era of carbon allotropes. *Nat Mater* 9, 868–871 (2010).

87. Pierson, H. O. Handbook of Carbon, Graphite, Diamond, and Fullerenes, Processing, Properties and Applications. (1993).

88. Robertson, J. Review Properties of diamond-like carbon. *Surf. Coatings Technol.* 50, 185–203 (1992).

89. Jenkins, G. M. & Kawamura, K. *Polymeric carbons: carbon fibre, glass and char*. (Cambridge University Press, 1976).

90. Kim, J., Song, X., Kinoshita, K., Madou, M. & White, R. Electrochemical Studies of Carbon Films from Pyrolyzed Photoresist. *J. Electrochem. Soc.* 145, 2314 (1998).

91. Singh, A., Jayaram, J., Madou, M. & Akbar, S. Pyrolysis of Negative Photoresists to Fabricate Carbon Structures for Microelectromechanical Systems and Electrochemical Applications. *J. Electrochem. Soc.* 149, E78 (2002).

92. Rosalind E. Franklin. Formation and structure of polymeric carbons. *Proc. R. Soc. London A Math. Phys. Eng. Sci.* 327, (1972).

93. McCreery, R. L. Electroanalytical chemistry. *Marcel Dekker, Inc., New York* 17, 221–374 (1991).

94. Khan, W., Sharma, R. & Saini, P. Carbon Nanotube-Based Polymer Composites: Synthesis, Properties and Applications. in *Carbon Nanotubes - Current Progress of their Polymer Composites* (InTech, 2016). doi:10.5772/62497

95. Jenkins, G. M. & Kawamura, K. Structure of glassy carbon. *Nature* 231, 175–176 (1971).

96. Harris †, P. J. F. Fullerene-related structure of commercial glassy carbons. *Philos. Mag.* 84, 3159–3167 (2004).

97. McNaught, A. D. & Wilkinson, A. IUPAC. *Compend. Chem. Terminol. ('gold book'), 2nd edn. Blackwell Sci. Publ. Oxford. XML on-line corrected version Creat. by Nic M, Jirat J, Kosata B* (1997).

98. Madou, M. J. *Manufacturing techniques for microfabrication and nanotechnology*. 2, (CRC press, 2011).

99. Madou, M. J. Fundamentals of microfabrication: the science of miniaturization. (2002).

100. Prakash Parida, O. & Bhat, N. CHARACTERIZATION OF OPTICAL PROPERTIES OF SU-8 AND FABRICATION OF OPTICAL COMPONENETS.

101. Ren Yang & Wanjun Wang. A numerical and experimental study on gap compensation and wavelength selection in UV-lithography of ultra-high aspect ratio SU-8 microstructures. *Sensors Actuators B* 110, 279–288 (2005).

102. Harsha, K. S. *Principles of vapor deposition of thin films*. (Elsevier, 2005).

103. Robbie, K. & Brett, M. J. Sculptured thin films and glancing angle deposition: Growth mechanics and applications. *http://oasc12039.247realmedia.com/RealMedia/ads/click_lx.ads/test.int.aip.org/adtest/L23/1268386150/x01/AIP/HA_AVS46_1640Cov_June17/AVS64_1640x440.jpg/4a39503479566d423253454144766458?x* (1998). doi:10.1116/1.580562

104. Savale, P. A. Physical Vapor Deposition (PVD) Methods for Synthesis of Thin Films: A Comparative Study. *Arch. Appl. Sci. Res.* 8, 1–8 (2016).

105. Franklin, R. E. Crystallite growth in graphitizing and non-graphitizing carbons. *Proc. R. Soc. London A Math. Phys. Eng. Sci.* 209, (1951).

106. Fitzer, E. & Schafer, W. THE EFFECT OF CROSSLINKING ON THE FORMATION OF GLASSLIKE CARBONS FROM THERMOSETTING RESINS*. *Carbma* 8, 353–364 (1970).

107. Wang, C. & Madou, M. From MEMS to NEMS with carbon. *Biosens. Bioelectron.* 20, 2181–2187 (2005).

108. Wang, C., Zaouk, R., Park, B. Y. & Madou, M. J. Carbon as a MEMS material: micro and nanofabrication of pyrolysed photoresist carbon. *Int. J. Manuf. Technol. Manag.* 13, 360 (2008).

109. Mariotti, D. & Sankaran, R. M. Perspectives on atmospheric-pressure plasmas for nanofabrication. *J. Phys. D. Appl. Phys.* 44, 174023 (2011).

110. Schartel, B. *et al.* Pyrolysis of epoxy resins and fire behavior of epoxy resin composites flame-retarded with 9,10-dihydro-9-oxa-10-phosphaphenanthrene-10-oxide additives. *J. Appl. Polym. Sci.* 104, 2260–2269 (2007).

111. Kawamura, K. & Kimura, S. Glass-like Carbon Made from Epoxy Resin Cured with 2,4,6-Trinitrophenol. *Bull. Chem. Soc. Jpn.* 56, 2499–2503 (1983).

112. Rwei, S.-P., Kao, S.-C., Liou, G.-S., Cheng, K.-C. & Guo, W. Curing and pyrolysis of epoxy resins containing 2-(6-oxido-6H-dibenz(c,e)(1,2)oxaphosphorin-6-yl)-1,4-naphthalenediol or bisphenol S. *Colloid Polym. Sci.* 281, 407–415 (2003).

113. Straus, S. & Wall, L. A. Pyrolysis of Polyarnides. *J Res Natl Bur Stand* 60, 39–45 (1958).

114. Leichtnam, J.-N., Schwartz, D. & Gadiou, R. The behaviour of fuel-nitrogen during fast pyrolysis of polyamide at high temperature. *J. Anal. Appl. Pyrolysis* 55, 255–268 (2000).

115. Fitzer, E., Schaefer, W. & Yamada, S. The formation of glasslike carbon by pyrolysis of polyfurfuryl alcohol and phenolic resin. *Carbon N. Y.* 7, 643–648 (1969).

116. Schueller, O. J. ., Brittain, S. T. & Whitesides, G. M. Fabrication of glassy carbon microstructures by soft lithography. *Sensors Actuators A Phys.* 72, 125–139 (1999).

117. Wang, Y. *et al.* Nanopatterned Carbon Films with Engineered Morphology by Direct Carbonization of UV-Stabilized Block Copolymer Films. *Nano Lett.* 8, 3993–3997 (2008).

118. Miskolczi, N., Bartha, L. & Angyal, A. Pyrolysis of Polyvinyl Chloride (PVC)-Containing Mixed Plastic Wastes for Recovery of Hydrocarbons. *Energy & Fuels* 23, 2743–2749 (2009).

119. Polakoff, P. L., Lapp, N. L. & Roger, R. Polyvinyl Chloride Pyrolysis Products. *Arch. Environ. Heal. An Int. J.* 30, 269–271 (1975).

120. Xu, Y. *et al.* Nanosized core/shell silicon@carbon anode material for lithium ion batteries with polyvinylidene fluoride as carbon source. *J. Mater. Chem.* 20, 3216 (2010).

121. Wei Chen *et al.* Integration of Carbon Nanotubes to C-MEMS for On-chip Supercapacitors. *IEEE Trans. Nanotechnol.* 9, 734–740 (2010).

122. Hassan, Y. M. *et al.* High temperature SU-8 pyrolysis for fabrication of carbon electrodes. *J. Anal. Appl. Pyrolysis* 125, 91–99 (2017).

123. Natu, R., Islam, M. & Martinez-Duarte, R. Shrinkage Analysis of Carbon Micro Structures Derived from SU-8 Photoresist. *ECS Trans.* 72, 27–33 (2016).

124. Chen, S.-Y. & Chen, I.-W. Cracking during Pyrolysis of Oxide Thin Films-Phenomenology, Mechanisms, and Mechanics. *J. Am. Ceram. Soc.* 78, 2929–2939 (1995).

125. Amato, L. *et al.* Novel Nanostructured Electrodes Obtained by Pyrolysis of Composite Polymeric Materials. *Electroanalysis* 27, 1544–1549 (2015).

126. Reichelt, R. Scanning Electron Microscopy. in *Science of Microscopy* 133–272 (Springer New York, 2007). doi:10.1007/978-0-387-49762-4_3

127. Oatley, C. W., Nixon, W. C. & Pease, R. F. W. Scanning Electron Microscopy. in 181–247 (1966). doi:10.1016/S0065-2539(08)61010-0

128. Goodhew, P. J., Beanland, R. & Humphreys, F. J. *Electron microscopy and analysis*. (Taylor &

Francis, 2001).

129. Thiel, B. L. & Toth, M. Secondary electron contrast in low-vacuum/environmental scanning electron microscopy of dielectrics. *J. Appl. Phys.* 97, 51101 (2005).

130. Stokes, D. J. Recent advances in electron imaging, image interpretation and applications: environmental scanning electron microscopy. *Philos. Trans. R. Soc. London A Math. Phys. Eng. Sci.* 361, (2003).

131. Danilatos, G. D. Review and outline of environmental SEM at present. *J. Microsc.* 162, 391–402 (1991).

132. Griffin, B. J. A new mechanism for the imaging of crystal structure in non-conductive materials: an application of charge-induced contrast in the environmental scanning electron microscope (ESEM). *Microsc. Microanal. YORK*- 3, 1197–1198 (2000).

133. Derek J. GardinerPierre R. Graves. *Practical Raman Spectroscopy*. (Springer Berlin Heidelberg, 1989). doi:10.1007/978-3-642-74040-4

134. Paul Rostron, Safa Gaber, D. G. Raman Spectroscopy, Review. *Int. J. Eng. Tech. Res.* 6, 2454–4698 (2016).

135. Pelletier, M. J. *Analytical applications of Raman spectroscopy*. (Wiley-Blackwell, 1999).

136. Hollander, J. M. & Jolly, W. L. X-ray photoelectron spectroscopy. *Acc. Chem. Res.* 3, 193–200 (1970).

137. deVries, J. E. Surface Characterization Methods—XPS, TOF-SIMS, and SAM A Complimentary Ensemble of Tools. *J. Mater. Eng. Perform.* 7, 303–311 (1998).

138. Desimoni, E., Casella, G. I., Morone, A. & Salvi, A. M. XPS determination of oxygen-containing functional groups on carbon-fibre surfaces and the cleaning of these surfaces. *Surf. Interface Anal.* 15, 627–634 (1990).

139. Siegbahn, K. ELECTRON SPECTROSCOPY FOR ATOMS, MOLECULES AND CONDENSED MATTER. (1981).

140. Kostecki, R. *et al.* Surface studies of carbon films from pyrolyzed photoresist. *Thin Solid Films* 396, 36–43 (2001).

141. Smits, F. M. Measurement of Sheet Resistivities with the Four-Point Probe. *Bell Syst. Tech. J.* 37, 711–718 (1958).

142. Shimamoto, A. *et al.* A Nondestructive Evaluation Method: Measuring the Fixed Strength of Spot-Welded Joint Points by Surface Electrical Resistivity. *J. Press. Vessel Technol.* 135, 21501 (2013).

143. Bard, A. J. & Faulkner, L. R. *Electrochemical methods : fundamentals and applications*. (Wiley, 2001).

144. Stacy Hunt DuVall & McCreery*, R. L. Control of Catechol and Hydroquinone Electron-Transfer Kinetics on Native and Modified Glassy Carbon Electrodes. (1999). doi:10.1021/AC990399D

145. Nicholson, R. S. Theory and Application of Cyclic Voltammetry for Measurement of Electrode Reaction Kinetics. *Anal. Chem.* 37, 1351–1355 (1965).

146. Bond†, A. M. & Stephen W. Feldberg*, †. Analysis of Simulated Reversible Cyclic Voltammetric Responses for a Charged Redox Species in the Absence of Added Electrolyte. (1998). doi:10.1021/JP9828437

147. Kissinger, P. T. & Heineman, W. R. Cyclic voltammetry. *J. Chem. Educ.* 60, 702 (1983).

148. Wang, J. *Analytical electrochemistry*. (Wiley-VCH, 2006).

149. Lovrić, M. Square-Wave Voltammetry. in *Electroanalytical Methods* 121–145 (Springer Berlin Heidelberg, 2010). doi:10.1007/978-3-642-02915-8_6

150. Ramaley, L. & Krause, M. S. Theory of square wave voltammetry. *Anal. Chem.* 41, 1362–1365 (1969).

151. Lvovich, V. F. & Wiley InterScience (Online service). *Impedance spectroscopy : applications to electrochemical and dielectric phenomena*. (Wiley, 2012).

152. Orazem, M. E. & Tribollet, B. *Electrochemical Impedance Spectroscopy*. (Wiley, 2011).

153. Caviglia Claudia. Real-time multi-parameter cell-based analysis platform. (DTU, 2014).

154. Whitesides, G. M. The origins and the future of microfluidics. *Nature* (2006). doi:10.1038/nature05058

155. Planar chips technology for miniaturization and integration of separation techniques into monitoring systems: Capillary electrophoresis on a chip. *J. Chromatogr. A* 593, 253–258 (1992).

156. Holger, B. & Laurie E.Locascio. Polymer microfluidic devices. *Talanta* 56, 267–287 (2002).

157. Sia, S. K. & Whitesides, G. M. Microfluidic devices fabricated in Poly(dimethylsiloxane) for biological studies. *Electrophoresis* 24, 3563–3576 (2003).

158. David Erickson & Dongqing Li. Integrated microfluidic devices. *Anal. Chim. Acta* 507, 11–26 (2004).

159. Yeo, L. Y., Chang, H.-C., Chan, P. P. Y. & Friend, J. R. Microfluidic Devices for Bioapplications. *Small* 7, 12–48 (2011).

160. Leanne Marle & Gillian M.Greenway. Microfluidic devices for environmental monitoring. *TrAC Trends Anal. Chem.* 24, 795–802 (2005).

161. Fair, R. B. *et al.* Chemical and Biological Applications of Digital-Microfluidic Devices. *IEEE Des. Test Comput.* 24, 10–24 (2007).

162. Hemant, S. *et al.* Pyrolytic 3D Carbon Microelectrodes for Electrochemistry. *E C S Trans. ,The Electrochem. Soc.* 72, 117–124 (2016).

163. Walker, G. M., Ozers, M. S. & Beebe, D. J. Insect cell culture in microfluidic channels. *Biomed. Microdevices* 4, 161–166 (2002).

164. Ribeiro, A. C. F. *et al.* Binary Mutual Diffusion Coefficients of Aqueous Solutions of Sucrose, Lactose, Glucose, and Fructose in the Temperature Range from (298.15 to 328.15) K. doi:10.1021/je0602061

165. Hirabayashi, M., Mehta, B., Khosla, A. & Kassegne, S. Functionalization of Pyrolyzed Carbon Structures for Bio-Nanoelectronics Platforms. *ECS Trans.* 50, 325–331 (2013).

166. Belkind, A. & Gershman, S. Plasma cleaning of surfaces. *Vac. Coat. Technol. Novemb.* 46–57 (2008).

167. Campo, A. del & Greiner, C. SU-8: a photoresist for high-aspect-ratio and 3D submicron lithography. *J. Micromechanics Microengineering* 17, R81–R95 (2007).

168. Cadarso, V. J. *et al.* Direct writing laser of high aspect ratio epoxy microstructures. *J. Micromechanics Microengineering* 21, 17003 (2011).

169. Lim, Y., Heo, J.-I. & Shin, H. Fabrication and application of a stacked carbon electrode set including a suspended mesh made of nanowires and a substrate-bound planar electrode toward for an electrochemical/biosensor platform. *Sensors Actuators B Chem.* 192, 796–803 (2014).

170. Suhith Hemanth, Thomas A.Anhøj, Claudia Caviglia & Stephan S.Keller. Suspended microstructures of epoxy based photoresists fabricated with UV photolithography. *Microelectron. Eng.* 176, 40–44 (2017).

171. Keller, S., Blagoi, G., Lillemose, M., Haefliger, D. & Boisen, A. Processing of thin SU-8 films. *J. Micromechanics Microengineering* 18, 125020 (2008).

172. Anhoj, T. A., Jorgensen, A. M., Zauner, D. A. & Hübner, J. The effect of soft bake temperature on the polymerization of SU-8 photoresist. *J. Micromechanics Microengineering* 16, 1819–1824 (2006).

173. Turner, A. P. F. Biosensors: sense and sensibility. *Chem. Soc. Rev.* 42, 3184–3196 (2013).

174. Bandodkar, A. J. & Wang, J. Non-invasive wearable electrochemical sensors: a review. *Trends Biotechnol.* 32, 363–371 (2014).

175. Wang, J. Glucose biosensors: 40 years of advances and challenges. *Electroanalysis* 13, 983 (2001).

176. Wang*, J. Electrochemical Glucose Biosensors. (2007). doi:10.1021/CR068123A

177. Mazzocchi, R. A. Medical Sensors – Defining a Pathway to Commercialization. *ACS Sensors* acssensors.6b00553 (2016). doi:10.1021/acssensors.6b00553

178. Perreault, F., Fonseca de Faria, A. & Elimelech, M. Environmental applications of graphene-based nanomaterials. *Chem. Soc. Rev.* 44, 5861–5896 (2015).

179. Mohanty, S. P. & Koucianos, E. Biosensors: A tutorial review. *IEEE Potentials* 25, 35–40 (2006).

180. Turner, A. Biosensors: Then and now. *Trends Biotechnol.* 31, 119–120 (2013).

181. Burke, A. M. & Gorodetsky, A. A. Electrochemical sensors: Taking charge of detection. *Nat.*

Chem. 4, 595–597 (2012).

182. Feldmann, H. (Cytologist) & Branduardi, P. *Yeast : molecular and cell biology*. (Wiley-Blackwell, 2012).

183. Wu, M.-H., Huang, S.-B. & Lee, G.-B. Microfluidic cell culture systems for drug research. *Lab Chip* 10, 939 (2010).

184. Park, J. Y., Takayama, S. & Lee, S.-H. Regulating microenvironmental stimuli for stem cells and cancer cells using microsystems. *Integr. Biol.* 2, 229 (2010).

185. van Midwoud, P. M., Verpoorte, E. & Groothuis, G. M. M. Microfluidic devices for in vitro studies on liver drug metabolism and toxicity. *Integr. Biol.* 3, 509 (2011).

186. Schwartz, M. W., Woods, S. C., Porte, D., Seeley, R. J. & Baskin, D. G. Central nervous system control of food intake. *Nature, Publ. online 06 April 2000; | doi10.1038/35007534* 404, 661 (2000).

187. Dopamine-containing neurons in the mammalian central nervous system: Electrophysiology and pharmacology. *Neurosci. Biobehav. Rev.* 12, 49–91 (1988).

188. Louis, J., Magal, E., Takayama, S. & Varon, S. Stem Cells in the Central Nervous System. *Science (80-.).* 259, 689–692 (1993).

189. Politis, M. & Lindvall, O. Clinical application of stem cell therapy in Parkinson's disease. *BMC Med.* 10, 1 (2012).

190. Courtois, E. T. *et al.* In vitro and in vivo enhanced generation of human A9 dopamine neurons from neural stem cells by Bcl-XL. *J. Biol. Chem.* 285, 9881–97 (2010).

191. Shih, Y.-R. V., Chen, C.-N., Tsai, S.-W., Wang, Y. J. & Lee, O. K. Growth of Mesenchymal Stem Cells on Electrospun Type I Collagen Nanofibers. *Stem Cells* 24, 2391–2397 (2006).

192. Hung, P.-S., Kuo, Y.-C., Chen, H.-G., Chiang, H.-H. K. & Lee, O. K.-S. Detection of Osteogenic Differentiation by Differential Mineralized Matrix Production in Mesenchymal Stromal Cells by Raman Spectroscopy. *PLoS One* 8, e65438 (2013).

193. Yildirim-Semerci, C., Benayahu, D., Adamovski, M. & Wollenberger, U. An Electrochemical Assay for Monitoring Differentiation of the Osteoblastic Cell Line (MBA-15) on the Sensor Chip. *Electroanalysis* 27, 1350–1358 (2015).

Paper I

Pyrolytic 3D Carbon Microelectrodes for Electrochemistry

S.Hemanth, C.Caviglia, L. Amato, T. A. Anhøj, A.Heiskanen, J. Emnéus, and S. S. Keller, *ECS Transactions*, 72 (2016), 117–124.

ECS Transactions, 72 (1) 117-124 (2016)
10.1149/07201.0117ecst ©The Electrochemical Society

Pyrolytic 3D Carbon Microelectrodes for Electrochemistry

S.Hemanth[a], C.Caviglia[a], L. Amato[a], T.A. Anhøj[b], A.Heiskanen[a], J. Emnéus[a], and S.S. Keller[a]

[a]Department of Micro- and Nanotechnology, DTU Nanotech, DK- 2800
[b] DTU Danchip, 2800 Kongens Lyngby, Denmark

This work presents the fabrication and characterization of suspended three-dimensional (3D) pyrolytic carbon microelectrodes for electrochemical applications. For this purpose, an optimized process with multiple steps of UV photolithography with the negative tone photoresist SU-8 followed by pyrolysis at 900ºC for 1h was developed. With this process, microelectrode chips with a three electrode configuration were fabricated and characterized with cyclic voltammetry (CV) using a 10mM potassium ferri-ferrocyanide redox probe in a custom made batch system with magnetic clamping. The 3D pyrolytic carbon microelectrodes displayed twice the higher peak current compared to 2D.

Introduction

Carbon materials have several attractive characteristics for microelectrodes in electrochemical applications, such as a wide potential window, good electrochemical activity, chemical stability, and ease in surface functionalization (1). The most common carbon microfabrication techniques (i.e. screen printing) produce two-dimensional (2D) electrodes. However, 3D microelectrodes provide larger surface area and thereby could enhance the sensitivity in electrochemical detection (2). Hence, several 3D microfabrication techniques have been explored amongst which the carbon MEMS (C-MEMS) approach is the most promising one for the fabrication of conductive 3D microstructures. In C-MEMS, a patterned polymer template is treated at high temperature (~900°C) in inert atmosphere (N_2 or Ar) and transformed into pyrolytic carbon. This process enables fabrication of 2D and 3D electrodes with the possibility to tailor designs and thereby sensitivities for electrochemical sensing applications. Due to this, pyrolytic carbon microelectrodes are becoming increasingly attractive for numerous applications, such as in novel sensors and scaffolds for cell monitoring (3–5). Nevertheless, fabrication of electrically conductive 3D carbon microelectrodes (3DCMEs) with structural dimensions that are comparable to the size of biological cells still remains challenging.

One of the most important factors in 3D C-MEMS technology is the definition of a mechanically stable 3D polymer precursor template for pyrolysis. Recently, various 3D polymer fabrication technologies evolved. Microfabrication methods such as two-photon, e-beam and X-ray lithography proved to be powerful tools in developing 3D micro/nanostructures but unfortunately still display a very low throughput and the required equipment is rather expensive (6,7). Some of the additive manufacturing technologies such as 3D printing or stereolithography provide a higher throughput but lack the micron range resolution (8). Therefore, in most C-MEMS processes, polymer microstructures were fabricated using standard UV photolithography with the chemically enhanced, negative tone epoxy photoresist SU-8 (9–11). This method is readily available

at a reasonable cost. Typically, SU-8 photolithography comprises spin coating, solvent evaporation, UV-exposure, polymerization and development (12,13). Each of these steps affect the photolithographic resolution and the properties of SU-8 structures such as stress or adhesion to the substrate. Therefore, depending on the desired application different process parameters have to be optimized to obtain well-resolved and mechanically stable 3D microstructures (14).

Different fabrication processes have been proposed to obtain suspended SU-8 microstructures. The most common process involves adding a polymerization-stop-layer between the structures to be suspended and the substrate (15). The complexity of this fabrication process increases as the structures become multilayered (i.e. more 3D). Another method includes doping of the SU-8 photoresist with nanoparticles to control the thickness of freestanding 3D structures (11). However, such an addition of Fe_2O_3 nanoparticles requires a number of preparation steps which severely limit the flexibility of the process. The most promising processes to define suspended layer so far are using a partial UV exposure of SU-8 photoresist films either at a lower wavelength (313nm) or/and a very low dose (15,16).

In this work, we developed a multi-step UV photolithography process to fabricate a 3D SU-8 polymer template which was pyrolyzed to define 3D carbon microelectrodes for electrochemistry. The fabrication of suspended microstructures in a single layer of SU-8 was optimized. The process was used to define 3D carbon microstructures acting as the working electrodes (WE) in microelectrode chips with a three electrode configuration. The electrochemical performance of 2D and 3D carbon microelectrodes was compared with cyclic voltammetry (CV) in a batch system with 10mM potassium ferri-ferrocyanide standard redox probe.

Methods

Microelectrode chips

The microelectrode chips were fabricated with multiple steps of UV photolithography followed by pyrolysis as shown schematically in Figure 1.a - e. First, the process of fabricating suspended layers from a single layer of SU-8 was optimized by adjusting the partial exposure dose (D_3) (16). The optimized process was used to fabricate 3DCMEs on the working electrode of the microelectrode chips. Figure 1.f and g shows the top view of the microelectrode chip without and with passivation layer (SU-8). The process is explained along the cross-section AA` (Figure 1. f).

Approximately 5 ml of negative photoresist (SU-8 2005 from MicroChem, USA) were manually dispensed on a 4-inch Si/SiO_2 substrate and spin coated (RCD8 T, Süss Micro-Tec, Germany) to deposit a 6µm thick layer. A solvent evaporation for 2h at room temperature was followed by a UV exposure step with an exposure dose, D_1= 147 $mJcm^{-2}$ in an EVG620 aligner (EVGroup, Austria) to define the working and counter electrodes (Figure 1.a) (13). The aligner was equipped with a mercury lamp and a long pass filter (SU-8 filter), adjusted to a constant intensity of 7 $mWcm^{-2}$ at 365 nm. This is followed by a post-exposure bake (PEB) at 50 ºC for 1 h on a programmable hotplate (Harry Gestigkeit GmbH, Germany). A second layer of SU-8 2075 was manually dispensed and

spin coated to a thickness of 66µm. The edge bead was removed by dispensing propylene glycol methyl ether acetate (PGMEA) at the edge of the rotating wafer (300 rpm). A soft bake (SB) at 50 ºC for 6h is followed by a two-step UV photolithography to achieve 3D microstructures. The first exposure (D_2 =147 mJcm^{-2}) defines the supporting pillars (Figure 1.b) and the partial exposure (D_3) defines the suspended layer (Figure 1.c). D_3 was optimized to limit the crosslinking to the top of the SU-8 layer. This was followed by a PEB at 50 ºC for 8 h. Development was performed in PGMEA in two steps of 10 min followed by isopropanol rinse for 30 s and drying in air (Figure 1.d). Next, an additional flood exposure with a total dose D = 500 mJcm^{-2} and a hard-bake at 90 ºC for 15 h were performed to increase the structural stability of SU-8 achieved by improved crosslinking. The polymer template is pyrolyzed in an ATV PEO604 furnace (ATV Tech., Germany) in inert atmosphere (N_2) in two steps, 200 ºC for 30 min and 900 ºC for 1h with a ramp of 2 ºmin^{-1} to produce suspended carbon microstructures.

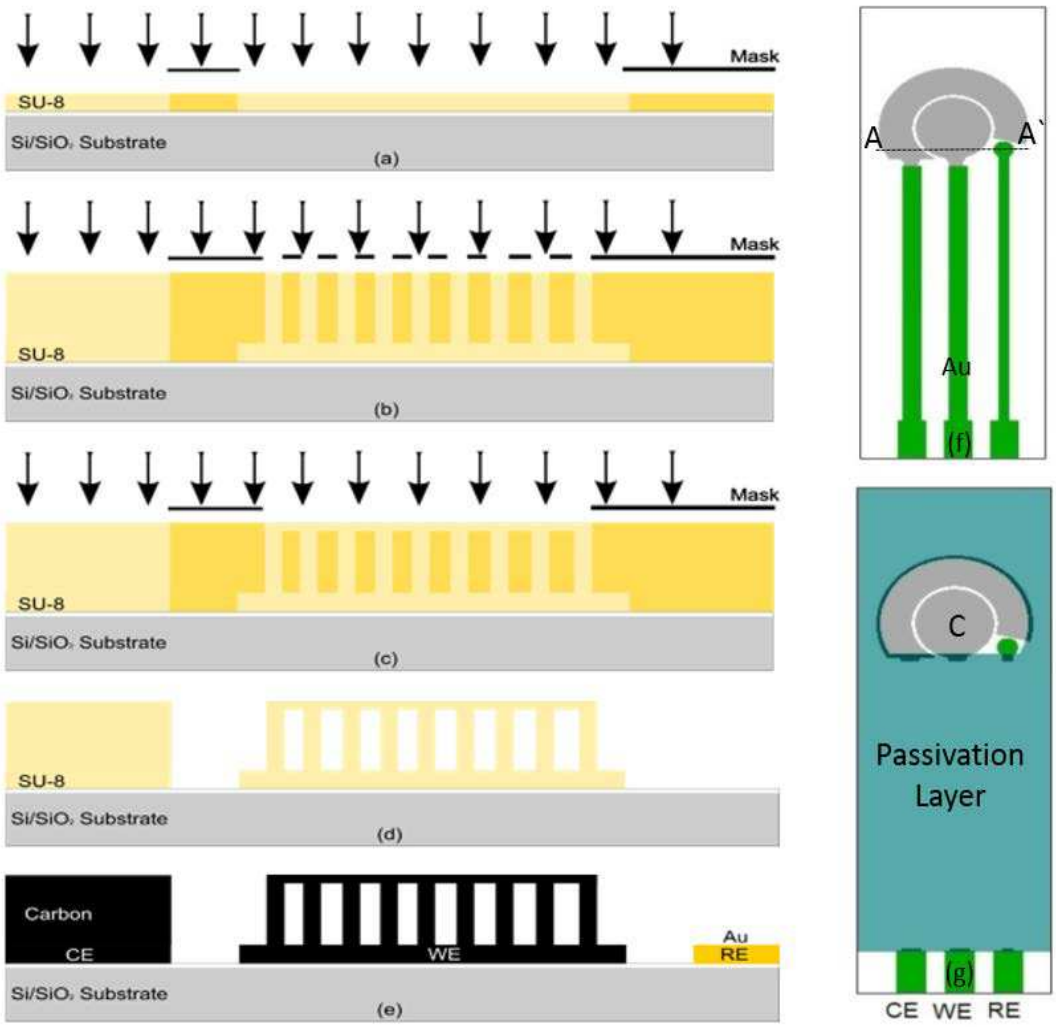

Figure 1. Schematic of the microfabrication process (a) SU-8 (2005) is spin coated, baked UV exposed and post exposure baked (b) Second layer of SU-8 (2075) is spin coated, baked and UV exposed (c) short UV exposure and post exposure bake (d) Development in PGMEA (e) Pyrolysis at 900ºC for 1h and e-beam Au deposition through a shadow mask (f) and (g) shows the top view of the microelectrode chip without and with passivation (SU-8) layer

A gold pseudo-reference electrode and gold contact pads were deposited by e-beam evaporation through a shadow mask (Figure 1.e). For passivating the contact leads, a 2µm thick film of SU-8 2002 was spin coated and patterned as described above for the SU-8 2005 including the final flood exposure and hard bake.

Batch system with magnetic clamping

A self-aligning, magnetic clamping system was developed for electrochemical characterization of the microelectrode chips. Figure 2 shows the schematic of different layers in the batch system. Rare earth magnets were used to facilitate clamping and exchange of the microelectrode chips. A CO_2 laser (Epilog Laser, USA) was used for drilling and dicing of the PMMA parts followed by bonding them using pressure sensitive adhesive (PSA) in a bonding press (P/O Webber, Germany) at 35ºC with a pressure of 150 bar for 10 min. The top plate defines a circular well with diameter 8 mm above the electrode area suitable for experiments in batch conditions. Furthermore, a trench was engraved in the top plate accomodating an O-ring to avoid any leakage in the cavity. The bottom plate provided the slot for placing the microelectrode chips.

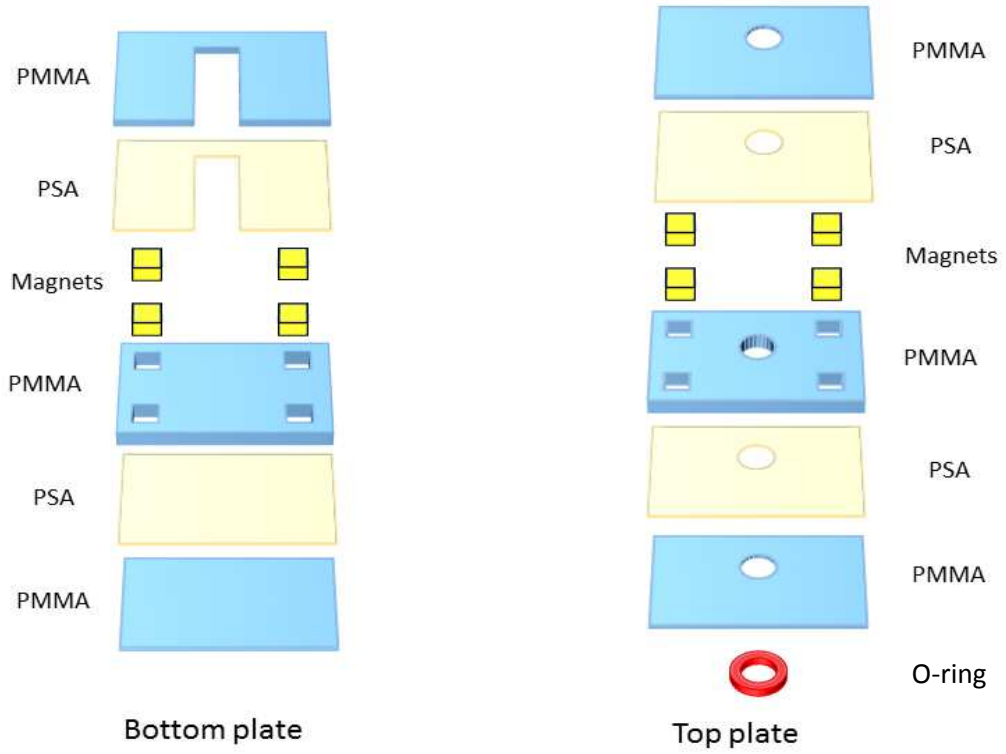

Figure 2. Different components in the magnetically clamped batch system

Electrochemical Characterisation

For electrochemical analysis, cyclic voltammetry (CV) was performed using a standard 10 mM potassium ferri-ferrocyanide redox probe in the batch systems. The microelectrode chips (2D and 3D) were pretreated in O_2 plasma (Electronic Diener, Germany) at 50W for 60 seconds. Then the chips were placed in the bottom plate of the batch system and sealing was achieved with the O-ring of the top plate. 350 µL of redox

probe were pipetted on the electrode for each measurements. For CV, a voltage of -0.6 V to +0.6 V in steps of 100 mV was applied with a Potentiostat (Autolab PGSTAT302N, Netherland).

Results and Discussion

Microfabrication of electrodes

The optimization of the partial exposure dose (D_3) is critical for the fabrication of 3D suspended SU-8 microstructures. Therefore, an initial series of experiments on various test structures was performed using a single layer of SU-8 and two UV exposures (D_2 and D_3). Very low exposure doses D_3 were selected, in the attempt to achieve a gradient in the concentration of activated photoinitiator molecules in the SU-8 film. The exposure dose D_3 was varied from 21 - 42 $mJcm^{-2}$. The results of the optimization of the partial exposure are shown in Figure 3. The exposure dose, D_3 = 21 $mJcm^{-2}$ is insufficient for the crosslinking of the top layer of SU-8 film. Hence, after the development in PGMEA only SU-8 pillars from the long UV exposure process remain (Figure 3.a). A higher exposure dose of D_3 = 28 $mJcm^{-2}$ limits the crosslinking to the top surface of the SU-8 film, which results in suspended 3D structures (Figure 3.b). The thickness of the suspended layer is 18 µm. Higher dose (D_3 = 35 $mJcm^{-2}$ and 42 $mJcm^{-2}$) causes complete crosslinking of the SU-8 film (Figure 3.c, d). These results are in agreement with those obtained by Lim et al. and demonstrate that the process window in terms of exposure dose is very narrow requiring precise control of the exposure conditions (16).

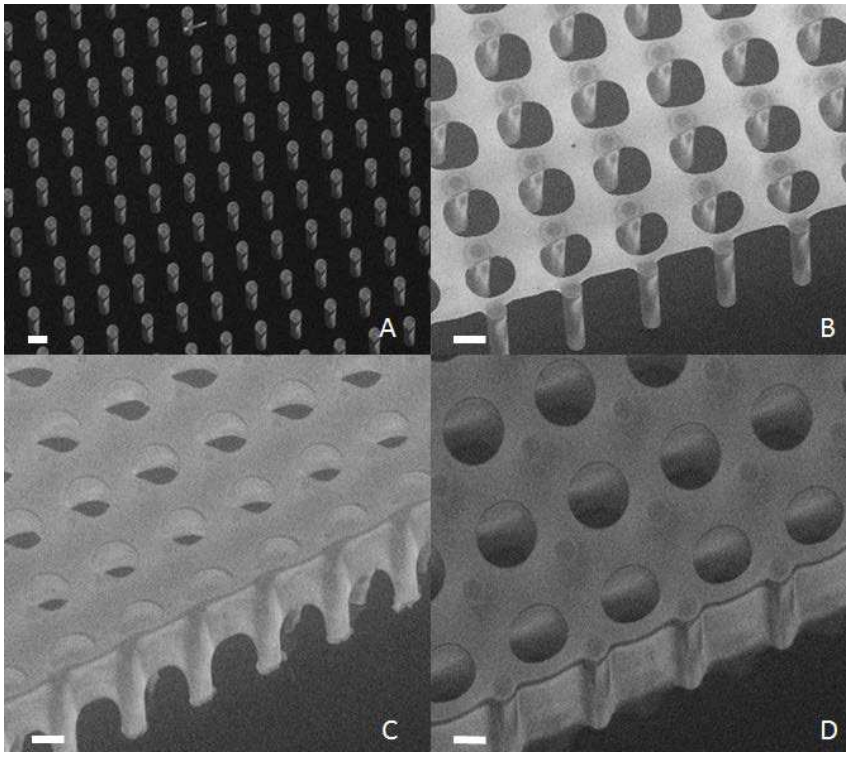

Figure 3. Optimization of partial UV exposure (D_2) with different exposure dose D_2: (a) 21 $mJcm^{-2}$; (b) 28 $mJcm^{-2}$; (c) 35 $mJcm^{-2}$; (d) 42 $mJcm^{-2}$ (Scale bar – 25µm)

The two steps of UV exposure followed by pyrolysis result in 3D carbon microstructures with various feature sizes (Figure 4). Figure 4 illustrates the carbon microstructures obtained through pyrolysis of the SU-8 template and shows the large shrinkage during pyrolysis. The final height of the structures was 37 µm and the thickness of the suspended carbon film was approximately 2.4 µm. The smallest feature size fabricated in the suspended layer was approximately 5.6 µm as shown in Figure 4.d. The results show that once the structures are defined in SU-8, the overall design of the 3D microstructures are maintained during pyrolysis even though a considerable shrinkage is observed. The optimized process was transferred to the fabrication of the complete microelectrode chip as described in figure 1. Figure 5.a and b shows 2D and 3D working electrodes obtained respectively. And Figure 5 c shows SEM image of working electrode in a 3D microelectrode chip (Figure 5. b).

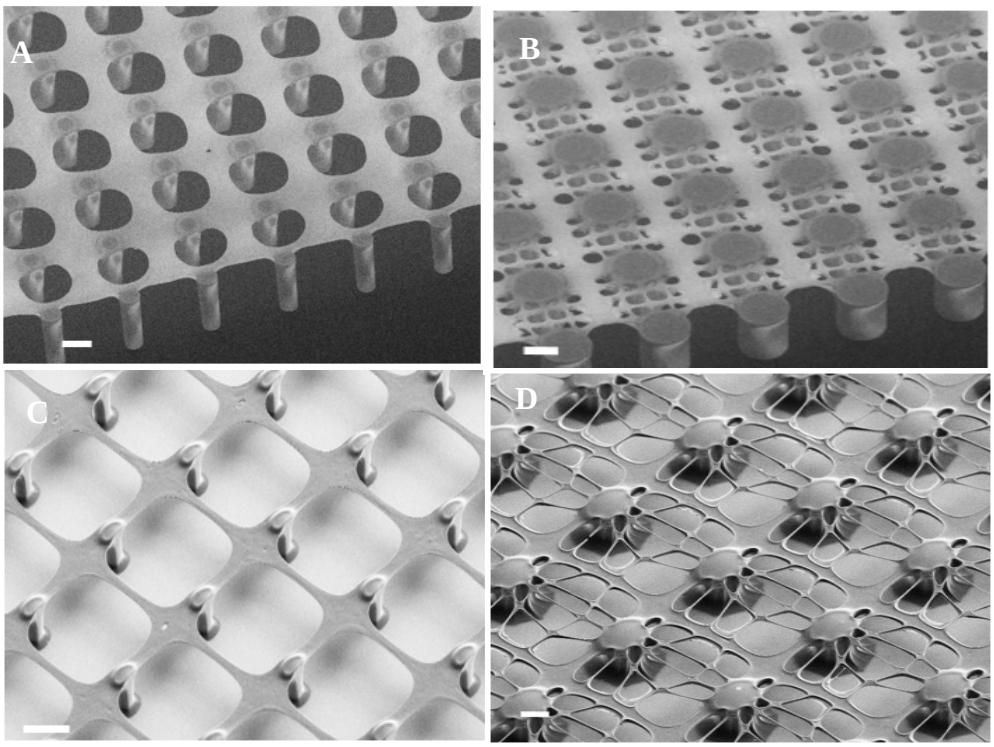

Figure 4. SEM images of (a) and (b) SU-8 polymer template; (c) and (d) are the corresponding carbon microstuctures respectively (Scale bar – 25µm)

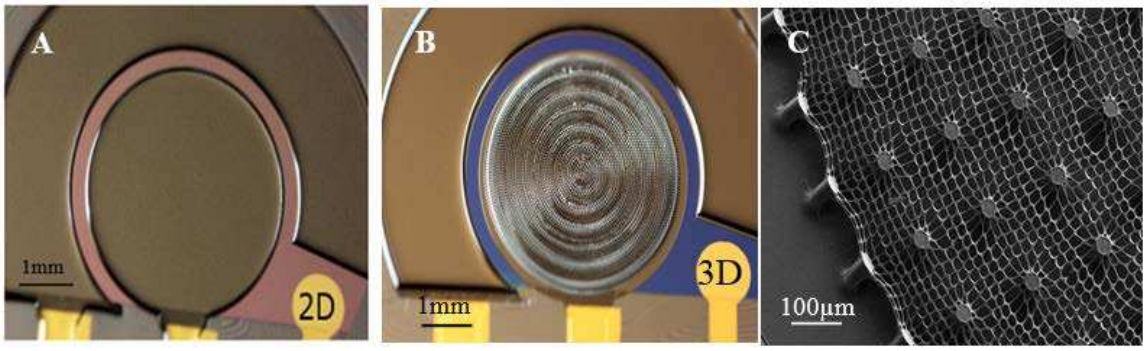

Figure 5. Microelectrode chips (a) 2D working electrode (b) 3D working electrode (c) SEM image of 3D working electrode

Electrochemical characterization

Figure 5.a and b show the two different microelectrode designs characterized with CV in the magnetically clamped batch systems. The experimental step-up is shown in Figure 6.a. Figure 6.b shows the mean values and the standard deviation obtained with three microelectrode chips of each design. The peak current (I_p) of 2D and 3D chips are 29µA and 57µA respectively and the peak separation (ΔE_p) is 0.3 V and 0.24V for 2D and 3D chips respectively.

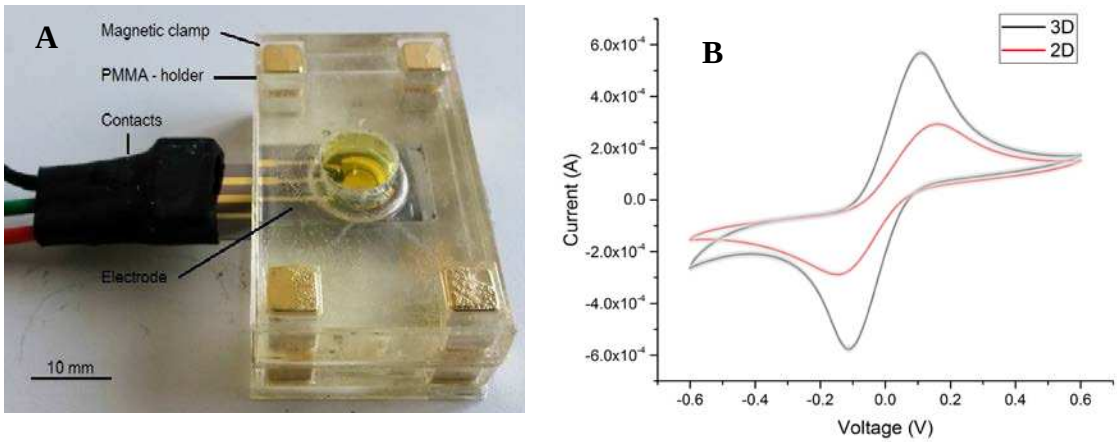

Figure 6. (a) Experimental set-up, (b) CV of 2D and 3D microelectrode chips

The surface area of the working electrode on the 3D microelectrode chips is approximately 3.5 times larger than for the 2D WE. This explains the higher current when compared to 2D electrodes.

Conclusion

SU-8 templates with suspended features in the micrometer range were successfully fabricated and pyrolyzed to obtain microelectrode chips with 3D carbon microelectrodes as working electrode. A two-step (D_2 and D_3) UV exposure was optimized to fabricate the suspended layer. Small variations of the partial exposure dose D_3 result in complete/no crosslinking of the SU-8 layer, demonstrating the narrow window for D_3. The higher signal in CV for 3D microelectrode chips demonstrates an increase of the surface area compared to the 2D configuration which should result in a higher sensitivity for electrochemical sensing. With unique properties of carbon, the proposed fabrication process can be used to customize ad-hoc carbon microelectrodes for specific applications such as biosensors.

Acknowledgments

The authors acknowledge funding by the Young Investigator Program of the Villum Foundation, project no. VKR023438.

References

1. McCreery RL. *Chem Rev*.108(7):2646–87 (2008).
2. Kamath RR, Madou MJ. Anal Chem. 86(6):2963–71 (2014).
3. Amato L, Heiskanen A, Caviglia C, Shah F, Zór K, Skolimowski M, et al. *Adv Funct Mater*. 24(44):7042–52 (2014).
4. Hirabayashi M, Mehta B, Vahidi NW, Khosla A, Kassegne S. *J Micromechanics Microengineering*.;23(11):115001 (2013).
5. Kassegne S, Wondimu B, Majzoub M, Shin J. *Proc SPIE*. 7266(619):726615, 1–6 (2008).
6. Campo A del, Greiner C. *J Micromechanics Microengineering*.17(6):R81–95 (2007).
7. Cadarso VJ, Pfeiffer K, Ostrzinski U, Bureau JB, Racine G a, Voigt A, et al. *J Micromechanics Microengineering*.21(1):017003 (2011).
8. Melchels FPW, Feijen J, Grijpma DW. *Biomaterials*.31(24):6121–30 (2010).
9. Martinez-Duarte R. *Micromachines*.5(3):766–82 (2014).
10. Amato L, Heiskanen A, Hansen R, Gammelgaard L, Rindzevicius T, Tenje M, et al. *Carbon*.94:792–803 (2015).
11. Wang C, Madou M. *Biosens Bioelectron*. 20(10 SPEC. ISS.):2181–7 (2005).
12. Shaw JM, Gelorme JD, LaBianca NC, Conley WE, Holmes SJ. *IBM J Res Dev*. 41(1.2):81–94 (1997).
13. Keller S, Blagoi G, Lillemose M, Haefliger D, Boisen A. *J Micromechanics Microengineering*. 18:125020 (2008).
14. Amato L, Keller SS, Heiskanen A, Dimaki M, Emnéus J, Boisen A, et al. *Microelectron Eng*.;98:483–7 (2012).
15. Ceyssens F, Puers R. *J Micromechanics Microengineering*. 16(6):S19–23 (2006).
16. Lim Y, Heo J-I, Shin H. *Sensors Actuators B Chem*.192(2014):796–803 (2014).

Paper II

Suspended 3D pyrolytic carbon microelectrodes for electrochemistry

Hemanth.S, Caviglia.C and S.S.Keller, *Carbon*, 121 (2017), 226–234.

Carbon 121 (2017) 226–234

Contents lists available at ScienceDirect

Carbon

journal homepage: www.elsevier.com/locate/carbon

Suspended 3D pyrolytic carbon microelectrodes for electrochemistry

Suhith Hemanth*, Claudia Caviglia, Stephan Sylvest Keller

Department of Micro- and Nanotechnology, DTU Nanotech, 2800 Kongens Lyngby, Denmark

ARTICLE INFO

Article history:
Received 13 March 2017
Received in revised form
17 May 2017
Accepted 29 May 2017
Available online 30 May 2017

ABSTRACT

Carbon microelectrodes have a wide range of applications because of their unique material properties and biocompatibility. This work presents the fabrication and characterization of suspended pyrolytic carbon microstructures serving as three-dimensional (3D) carbon microelectrodes for electrochemical applications. A 3D polymer template in epoxy based photoresist (SU-8) was fabricated with multiple steps of UV photolithography and pyrolysed at 900 °C to obtain 3D carbon microelectrodes. The pyrolytic carbon microstructures were characterized by SEM, Raman spectroscopy and XPS to determine the mechanical stability, shrinkage and material properties. The smallest feature size fabricated in the suspended carbon layer was 2 μm. A three electrode microelectrode chip with 3D pyrolytic carbon microstructures as the working electrode was designed and fabricated. The electrodes were characterized with cyclic voltammetry (CV) and impedance spectroscopy (EIS) using potassium ferri-ferrocyanide redox probe in a custom made batch system with magnetic clamping. Different 3D pyrolytic carbon microelectrodes were compared and the optimal design displayed twice the peak current and half the charge transfer resistance as compared to 2D carbon electrodes. The higher sensitivity of 3D carbon microelectrodes for electrochemical sensing was illustrated by dopamine detection.

1. Introduction

Advancements in the fabrication of 3D microelectrodes are of interest for numerous applications such as electrochemical sensors, energy storage devices and smart scaffolds for tissue engineering sensors [1–4]. The main advantage of 3D microelectrodes is that the larger electrode surface area potentially provides higher sensitivity for electrochemical sensing than the currently used 2D electrodes [5]. Furthermore, the 3D nature of the electrodes better mimics the natural environment of cells, which is relevant for applications in bioelectrochemistry or tissue engineering [6,7]. Additionally to large surface area, optimal 3D microelectrodes should provide low resistivity, good structural and chemical stability, excellent reproducibility and low fabrication costs. Several processes have been proposed to fabricate 3D microelectrodes. With electroplating [8–10], injection molding [11], microsolidics [12] and screen printing [13] it can be difficult to control the feature size and/or a long and expensive process is required that may result in low-quality surfaces. Furthermore, the fabrication of structures with a high-aspect ratio is difficult to achieve [1]. Additive manufacturing technologies such as 3D printing lack the resolution down to a few microns, which so far limits the fabrication to macroelectrodes [14]. Electrodeless electroplating is based on the use of a femtosecond laser and the writing is done in a serial way, leading to long processing times. Furthermore, this process results in a high surface roughness [15,16]. Growth of carbon nanotubes requires highly controlled environments and fabrication of patterned high aspect ratio structures is challenging [17]. The combination of electroplating with sputtering and laser scribing is a complex process and also suffers from the above mentioned issues [18]. Regarding metal ion implantation, the process is based on the use of a shadow mask which limits the achievable resolution and density of the structures. Furthermore, one metal ion implantation step is only effective for a certain orientation and thus several steps are needed to obtain fully-coated 3D structures [19].

One of the most simple and cost-effective techniques for 3D microelectrode fabrication is carbon MEMS (C-MEMS). There, a patterned polymer template is treated at high (~1000 °C) temperatures in inert atmosphere (N_2 or Ar) and transformed into a pyrolytic carbon electrode [20]. This process enables fabrication of 2D and 3D electrodes with the possibility for ad-hoc tailoring of designs to achieve unique sensitivities for specific applications. Additionally, carbon materials used as microelectrodes offer several attractive properties, such as wide electrochemical potential

* Corresponding author.
E-mail address: suhem@nanotech.dtu.dk (S. Hemanth).

http://dx.doi.org/10.1016/j.carbon.2017.05.090
0008-6223/

window, biocompatibility, chemical stability, and ease of functionalization [21]. These properties identify carbon as an ideal material for electrodes to be used as biosensors or in energy storage devices [5,7,22,23].

In most C-MEMS processes, polymer templates have been fabricated using the chemically enhanced, negative tone epoxy photoresist (SU-8). SU-8 is composed of bisphenol-A novolac resin (EPON® SU-8 resin, Shell Chemical Company, The Hague, The Netherlands) in an organic solvent, such as cyclopentanone or gamma-butyrolactone (GBL) and a photoinitiator usually being triarylsulfonium hexafluoroantimonate [24]. Fabrication techniques such as X-ray, e-beam and two-photon lithography have been employed for fabrication of 3D polymer templates for pyrolysis [25–27]. The limiting factor for these techniques is the low throughput as compared to standard UV photolithography. Different fabrication processes have been proposed to fabricate 3D SU-8 microstructures with UV photolithography e.g. using a polymerization stop layer SU-8 foil or highly optimized UV exposures at different wavelengths [28–30]. The complexity of the fabrication process increases as the structures become multilayered (i.e. more 3D). Furthermore, suspended SU-8 macrostructures have been fabricated with grayscale photolithography, but without achieving micron or submicron resolution [31].

Recently, we proposed a multi-step UV photolithography process followed by pyrolysis at 900 °C to obtain 3D carbon microelectrodes [32]. In this work, the optimized process was used to fabricate a three electrode microelectrode chip, with 3D carbon as the working electrode. The material properties of the pyrolytic carbon were analyzed with Raman spectroscopy and X-ray photoelectron spectroscopy (XPS). Mechanical stability and shrinkage of different designs of 3D carbon microelectrodes were characterized with optical microscopy and SEM. For electrochemical characterization cyclic voltammetry (CV) was conducted using potassium ferri-ferrocyanide as standard redox probe. The electron transfer on the optimal 3D microelectrode design was analyzed in detail using CV and electrochemical impedance spectroscopy (EIS). The results were compared to 2D microelectrodes (2D) and 2D microelectrodes with micropillars ($2D_p$). Finally, enhanced dopamine detection with square wave voltammetry (SWV) was demonstrated.

2. Experimental section

2.1. Microelectrode chips

Three electrode microelectrode chips with overall dimensions of 1 cm × 3 cm were fabricated as shown in Fig. 1. The microelectrode chips consists of pyrolytic carbon working (WE) and counter electrodes (CE). The circular working electrode has a diameter of 4 mm. An Au pseudo reference electrode (RE) and contact pads are deposited by e-beam evaporation. The Au contact leads are passivated with SU-8 (Fig. 1K).

2.2. Microfabrication of 3D carbon microelectrodes

The fabrication steps of the 3D carbon microelectrode chips are schematically described in Fig. 1 (A–J). Fig. 1K shows the top view of a microelectrode chip with and without passivation layer (SU-8). The process is explained along cross-section AA′ (Fig. 1K). First, a 0.6 μm thick SiO_2 layer was deposited by thermally oxidation on a 4-inch Si wafer (Fig. 1B). The Si/SiO_2 substrate was dehydrated in an oven at 250 °C for 2 h before spin coating the resist.

Approximately 5 ml of negative photoresist (SU-8 2035 from MicroChem, USA) were manually dispensed on the 4-inch Si/SiO_2 substrate and spin coated (RCD8 T, Süss Micro-Tec, Germany) to deposit a 17 μm thick layer (Fig. 1C). A soft-bake at 50 °C for 15 min on a programmable hotplate (Harry Gestigkeit GmbH, Germany) was followed by a UV exposure step with an exposure dose, $D_1 = 210\ mJcm^{-2}$ in an EVG620 aligner (EVGroup, Austria) to define WE and CE (Fig. 1D). The aligner was equipped with a mercury lamp and a long pass filter (SU-8 filter), which was adjusted to a constant intensity of 7 $mWcm^{-2}$ at 365 nm. This was followed by a post-exposure bake (PEB) at 50 °C for 1 h. A second layer of SU-8 2075 was spin coated using a two-step process. A spread cycle of 30 s at 700 rpm with 100 $rpms^{-1}$ acceleration was applied, followed by a thinning cycle at 2100 rpm for 60 s with 500 $rpms^{-1}$ acceleration which yielded a 98 μm thick film. The edge bead was removed by

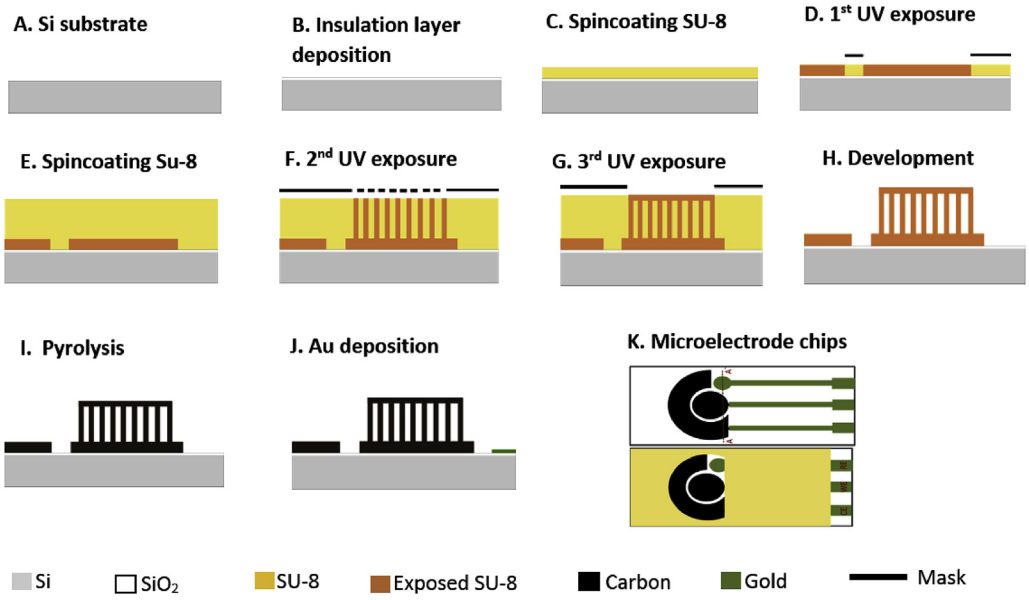

Fig. 1. Schematic of carbon microelectrode fabrication (A) Starting Si substrate (B) Thermal oxidation (C) SU-8 2035 is spin coated and soft baked (D) 1st UV exposure and post exposure bake (E) Second layer SU-8 2075 is spin coated and baked (F) 2nd UV exposure (G) short 3rd UV exposure and post exposure bake (H) Development in PGMEA (I) Pyrolysis at 900 °C for 1 h (J) e-beam Au deposition through a shadow mask; (K) Top view of the microelectrode chip without and with passivation (SU-8 2005) layer. (A colour version of this figure can be viewed online.)

dispensing propylene glycol methyl ether acetate (PGMEA) at the edge of the rotating wafer (300 rpm) for 30 s resulting in a uniform SU-8 layer (Fig. 1E). A soft bake (SB) at 50 °C for 6 h was followed by a two-step UV photolithography to achieve 3D suspended microstructures. The first exposure ($D_2 = 147$ mJcm^{-2}) defined the supporting pillars (Fig. 1F) and the partial exposure ($D_3 = 28$ mJcm^{-2}) defined the suspended layer (Fig. 1G) [32]. This was followed by a PEB at 50 °C for 8 h. Development was performed in PGMEA in two steps of 10 min each, followed by isopropanol rinse for 30 s and drying in air (Fig. 1H). Next, an additional flood exposure with a total dose D = 500 mJcm^{-2} and a hard-bake at 90 °C for 15 h were performed. This procedure has earlier been used to minimize residual stress and enhance temporal stability of SU-8 due to improved crosslinking [33]. For analyzing the mechanical stability and shrinkage five different designs of 3D microelectrode were fabricated. The varied parameters were pillar diameter (d), pitch between the pillars (ϕ), and diameter (w) and center-to-center distance (c) of the holes in the suspended layer.

The polymer (SU-8) templates were pyrolysed in an ATV PEO604 furnace (ATV Tech., Germany) in inert atmosphere (N_2) in two steps, 200 °C for 30 min and 900 °C for 1 h with a ramp of 2 °C min^{-1} to produce 3D microelectrodes with suspended carbon (Fig. 1I) [34].

An Au pseudo-reference electrode and Au contact pads were deposited by e-beam evaporation through a shadow mask prepared using laser machining (Fig. 1J). For passivating the contact leads, a 6 μm thick film of SU-8 2005 was spin coated and patterned as described above for the SU-8 2035 including the final flood exposure and hard bake.

For comparison of the electrochemical behavior, 2D microelectrode chips (Fig. 1 without steps 1.E–1.G) and 2D microelectrode chips with micropillars (Fig. 1 without step 1.G) were fabricated with identical process parameters.

2.3. Raman spectroscopy

In order to evaluate the graphitization (i.e. disorder and crystallite) of the pyrolytic carbon 2D carbon films with a thickness of 2 μm were fabricated with identical process parameters as described above. The samples were analyzed by visible Raman spectroscopy performed using a Raman microscope (Model DXR, Thermo Fisher Scientific Inc., Denmark) with an excitation wavelength of 532 nm. All the spectra were recorded with a 10× long working distance objective and 10 mW laser power. The Raman spectra were analyzed using OMNIC software from Thermo Scientific.

2.4. X-ray photoelectron spectroscopy (XPS)

The surface composition of pyrolytic carbon films was characterized using XPS. The analysis was carried out in a Thermo K-Alpha XPS instrument with a monochromatic Al–Kα-source. The binding energy survey from 0 to 1350 eV was performed followed by spectral analysis in the C_{1s} and O_{1s} binding energy ranges. The atomic percentages of surface elements were extracted using the software package Avantage, provided by Thermo Fisher Scientific.

2.5. Electrochemical characterization

Prior to testing, the microelectrode chips (2D, $2D_p$ and 3D) were pretreated in O_2 plasma (Electronic Diener, Germany) at 50 W for 65 s. CV and EIS were performed using 300 μL potassium ferriferrocyanide $[Fe(CN)_6]^{4-}/[Fe(CN)_6]^{3-}$ redox probe in phosphate buffered saline (PBS). During the measurements the chips were allocated in self-aligning and magnetic clamping batch systems made of poly methyl methacrylate (PMMA) and pressure sensitive adhesive (PSA) as described in earlier work [32]. For every configuration analyzed, four chips from different fabrication batches were used. The different designs of 3D carbon microelectrodes were characterized using CV with 10 mM $[Fe(CN)_6]^{4-}/[Fe(CN)_6]^{3-}$ solution. Cyclic voltammograms were acquired using a three-electrode configuration and a scan rate of 100 mVs^{-1} in a potential range from −600 mV to 600 mV. The optimal 3D carbon microelectrode design was analyzed in detail with CV using different concentrations and scan rates and with EIS. EIS spectra were performed using a two-electrode configuration (WE and CE) in the frequency range of 0.1–10^6 Hz, applying a sinusoidal potential of 10 mV and acquiring 10 points/decade. The frequency response was fitted with an equivalent circuit. The electrochemical behavior was compared to 2D and $2D_p$ carbon microelectrodes. Square wave voltammetry (SWV) was performed on carbon electrodes for detection of different concentrations of dopamine hydrochloride (Sigma-Aldrich, USA). Measurements were acquired using a potentiostat (Autolab PGSTAT128N, Metronohm Autolab) and the software package NOVA was used to analyze the acquired data.

3. Results and discussion

3.1. 3D carbon microelectrode fabrication

Different designs of 3D carbon microelectrodes were fabricated on the working electrode of a microelectrode chip. The 3D carbon microelectrodes consisted of three layers-a suspended grid layer, micropillars supporting the suspended structures and a planar base. Five different designs (design 1–5) of 3D carbon microelectrode with varying micropillars and suspended layers were fabricated to analyze their mechanical stability and the influence of the 3D geometry on the electrochemical performance. The nominal mask dimensions for the different designs and the final values measured after pyrolysis are summarized in Table 1. Fig. 2A-C shows three different polymer templates before pyrolysis of design 1, 3 and 5 respectively. An overview of the working electrode in the microelectrode chip is shown in Fig. 2D. Fig. 2E-I demonstrate that

Table 1
Nominal and actual dimensions for different 3D carbon microelectrode designs.

Design	Pillar diameter (d)		Pillar pitch (Φ)	Hole diameter (w)		Hole pitch (c)	Unit cell
	Nominal	Carbon		Nominal	Carbon		
Design 1	10 μm	6.7 μm	50 μm	25 μm	29 μm	50 μm	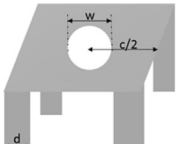
Design 2	20 μm	12 μm	50 μm	25 μm	29 μm	50 μm	
Design 3	20 μm	12 μm	75 μm	10 μm	14 μm	20 μm	
Design 4	50 μm	30 μm	100 μm	50 μm	63 μm	100 μm	
Design 5	50 μm	30 μm	100 μm	10 μm	14 μm	20 μm	

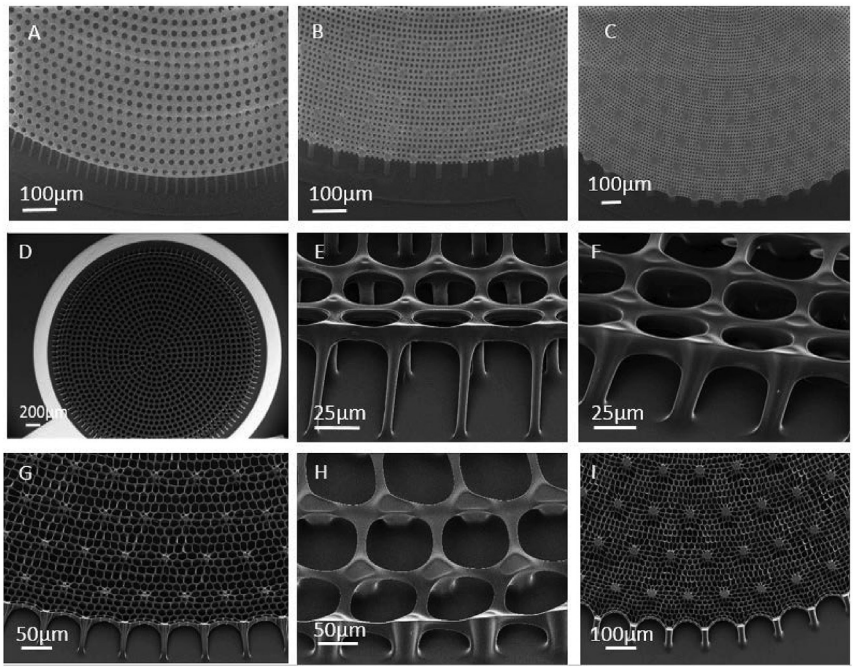

Fig. 2. (A)–(C) SU-8 polymer templates of designs 1,3 and 5 respectively; (D) Overview of working electrode of microelectrode chip with 3D carbon (design 1); (E)–(I) Different 3D carbon microelectrodes with designs 1–5.

for all the five different 3D carbon microelectrode designs suspended microstructures were successfully fabricated. For the designs with Φ = c (design 1, 2 and 4) fabrication was very reproducible and resulted in regular suspended grids without defects. The minimal feature size of the suspended layer for these designs was around 7 µm after pyrolysis. For designs 3 and 5 with Φ > c corresponding to multiple holes between micropillars the smallest feature size of the suspended layer was 2 µm. However, for those two designs fabrication was not reproducible and defects in the suspended layer were frequently observed. An observation for all designs are edge effects. The pillars at the edge of the electrode area are subjected to more stress which results in leaning towards the center.

3.2. 3D carbon shrinkage analysis

One of the major challenges in 3D microelectrode fabrication with the proposed process was the shrinkage during the pyrolysis. High shrinkage results in higher residual stress, which in turn can results in deformation, delamination and collapse of 3D microstructures. The values of nominal and actual pillar diameters and hole sizes reported in Table 1 demonstrate that considerable shrinkage was observed for all 3D microelectrode designs.

Fig. 3 A and B shows an example of a SU-8 template and the corresponding carbon structures, respectively. We investigated the vertical and lateral shrinkage of the pillars and vertical shrinkage of the suspended structures by SEM imaging before and after pyrolysis. The % shrinkage *S* was expressed as [35]:

$$\boldsymbol{S} = 1 - \frac{\boldsymbol{Carbon}}{\boldsymbol{SU} - 8} \tag{1}$$

where "SU-8" is a dimensional parameter of the SU-8 microstructure before pyrolysis such as the height, pillar diameter or suspended layer thickness and "carbon" is the dimension of the

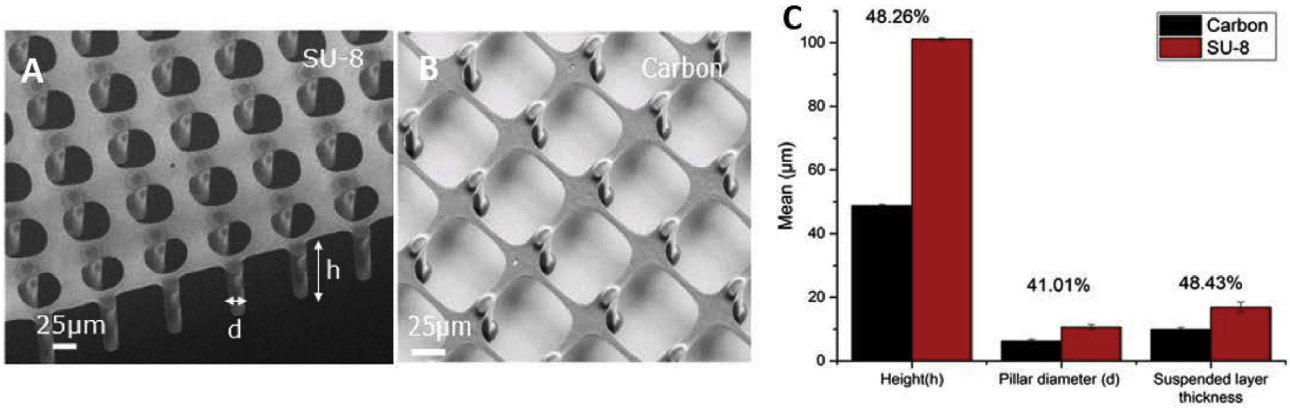

Fig. 3. (A) SU-8 polymer microstructure template, (B) Corresponding carbon microstructures and (C) Percentage shrinkage analysis for design 1. (A colour version of this figure can be viewed online.)

corresponding carbon microstructure after pyrolysis. The total height (h), pillar diameter (d) and suspended layer thickness decreased by 48.3%, 41.0% and 48.4% respectively. The percentage of shrinkage is comparable to reported values for pyrolysis of SU-8 [36,37]. The large shrinkage occurs due to multiple concurrent reactions happening during pyrolysis which include dehydrogenation, cyclization, condensation, hydrogen transfer and isomerization [38,39]. Fig. 2 demonstrates that despite the large shrinkage all 3D microelectrode designs were structurally intact after fabrication. However, the defects observed for design 3 and 5 were probably a result of the residual stress due to shrinkage.

3.3. Raman spectroscopy and XPS

Raman spectroscopy provides information about the degree of disorder of pyrolytic carbon. In pyrolytic carbon, the E_{2g} vibrational mode at 1580 cm^{-1} (also present in graphite) and the A_{1g} vibrational mode at 1360 cm^{-1} are Raman active [40]. The E_{2g} mode results in a peak in the Raman spectrum, called "G" peak, where G stands for "graphite". The G peak is caused by bond stretching of all sp_2 hybridized C atoms in rings as well as in chains. When the symmetry in the graphite lattice is broken due to presence of disordered regions, the A_{1g} mode becomes active. This results in a new peak near 1360 cm^{-1}, called the "D" peak where D stands for disordered [41]. Fig. 4A shows the Raman spectra of pyrolytic carbon derived from SU-8 photoresist where both D and G peaks are identified, which means that both amorphous and graphitic regions are present as reported previously for pyrolytic carbon [42]. Here, the observed upshift of the G peak to 1596 cm^{-1} is probably due to the presence of disordered graphite [43].

XPS survey spectra were used to evaluate the atomic percentage composition of pyrolytic carbon derived from SU-8 polymer precursors. The analysis showed carbon (C_{1s}) and oxygen (O_{1s}) peaks between 280–290 eV and 525–540 eV respectively (Fig. 4B) which is in accordance with previously reported results for pyrolytic carbon [42]. The carbon microelectrode consists of 94.3% of carbon and 5.7% oxygen.

3.4. Cyclic voltammetry (CV)

CV was performed on all five designs of 3D carbon microelectrodes (Table 1 and Fig. 5). For each design, four chips of from different fabrication batches were characterized using 10 mM potassium ferri-ferrocyanide as redox probe. Fig. 5A shows representative CVs for 3D carbon microelectrodes recorded with design 1, 2 and 4 which displayed reproducible electrochemical behavior.

Fig. 5 B summarizes the mean anodic peak current I_a of different designs (N = 4 chips) along with their respective estimated surface area (calculation see supplementary information S1). All 3D microelectrode designs displayed higher peak currents than the 2D microelectrode. The recorded peak current increased for 3D microelectrodes with an increase in estimated surface area. In a reversible redox system, the peak current is directly proportional to the electron transfer on the surface [44]. This is well reflected in the

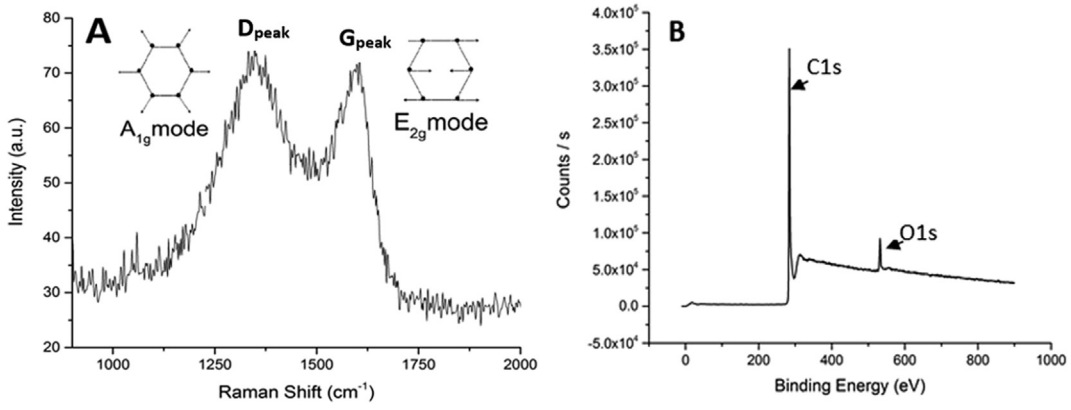

Fig. 4. (A) Raman and (b) XPS spectra of carbon microelectrode.

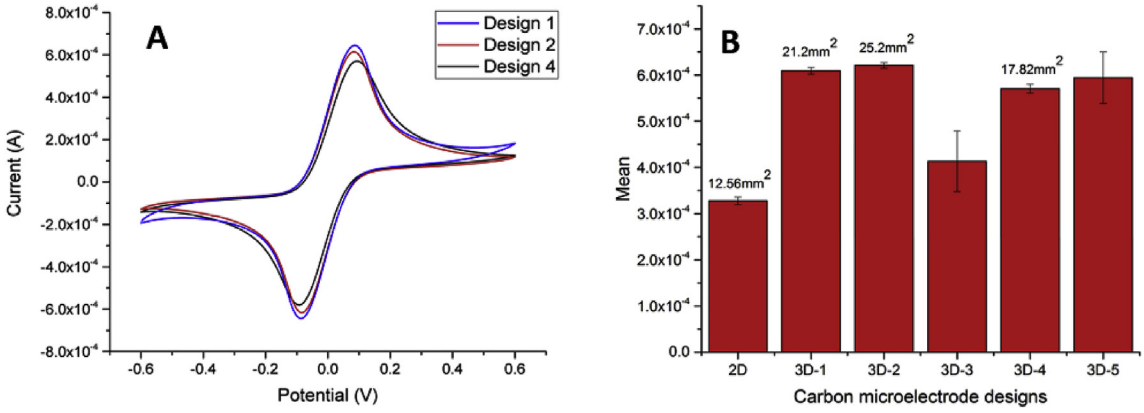

Fig. 5. (A) CV of 2D and different 3D carbon microelectrode designs (1, 2 and 4) (B) anodic peak current with standard deviations for 2D and 3D microelectrodes (N-4 chips). (A colour version of this figure can be viewed online.)

experiments, where for example the 3D microelectrode design 1 with surface area 21.2 mm^2 gives a peak current $I_a = 0.61$ mA which is a twofold higher signal compared to the 2D electrode with $I_a = 0.32$ mA for a surface area of 12.6 mm^2. The current density obtained by normalization with the estimated surface area was 0.25 mA cm^{-2} for 2D, 0.28 mA cm^{-2} for design 1, 0.24 mA cm^{-2} for design 2 and 0.28 mA cm^{-2} for design 4. The comparable values 2D and 3D electrodes indicate that all parts of the 3D carbon microelectrodes are electrically connected and able to contribute to the electron transfer at the WE.

For design 3 and 5 lack of reproducibility was observed for the electrochemical measurements, which was reflected in the higher standard deviation of the measured peak current in Fig. 5B. This is attributed to the defects and irregularities of the suspended carbon layer observed by SEM as discussed earlier. Furthermore, calculation of the surface area for these two designs was very difficult due to the small features in the suspended carbon layers.

Design 1 was selected for further detailed electrochemical analysis, since it had the smallest pillar dimensions with high redox peak currents and was also highly reproducible. In all the following experiments, this optimal 3D carbon microelectrode was compared with planar carbon microelectrodes (2D) and 2D microelectrodes with micropillars on top ($2D_p$). These three different microelectrodes (2D, $2D_p$ and 3D) are shown in Fig. 6A-E. CV was carried out with 10 mM potassium ferri-ferrocyanide redox probes. Fig. 6F shows that the 3D microelectrodes provided a higher peak current and a lower potential difference (ΔE_p). The peak current is directly proportional to the electron transfer on the electrode surface, which is higher for 3D microelectrodes ($I_a = 0.58 \pm 0.008$ mA) as compared to 2D ($I_a = 0.29 \pm 0.01$ mA) or $2D_p$ (0.42 ± 0.004 mA) microelectrode. ΔE_p is mainly influenced by diffusion rates of the analyte, which is 59 mV for an ideal case but generally is higher for practical applications. Hence 3D carbon microelectrodes with a smaller $\Delta E_p = 210$ mV has a higher diffusion as compared to 2D electrode $\Delta E_p = 295$ mV.

The reversibility of the electron transfer for the 2D, $2D_p$ and 3D

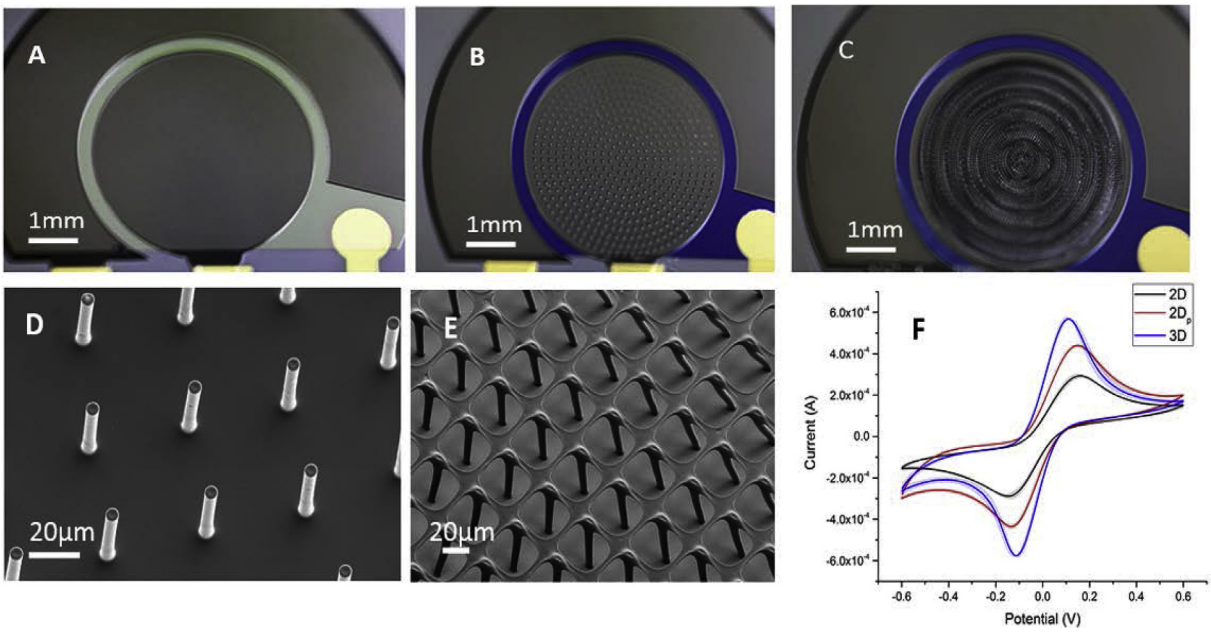

Fig. 6. (A–B) Carbon microelectrodes: A- 2D, B- $2D_p$ and C- 3D (design 1), (D–E) SEM image of working electrode of $2D_p$ and 3D, (F) CV with 10 mM $Fe(CN)_6^{3-/4-}$ (N = 4 chips). (A colour version of this figure can be viewed online.)

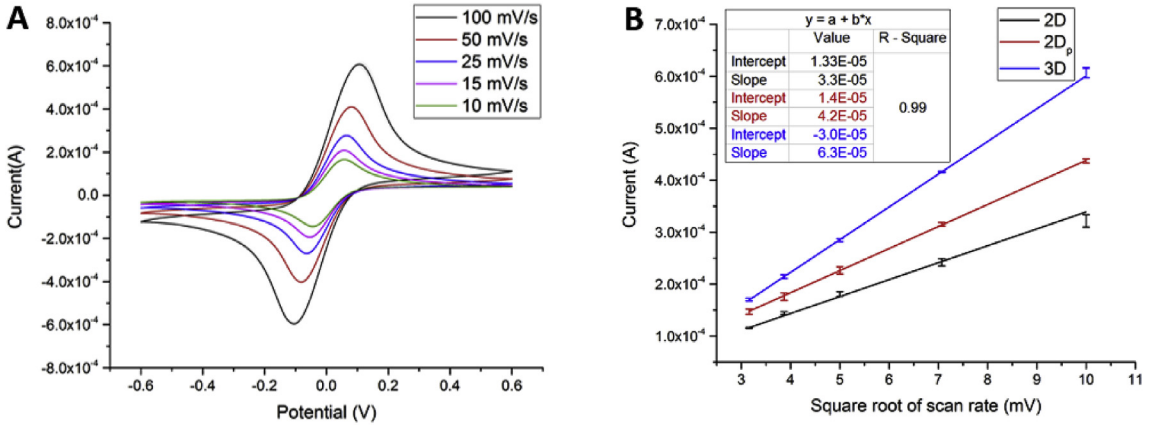

Fig. 7. (A) 3D microelectrode CV with different scan rates (B) Average with standard deviation of peak currents as a linear relation of square root of scan rates (N = 4). (A colour version of this figure can be viewed online.)

carbon microelectrodes was analyzed by CV at different scan rates with a constant concentration of 10 mM potassium ferri-ferrocyanide redox probes. Fig. 7A shows representative cyclic voltammograms recorded for 3D carbon microelectrodes at different scan rates. Fig. 7B demonstrates that the peak currents are directly proportional to the square root of the scan rate, which is the case for reversible systems as described by the Randles-Sevcik equation [44]. CV's at different scan rates for 2D and $2D_p$ electrodes are given in supplementary information S2. 3D carbon microelectrodes showed a higher electron transfer as compared to 2D and $2D_p$ (Fig. 7B). The ΔE_p was found to be constant at different scan rates, as it is the case for a stable diffusion controlled reversible reaction system.

The 2D, $2D_p$ and 3D carbon microelectrodes were also characterized for different concentrations (1.25 mM, 2.5 mM, 5 mM, 10 mM, 15 mM and 20 mM) of potassium ferri-ferrocyanide redox probes at a constant scan rate of 100 mVs^{-1}. Fig. 8A shows representative cyclic voltammograms of 3D carbon microelectrodes with different concentration of $Fe(CN)_6^{3-/4-}$. Fig. 8B demonstrates that the peak current increases linearly with an increase in concentration as described by the Randles-Sevcik equation [44]. CV's with different concentrations of the redox probe for 2D and $2D_p$ electrodes are given in supplementary information S3. Also in this case, the ΔE_p was found to be constant for a given configuration. The electrochemical characterization showed that the electrode reaction was diffusion controlled. The electron transfer (peak current) was found to be higher (2 folds) for 3D microelectrodes when compared to 2D for all concentrations.

The sensitivity of the 3D carbon microelectrodes was 56.2 μA mM^{-1} (slope of the fitting in Fig. 8B) and 4.5 μA mM^{-1} mm^{-2} (considering WE footprint area = 12.56 mm^2), which is higher than the reported values for unmodified carbon microelectrodes [43,45–47]. The higher sensitivity is due the increase in the surface area of the working electrode. The sensitivity of 2D and $2D_p$ chips are 25.5 μA mM^{-1} and 41.3 μA mM^{-1} respectively.

3.5. Electrochemical impedance spectroscopy (EIS)

EIS allows for further characterization of the carbon microelectrodes and it is a useful tool to understand the properties of an entire electrochemical set-up including electrode material properties and external interfacing instrumentations [48]. Based on the results obtained with EIS an equivalent circuit for the electrode can be determined, which clearly illustrates the device properties. Fig. 9A shows the Nyquist plot for 2D, $2D_p$ and 3D carbon microelectrode with the standard deviation (N = 4 chips). An equivalent circuit, derived from a modified Randels model [36], was used to fit the impedance spectra obtained with different electrode configurations. Fig. 9B shows the equivalent circuit used (inset) and the

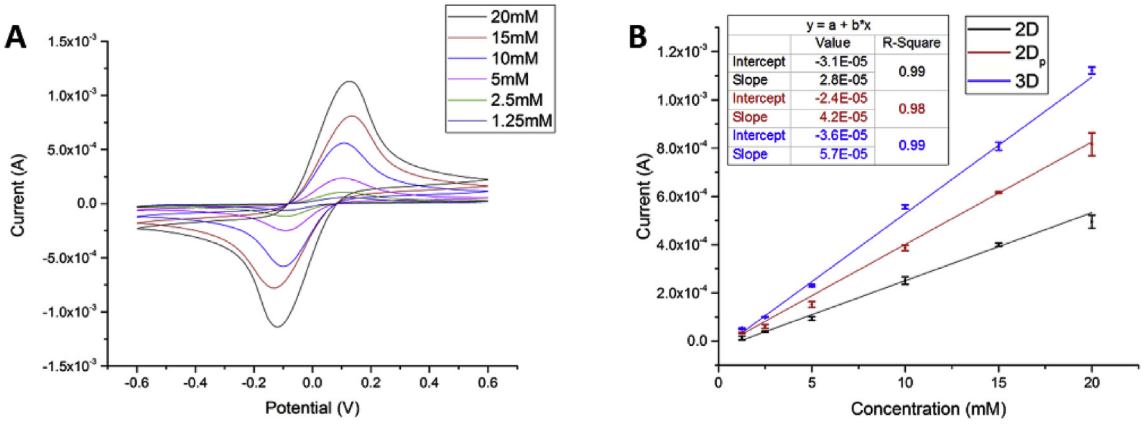

Fig. 8. (A) CV of 3D carbon microelectrode with different concentration of $Fe(CN)_6^{3-/4-}$ concentrations (B) Average of peak currents with standard deviation at different concentrations of $Fe(CN)_6^{3-/4-}$ (N = 4). (A colour version of this figure can be viewed online.)

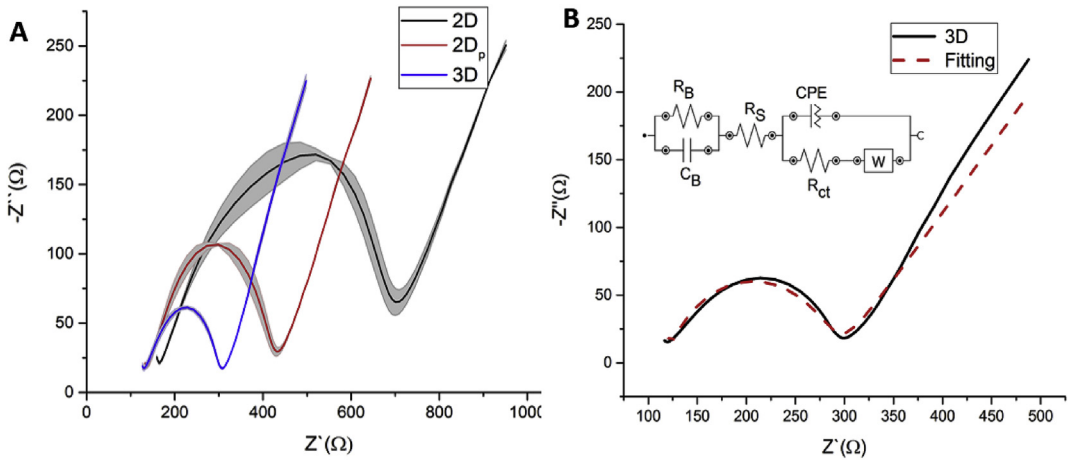

Fig. 9. (A) Impedance spectra of pyrolytic carbon microelectrodes with their standard deviation (N = 4) (B) Impedance spectra for 3D carbon microelectrode (design 1) with equivalent circuit fitting. (A colour version of this figure can be viewed online.)

Table 2
Equivalent mean circuits values with standard deviation (N − 4) of different carbon microelectrode configurations.

	$R_B(\Omega)$	C_B(nF)	$R_S(\Omega)$	R_{ct} (Ω)	Q (μMho)	W (mMho)	α
2D	34.2 ± 3.12	43.10 ± 0.11	133 ± 1.77	554.12 ± 12.98	15.41 ± 1.87	3.63 ± 0.05	0.82 ± 0.02
$2D_p$	30.32 ± 1.96	54.40 ± 0.08	116 ± 1.06	281.3 ± 9.21	6.03 ± 0.26	4.10 ± 0.04	0.79 ± 0.01
3D	23.60 ± 2.13	66.90 ± 0.20	103 ± 1.50	161.54 ± 5.23	4.66 ± 0.24	4.55 ± 0.08	0.75 ± 0.01

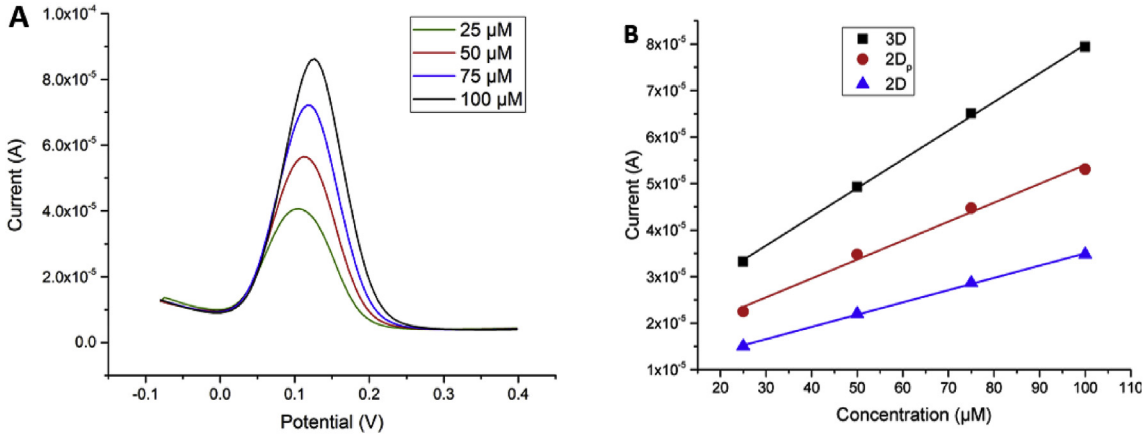

Fig. 10. (A) Square wave voltammetry for different concentration of dopamine with 3D microelectrodes (B) Different concentration of dopamine detection with 3D, $2D_p$ and 2D electrode. (A colour version of this figure can be viewed online.)

fitting for a representative Nyquist plot of a 3D carbon microelectrode. The bulk carbon electrode material can be modeled by a series of capacitances (C_B) and resistances (R_B) in parallel or an equivalent R_B and C_B [36]. The resistance of the electrolyte and the charge transfer at the electrode surface can be represented by resistances R_S and R_{ct}, respectively, as shown in Fig. 9B.

Table 2 summarizes the values of equivalent circuit components extracted from the fitting of the experimental data where Q is the constant phase element (CPE) at a frequency ω − 1, α is the multiplication factor of the phase angle and W is the Warburg impedance.

The semicircle at the high frequency corresponds to the electron-transfer kinetics of the redox probe at the electrode interface, while the linear part at the lower frequency is due to the diffusion-limited electron-transfer processes [48]. The charge transfer resistance R_{ct} for the 3D microelectrodes was considerably smaller than for $2D_p$ or 2D microelectrodes. The decrease of the R_{ct} is mainly due the increased surface area of 3D carbon microelectrodes which is also shown by an increase of peak current during CV. With the increase in surface area, the bulk capacitance (C_B) increases and bulk resistance (R_B) decreases. This is mainly due sp^2 and sp^3 regions in the pyrolytic carbon electrodes which acts as conducting and insulating regions respectively. Generally R_S is the solution resistance, but for a microelectrode an additional resistance due to the electrochemical system is present. Hence a decrease in R_S for 3D carbon microelectrode. Increased surface area for a 3D carbon microelectrode increases the overall roughness and inhomogeneous electron transfer which can be seen by a decrease in α [21].

3.6. Dopamine (DA) detection with square wave voltammetry

Dopamine is an important neurotransmitter in the central nervous system (CNS) [7]. Lack of dopamine releasing neurons in the CNS leads to neurodegenerative disorders such as Parkinson's disease [49]. Dopamine sensing experiments with 2D, $2D_p$ and 3D carbon microelectrodes were conducted. Fig. 10A shows the results obtained for dopamine detection on 3D carbon microelectrodes. Fig. 10B shows the linear increase of the peak current with the increase in DA concentrations. The SWV's for DA detection on 2D and $2D_p$ electrodes are given in supplementary information S5. The highly sensitive 3D carbon microelectrodes resulted in twice the peak current compared to 2D electrodes for dopamine detection. For 25 μM dopamine, the 2D and 3D carbon microelectrodes resulted in currents of 33.2 μA and 15.0 μA respectively which corresponds to a two-fold increase of the response for DA detection using 3D carbon microelectrodes. The sensitivity of the DA detection on 3D carbon microelectrodes was 0.87 μA μM^{-1} (slope of the fitting in Fig. 10B) and 0.069 μA μM^{-1} mm^{-2} (considering WE footprint area = 12.56 mm^2), which is higher than the reported values for other unmodified carbon microelectrodes [7,50,51].

4. Conclusion

Suspended multilayer SU-8 polymer templates were successfully fabricated with multiple steps of UV photolithography and pyrolysed to obtain 3D carbon microelectrodes. Five designs of 3D carbon microelectrodes were characterized for shrinkage and mechanical stability with optical microscopy, SEM, Raman and XPS. Designs with pillar pitch (Φ) = hole pitch (c) (design 1, 2 and 4) were successfully fabricated with a very low reproducibility with a feature size of 7 μm. The smallest feature size of pyrolysed carbon observed on the suspended layer was 2 μm (design 3 and 5) with less throughput. 3D carbon microelectrodes (design 1–5) were successfully fabricated even with a high shrinkage of 48.3%, 41.0% and 48.4% for height, pillar diameter and suspended layer thickness respectively. An electrochemical chip with 3D carbon microelectrodes as working electrode, carbon as counter and gold as pseudo-reference was fabricated for electrochemical characterization. CV and EIS were used for electrochemical characterization. CV resulted in twice the peak current for 3D microelectrode as compared to 2D electrode. Further 3D microelectrodes were characterized by CV (different scan rate and concentration) and EIS, which confirmed that 3D microelectrodes provide a higher electron transfer and

lower charge transfer resistance compared to 2D electrodes due to the larger surface area. Finally 3D carbon microelectrodes were used to enhance DA detection, which also resulted in twice the higher current response as compared to 2D carbon electrodes.

Acknowledgements

The authors acknowledge funding by the Young Investigator Program of the Villum Foundation, project no. VKR023438.

Appendix A. Supplementary data

Supplementary data related to this article can be found at http://dx.doi.org/10.1016/j.carbon.2017.05.090.

References

[1] R. Martinez-Duarte, Microfabrication technologies in dielectrophoresis applications-a review, Electrophoresis 33 (21) (2012) 3110–3132.
[2] J.W. Long, B. Dunn, D.R. Rolison, H.S. White, Three-dimensional battery architectures, Chem. Rev. 104 (10) (Oct. 2004) 4463–4492.
[3] A. Fendyur, M.E. Spira, Toward on-chip, in-cell recordings from cultured cardiomyocytes by arrays of gold mushroom-shaped microelectrodes, Front. Neuroeng. 5 (August) (2012) 1–10.
[4] Y. Rui, J. Liu, Y. Wang, C. Yang, Parylene-based implantable Pt-black coated flexible 3-D hemispherical microelectrode arrays for improved neural interfaces, Microsyst. Technol. 17 (3) (2011) 437–442.
[5] R.R. Kamath, M.J. Madou, Three-dimensional carbon interdigitated electrode arrays for redox-amplification, Anal. Chem. 86 (6) (2014) 2963–2971.
[6] F. Santoro, J. Schnitker, G. Panaitov, A. Offenhäusser, On chip guidance and recording of cardiomyocytes with 3D mushroom-shaped electrodes, Nano Lett. 13 (11) (2013) 5379–5384.
[7] L. Amato, A. Heiskanen, C. Caviglia, F. Shah, K. Zór, M. Skolimowski, M. Madou, L. Gammelgaard, R. Hansen, E.G. Seiz, M. Ramos, T.R. Moreno, A. Martínez-Serrano, S.S. Keller, J. Emnéus, Pyrolysed 3D-carbon scaffolds induce spontaneous differentiation of human neural stem cells and facilitate real-time dopamine detection, Adv. Funct. Mater. 24 (44) (2014) 7042–7052.
[8] F. Greiner, S. Quednau, F. Dassinger, R. Sarwar, H.F. Schlaak, M. Guttmann, P. Meyer, Fabrication techniques for multiscale 3D-MEMS with vertical metal micro- and nanowire integration, J. Micromechanics Microengineering 23 (2) (2013) 25018.
[9] S. Lee, J. Ahn, J.-M. Seo, H. Chung, D.-I. Cho, Electrical characterization of 3D Au microelectrodes for use in retinal prostheses, Sensors 15 (6) (2015) 14345–14355.
[10] J. Voldman, M.L. Gray, M. Toner, M.A. Schmidt, A microfabrication-based dynamic array cytometer, Anal. Chem. 74 (16) (2002) 3984–3990.
[11] V. Piotter, T. Benzler, T. Gietzelt, R. Ruprecht, J. Hauelt, Micro powder inject. molding, Adv. Eng. Mater. 2 (10) (2000) 639–642.
[12] A.C. Siegel, D.A. Bruzewicz, D.B. Weibel, G.M. Whitesides, Microsolidics: fabrication of three-dimensional metallic microstructures in poly(-dimethylsiloxane), Adv. Mater. 19 (5) (2007) 727–733.
[13] S. Kim, J. Park, K. Kang, C.-O. Park, I. Park, Direct metal micropatterning on needle-type structures towards bioimpedance and chemical sensing applications, J. Micromechanics Microengineering 25 (1) (2015) 15002.
[14] S.-Y. Wu, C. Yang, W. Hsu, L. Lin, 3D-printed microelectronics for integrated circuitry and passive wireless sensors, Microsyst. Nanoeng. 1 (April) (2015) 15013.
[15] J. Xu, D. Wu, J.Y. Ip, K. Midorikawa, K. Sugioka, Vertical sidewall electrodes monolithically integrated into 3D glass microfluidic chips using water-assisted femtosecond-laser fabrication for in situ control of electrotaxis, RSC Adv. 5 (31) (2015) 24072–24080.
[16] P. Paiè, F. Bragheri, R.M. Vazquez, R. Osellame, Straightforward 3D hydrodynamic focusing in femtosecond laser fabricated microfluidic channels, Lab Chip 14 (11) (2014) 1826–1833.
[17] A. Hart, H. Taylor, 2D and 3D growth of carbon nanotubes on substrates, from nanometre to millimetre scales, Int. J. Nanomanuf. X (Y) (2007) 1–9.
[18] S. Rajaraman, S.-O. Choi, R.H. Shafer, J.D. Ross, J. Vukasinovic, Y. Choi, S.P. DeWeerth, A. Glezer, M.G. Allen, Microfabrication technologies for a coupled three-dimensional microelectrode, microfluidic array, J. Micromechanics Microengineering 17 (1) (2006) 163–171.
[19] J.-W. Choi, S. Rosset, M. Niklaus, J.R. Adleman, H. Shea, D. Psaltis, 3-Dimensional electrode patterning within a microfluidic channel using metal ion implantation, Lab Chip 10 (6) (2010) 783–788.
[20] C. Wang, M. Madou, From MEMS to NEMS with carbon, Biosens. Bioelectron. 20 (10) (2005) 2181–2187. SPEC. ISS.
[21] R.L. McCreery, Advanced carbon electrode materials for molecular electrochemistry, Chem. Rev. 108 (7) (2008) 2646–2687.
[22] M. Beidaghi, C. Wang, Micro-supercapacitors based on three dimensional interdigital polypyrrole/C-MEMS electrodes, Electrochim. Acta 56 (25) (2011) 9508–9514.
[23] R. Martinez-Duarte, R. Gorkin, K. Abi-Samra, and M. J. Madou, "The integration of 3D carbon dielectrophoresis on a rotating platform," TRANSDUCERS 2009-15th Int. Conf. Solid-State Sensors, Actuators Microsystems, pp. 2147–2150, 2009.
[24] R. Martinez-Duarte, SU-8 photolithography as a toolbox for carbon MEMS, Micromachines 5 (3) (2014) 766–782.
[25] A. del Campo, C. Greiner, SU-8: a photoresist for high-aspect-ratio and 3D submicron lithography, J. Micromechanics Microengineering 17 (6) (2007) R81–R95.
[26] V.J. Cadarso, K. Pfeiffer, U. Ostrzinski, J.B. Bureau, G. a Racine, A. Voigt, G. Gruetzner, J. Brugger, Direct writing laser of high aspect ratio epoxy microstructures, J. Micromechanics Microengineering 21 (1) (2011) 17003.
[27] K. Ohlinger, Y. Lin, Z. Poole, K.P. Chen, Undistorted 3D microstructures in SU8 formed through two-photon polymerization, AIP Adv. 1 (3) (2011).
[28] Y. Lim, J.-I. Heo, H. Shin, Fabrication and application of a stacked carbon electrode set including a suspended mesh made of nanowires and a substrate-bound planar electrode toward for an electrochemical/biosensor platform, Sensors Actuators B Chem. 192 (2014) 796–803.
[29] F. Ceyssens, R. Puers, Creating multi-layered structures with freestanding parts in SU-8, J. Micromechanics Microengineering 16 (6) (2006) S19–S23.
[30] J. Melai, V.M. Blanco Carballo, C. Salm, J. Schmitz, Suspended membranes, cantilevers and beams using SU-8 foils, Microelectron. Eng. 87 (5–8) (2010) 1274–1277.
[31] A. Rammohan, P.K. Dwivedi, R. Martinez-Duarte, H. Katepalli, M.J. Madou, A. Sharma, One-step maskless grayscale lithography for the fabrication of 3-dimensional structures in SU-8, Sensors Actuators, B Chem. 153 (1) (2011) 125–134.
[32] S. Hemanth, C. Caviglia, L. Amato, T.A. Anhøj, A. Heiskanen, J. Emnéus, S.S. Keller, Pyrolytic 3D carbon microelectrodes for electrochemistry, ECS Trans. 72 (1) (2016) 117–124.
[33] L. Amato, S.S. Keller, A. Heiskanen, M. Dimaki, J. Emnéus, A. Boisen, M. Tenje, Fabrication of high-aspect ratio SU-8 micropillar arrays, Microelectron. Eng. 98 (2012) 483–487.
[34] L. Amato, A. Heiskanen, R. Hansen, L. Gammelgaard, T. Rindzevicius, M. Tenje, J. Emnéus, S.S. Keller, Dense high-aspect ratio 3D carbon pillars on interdigitated microelectrode arrays, Carbon N. Y. 94 (2015) 792–803.
[35] R. Martinez-duarte, P. Renaud, M.J. Madou, A Novel Approach to Dielectrophoresis Using Carbon Electrodes, 2011, pp. 2385–2392.
[36] L. Amato, A. Heiskanen, R. Hansen, L. Gammelgaard, T. Rindzevicius, M. Tenje, J. Emnéus, S.S. Keller, Dense high-aspect ratio 3D carbon pillars on interdigitated microelectrode arrays, Carbon N. Y. 94 (Nov. 2015) 792–803.
[37] E.C.S. Transactions, T.E. Society, Shrinkage analysis of carbon micro structures derived from SU-8 photoresist, ECS Trans. 72 (1) (2016) 27–33. R. Natu, M. Islam and R. Martinez-Duarte Department of Mechanical Engineering, Clemson University, Clemson, South Carolina 29634, USA.
[38] K.S. Chen, R.Z. Yeh, Pyrolysis kinetics of epoxy resin in a nitrogen atmosphere, J. Hazard. Mater. 49 (2–3) (1996) 105–113.
[39] C.-C.M. Ma, C.-Y. Chen, H.-C. Kuan, W.-C. Chang, Processability, thermal, mechanical, and morphological properties of novolac type-epoxy resin-based carbon-carbon composite, J. Compos. Mater. 38 (4) (2004) 311–322.
[40] P.K. Chu, L. Li, Characterization of amorphous and nanocrystalline carbon films, Mater. Chem. Phys. 96 (2–3) (2006) 253–277.
[41] T. Takahagi, A. Ishitani, XPS study on the surface structure of carbon fibers using chemical modification and C1s line shape analysis, Carbon 26 (3) (1988) 389–396.
[42] R. Kostecki, B. Schnyder, D. Alliata, X. Song, K. Kinoshita, R. Kötz, Surface studies of carbon films from pyrolyzed photoresist, Thin Solid Films 396 (2001) 36–43.
[43] A.C. Ferrari, Raman spectroscopy of graphene and graphite: disorder, electron – phonon coupling, doping and nonadiabatic effects, Solid State Commun. 143 (2007) 47–57.
[44] P. Zanello, Inorganic Electrochemistry, Royal Society of Chemistry, Cambridge, 2003.
[45] K.K. Mistry, S. Deepthy, C.R. Chaudhuri, H. Saha, Electrochemical characterization of some commercial screen-printed electrodes in different redox substrates, Curr. Sci. 109 (8) (2015) 1427–1436.
[46] P. Fanjul-Bolado, D. Hernández-Santos, P.J. Lamas-Ardisana, A. Martín-Pernía, A. Costa-García, Electrochemical characterization of screen-printed and conventional carbon paste electrodes, Electrochi. Acta 53 (10) (1 April 2008) 3635–3642.
[47] H. Luo, Z. Shi, N. Li, Z. Gu, Q. Zhuang, Investigation of the electrochemical and electrocatalytic behavior of single-wall carbon nanotube film on a glassy carbon electrode, Anal. Chem. 73 (5) (2001) 915–920.
[48] A.J. Bard, Faulkner, Electrochem. Methods 30 (1) (2000).
[49] M. Politis, O. Lindvall, Clinical application of stem cell therapy in Parkinson's disease, BMC Med. 10 (1) (2012) 1.
[50] R.S. Pai, K.M. Walsh, M.M. Crain, T.J. Roussel, D.J. Jackson, R.P. Baldwin, R.S. Keynton, J.F. Naber, Fully integrated three-dimensional electrodes for electrochemical detection in Microchips: fabrication, characterization, and applications, Anal. Chem. 81 (12) (2009) 4762–4769.
[51] D.J. Fischer, W.R. Vandaveer, R.J. Grigsby, S.M. Lunte, Pyrolyzed photoresist carbon electrodes for microchip electrophoresis with dual-electrode amperometric detection, Electroanalysis (2005) 1153–1159.

Supplementary information

S1. Surface area calculation

The total surface are is calculated as :

A_{total} = Area of the base + (no. of pillars x pillars cylinderical area) + (2x (Area of the suspended layer- area of the holes on the suspended layer)s – area of the pilars top

Design 1: 21.2 mm^2

Design 2: 25.2 mm^2

Design 4: 17.82 mm^2

S2. Different scan rate CV for 2D and $2D_p$

CV with different scan rate (100 mVs^{-1}, 50 mVs^{-1}, 25 mVs^{-1}, 15 mVs^{-1}, 10 mVs^{-1}) was performed with $Fe(CN)_6^{3-/4-}$(10 mM) on 2D and $2D_p$ configuration of working electrode. Figure A.A and Figure A.B shows the CV of 2D and $2D_p$ carbon electrodes in $Fe(CN)_6^{3-/4-}$ respectively.

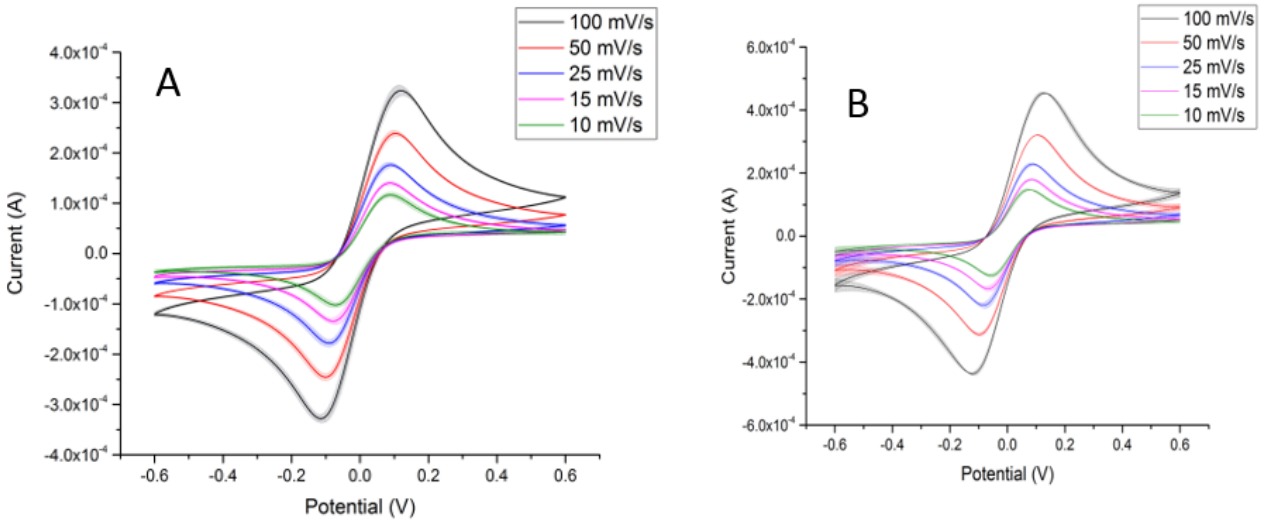

Figure A: CV of 2D and $2D_p$ with different scan rates in 10 mM $Fe(CN)_6^{3-/4-}$

*Corresponding author. Tel: +4531477553. E-mail: suhem@nanotech.dtu.dk (Suhith Hemanth)

S3. Different concentrations CV for 2D and $2D_p$

CV with different concentration of $Fe(CN)_6^{3-/4-}$ (20 mM, 15 mM, 10 mM, 5mM, 2.5 mM and 1.25 mM) was performed on 2D and $2D_p$ configuration of working electrode with 100 mVs^{-1} scan rate.

Figure B.A and B shows the CV of 2D and $2D_p$ carbon electrodes in $Fe(CN)_6^{3-/4-}$ respectively.

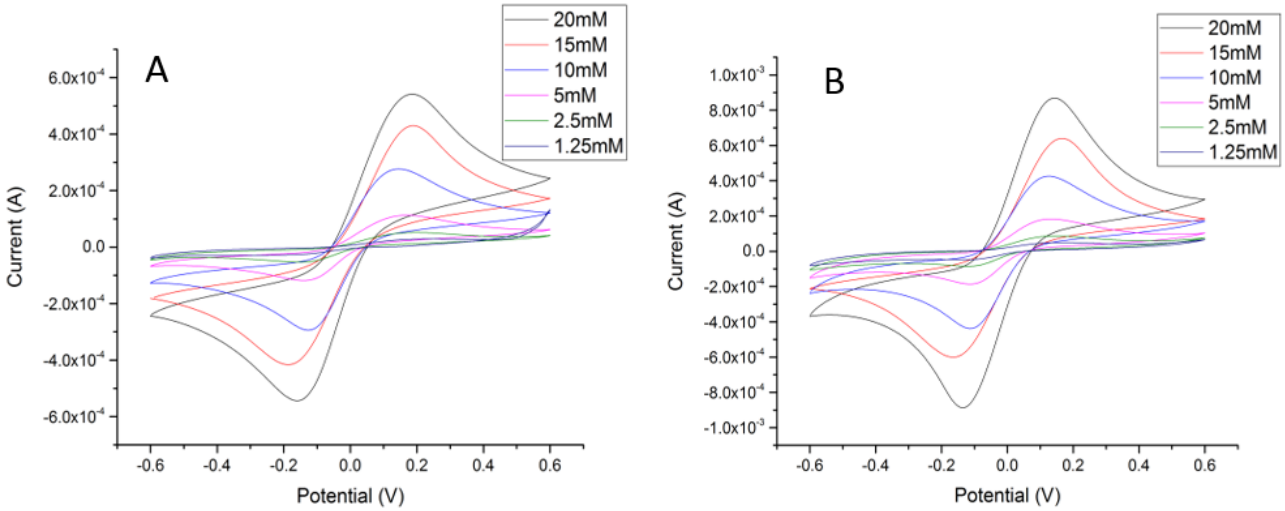

Figure B : CV of 2D and $2D_p$ with different concentrations of $Fe(CN)_6^{3-/4-}$

S4. XPS

XPS was performed on a flat carbon surface. Figure C shows the carbon peak at 285 eV.

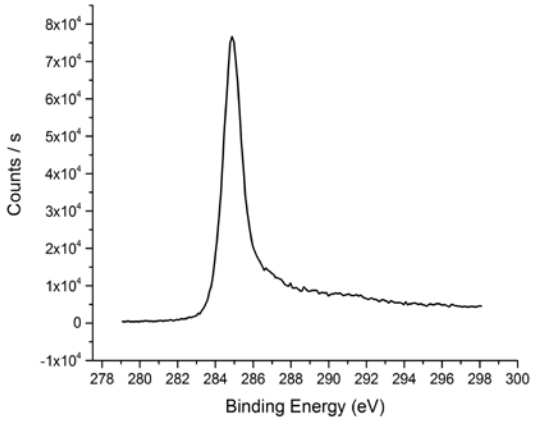

Figure C: XPS spectra of carbon microelectrode

S5. Dopamine detection

Different concentrations of dopamine (25 µM, 50 µM, 75 µM and 100 µM) was detected on 2D and $2D_p$ as shown in Figure D.A and B respectively.

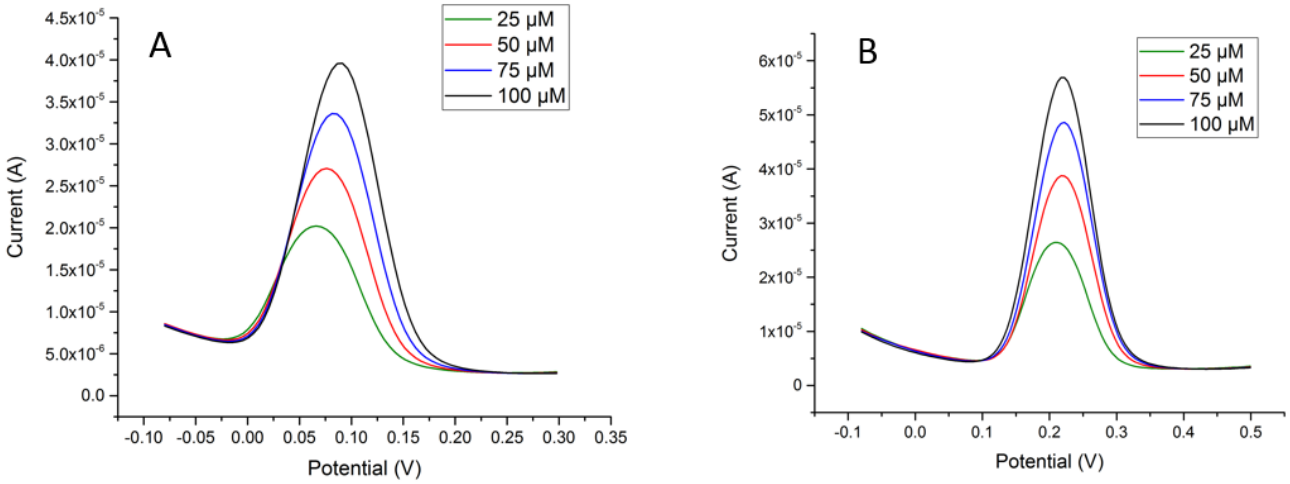

Figure D : Dopamine detection with (A) 2D and (B) $2D_p$ carbon microelectrode

Paper III

Suspended microstructures of epoxy based photoresist fabricated with UV Photolithograhy

S. Hemanth, T. A. Anhøj, C.Caviglia and S. S. Keller, Microelectronic Engineering 176 (2017) 40-44.

Microelectronic Engineering 176 (2017) 40–44

Contents lists available at ScienceDirect

Microelectronic Engineering

journal homepage: www.elsevier.com/locate/mee

Research paper

Suspended microstructures of epoxy based photoresists fabricated with UV photolithography

Suhith Hemanth [a,*], Thomas A. Anhøj [b], Claudia Caviglia [a], Stephan S. Keller [a]

[a] Department of Micro and Nanotechnology, DTU Nanotech, 2800 Kongens Lyngby, Denmark
[b] DTU Danchip, 2800 Kongens Lyngby, Denmark

ARTICLE INFO

Article history:
Received 27 October 2016
Received in revised form 14 December 2016
Accepted 23 January 2017
Available online 27 January 2017

Keywords:
405 nm UV photolithography
Suspended microstructures
SU-8
mr-DWL

ABSTRACT

In this work we present an easy, fast, reliable and low cost microfabrication technique for fabricating suspended microstructures of epoxy based photoresists with UV photolithography. Two different fabrication processes with epoxy based resins (SU-8 and mr-DWL) using UV exposures at wavelengths of 313 nm and 405 nm were optimized and compared in terms of structural stability, control of suspended layer thickness and resolution limits. A novel fabrication process combining the two photoresists SU-8 and mr-DWL with two UV exposures at 365 nm and 405 nm respectively provided a wider processing window for definition of well-defined suspended microstructures with lateral dimensions down to 5 μm when compared to 313 nm or 365 nm UV photolithography processes.

1. Introduction

The epoxy-based photoresist SU-8 is well established for the microfabrication of 3D microstructures for various applications such as tissue engineering, microelectromechanical systems (MEMS) and microfluidics [1–6]. Furthermore SU-8 is also the most common polymer template for the fabrication of pyrolytic carbon electrodes using the Carbon MEMS (C-MEMS) process [7]. The resist allows fabrication of high aspect ratio microstructures with high mechanical and chemical stability using standard UV photolithography due to the low absorption of UV wavelengths above 350 nm [8]. At the same time, the low UV absorption results in challenges for fabrication of overhanging or suspended features by subsequent steps of SU-8 photolithography. In the past, different fabrication processes have been proposed for the fabrication of suspended 3D SU-8 microstructures. Advanced methods such as X-ray, e-beam and two-photon lithography have been proposed for fabrication of high resolution 3D microstructures [9–12]. The limiting factor for these techniques is the low throughput.

Alternatively, several approaches using UV photolithography have been introduced. The most common process involves adding a polymerization-stop-layer between the structures to be suspended and the substrate [13,14]. Alternatively lamination of a polymer foil on top of a patterned template followed by patterning of the foil has been proposed [15,16]. The complexity of these fabrication processes increases as the structures become multi-layered (i.e. more 3D). Another method includes doping of SU-8 with nanoparticles or tailoring of the photoinitiator concentration to control the thickness of suspended layers. However adding nanoparticles such as Fe_2O_3 or increasing the concentration of photoinitiator requires an additional preparation step [17,18]. Furthermore, suspended macrostructures have been fabricated with grayscale photolithography, but without achieving micron or submicron resolution [7].

Recently, fabrication of suspended SU-8 layers by partial exposure at a wavelength of 365 nm has been demonstrated [19–21]. The limiting factor of this fabrication process is the narrow processing window (5 ± 1 s UV exposure) for the partial exposure [22]. We observed that minor variations in parameters such as the baking temperature, humidity and exposure dose resulted in cracks and difficulties to control the suspended layer thickness (Fig. 1.A). Furthermore, instability of the features with a size smaller than 10 μm was seen (Fig. 1.B). Alternatively, the use of a lower wavelength (313 nm) to crosslink or pattern the suspended layer has been proposed [14]. At this wavelength, the absorption by the SU-8 is increased resulting in lower penetration depth of the UV radiation.

In this work, we introduce a third approach for fabrication of suspended layers of epoxy based photoresists with UV photolithography using a higher wavelength of 405 nm. The combination of two different photoresists (SU-8 and mr-DWL) is exploited to fabricate suspended layers with a precise lateral and longitudinal resolution. The novel approach is compared with a process using partial exposure at wavelengths of 313 nm to crosslink the suspended layers. Compared to earlier work, all the processes were carried out with a low temperature baking profile to minimize the thermal stress [23,24]. After optimization of the exposure dose, both fabrication processes result in a well-defined suspended layer in lateral direction. However, the fabrication

* Corresponding author.
E-mail address: suhem@nanotech.dtu.dk (S. Hemanth).

http://dx.doi.org/10.1016/j.mee.2017.01.026
0167-9317/

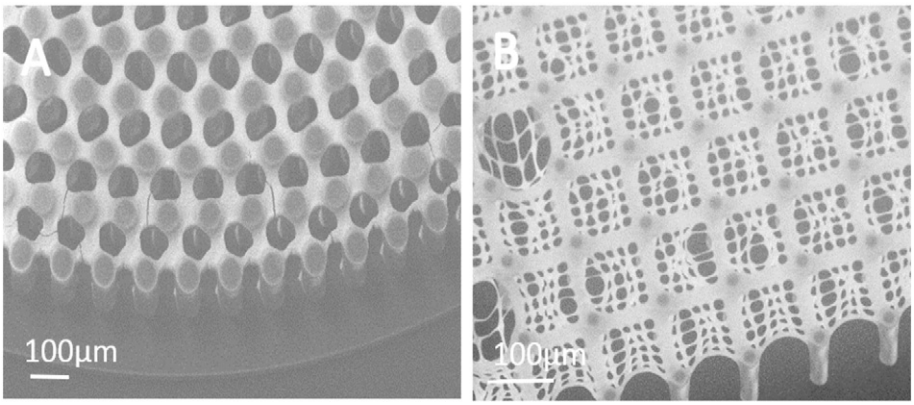

Fig. 1. Defects in suspended SU-8 layer fabricated with 365 nm partial UV exposure according to [22] (A) Cracks on the suspended layer and (B) Unstable suspended SU-8 microstructures.

process with 405 nm and mr-DWL provides a wider processing window and improved control of the thickness of the suspended layer.

2. Methods

2.1. 313 nm UV photolithography

The fabrication of suspended microstructures using 313 nm photolithography is illustrated in Fig. 2. Schematic of the 313 nm UV lithography process: (A) SU-8 is spin coated on a Si/SiO_2 substrate and soft-baked; (B) 1st UV exposure at 365 nm; (C) 2nd partial UV exposure at 313 nm and post-exposure bake; (D) Development in PGMEA. Approximately 5 ml of SU-8 2075 (MicroChem, USA) were manually dispensed on a 4-in. Si/SiO_2 substrate and coating was performed using a two-step spin process on a RCD8 T spin-coater (Süss Micro-Tec, Germany). A spread cycle of 30 s at 700 rpm with 100 $rpms^{-1}$ acceleration was applied, followed by a thinning cycle at 1600 rpm for 60 s with 100 $rpms^{-1}$ acceleration yielding a uniform 98 µm thick film. The edge bead was removed by dispensing propylene glycol methyl ether acetate (PGMEA) at the edge of the rotating wafer at 300 rpm for 30 s (Fig. 2A). To minimize the thermal stress low temperature baking steps were used [24]. The wafers were placed on a programmable hotplate (Harry Gestigkeit GmbH, Germany) at room temperature and ramped to 50 °C at 2 °$Cmin^{-1}$ followed by a soft bake (SB) for 5 h at 50 °C and natural cooling for 2 h. The SU-8 layer was patterned by UV exposure on an EVG620 aligner (EVGroup, Austria) equipped with a mercury lamp and a long pass filter (SU-8 filter), adjusted to a constant intensity of 7 $mWcm^{-2}$ at 365 nm in soft contact mode through a mask. The intensity was measured with a UV-Optometer (SUSS UV-Optometer, SÜSS MicroTec AG, Germany) using a probe 365/405 channel 365, which is sensitive between 345 nm and 385 nm, where 365 nm intensity is the maximum for a mercury lamp. The SU-8 filter blocks all wavelengths below 345 nm. The mask (M_1) includes designs of micropillar arrays with various pillar diameters ($d = 10 - 50$ µm) with a varying pitch ($a = 25 - 250$ µm). The first UV exposure with a dose $D_1 = 210$ $mJcm^{-2}$ (Fig. 2.B) was followed by a second partial UV exposure at 313 nm with dose D_{313} through a second mask (M_2). For the partial exposure, the filter was changed to a 313 nm (250 nm to 350 nm) short pass filter. A constant intensity of 1.05 $mWcm^{-2}$ was measured with a UV-Optometer using a 320 nm probe which is sensitive between 290 nm and 345 nm including the predominate line for a mercury lamp at 313 nm. The partial exposure dose D_{313} was optimized to obtain well resolved microstructures on the suspended layer connecting the pillars (.C). The mask (M_2) includes distribution of holes with diameters ($w = 10$ µm $- 50$ µm) and varying pitch ($y =$ 5 µm $- 200$ µm) which defines the suspended layer. For the post

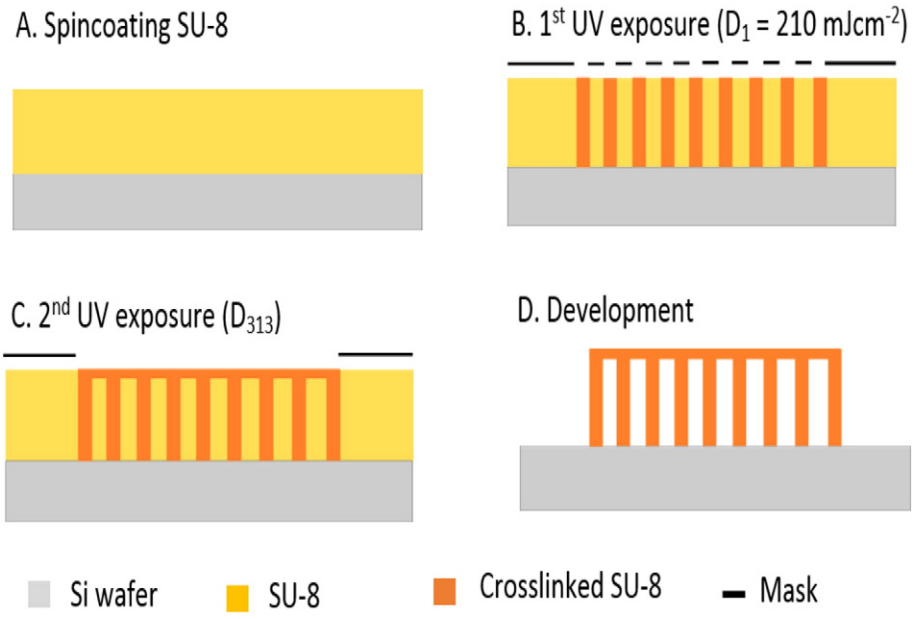

Fig. 2. Schematic of the 313 nm UV lithography process: (A) SU-8 is spin coated on a Si/SiO_2 substrate and soft-baked; (B) 1st UV exposure at 365 nm; (C) 2nd partial UV exposure at 313 nm and post-exposure bake; (D) Development in PGMEA.

exposure bake (PEB), a baking temperature of 50 °C for 5 h with a ramp of 2 °Cmin^{-1} followed by a natural cooling down to room temperature was used. The development in PGMEA was performed in two steps of 10 min followed by rinsing in isopropanol for 30 s and drying in air (Fig. 2.D)

2.2. 405 nm UV photolithography

The fabrication of suspended microstructures with 405 nm UV photolithography is shown in Fig. 3. The supporting SU-8 pillars were fabricated as described in Section 2.1 (Fig. 3.A and B). After the first SU-8 exposure (Fig. 3.B), approximately 5 ml of mr-DWL 40 (Microresist technology GmbH, Germany) were spin coated on the SU-8 at 4000 rpm for 60 s with 100 rpms^{-1} acceleration yielding a uniform 17 μm thick film. The polymer stack was SB at 50 °C for 1 h (Fig. 3.C). The aligner was equipped with two filters: The 365 nm broad band filter described above (SU-8 filter) and a 10 mm thick PMMA sheet (SPMMA0050NR00, NordiskPlast, Denmark) mainly to filter out the i-line at 365 nm wavelength. With this configuration the constant intensities at 313 nm, 365 nm and 405 nm were 0 mWcm^{-2}, 0.33 mWcm^{-2} and 10.50 mWcm^{-2} respectively. The intensity at 405 nm was measured with the UV-Optometer using probe 365/405 channel 405, which is sensitive between 345 nm and 460 nm, including three dominate lines at 365 nm, 405 nm and 435 nm. The 365 nm intensity is half the intensities at 405 nm and 435 nm, hence the measured intensity at 405 nm was obtained by subtracting the intensities at 365 nm and 435 nm. The exposure dose for mr-DWL 40 D_{405} was optimized to obtain well resolved microstructures on the suspended layer (Fig. 3.D).

This step was followed by a PEB at 50 °C for 5 h and development in PGMEA in two steps of 10 min each, rinsing in isopropanol for 30 s and drying in air (Fig. 3.E).

3. Results and discussion

3.1. 313 nm UV photolithography process

For UV photolithography with 365 nm wavelength both the lateral dimensions and the thickness of the suspended layer have been difficult to control and reproduce. Here, a low wavelength (313 nm) was used to limit the cross-linking to the top surface. SU-8 absorbs considerably more UV radiation at wavelengths below 350 nm [8]. Therefore, activation of the photoinitiator in the bulk of the resist film is reduced and crosslinking can be limited to the top surface when using lower wavelengths for the partial exposure [8,14].

We optimized a low temperature process to successfully fabricate suspended SU-8 layers with UV exposure at 313 nm wavelength for a large range of exposure doses D_{313} (Fig. 4). The UV exposure at 313 nm limited photoinitiator activation to the top surface and allowed to reduce the thickness of the suspended layer (approximately 11 μm) compared to exposure at 365 nm. However, the high absorption at 313 nm combined with diffusion of the photoinitiator resulted in overexposure and complete crosslinking of the top surface without any patterns for an exposure dose $D_{313} = 10$ mJcm^{-2} (Fig. 4.A). Even for a lower exposure dose of 5.25 mJcm^{-2} (5 s of UV exposure) the structures were still over exposed and no replication of the mask design M_2 was achieved (Fig. 4.B). With an exposure dose of 3.15 mJcm^{-2} (3 s of UV exposure) the patterns on M_2 were replicated (Fig. 4.C and D). The thickness of the suspended layer was approximately 11 μm for all three exposure doses (D_{313}). The holes with 10 μm diameter and pitch 5 μm were successfully fabricated on the suspended layer as showed in Fig. 4.C. This demonstrates that the processing window for fabrication of suspended SU-8 structures with high lateral photolithographic resolution remains quite narrow when using UV exposure at 313 nm. As a major drawback, it is not possible to control lateral resolution and thickness of the suspended layer independently, because both parameters depend on the exposure dose. This results in a less flexible process for fabricating patterned suspended layers with different thicknesses.

3.2. 405 nm UV lithography process

The limitation to control both lateral resolution and the suspended layer thickness precisely, lead us to explore a new fabrication process. The negative epoxy photoresist mr-DWL 40 has a photoinitiator which can be activated at 405 nm. At the same time, SU-8 should not be cross-linked after UV exposure at 405 nm wavelength. First, the SU-8 crosslinking at 405 nm was evaluated by exposing 98 μm thick SU-8

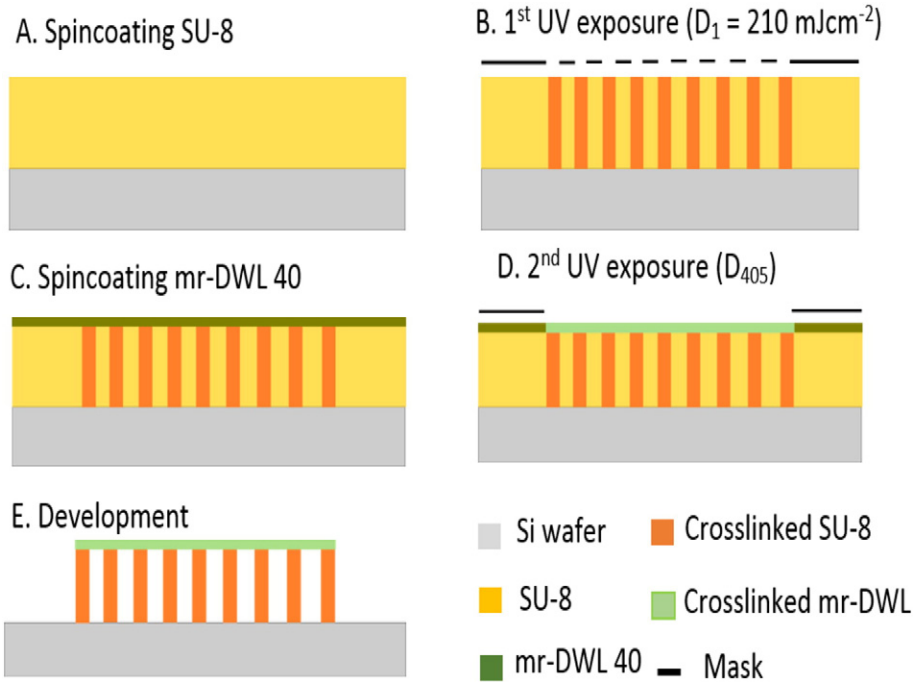

Fig. 3. Schematic of 405 nm microfabrication process: (A) SU-8 is spin coated on a Si/SiO_2 substrate and soft-baked; (B) 1st UV exposure at 365 nm; (C) mr- DWL 40 spin coating on SU-8; (D) 2nd UV exposure at 405 nm and post-exposure-bake; (E) Development in PGMEA.

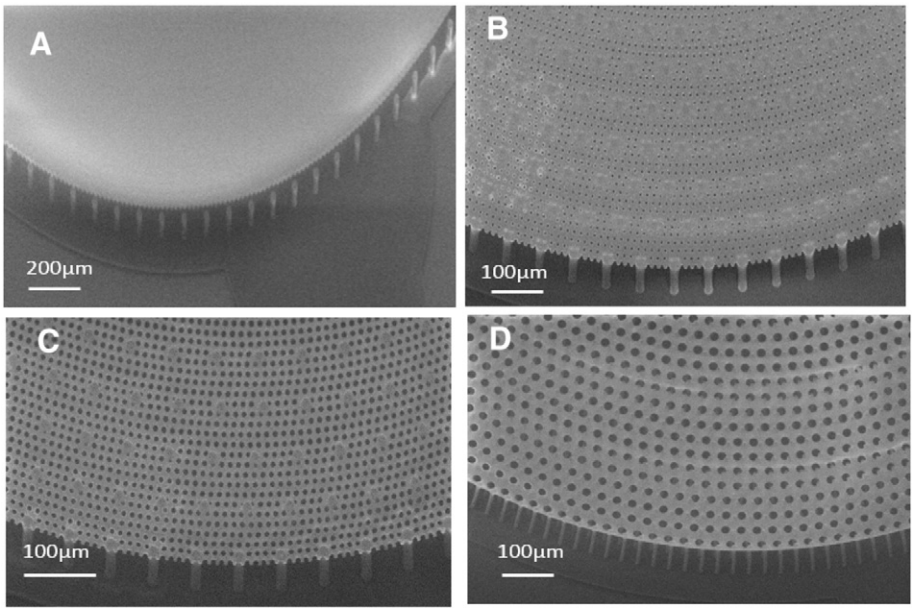

Fig. 4. Second partial UV exposure optimization with D_{313} (A) 10.50 mJcm^{-2} (B) 5.25 mJcm^{-2} and (C) and (D) 3.15 mJcm^{-2}.

layers with an exposure dose of 220.5 mJcm^{-2} (21 s of UV exposure). After development no SU-8 structures remained on the substrate. Next, the complete fabrication sequence illustrated in Fig. 3 was performed. Fig. 5 shows that suspended layers with a well-defined thickness of 17 µm were obtained for a large range of exposure dose D_{405}. Exposure doses of 105 mJcm^{-2} (Fig. 5.A) and 52.5 mJcm^{-2} (Fig. 5.B) resulted in overexposure and the mask (M_2) patterns were not replicated. For an exposure dose $D_{405} = 31.50$ mJcm^{-2} (3 s of UV exposure) well-defined suspended layers were fabricated.

With this fabrication process it is possible to define the pattern only in the mr-DWL polymer (suspended layer) without affecting the supporting SU-8 structures. The thickness of the suspended layer is defined by a spin coating step and the lithographic resolution of the suspended layer is defined by the UV exposure dose at 405 nm. This increases the processing window for patterning the suspended layer and allows independent tailoring of the two parameters.

4. Conclusion

Suspended SU-8 microstructures were fabricated with UV photolithography using two different wavelengths (313 nm and 405 nm). For the process using 313 nm, the optimized partial exposure dose $D_{313} = 3.15$ mJcm^{-2} for a low temperature baking process was used to fabricate a well-defined suspended layer with 5 µm suspended structures. This approach limited crosslinking to the top layer of the SU-8 film and increased the processing window for the exposure dose compared to earlier work performed with 365 nm [22]. However, simultaneous control of the thickness of the suspended microstructures was

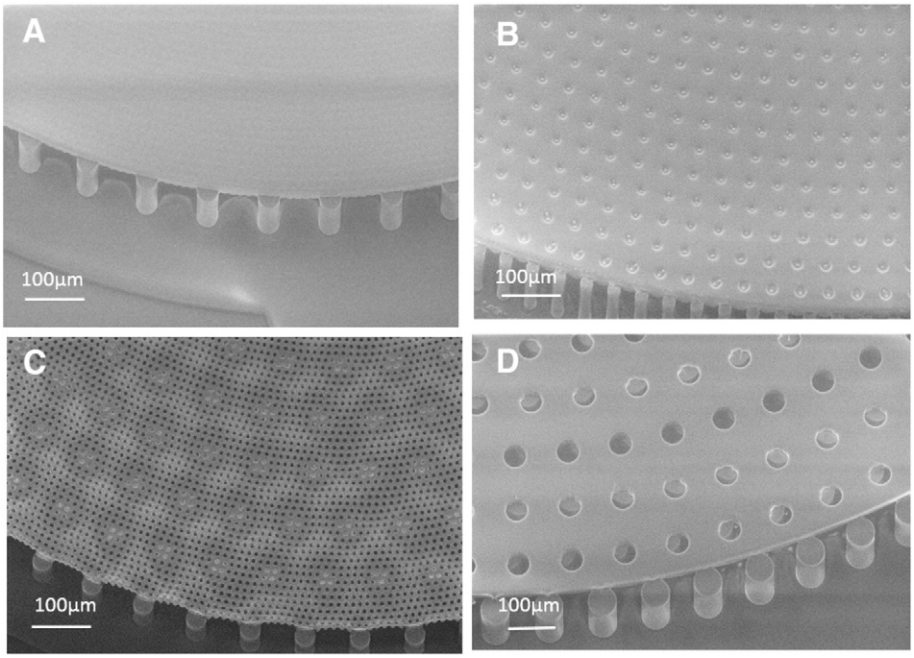

Fig. 5. Second UV exposure D_{405} optimization (A) 105 mJcm^{-2} (B) 52.5 mJcm^{-2} (C) and (D) 31.50 mJcm^{-2}.

impossible. To achieve this, a novel process using UV lithography at 405 nm was optimized after spin coating a layer of a second epoxy based photoresist mr-DWL 40. The filtering of the lower wavelengths was achieved by simply inserting a PMMA sheet in a standard UV aligner. The optimized exposure dose for well resolved microstructures on a mechanically stable suspended layer of mr-DWL was $D_{405} = 31.50\ mJcm^{-2}$. In conclusion, a change in wavelength and the introduction of an additional spin coating step allowed optimal control of both thickness and lateral resolution and thereby improved processing flexibility. In future work, the suspended SU-8 structures will be used as a polymer template for C-MEMS to fabricate 3D carbon microelectrode.

Acknowledgements

The authors acknowledge funding by the Young Investigator Program of the Villum Foundation, project no. VKR023438.

References

[1] L. Jiang, M. Zhang, J. Li, W. Wen, J. Qin, Simple localization of nanofiber scaffolds via SU-8 photoresist and their use for parallel 3d cellular assays, Adv. Mater. 24 (16) (2012) 2191–2195.
[2] N. Ferrell, J. Woodard, D. Hansford, Fabrication of polymer microstructures for MEMS: sacrificial layer micromolding and patterned substrate micromolding, Biomed. Microdevices 9 (6) (Oct. 2007) 815–821.
[3] M. Aguirregabiria, M. Tijero, M.T. Arroyo, J. Elizalde, J. Berganzo, I. Aranburu, F.J. Blanco, K. Mayora, A new SU-8 process to integrate buried waveguides and sealed microchannels for a Lab-on-a-Chip, Sensors Actuators B Chem. 114 (2006) 542–551.
[4] P. Abgrall, C. Lattes, V. Conédéra, H. Sato, H. Matsumura, S. Keino, An all SU-8 microfluidic chip with built-in 3D fine microstructures, J. Micromech. Microeng. 16 (2006) 2318–2322.
[5] S. Tuomikoski, S. Franssila, Free-standing SU-8 microfluidic chips by adhesive bonding and release etching, Sensors Actuators A Phys. 120 (2005) 408–415.
[6] P. Abgrall, C. Lattes, V. Conédéra, X. Dollat, S. Colin, A.M. Gué, A novel fabrication method of flexible and monolithic 3D microfluidic structures using lamination of SU-8 films, J. Micromech. Microeng. 16 (1) (Jan. 2006) 113–121.
[7] R. Martinez-Duarte, SU-8 photolithography as a toolbox for carbon MEMS, Micromachines 5 (3) (2014) 766–782.
[8] O.P. Parida, N. Bhat, Characterization of optical properties of SU-8 and fabrication of optical components, ICOP 2009-International Conf. Opt. Photonics CSIO, 2009 p. PS3. E.8.
[9] A. del Campo, C. Greiner, SU-8: a photoresist for high-aspect-ratio and 3D submicron lithography, J. Micromech. Microeng. 17 (6) (2007) R81–R95.
[10] V.J. Cadarso, K. Pfeiffer, U. Ostrzinski, J.B. Bureau, G.a Racine, A. Voigt, G. Gruetzner, J. Brugger, Direct writing laser of high aspect ratio epoxy microstructures, J. Micromech. Microeng. 21 (1) (2011) 17003.
[11] H. Sun, S. Kawata, Two-photon Photopolymerization and 3D Lithographic Microfabrication, Springer, US, 2004.
[12] Y. Ma, Y. Xia, J. Liu, S. Zhang, J. Shao, B.R. Lu, Y. Chen, Processing study of SU-8 pillar profiles with high aspect ratio by electron-beam lithography, Microelectron. Eng. 149 (2016) 141–144 January.
[13] Y. Lim, J.-I. Heo, H. Shin, Fabrication and application of a stacked carbon electrode set including a suspended mesh made of nanowires and a substrate-bound planar electrode toward for an electrochemical/biosensor platform, Sensors Actuators B Chem. 192 (2014) (2014) 796–803.
[14] F. Ceyssens, R. Puers, Creating multi-layered structures with freestanding parts in SU-8, J. Micromech. Microeng. 16 (6) (2006) S19–S23.
[15] J. Melai, V.M. Blanco Carballo, C. Salm, J. Schmitz, Suspended membranes, cantilevers and beams using SU-8 foils, Microelectron. Eng. 87 (5–8) (2010) 1274–1277.
[16] P. Abgrall, S. Charlot, R. Fulcrand, L. Paul, A. Boukabache, A.M. Gué, Low-stress fabrication of 3D polymer free standing structures using lamination of photosensitive films, Microsyst. Technol. 14 (8) (2008) 1205–1214.
[17] C. Wang, M. Madou, From MEMS to NEMS with carbon, Biosens. Bioelectron. 20 (10) (2005) 2181–2187 SPEC. ISS.
[18] M. Kitsara, M. Chatzichristidi, D. Niakoula, D. Goustouridis, K. Beltsios, P. Argitis, I. Raptis, Layer-by-layer UV micromachining methodology of epoxy resist embedded microchannels, Microelectron. Eng. 83 (4–9) (2006) 1298–1301 SPEC. ISS.
[19] Y. Lim, J.-I. Heo, M. Madou, H. Shin, Monolithic carbon structures including suspended single nanowires and nanomeshes as a sensor platform, Nanoscale Res. Lett. 8 (2013) 492.
[20] J.a. Lee, S.W. Lee, K.-C. Lee, S. Il Park, S.S. Lee, Fabrication and characterization of free-standing 3D carbon microstructures using multi-exposures and resist pyrolysis, J. Micromech. Microeng. 18 (3) (2008) 35012.
[21] M. Gaudet, J.C. Camart, L. Buchaillot, S. Arscott, Variation of absorption coefficient and determination of critical dose of SU-8 at 365 nm, Appl. Phys. Lett. 88 (2) (2006) 1–3.
[22] S. Hemanth, C. Caviglia, L. Amato, T.A. Anhøj, A. Heiskanen, J. Emnéus, S.S. Keller, Pyrolytic 3D carbon microelectrodes for electrochemistry, ECS Trans. 72 (1) (2016) 117–124.
[23] S. Keller, G. Blagoi, M. Lillemose, D. Haefliger, A. Boisen, Processing of thin SU-8 films, J. Micromech. Microeng. 18 (2008) 125020.
[24] T.A. Anhoj, A.M. Jorgensen, D.A. Zauner, J. Hubner, The effect of soft bake temperature on the polymerization of SU-8 photoresist, J. Micromech. Microeng. 16 (9) (Sep. 2006) 1819–1824.

Paper IV

3D suspended interdigitated carbon ultramicroelectrodes

Ioannis Mantis, Suhith Hemanth, Claudia Caviglia and Stephan Sylvest Keller

3D suspended interdigitated carbon ultramicroelectrodes

Ioannis Mantis [a], Suhith Hemanth [a], Claudia Caviglia [a], and Stephan Sylvest Keller [a]

[a]Department of Micro- and Nanotechnology, DTU Nanotech, 2800 Kongens Lyngby, Denmark

Abstract

This work presents the fabrication and characterization of 3D interdigitated pyrolytic carbon ultramicroelectrodes. The 3D interdigitated polymer template is pyrolyzed at 1100 ºC for 1 h in N_2 environment to obtain 3D carbon interdigitated ultramicroelectrodes (IDUME). A 3D interdigitated polymer template is fabricated by multiple steps of UV exposure of epoxy based resins. The suspended interdigitated microstructures were fabricated using a UV exposure at 405 nm wavelength. The mechanical stability and electrochemical performance of different designs of 3D IDUMEs were compared. The 3D IDUMEs were characterized by scanning electron microscopy (SEM) and optical microscopy, cyclic voltammetry (CV) and impedance spectroscopy (EIS). The electrochemical characterization shows the higher sensitivity (2 folds) for 3D IDUME compared to 2D IDE. Finally the 3D IDUMEs were used for 4-Aminophenol (4-AP) detection.

Keywords: Ultramicroelectrodes, 3D Pyrolytic carbon, Interdigitated electrodes, UV-photolithography

1. Introduction

Interdigitated electrodes (IDEs) have been used in many different applications such as bioelectrochemistry [1,2], chemical sensors [3], supercapacitors [4], and microbatteries [5]. IDEs offer several advantages, such as working with low volumes of sample, enhanced sensitivity and detection limits [6–9]. The IDEs are adventurous mainly in electrochemical application because of its increased surface area of the electrode. Furthermore, the small feature size of the IDEs facilitates the ultramicroelectrodes behavior [10]. IDUME exhibit various advantageous properties, for instance improved current densities, with even lower values of measured current and reduced double-layer capacitance [11]. They obtain steady-state current even in unstirred solutions which enables measurements performed for chemical and electrochemical kinetics analyses [12]. They achieve comparably higher scan-rate in voltammetry experiments and enable their application in media with higher resistivity [11]. Using IDUME, fast measurements are yielded through current-potential curves (CV) and less ohmic drop, interfacial capacitance and time constants are offered in electrochemical studies. Improved faradaic-to-charging current and signal-to-noise ratio achieve higher sensitivities [13,14]. Increasing current response of electrodes has been observed by increasing the overall surface area [13]. Due these advantages, numerous studies have been extensively focused on having an IDUME as working electrode in comparison with other simpler configurations [15].

Several fabrication techniques have been proposed to fabricate IDEs such as screen printing [16], inject printing [17] laser writing [18,19] and hot embossing [20,21]. These techniques are limited for fabricating planar (2D) electrodes which limits the overall sensitivity. The sensitivity of the electrode can be increased by increasing the surface area of the electrodes (i.e. 3D electrodes). Some of the fabrication techniques used for fabricating 3D IDE are 3D printing [22,23], electroplating [24] and carbon MEMS (C-MEMS) [25–31]. 3D printing lacks the resolution down to few micron and electroplating of metals on 3D substrate can lead to an expensive process. C-MEMS constitutes a cost-effective process and simple approach for fabrication of 3D carbon microelectrodes. . In this process, a polymer precursor is patterned using photolithography and subsequently the polymer precursor is transformed into pyrolytic carbon through high temperature treatment (900-1100 ^{o}C) in an inert atmosphere (N_2 or Ar) [33]. In comparison with other methods, it offers easier control of feature size, higher surface quality and structures with higher aspect ratios [32]. Different C-MEMS fabrication processes have been presented to obtain the polymer template such as e-beam [34], X-ray [35] and UV photolithography [36]. The latter one constitutes the most effective as it achieves high throughput, resolution in the micron or submicron scale.

Numerous attempts have been performed to fabricate carbon IDUMEs [37]. Several designs have been investigated by varying geometrical parameters [38–41]. Amato et al. fabricated pillars on top of fingers in the attempt to create 3D structures and achieve increased electrochemical response [42]. The same geometry was fabricated by Beidaghi and Agrawal et al. for energy storage applications [4]. Nevertheless, the results in the pre-mentioned works did not offer more complex 3D structures with suspended layer on top of the supporting pillars.

In this work, 3D carbon IDUMEs with suspended layer on supporting pillars are demonstrated for the first time. The 3D polymer template was fabricated by multiple UV exposure similar to the process described in our previous work [43]. The epoxy based photoresist (SU-8 and mr-DWL 40) was used to fabricate 3D polymer template with suspended interdigitated microstructures. The suspended layer (mr-DWL 40) was fabricated with a UV exposure at 405 nm wavelength which limits the crosslinking only to the mr-DWL 40. Optical imaging and SEM was used to evaluate the structural stability of carbon IDUMEs. Different designs of IDUME was fabricated by varying the fingers width (w), fingers pitch (Φ) and pillar diameter (d) to optimize the 3D carbon IDUMEs configuration. The fabricated 3D IDUME was also characterized electrochemically with cyclic voltammetry (CV) and electrochemical impedance spectroscopy (EIS).

2. Experimental section

2.1 Chip design

In this work, 2D and 3D IDE were designed and fabricated. The dimensions for each chip were chosen to be 21 mm and 10 mm for width and length, respectively (Figure 1.C). Figure 1.A presents IDE design being consisted of two combs with parallel fingers having symmetric gap among them and contact pads for electrical connection. In electrochemical measurements one comb was used as working (WE) and one as counter electrode (CE) (Figure 1.B). Only the area of the carbon fingers is being left exposed during electrochemical measurements through a window of 4 mm diameter (Figure 1.C).

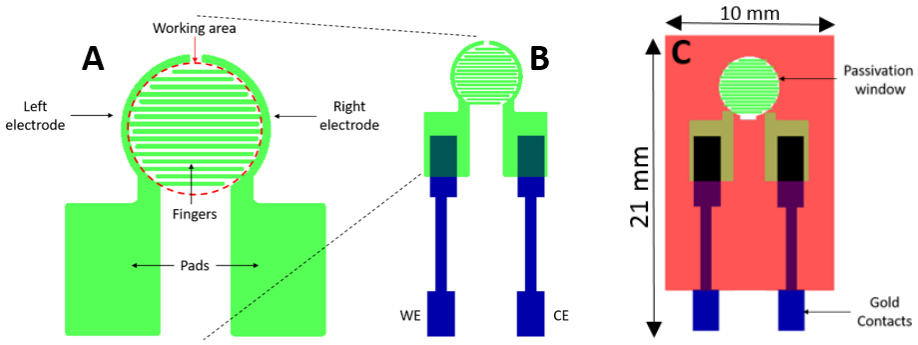

Figure 1 (A) Definition of different areas of interest on IDE design (B) Design of metal contacts (C) Design of passivation layer defining the working carbon area (D) Final fabricated micorchip

2. 2 3D polymer template fabrication

The schematic of fabrication process for fabricating 3D suspended polymer template is present in Figure 2. A 4-inch Si wafer is chemically cleaned with RCA to remove organic residues [44]. Subsequently, the wafer was thermally oxidized for 1.04 h with annealing time of 20 min achieving a SiO_2 layer of 604 nm (Figure 2.B), following by baking in an oven at 250 ^{o}C for 2 h to obtain higher dehydration.

3D polymer template was fabricated using three subsequent UV photolithographic processes. The 3D polymer template has three levels, first level is the fingers, pillars on fingers and a suspended layer created on the pillars.

The first lithographic process starts with SU-8 2035 spin coating (MicroChem, USA, Figure 2.C). The spinning consists of two steps, at 1000 rpm with 200 $rmps^{-1}$ for 10 s and at 5000 rpm with 1000 $rpms^{-1}$ for 120 s to spread the resist and defining the thickness (15 µm) respectively. This is followed by a soft-bake (SB) for 15 min at 50 ^{o}C on a programmable hotplate (Harry Gestigkeit GmbH, Germany) with a ramp of 2 $^{o}Cmin^{-1}$. Subsequently, the resist layer UV exposed with a dose of D_1 = 140 $mJcm^{-2}$ (Figure 2.D), followed by a post-exposure bake (PEB) for 2 h at 50 ^{o}C choosing the same ramp. The intensity of the UV light was set constant at 7 $mWcm^{-2}$ at 365 nm wavelength using an EVG620 aligner (EVGroup, Austria) equipped with a mercury lamp and a long pass SU-8 filter.

Subsequently a second layer of SU-8 2075 was spin coated (Figure 2.E) with three steps on top of the resist of the previous described lithographic step. Firstly, for 30 s at 700 rpm with 100 $rpms^{-1}$ and 60 s at 1600 rpm with 100 $rpms^{-1}$, followed by a third spinning for 30 s at 300 rpm to remove the edge bead by dispensing propylene glycol methyl ether acetate (PGMEA, mr-Dev 600, Dowanol™ PMA) resulting in a 100 µm thick SU-8. The liquid dispensed automatically with a mechanical arm at the edge of the wafer rotating at

100 $rpms^{-1}$ for 30 s. SB and PEB both for 5 h at 50 ^{o}C, with an UV exposure (UVE) step (Figure 2.F) in between performed again. The exposure dose was chosen at D_2 = 210 $mJcm^{-2}$.

The third layer of mr-DWL-40 photoresist (Microresist technology GmbH, Germany) is spin coated for 60 s at 4000 rpm with 100 $rpms^{-1}$ to get a 17 μm thick layer (Figure 2.G). SB performed for 1 h at 50 ^{o}C, followed by UV exposure (Figure 2.H) with an optimized exposure dose of D_3. Additional Poly(methyl methacrylate) filter (PMMA, NordiskPlast, Denmark) which has a constant intensity of 10.5 $mWcm^{-2}$ at 405 nm is added which also blocks the 365 nm wavelength. PEB followed with parameters chosen to be the same with the SB of this particular lithographic process.

Figure 2.I presents the cross-linked areas of polymer after exposure. The uncross-linked areas of resist were removed through development (Figure 2.J) by simple immersion in PGMEA in two steps of 15 min each. Any residues remaining was removed by isopropanol rinse and at the end of the process the wafers left to be dried at room temperature.

An additional flood exposure (FE) of two steps both with the same dose D_4 = 250 $mJcm^{-2}$ and a waiting time of 30 s among them took place without using any mask, followed by hard-baking (HB) for 15 h at 90 ^{O}C with ramp 2 $^{o}Cmin^{-1}$.

Fabrication of structures consisting only the first level (2D) follows the same described recipe until the PEB of this particular layer excluding the process steps formatting the next levels with pillars or suspended structures (Figure 2.A-D and Figure 2.I-J) The same approach is followed if electrodes consisting only with first level and supporting pillars ($2D_p$) are required (Figure 2.A-F and Figure 2 I-J).

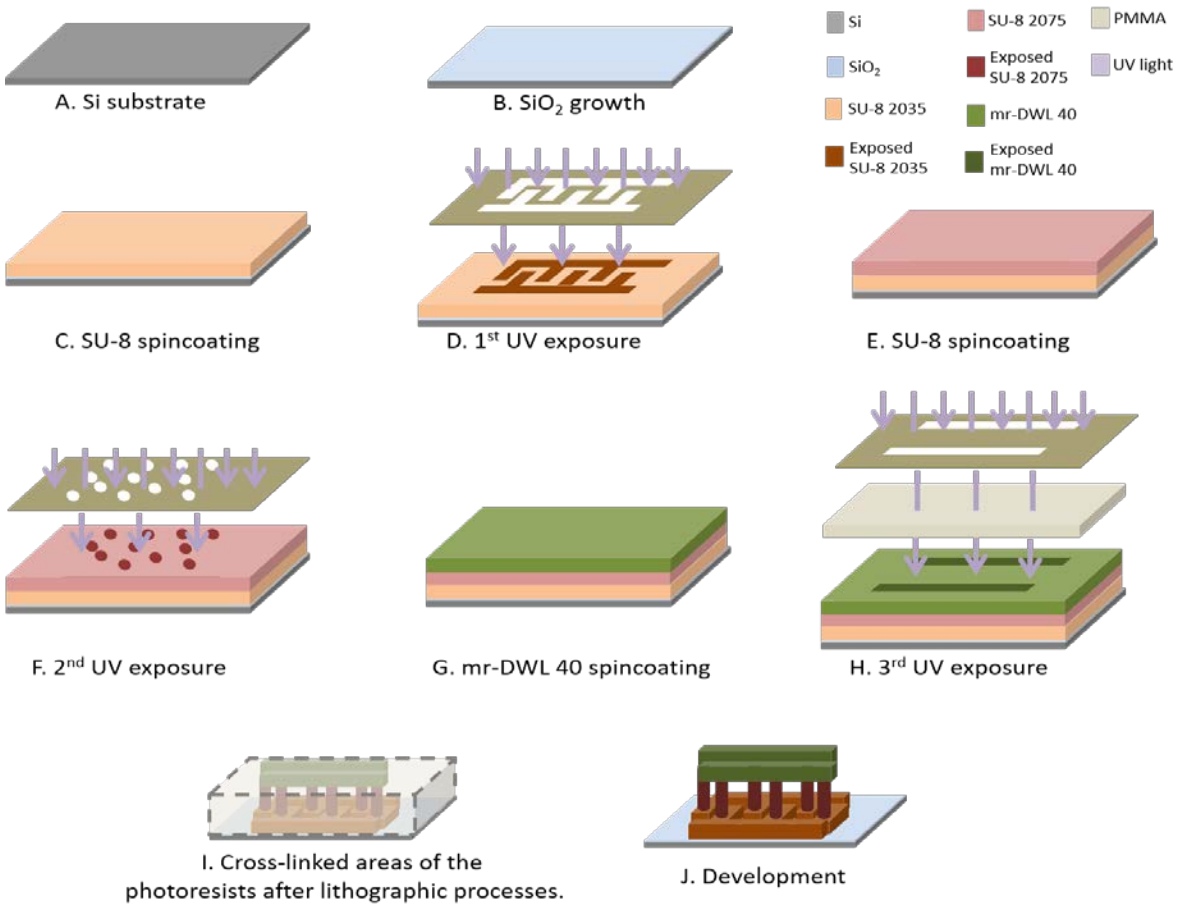

Figure 2 Schematic of photolithographic process of 3D polymer microfabrication (A) Initial Si wafer (B) Wet thermal oxidation (C) Spin coating of SU-8 2035 (D) Soft-bake, 1st UV exposure and post-bake (E) Spin coating of SU-8 2075 (F) 2nd UV exposure between a soft and post-bake step (G) Spin coating of mr-DWL 40 (H) 3rd UV exposure between a soft and post-bake step (I) Cross and uncross-linked areas of photoresist after exposure (J) Development in PGMEA

Table 1 Summarize of design dimensions for geometrical parts of 3D polymer templatesummarizes the five 3D polymer template designs selected for our study. ‘’C’’ indicates designs with suspended stripes connecting different fingers of the same comb (Figure 3.A). Accordingly, ‘’P’’ indicates design with suspended stripes connecting pillars of the same finger (Figure 3.B).

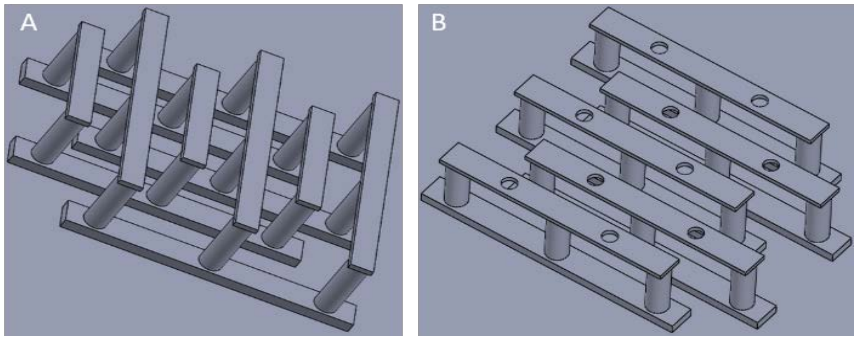

Figure 3 Different designs of suspended layer (A) strips connecting different fingers of the same comb(C) and (B)strips connecting pillars of the same finger (P)

Table 1 Summarize of design dimensions for geometrical parts of 3D polymer template

Design no.	2D finger		Pillars		Stripe in Suspended Layer		
	Width (µm)	Gap (µm)	Diameter (um)	Height (um)	Width (um)	Height (um)	Type
1	25	25	20	100	20	17	P**
2	25	25	20		10		C
3	100	100	50		50		P**
4	100	100	50		25		C
5	100	100	2x20*		10		C

* 2x20 indicates two pillars of 20 µm diameters placed in the same area of single pillars.

**Holes of 20 µm diameter was added on the stripes for ‘’P’’ design.

2.3 3D carbon IDUME

The carbon electrodes derived by pyrolysis (Figure 4) of photo-patterned polymer (Figure 2.J) structures at 1100 ^{O}C for 1h. An ATV PEO604 furnace (ATV Tech., Germany) was used with inert atmosphere (N_2) and a temperature ramp of 10 ^{O}Cmin^{-1}. After pyrolysis, oxygen plasma was performed targeting to remove carbon residues or other compounds between the electrode fingers. The duration of plasma treatment was optimized by keeping oxygen flow of 120 sccm and power of 500 W constant.

Figure 4 3D carbon microelectrode derived by pyrolysis of polymer template

2.4 IDUME chip

The gold (Au) and Chromium (Cr) were deposited through a shadow mask using E-Beam evaporation (Alcatel SCM 600 from Bittmann, Germany, Figure 5.A) which acts as contact leads and pads. A 20 nm of Cr is used for better adhesion layer for Au (thickness of 200 nm) on carbon and Si/SiO_2 substrate.

A passivation layer (PL) was created using the same concept of UV photolithography (Figure 5.B). PL is used to define the carbon working electrode region during electrochemical experiments. Initially, the wafers heated at 250 ^{o}C and SU-8 2005 is spin coated 2000 rpm for 2min to obtain a 5 μm thick layer. Afterwards, SB at room temperatures for 15 min and UV exposed in two steps with a wait time of 36 sec and exposure dose of D_5=250 mJcm^{-2} each. PEB took place for 1 h, followed by development with two steps of 5 min each. The fabricated chips were diced in an automatic dicing saw (Disco DAD321, US).

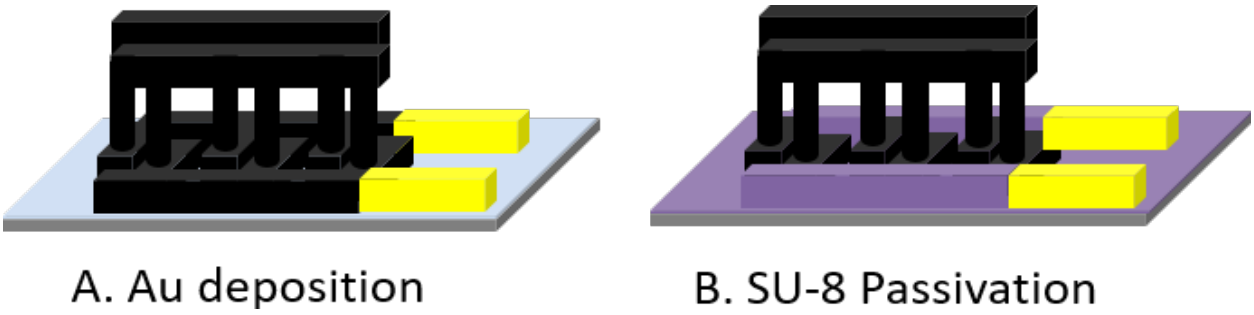

Figure 5 (A) Au deposition by E-Beam evaporation (B) Definition of carbon working area through passivation layer of SU-8

2.5 Characterization through imaging

The layer thicknesses was measured using a profilometer (Dektak 8 stylus). Three measurements were taken on three different chips (three different batches) at the same area of the electrode before and after pyrolysis. The topology, both of SU-8 and carbon microstructures, was studied through an optical microscope (Nikon ECLIPSE L200) and scanning electron microscope (SEM Zeiss Supra 40VP) for all designs to investigate the geometrical stability and the influence of the pyrolysis step. SEM images were captured in high and low vacuum (HV and LV) for carbon and polymer structures respectively. The polymer structures presented charging effects due to their conductive properties. This effect was reduced by choosing pressure for LV at17 mbar.

2.6 Electrochemical Characterization

For the electrochemical characterization, the electrode chips were placed in a self-aligning magnetic clamping batch system, fabricated using different layers of poly methyl methacrylate (PMMA) [45]. The experimental set-up is described in our previous works [45,46]. The electrochemical performance was evaluated through cyclic voltammetry (CV) in potassium ferri-ferrocyanide ($[Fe(CN)_6]^{4-}$/$[Fe(CN)_6]^{3-}$) as redox probe in a three-electrode system configuration. The carbon microelectrodes played the role of working and counter electrode. An external Ag/AgCl was used as reference electrode. CV was performed for all designs of 2D and 3D IDUMEs between -0.6 and 0.6 V and repeated for four different chips of each design. Subsequently, electrochemical impedance spectroscopy (EIS) was performed using a two-electrode

configuration (WE and CE). A sinusoidal potential of 10 mV was applied in the frequency range of 0.1-10^6 Hz at steps of 10 points/decade. Square wave voltammetry (SWV) was used for 4-Aphinomenol detection. A potentiostat (Autolab PGSTAT128N, Metronohm Autolab) was used for all electrochemical measurements. NOVA software was used to analyze the acquired data.

3. Results and discussion

3.1 UV exposure optimization (D_3)

According to Suhith et al. the fabrication of the suspended layer on a supporting pillars required an UV exposure dose of 31.5 mJ cm^{-2} [43]. An attempt to fabricate 3D suspended layer with this dose showed the need to further optimization for our microstructures of interest (Figure 6.A). The stripes in the suspended layer was mechanically unstable due to the lack of UV-exposure. Therefore, higher exposure dose of 52.5 mJ cm^{-2} (Figure 6.B) was tested. Fabrication results showed a well-defined and approximately identical microstructures.

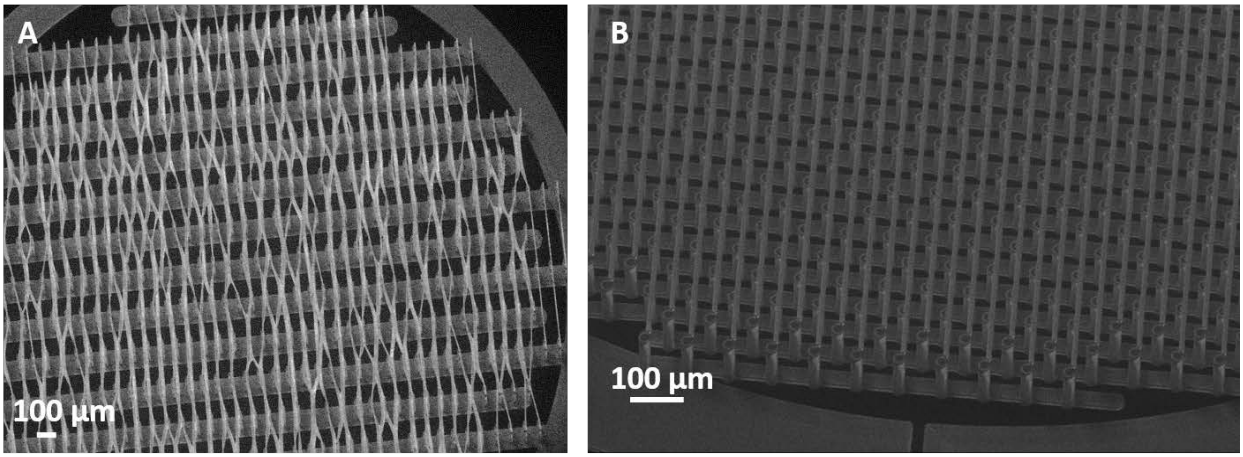

Figure 6 3D SU-8 microstructures fabricated with an exposure dose (D_3) of (A) 31.5 mJ cm^{-2} and (B) 52.5 mJ cm^{-2}

3.2 Plasma treatment optimization

Resistance measurements between two electrodes showed a significant change after plasma treatment. All values are available in supplementary information S1. The plasma treatment for 5 min enhanced the resistance values from kilo ohm (KΩ) to mega ohm (MΩ). Additional 10 min of plasma treatment increased resistance values to giga ohm (GΩ). Furthermore, additional 15 min of treatment did not show any

significant change in resistance. Therefore a plasma treatment of 15 mins is used to remove any residual carbon after pyrolysis and increase the resistance between two electrodes.

3.3 3D IDUME fabrication

Figure 7.A-B presents polymer templates of design 1 and design 2. The according structures after pyrolysis can be observed in Figure 7.D and E. Figure 7.C shows the 2D IDE with a figure width of 19 μm. Figure 7.F presents 5.2 μm stripes as the smallest feature in the suspended layer.

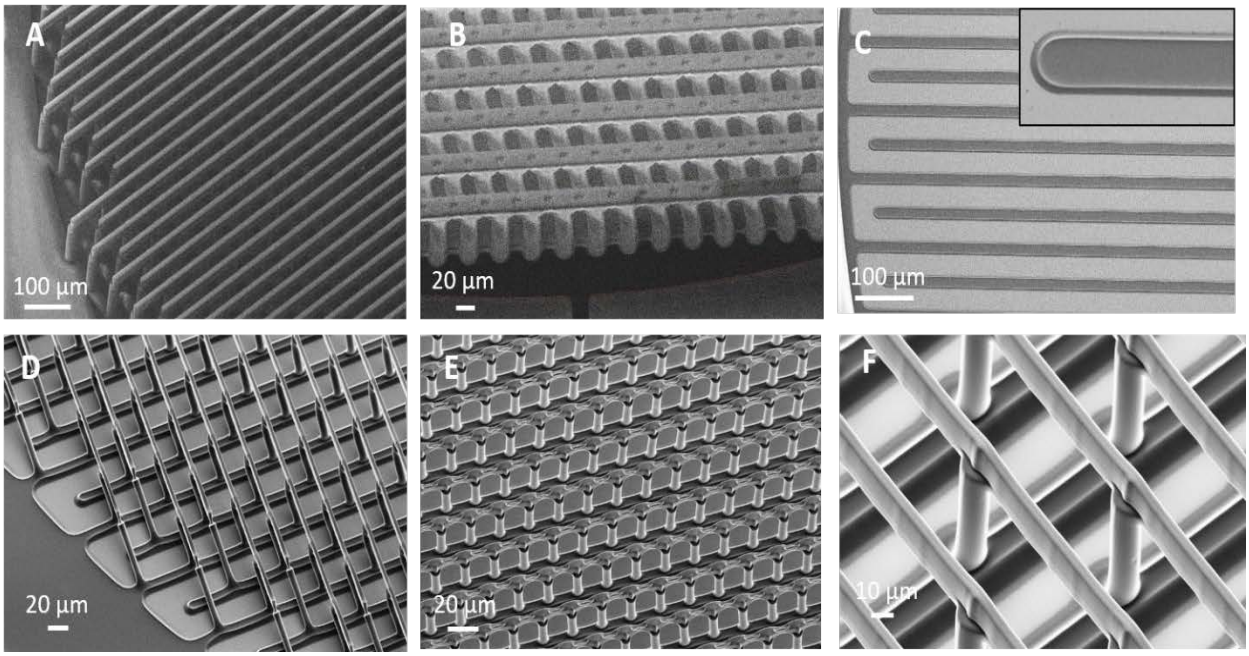

Figure 7 Carbon 3IDUME (A)-(B) Polymer structures of designs 1 and 2 respectively (C)-(E) 2D , Design 1 and 2 after pyrolysis (F) Stripe of 5.2 μm as the smallest feature of the suspended layer in this category

Figure 8.A, C and E shows the 3D suspended polymer template for design 3, 4 and 5 respectively. The corresponding carbon structures are shown in Figure 8.B, D and F. The structural topology of the 3D carbon structures found in accordance with the initial designs. The overall stability of the structures and the smallest feature of 5.2 μm width stripe in the suspended layer was fabricated with good mechanical stability. Additionally, under the same approach by increasing the number of the pillars, decreasing their diameter and using the same pitch among them, the durability of the system to support the suspended layer was not influenced (Figure 8.F).

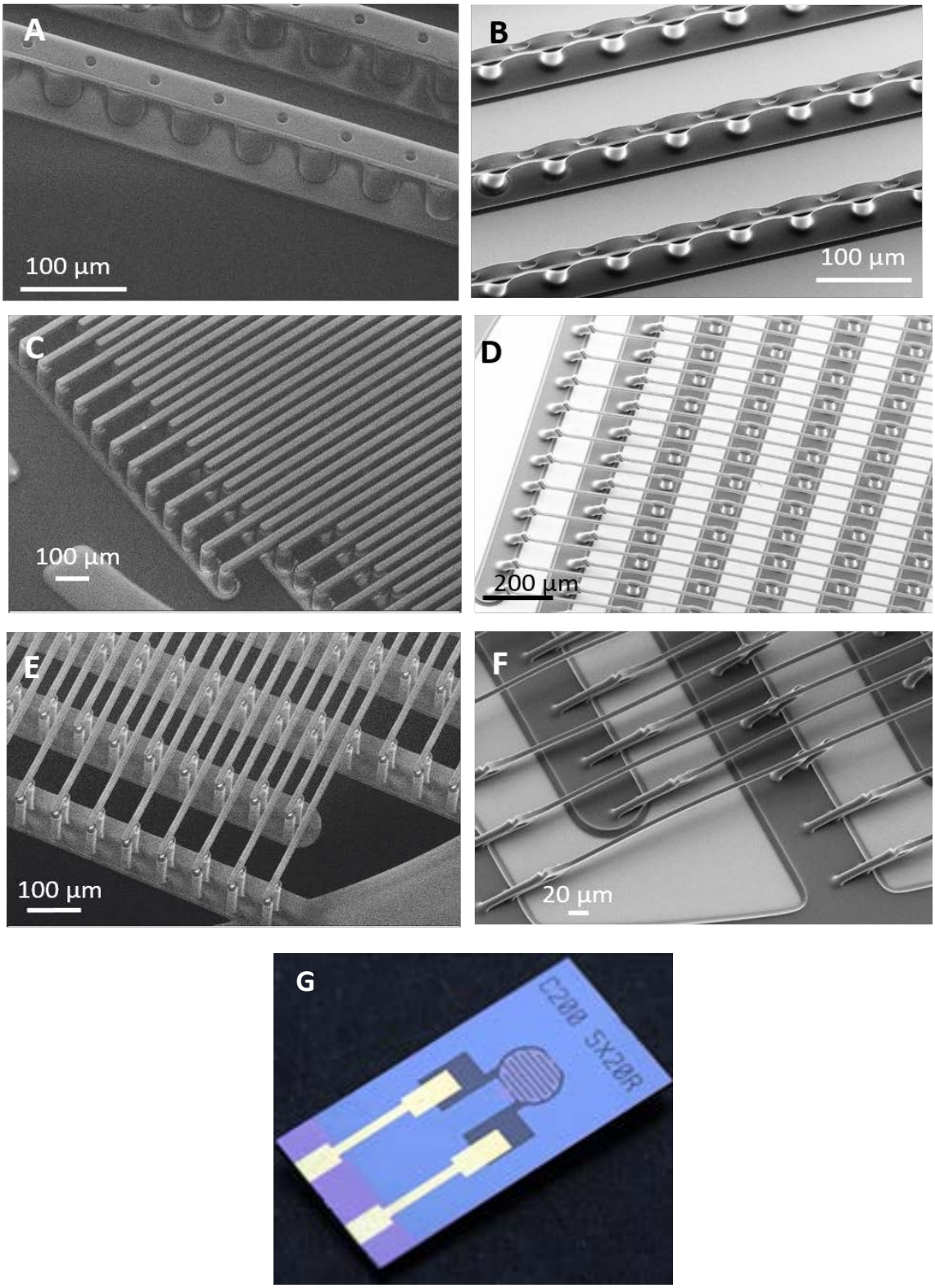

Figure 8: (A),(C) and (E) Polymer 3D structures of designs 3,4 and 5 respectively; (B),(D)and (F) 3D carbon microstructures of designs 3,4 and 5 respectively and (G) 2D IDE chip

Deviation of the initial designs can be observed only on pillars at the edges of the suspended layers. Increased stress during pyrolysis results in bending of the supporting pillars towards the direction where the stripes are extended (Figure 9.A-B). As it can be noticed, the inclination of the pillars does not introduce any contact with neighboring structural parts. The same reason causes stretching of the holes in design 1 and design 3 (Figure 9.C-D).

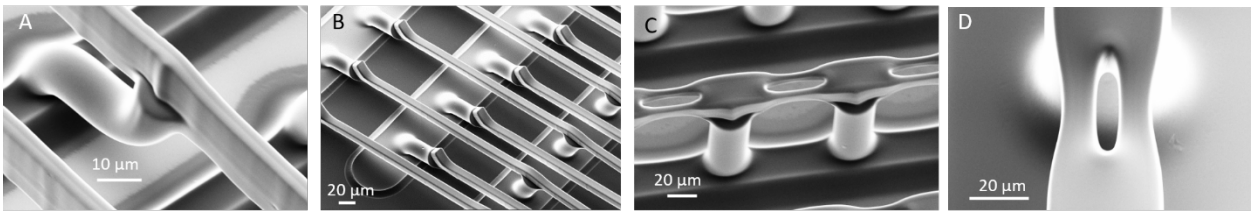

Figure 9 (A)-(B) Bending of pillars, with 20 and 50 μm diameter respectively, due to residual stresses (C)-(D) Streching of holes in the suspended layer for design 1 and design 3

3.4 3D carbon shrinkage analysis

During pyrolysis, chemical process of cyclization, condensation, isomerization and aromatization conclude reduction of the mass, driving the overall systems to undergo shrinkage [32,47]. This phenomenon should be investigated by recording differences in geometry before and after pyrolysis. In this study, dimensions of all three structural levels have been recorded. Specifically, width (W) of fingers in the first level, the diameter (D) and the height (Hp) of the pillars, widths of different stripes in the suspended layer and the height of the suspended layer (Hs). Figure 10 describe the dimensions before and after pyrolysis together with the shrinkage percentage (see supplementary information S2 for more information). Measurements of the geometrical aspects were taken through SEM images using Image-J software.

Figure 10 offers a quantitative evaluation of the shrinkage in all structural parts. In the ground level, fingers with 25 μm design width, found having shrinkage of 21.95 % (W1) after pyrolysis, value being considerably larger than the shrinkage of 7.89 % (W2) for fingers with larger width (100 μm). The same trend is observed for stripes with different widths in the suspended layer (W3-W6). For instance, stripes in the suspended layer having initial design width of 10 μm present shrinkage of 67.67 % (W3) larger than the values of shrinkage for the next smaller design width (W4). The same conclusion can be done again by comparing shrinkage between W4-W5 and W5-W6. Considering these observations, it can be concluded that structural parts with smaller values of widths undergo larger shrinkage during pyrolysis in comparison with larger widths. The same trend is observed for the height of various levels. All pillars having design height of 100 μm were experienced shrinkage of 60.32 % in comparison with 12.25 % for the height of the suspended layer.

Moreover, by comparing structural parts in various levels but with the same geometrical characteristic, different trend can be observed. Particularly, fingers of 25 μm in the first level undergo smaller shrinkage (W1) in comparison with stripes of the same width in the suspended layer (W5). This can be explained by the attachment of the one side of structural parts in the first level with the substrate, blocking contracting forces developed during pyrolysis.

Shrinkage of pillars' diameter found with comparable values between 40-50% in accordance with reported values in literature [42]. Additionally, shrinkage regarding the total height found again in agreement with previous studies approximately 50% [32].

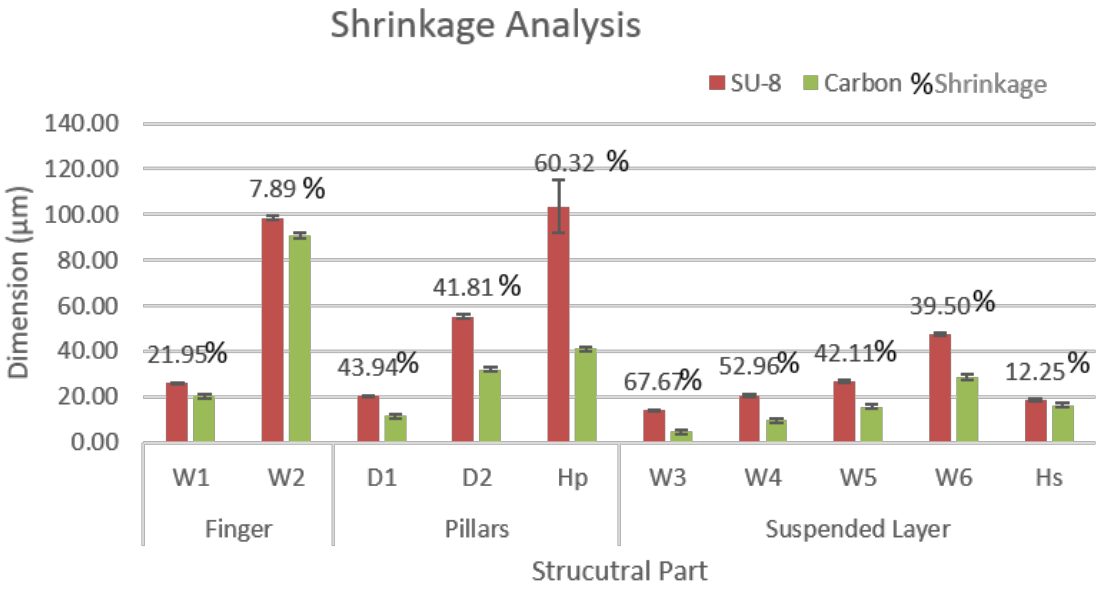

Figure 10 Shrinkage analysis for different strucutral parts(N =3)

3.5 Cyclic voltammetry (CV)

CV was performed on the all five designs of 3D IDMUE, 2D IDEs with pillars ($2D_p$) and 2D IDE in 10 mM $[Fe(CN)_6]^{4-}/[Fe(CN)_6]^{3-}$ in PBS with 100 mVs^{-1} scan rate (Figure 11.A). Creating more structural levels on a 2D configuration, for instance pillars or a suspended layer, the surface area is increased, thus the peak current. Figure 11 validates this aspect as the peak currents for voltammograms of 3D structures were found clearly higher ($I_{p(design1)}$ = 0.465 mA) than $2D_p$ (I_p = 0.234 mA) and 2D (I_p = 0.136 mA) electrodes. The voltammogram of 3D IDUME in ferri-ferrocyanide showed ultramicroelectrodes behavior except for design 3. Design 3 is described by an asymmetric peaks, a typical response in conventional microelectrodes. As the width is decreased, the current response is altered. Current peaks disappear and the

voltammogram obtains sigmoidal shape which is characteristic behavior of ultra-microelectrodes (Design 1, 2, 4 and 5). The shape of diffusion areas is influenced by the size of the electrode. As the size of the electrode is relatively reduced, transport of electrochemical species at the edge where the electrode meets the insulating material on the substrate is comparable with the diffusion across the electrode surface (edge effect), this results in a hemispherical diffusion profile. Hemispherical diffusion at the edges of microelectrodes enhances rates of mass transport of electroactive species, improving the overall diffusion current. Therefore, the plateau current is obtained for 3D carbon electrodes with design 1, 2, 4 and 5. The 3D IDUME with fingers width of 25 µm (Design 1 and 2) presented the highest peak current ($I_{p(design1)}$ = 0.465 mA), due to their higher electrode surface area. Therefore, only design 1 and 2 will be considered for all further analysis. No safe conclusion can be expressed on the performance between design 1 and design 2 3D IDUMEs. Even if IDUME of design 2 presented higher peak currents, the lower reproducibility indicated by the standard deviation doesn't allow a clear conclusion (Figure 11.B).

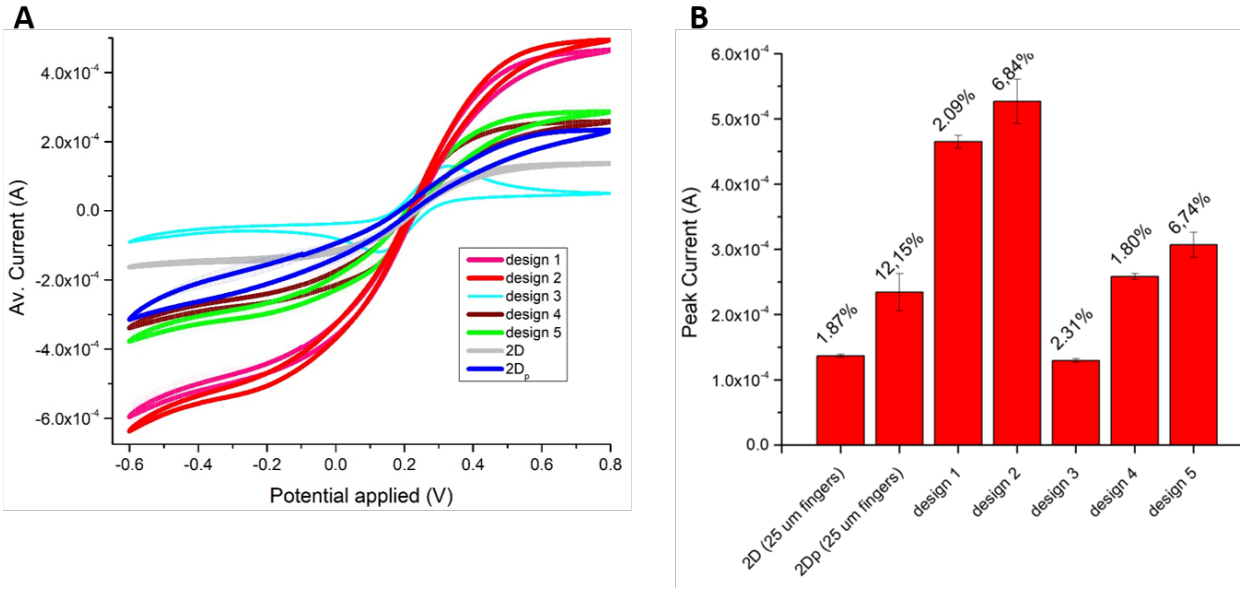

Figure 11 (A) Comparison of 2D(finger width = 25 µm), $2D_p$(finger width = 25 µm, pillar diameter = 20 µm) and 3D microelectrodes through CV (B) Peak current values for each design with SD (N=3)

In order to further characterize the electrochemical performance of the different 3D IDUME (Design 1 and 2), CV's with different concentrations of $[Fe(CN)_6]^{4-}/[Fe(CN)_6]^{3-}$e (1 mM, 2.5 mM, 5 mM, 7.5 mM, 10 mM). Representative voltammograms for each concentration for 3D IDUME, design 1 are shown in Figure 12.A. Voltammogram for design 2 is shown in supplementary information S3. Figure 12.B shows mean peak current values (N=3) of 2D (finger width 25 µm), design 1 and design 2 for all chosen concentrations (find slope and intersection of the plots in supplementary information S4). For all designs, the peak current recordings indicate linear relationship with increasing concentration in accordance with Randles-Sevcik equation [48]. Figure 12.B shows in general, higher signals for the 3D IDMUEs in comparison with 2D IDE

with the same dimensions of fingers. It is possible to identify to different sensitivity regions. Above 5 mM, the peak current values of 3D IDUME were found more than two times higher compared to the 2D IDE. Below 5 mM, the ratio was found less than two (1.88 for $3D_{design1}$/2D, 1.90 for $3D_{design2}$/2D).

By comparing the design 1 and design 2, a similar response is observed in detecting ferri-ferrocyanide for concentrations between 1 mM and 10 mM. The peak currents are considered the same, taking also into account the standard deviation in the measurements. Distinct difference is only present for the highest concentration of 10 mM. The lowest concentration detected was 1 mM. The sensitivity for design 1, design 2 and 2D electrodes were found to be 38.92 μA mM^{-1},42.23 μA mM^{-1} and 14.51 μA mM^{-1} respectively, using the slope of each fitting in Figure 12.B.

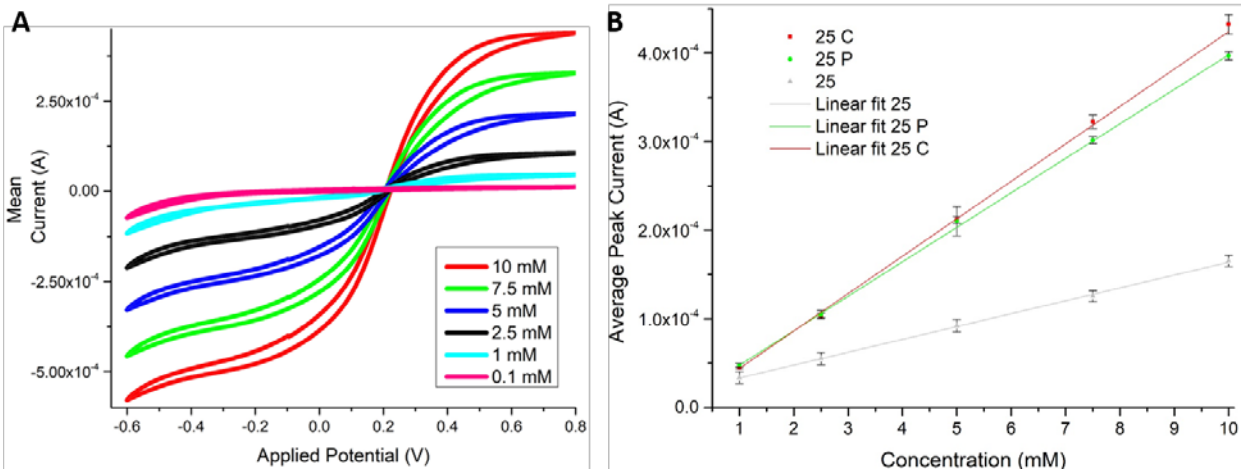

Figure 12 CV for different concentrations of ferri-ferrocyanide (A) Voltammograms of 3D IDMUE (design 2) (B) Peak current recordings for investigated designs

To further characterize the IDEs electrochemical behavior, cyclic voltammograms of 3D IDUME (design 2) were recorded (Figure 13.A) with different scan rates (10 mVs^{-1}, 15 mVs^{-1}, 25 mVs^{-1}, 50 mVs^{-1}, 100 mVs^{-1}, 200 mVs^{-1}, 500 mVs^{-1}, 750 mVs^{-1}, 1000 mVs^{-1}, 1500 mVs^{-1}) using 10 mM of the redox probe $[Fe(CN)_6]^{4-}$/$[Fe(CN)_6]^{3-}$ in PBS. Figure 13.B demonstrates the relationship between peak currents and square root of scan rates for 3D microelectrodes with design 1, design 2 and 2D IDE (25 μm fingers). Linear fit was achieved for the recorded peak current values. Both designs of 3D microelectrodes present higher values of peak current for all scan rates in comparison with the 2D, validating the improved performance due to increased surface area. Related parameters for all fittings are available in supplementary information S5.

By observing the voltammograms response, different behaviors in electrochemical response was identified between higher and lower scan rates. At scan rates below 500 mVs^{-1}, the linear diffusion transits to radial diffusion (or nonlinear diffusion), and consequently, a steady state was attained. Figure 13 .B shows the

limiting current was almost constant in the scan rate range from 10 to 100 mVs^{-1} (CVs in shown in supplementary information S6) due to the radial diffusion, which is characteristic of ultramicroelectrode arrays. At scan rates above 500 mVs^{-1}, linear diffusion dominates within individual electrodes and a broad peak shaped cyclic voltammogram curve was obtained (Figure 13.A), indicative of the Cottrel state [49]. In Figure 13 .B, the limiting current was increased linearly with increases in the scan rate for scan rates after the transitory behavior observed between 100 mVs^{-1} and 500 mVs^{-1}, as described by the Randles-Sevcik equation. This is typical of macroelectrodes or conventionally sized electrodes due to the diminution of the diffusion layer thickness when compared with the dimensions of the microelectrodes.

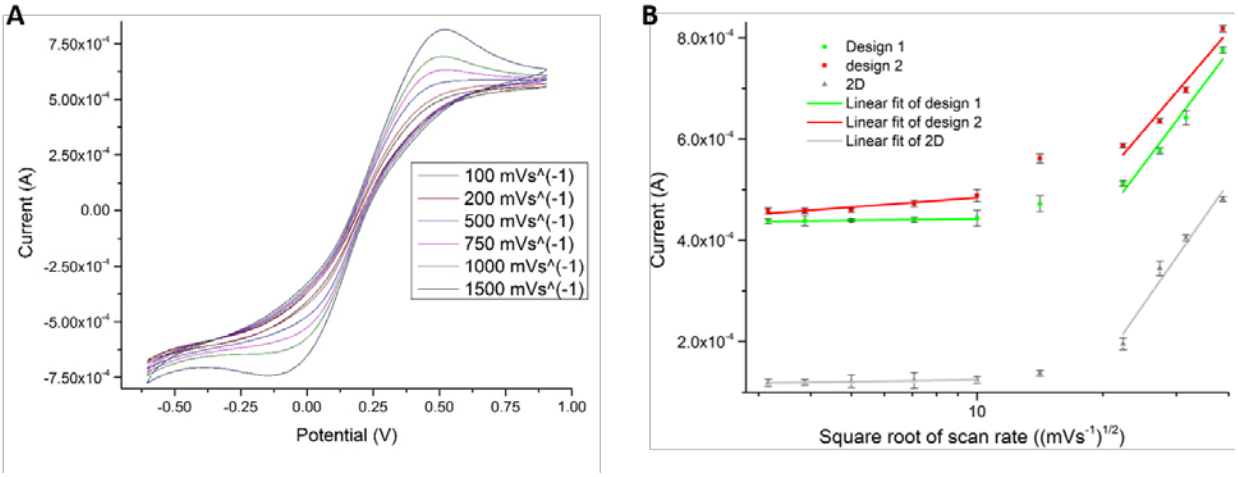

Figure 13 CVs for different scan rates in 10 mM of ferri-ferrocyanide (A) Voltammograms of 3D IDUME (design 2) (B) Peak current recordings for investigated designs

3.6. Electrochemical impedance spectroscopy (EIS)

EIS allows for further characterization of the carbon microelectrodes and it is a useful tool to understand the properties of an entire electrochemical set-up including electrode material properties and external interfacing instrumentations [50]. Figure 14 shows the Nyquist plot for 2D IDE and 3D IDUME (design 1 and 2) with the standard deviation (N = 3 chips). The semi-circle in the Nyquist plot determines the charge transfer resistance (R_{ct}) or the resistance on the electrode surface. It is clear from Figure 14 that the 3D IDUME (design 2) has the least R_{ct}. This is mainly due to the increased surface area which is also shown in CVs.

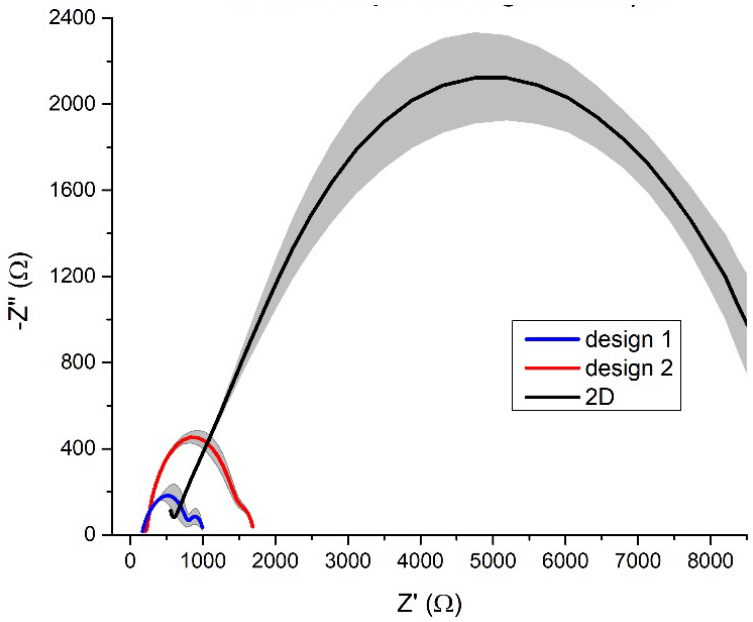

Figure 14: EIS spectra of 2D and 3D IDUME (design 1 and 2)

3.7 4-Aphinomenol (4-AP) detection

4-AP has been widely used in various fields, such as medicine, sulfur and azo dyes, petroleum industry, and photography [51]. It can be formed by the degradation of paracetamol and its analogs in the human body and during storage [51]. 4-AP is toxic and irritable to the eyes, skin and respiratory system, and the target sites of 4-AP in the body are blood and the kidneys [51]. EU Directive 2455/2001/EC sets a maximum concentration of 0.5 μgL^{-1} in drinking water and their individual concentration should not exceed 0.1 μgL^{-1} [52]. Therefore, as 4-AP is both biochemically and environmentally hazardous, the determination of trace amounts of 4-AP in matrices such as water, pharmaceutical formulations and human fluids, is important.

Square wave voltammetry (SWV) was chosen for the electrochemical detection of 4-AP as it is more sensitive compared to other voltammetric techniques [53]. Different concentrations (100 μM, 50 μM, 25 μM, 12.25 μM, 6.125 μM, 3.0625 μM) of 4-AP were chosen for electrochemical detection. Figure 15.A presents current responses for 4-Aphinomenol detection. The lowest detection limit found 3.0625 μM. Figure 15.B demonstrates increase of peak current values with increasing concentration of 4-AP. 3D IDUME (design 2) presented improved performance of detection for all values of concentration in comparison with the 2D IDE. The difference in detection ability among the two geometries converges in the lowest concentrations of 4-AP. Linear fitting observed only among specific values in the chosen range of concentrations. The sensitivity of 3D IDUME was calculated to be 1.48 $\mu A\ \mu M^{-1}$ and 0.46 $\mu A\ \mu M^{-1}$ for concentration range between 1 μM -12.25 μM and 25 μM-100 μM respectively (0.07 $\mu A\ \mu M^{-1}$ for 2D system). This

electrochemical analysis validates the advantage of using 3D IDUME. Parameters related with the fitting of the experimental data are available in supplementary information S7.

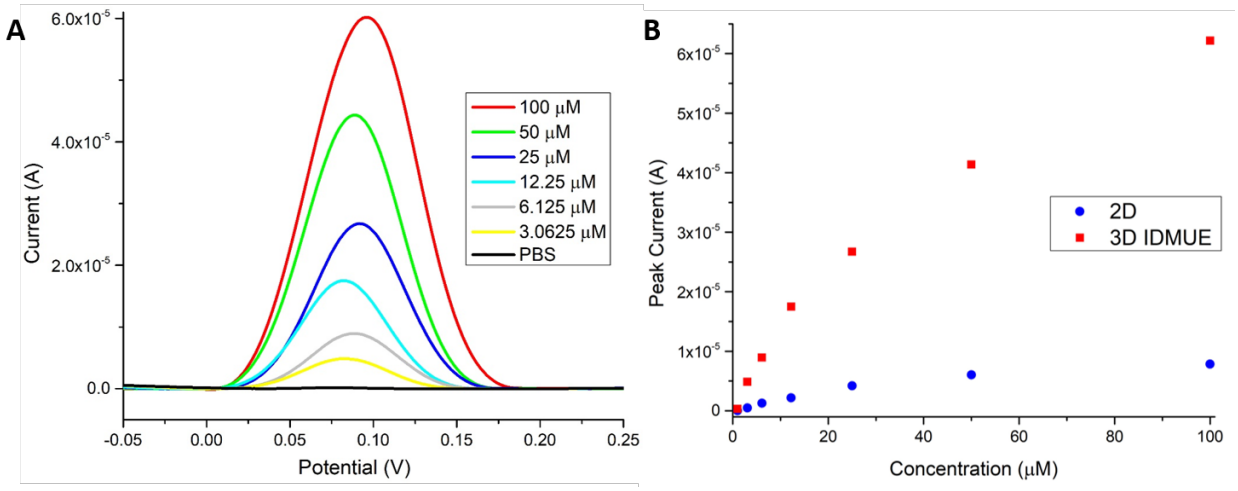

Figure 15 (A) Electrochemical detection of 4-AP using SWV using100 µM-1 µM range of concentrations (B) Peak current recordings of 2D IDE and 3D IDMUE (design 2) for different concentrations

4. Conclusion

The 3D IDUME was successfully fabricated and characterized. The fabrication process to fabricate suspended layers on micropillars was optimized. The optimized UV exposure dose to fabricate a well resolved suspended layer was D_3 = 52.5 mJ cm^{-2}. Five different designs of 3D IDUME was evaluated for mechanical stability and electrochemical performance (higher I_p and lower R_{ct}). All five design shows high mechanical stability after pyrolysis. Design 1 and 2, resulted in higher I_p during CVs, due to their higher surface areas. 3D IDUME was also compared to 2D IDE for electrochemical performance. 3D IDUME gave a higher signal (2 folds) then 2D IDEs. EIS analysis also showed the lesser resistance on the 3D IDUME when compared to 2D IDE. 3D IDUMEs and 2D IDEs were successfully used for 4-AP detection using SWV. 3D IDUME gave a higher signal (~ 2 folds) when compared to 2D IDEs.

Reference

1. Mamas I.Prodromidis. Impedimetric immunosensors—A review. *Electrochim. Acta* 55, 4227–4233 (2010).
2. R.Ehret *et al.* Monitoring of cellular behaviour by impedance measurements on interdigitated electrode structures. *Biosens. Bioelectron.* 12, 29–41 (1997).
3. Arshak, K., Moore, E., Lyons, G. M., Harris, J. & Clifford, S. A review of gas sensors employed in electronic nose applications. *Sens. Rev.* 24, 181–198 (2004).
4. Agrawal, R., Beidaghi, M., Chen, W. & Wang, C. Carbon microelectromechanical systems (C-MEMS) based microsupercapacitors. *Proc. SPIE - Int. Soc. Opt. Eng.* 9493, 1–7 (2015).
5. Sun, K. *et al.* 3D Printing of Interdigitated Li-Ion Microbattery Architectures. *Adv. Mater.* 25, 4539–4543 (2013).
6. Van Gerwen, P. *et al.* Nanoscaled interdigitated electrode arrays for biochemical sensors. in *Proceedings of International Solid State Sensors and Actuators Conference (Transducers '97)* 2, 907–910 (IEEE).
7. M.Kitsara *et al.* Single chip interdigitated electrode capacitive chemical sensor arrays. *Sensors Actuators B Chem.* 127, 186–192 (2007).
8. Dam, V. A. T., Olthuis, W. & van den Berg, A. Redox cycling with facing interdigitated array electrodes as a method for selective detection of redox species. *Analyst* 132, 365 (2007).
9. Sunil Rana, Robin H Page & Calum J McNeil. Impedance spectra analysis to characterize interdigitated electrodes as electrochemical sensors. *Electrochim. Acta* 56, 8559–8563 (2011).
10. Yang, X. The voltammetric performance of interdigitated electrodes: Computation and experimentation. (University of Georgia, 2008).
11. Orozco, J., Fernández-sánchez, C. & Jiménez-jorquera, C. Ultramicroelectrode Array Based Sensors: A Promising Analytical Tool for Environmental Monitoring. *Sensors* 10, 475–490 (2010).
12. Aoki, K. J. Theory of ultramicroelectrodes. *Electroanalysis* 5, 627–639 (2017).
13. Xie, X. Assessment of an ultramicroelectrode array (UMEA) sensor for the determination of trace concentrations of heavy metals in water. (Universität Karlsruhe, 2004).
14. Andrieux, C. P., Garreau, D., Hapiot, P., Pinson, J. & Saveant, J. . Fast sweep cyclic voltammetry at ultra-microelectrodes. *Electroanal. Chem* 243, 321–335 (1988).
15. Grover, W. H. Interdigitated Array Electrode Sensors : Their Design , Efficiency , and Applications. *Honors thesis , University of Tennessee* 3, (1999).
16. Dubourg, G., Segkos, A., Katona, J. & Radovi, M. Miniaturized Humidity Sensors Using Screen-Printed TiO2 Nanoparticles as Sensitive Layer. *Sensors* 17, 1854 (2017).
17. Zou, Z., Kai, J., Rust, M. J., Han, J. & Ahn, C. H. Functionalized nano interdigitated electrodes arrays on polymer with integrated microfluidics for direct bio-affinity sensing using impedimetric measurement. *ScienceDirecct* 136, 518–526 (2007).
18. Electrochemical, A., June, S. L. & Kostecki, R. Fabrication of Interdigitated Carbon Structures by Laser Pyrolysis of Photoresist. *Electrochem. Solid-State Lett.* 3–6 (2002). doi:10.1149/1.1473256
19. El-kady, M. F. & Kaner, R. B. Scalable fabrication of high-power graphene micro-supercapacitors for flexible and on-chip energy storage. *Nat. Commun.* 4, 1475–1479 (2013).
20. Schift, H., David, C. & Gobrecht, J. Nanostructuring of polymers and fabrication of interdigitated electrodes by hot embossing lithography. *Microelectron. Eng.* 46, 121–124 (1999).
21. Gobrecht, J. Hot embossing in polymers as a direct way to pattern resist. *Microelectron. Eng.* 41/42, 575–578

(1998).

22. Liu, C. *et al.* Fabrication and Characterization of 3D-Printed Highly-Porous 3D LiFePO4 Electrodes by Low Temperature DirectWriting Process. *Materials (Basel).* 10, 934 (2017).

23. Zhao, C., Wang, C. & Beirne, S. Three dimensional (3D) printed electrodes for interdigitated supercapacitors. *Electrochem. commun.* 41, 20–23 (2014).

24. Kashimura, Y., Nakashima, H., Furukawa, K. & Torimitsu, K. Fabrication of nano-gap electrodes using electroplating technique. *Thin Solid Films* 438–439, 317–321 (2015).

25. Malladi, K., Wang, C. & Madou, M. Fabrication of suspended carbon microstructures by e-beam writer and pyrolysis. *Carbon N. Y.* 44, 2602–2607 (2006).

26. Volder, F. L. De *et al.* Hierarchical Carbon Nanowire Microarchitectures Made by. *ACSNano* 5, 6593–6600 (2011).

27. Lee, J. A., Lee, S. W., Lee, K., Park, S. Il & Lee, S. S. Fabrication and characterization of freestanding 3D carbon microstructures using multi-exposures and resist pyrolysis. *J. Micromechanics Microengineering* 18, 35012 (2008).

28. Mardegan, A. *et al.* Optimization of Carbon Electrodes Derived from Epoxy-based Photoresist. *J. Electrochem. Soc.* 160, 132–137 (2013).

29. Beidaghi, M. & Wang, C. Micro-supercapacitors based on three dimensional interdigital polypyrrole/C-MEMS electrodes. *Electrochim. Acta* 56, 9508–9514 (2011).

30. Beidaghi, M., Chen, W. & Wang, C. Electrochemically activated carbon micro-electrode arrays for electrochemical micro-capacitors. *J. Power Sources* 196, 2403–2409 (2011).

31. Wang, C. & Madou, M. J. Fabrication and properties of a carbon / polypyrrole three-dimensional microbattery. *J. Power Sources* 178, 795–800 (2017).

32. Hemanth, S., Caviglia, C. & Keller, S. S. Suspended 3D pyrolytic carbon microelectrodes for electrochemistry. *Carbon N. Y.* 121, 226–234 (2017).

33. Hemant, S. *et al.* Pyrolytic 3D Carbon Microelectrodes for Electrochemistry. *E C S Trans. ,The Electrochem. Soc.* 72, 117–124 (2016).

34. Mcintosh, K. A. *et al.* Terahertz photomixing with diode lasers in low-temperature-grown GaAs. *App. Phys. Lett.* 67, 3844–3846 (1995).

35. Ehrfeld, W. & Lehr, H. Deep X-ray lithography for the production of three-dimensional microstructures from metals, polymers and ceramics. *Radiat. Phys. Chem.* 45, 349–365 (1995).

36. Heo, J. I. *et al.* Carbon Interdigitated Array Nanoelectrodes for Electrochemical Applications. *J. Electrochem. Soc.* 158, J76–J80 (2011).

37. Basha, C. A. & Rajendran, L. Theories of Ultramicrodisc Electrodes : Review article. *Int. J. Electrochem. Sci.* 1, 268–282 (2006).

38. Polcari, D. *et al.* Fabrication of Carbon, Gold, Platinum, Silver, and Mercury Ultramicroelectrodes with Controlled Geometry. *Anal. Chem.* 87, 2565–2569 (2015).

39. Feeney, R. & Samuel, P. Microfabricated Ultramicroelectrode Arrays : Developments , Advances , and Applications in Environmental Analysis. *Electroanalysis* 12, 9 (2000).

40. Boron, M. & Nanocrystalline, D. Multichannel Boron Doped Nanocrystalline Diamond Ultramicroelectrode Arrays: Design, Fabrication and Characterization. *Sensors* 12, 7669–7681 (2012).

41. Kamath, R. R. & Madou, M. J. Three-Dimensional Carbon Interdigitated Electrode Arrays for Redox-Ampli fi cation. *Anal. Chem.* 86, 2963–2971 (2014).

42. Amato, L. *et al.* Dense high-aspect ratio 3D carbon pillars on interdigitated microelectrode arrays. *Carbon N. Y.* 94, 792–803 (2015).

43. Suhith Hemanth, Thomas A.Anhøj, Claudia Caviglia & Stephan S.Keller. Suspended microstructures of epoxy based photoresists fabricated with UV photolithography. *Microelectron. Eng.* 176, 40–44 (2017).

44. Kern, W. The Evolution of Silicon Wafer Cleaning Technology. *J. Electrochem. Soc.* 137, (1990).

45. S. Hemanth, C. Caviglia, L. Amato, T.A. Anhøj, A. Heiskanen, J. Emnéus, S. S. K. Pyrolytic 3D Carbon Microelectrodes for Electrochemistry. *ECS Trans.* 72, 117–124 (2016).

46. Hassan, Y. M. *et al.* High temperature SU-8 pyrolysis for fabrication of carbon electrodes. *J. Anal. Appl. Pyrolysis* 125, 91–99 (2017).

47. Natu, R., Islam, M. & Martinez-Duarte, R. Shrinkage Analysis of Carbon Micro Structures Derived from SU-8 Photoresist. *ECS Trans.* 72, 27–33 (2016).

48. McCreery, R. L. Electroanalytical chemistry. *Marcel Dekker, Inc., New York* 17, 221–374 (1991).

49. Bard & Allen, J. *Electrochemical methods: fundametals and applications*. (Wiley, 1980).

50. Bard, A. J. & Faulkner, L. R. *Electrochemical methods : fundamentals and applications*. (Wiley, 2001).

51. Wang, J., Shi, Z., Jin, J. & Liu, Q. Determination of 4-aminophenol using a glassy carbon electrode modified with a three-dimensionally ordered macroporous film of polycysteine. *Microchim Acta* 823–829 (2015). doi:10.1007/s00604-014-1393-4

52. Yadav, D. K. & Harjit, J. Determination of phenol compounds in waste water by using compelling agent : N-Phenyl-benzoic-hydroxamic acid. *J. Appl. Chem.* 7, 6–12 (2014).

53. Ozkan, S. A. The analytical application of square wave voltammetry on pharmaceutical analysis The Analytical Applications of Square Wave Voltammetry on Pharmaceutical. *Open Chem. Biomed. Methods J.* 3, 56–73 (2010).

Supplementary Information

S1 Plasma optimization after pyrolysis

Design no.	Resistance			
	Before plasma	After plasma		
		5 min (MΩ)	10 min (GΩ)	15 min (GΩ)
1	KΩ	325	1.4	1.42
2		478	1.2	1.25
3		256	1.5	1.51
4		542	1.5	1.52
5		468	1.3	1.35

S2 Shrinkage analysis

	Finger		Pillars			Suspended Layer				
	W_1	W2	D1	D2	Hp	W3	W4	W5	W6	Hs
SU-8	25.96	98.50	20.43	55.18	103.60	14.08	20.75	26.94	47.43	18.59
Carbon	20.26	90.73	11.45	32.11	41.11	4.55	9.76	15.59	28.69	16.31
Shrinkage (%)	21.95	7.89	43.94	41.81	60.32	67.67	52.96	42.11	39.50	12.25

S3 CV for design 2 with different concentrations

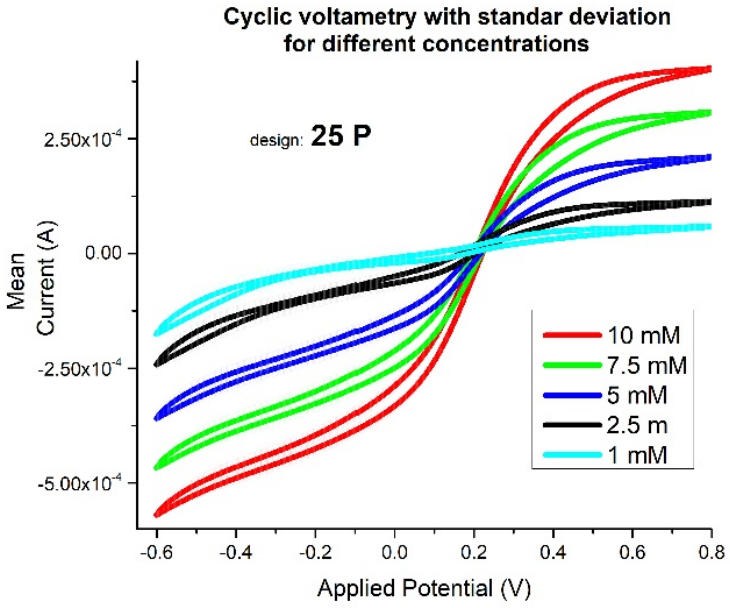

S4 Linear fitting of current values obtained from different concentrations

Equation		y=a+b*x					
Weight		Instrumental					
Design		Design 2		Design 1		2D	
Residual sum of squares		2.9738		0.36126		0.17478	
Pearson's r		0.99963		0.99997		0.99966	
Adj. R-Square		0.99901		0.99993		0.9991	
		Value	Standard Error	Value	Standard Error	Value	Standard Error
Mean	Intercept	1.83616E-6	1.58839E-6	8.76738E-6	7.36499E-7	1.88652E-5	1.37268E-6
	Slope	4.22382E-5	6.65261E-7	3.89272E-5	1.61738E-7	1.45148E-5	2.17332E-7

S5 Linear fitting of current values obtained from different scan rates

Design 1						
	Low concentration region			**High concentration region**		
Equation	y = a + b*x			y = a + b*x		
Weight	Instrumental			No Weighting		
Residual Sum of Squares	0.01301			1.21991E-9		
Pearson's r	0.97677			0.98376		
Adj. R-Square	0.93878			0.95167		
		Value	Standard Error		Value	Standard Error
Mean	Intercept	4.33036E-4	8.20474E-7	Intercept	-9.85607E-4	2.08392E-4
	Slope	9.19158E-6	1.16415E-6	Slope	0.0011	1.41633E-4

Design 2					
		Low concentration region		**High concentration region**	
Equation		y = a + b*x			
Weight		No Weighting			
Residual Sum of Squares		8.64687E-11		1.30443E-9	
Pearson's r		0.93654		0.97781	
Adj. R-Square		0.83613		0.93416	
		Value	Standard Error	Value	Standard Error
Mean	Intercept	4.22328E-4	1.00186E-5	-7.35271E-4	2.15489E-4
	Slope	6.18804E-5	1.33736E-5	9.66649E-4	1.46457E-4

2D						
	Low concentration region			**High concentration region**		
Equation	y = a + b*x			y = a + b*x		

Weight	Instrumental			No Weighting		
Residual Sum of Squares	0.00471			1.4093E-9		
Pearson's r	0.99502			0.98382		
Adj. R-Square	0.98676			0.95186		
		Value	Standard Error		Value	Standard Error
Mean	Intercept	1.1257E-4	5.14763E-7	Intercept	-0.00138	2.23985E-4
	Slope	1.22173E-5	7.06449E-7	Slope	0.00118	1.52231E-4

S6 CVs obtained from lower scan rates with design 2

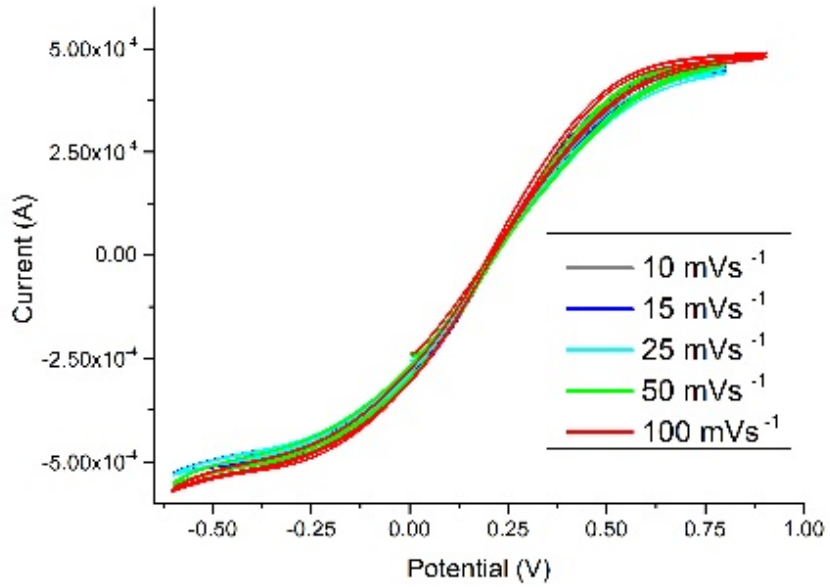

S7 4-AP detection linear fitting

Equation		y = a + b*x					
Weight		No Weighting					
Geometry		**3D**				**2D**	
Concentration range (μM)		**1 - 12.25**		**25 - 100**		**1-100**	
Residual Sum of Squares		1.2019E-12		5.05814E-12		5.54265E-12	
Pearson's r		0.99623		0.99601		0.94614	
Adj. R-Square		0.98871		0.98405		0.87421	
		Value	Standard Error	Value	Standard Error	Value	Standard Error
i_p	Intercept	-4.13619E-7	6.42268E-7	1.63318E-5	2.75449E-6	9.49382E-7	5.21624E-7
	Slope	1.4829E-6	9.12979E-8	4.6452E-7	4.16439E-8	**7.81305E-8**	1.19566E-8

Paper V

Bio-functionalized Graphene combined 3D Carbon Microelectrode as Ultra-sensitive Electrochemical Biosensor

Suhith Hemanth, Arnab Halder, Claudia Caviglia, Qijin Chi and Stephan Sylvest Keller

Bio-functionalized Graphene combined 3D Carbon Microelectrode as Ultra-sensitive Electrochemical Biosensor

Suhith Hemanth[1], Arnab Halder[2], Claudia Caviglia[1], Qijin Chi[2] and Stephan Sylvest Keller[1]
[1]DTU Nanotech, [2]DTU Chemistry
Technical University of Denmark, 2800 Kongens Lyngby, Denmark
suhem@nanotech.dtu.dk

Abstract

A highly sensitive enzyme-based electrochemical biosensor has been developed with bio-functionalized 3D pyrolytic carbon microelectrodes coated with reduced graphene oxide (RGO). The 3D carbon working electrode was micro fabricated and subsequently functionalized with graphene oxide and enzymes. The high sensitivity of the 3D carbon microelectrode is demonstrated with amperometric glucose sensing. The 3D carbon provided a higher sensitivity of 41 µA mM^{-1} cm^{-2} compared to 8 µA mM^{-1} cm^{-2} for 2D carbon for glucose detection. The stability analysis of the enzymes on the 3D carbon showed reproducible results over 7 days. The selectivity of the electrode was evaluated with solutions of glucose, Uric acid, Cholesterol and Ascorbic acid, which showed a significantly higher response for glucose.

Key words: 3D carbon microelectrodes, Graphene oxide, Glucose, electrochemical biosensor

Introduction

Electrochemical biosensors are one of the most successful sensor technologies in terms of real-world application and commercial maturity[1–5]. Therefore, research and development of electrochemical biosensor is presently one of the most active area for various important applications such as diseases diagnostics[6], environmental monitoring[7], food quality control[8], security and defense etc[9]. Electrodes are a central part for all electrochemical applications and are used as the transducer in electrochemical biosensing devices[10]. Therefore, evolution of electrodes is an integral part for advancement of electrochemical biosensors. Various conductive substrates have been used for development of electrodes in the past few decades[11]. Among them, carbon and its derivatives based electrodes are the most popular once. Carbon

based materials can be found as many different allotropes such as graphite, glassy carbon, carbon fibers, diamond, fullerene, nanotube etc[12]. Due to their wide availability, low-cost, high stability, high conductivity and excellent electrochemical performance, these carbon based materials became an obvious choice for wide ranges of electrochemical applications[11]. Furthermore, slow kinetics for oxidation of carbon facilitate the use of wide potential ranges (anodic direction) for various electrochemical experiments, which provides a crucial advantage compare to many different metal-based electrodes[13]. Therefore, carbon based two-dimensional (2D) electrodes are widely used for various electrochemical applications such as biosensors, super capacitors and fuel cells. However, the 2D carbon based electrodes provide limited surface area which is contributing to relatively lower performances and sensitivity for the electrochemical response when compared to 3D carbon electrodes [14]. Rational design of the electrodes and an increase in surface area for the same overall electrode area are potential solutions for this problem. In the last few years, three-dimensional (3D) electrodes are showing very promising response for diverse electrochemical applications[15]. However, those electrodes are often lacking in consistency of their performances due to poor control of the 3D structural defination.

In this work, we have used micro fabricated 3D pyrolytic carbon based electrodes for electrochemical biosensing and further compared to the biosensor performance with the one of a similarly fabricated 2D carbon electrode. Several microfabrication processes have been reported for the fabrication of 3D microelectrodes[16–20]. For our study one of the most simple and cost efficient techniques, Carbon MEMS (C-MEMS) was used to fabricate 3D carbon microelectrodes. In C-MEMS, a patterned polymer template is pyrolyzed at high temperature ($\sim 900\,^{o}C$) to obtain well-defined 3D carbon microelectrodes[21,22].Simialr to other carbon materials, pyrolytic carbon used for microelectrodes has several attractive properties such as a wide electrochemical potential window, ease of surface functionalization and biocompatibility[11,23–25] .

To demonstrate their application as an enzyme-based electrochemical biosensor, the pyrolytic carbon electrodes are coated with reduced graphene oxide functionalized with glucose oxidase and further used for measurement of glucose. Graphene is one of the mosty studied nanomaterials during the last decade due to its extraordinary properties[26]. Although pristine graphene itself is a zero band gap material[27], suitable functionalization of chemically synthesized graphene can convert it to an ideal material for many real world applications[28]. In this work, we have used chemically synthesized graphene bio-functionalized with enzyme to

develop a glucose biosensor based on 3D carbon microelectrodes. The reproducibility and selectivity of the biosensor with 3D electrodes were studied. The performance of biosensing response from 3D electrodes was further compared with the 2D electrode response. Finally, glucose level measurements in real human blood samples were performed using the 3D electrode.

Materials and methods

Microfabrication of 3D carbon microelectrodes

The fabrication of the microelectrodes is following the approach previously reported in literature[29]. UV- photolithography was used to pattern a polymer template (Figure 1. A and D) and pyrolyzed at 900°C for 1 h in N_2 atmosphere to obtain the corresponding carbon microelectrode (Figure 1. B and E). The pseudo gold (Au) reference is deposited through a shadow mask. The synthesized graphene oxide is drop-cased only on the working electrode of the electrochemical chip (Figure 1.C and F).

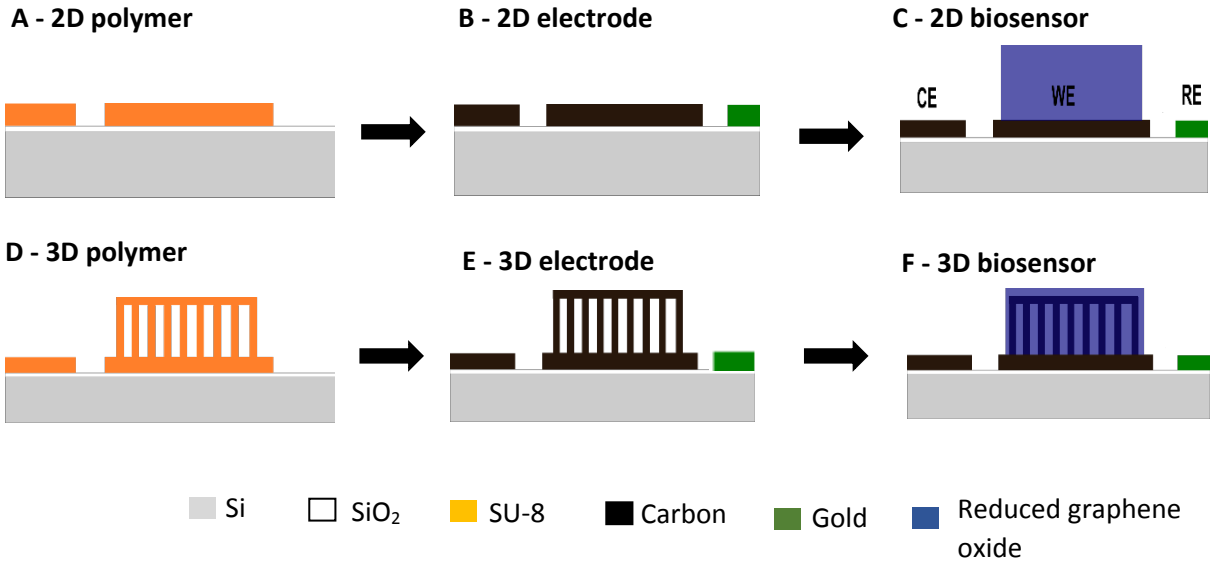

Figure 1: Schematic of 2D and 3D carbon biosensor fabrication (A) and (D) polymer template fabricated by multiple UV photolithography processes, (B) and (E) pyrolytic carbon fabricated by pyrolysis of the corresponding polymer template and (C) and (F) functionalized WE with reduced graphene oxide

Reduced graphene oxide synthesis (RGO)

The bio-functionalized graphene was synthesized by following a study reported previously in literature [30]. In the first step, pre-synthesized graphene oxide was functionalized and reduced by branched polymer PEI in a one-step method [31]. Next, the as synthesized RGO-PEI was coupled with ferrocene carboxylic acid to achieve the redox activity of the biosensing material.

Biosensor preparation

The ferrocene functionalized RGO-PEI material was dispersed in 1 ml 0.5 % ethanolic Nafion® solution by sonication. The solution was drop casted on the pre-cleaned (in O_2 plasma for 3 min) working electrode (WE) area of carbon microelectrodes and dried at room temperature overnight. Finally, for the preparation of the glucose biosensing electrode, 10 µl of glucose oxidase (GOx) solution (10 mg/ml) in a phosphate buffer (PBS, 10 mM, pH 7.0) were drop casted on the WE surface. The bio-functionalized 3D electrodes with enzymes were dried at 4°C overnight. Before performing electrochemical biosensing measurements, the electrodes were repeatedly washed with buffer solutions (PBS, 10 mM, pH 7.0) to remove the loosely bound enzymes.

All electrochemical measurements in this work were done at room temperature (23 ± 2 °C) using an Autolab System (Eco Chemie, Netherlands) operated by the NOVA 1.10 software or by a CHI 760C electrochemical workstation equipped with a Faradaic cage.

Result and discussion

The 2D and 3D carbon microelectrodes for enzymatic based electrochemical biosensing were fabricated as reported previously [14,29]. Figure 2.A and B shows the fabricated 2D and 3D carbon electrodes and Figure 2. C shows the 3D electrode after drop casting of the graphene oxide. The thickness of the carbon electrodes was 2.1 µm and 44 µm for 2D and 3D respectively. The 3D microelectrodes consist of pillars with a diameter of 6.7 µm and pitch of 50 µm. The suspended layer on top of the pillars has holes with diameter of 29 µm and pitch of 50 µm. The WE diameter was 4 mm. The surface area of the 3D microelectrodes was twice the surface area of 2D electrode [29].

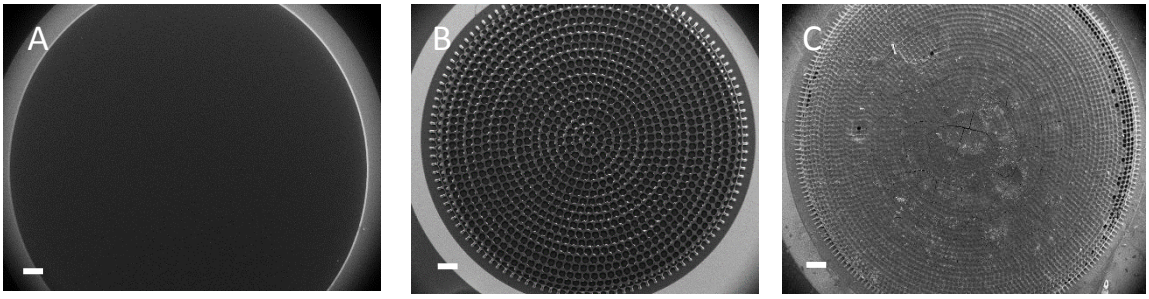

Figure 2: (A) 2D electrode (B) 3D electrode and (C) 3D electrode with graphene oxide (scale bar – 500 µm)

The electrochemical behavior of the bio-functionalized 3D electrode was first studied by cyclic voltammetry. Figure 3 exhibits the cyclic voltammetric response of 3D and 2D pyrolytic carbon electrodes coated with RGO and functionalized with GOx. The voltammetric response of the bio-functionalized 3D and 2D electrodes remains constant constant hundreds of scans in potential window of -0.2 to 0.5 V, which was a clear indication that the electrode material combined with the graphene based biosensing material is stable. As clearly seen in Figure 3, the CV obtained with bio-functionalized 3D electrodes had a much higher current response (3 folds) compared to the 2D electrode, which was very promising for the development of highly sensitive biosensing platform.

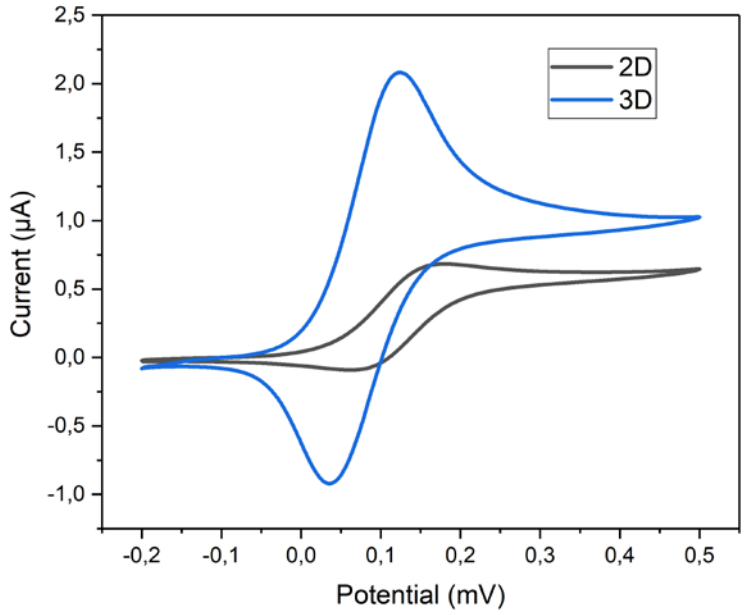

Figure 3 : Cyclic voltammogram of 2D/RGO/GOx and 3D/RGO/GOx in 10 mM PBS (pH 7.0) scan rate 20 mV/s.

In the next step, choronoamperometric glucose biosensing was performed by using both the 3D and 2D electrodes (Figure 4). The amperometric measurements were done by using 10 mM PBS electrolyte solution (pH 7.0) with the working electrode potential fixed at 0.15 V. For both the 3D and 2D electrodes, a linear range until 10 mM was achieved, which overlaps well with the normal human psychological blood glucose level (5-7 mM). However, the lower limit of detection for bio-functionalized 3D carbon microelectrodes is 1.2 µM and for 2D electrodes is 3 µM. Furthermore, the calculated sensitivity for choronoamperometric glucose biosensing is 41 µA mM^{-1} cm^{-2} and 8 µA mM^{-1} cm^{-2} for 3D and 2D electrodes respectively. This means that, the lower limit of detection is 2.5 times higher for the 3D electrode and the sensitivity is around 4.6 times higher for the 3D electrode due the larger active surface area of the 3D electrodes. The higher signal in 3D electrodes can be explained by the higher surface area of the electrode.

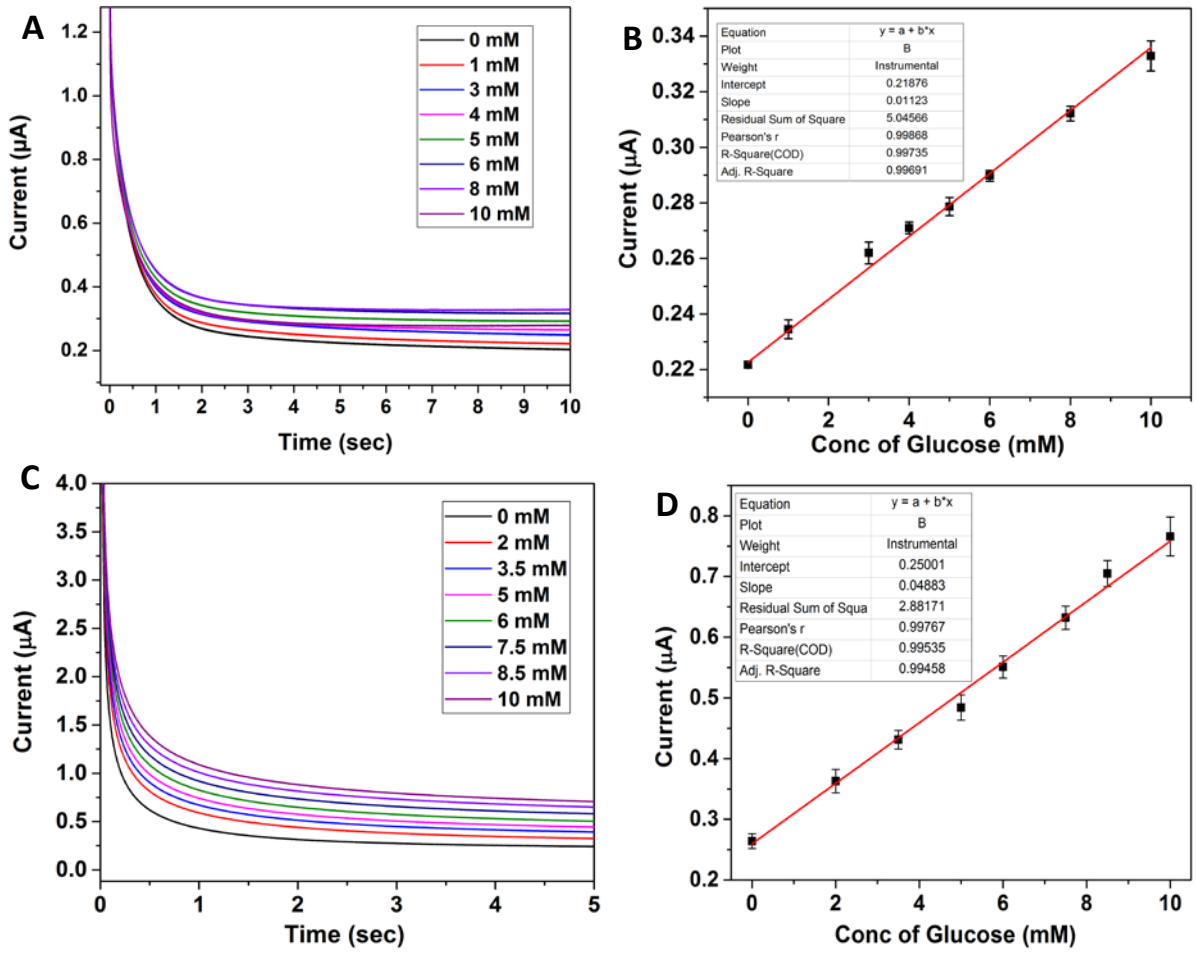

Figure 4 : (A) Choronoamperometric sensing of glucose (0-10 mM) at 2D/RGO/GOx in 10 mM PBS (pH 7.0) (B) Corresponding calibration plot obtained from concentration of glucose vs current. (C) Choronoamperometric sensing of glucose (0-10 mM) at 3D/RGO/GOx in 10 mM PBS (pH 7.0) (D) Corresponding calibration plot obtained from concentration of glucose vs current.

In order to evaluate for a realistic application of the 3D electrode coated with RGO, we have studied the selectivity of the sensor towards some common electroactive species existing in human blood samples, such as cholesterol, ascorbic acid, and uric acid (Figure 5). As seen from the amperometric measurement with GOx, there were no significant interferences from these compounds were observed. Furthermore, the negatively charged polymer (Nafion®) improves selectivity by repelling the uric acid and ascorbic acid through electrostatic repulsion.

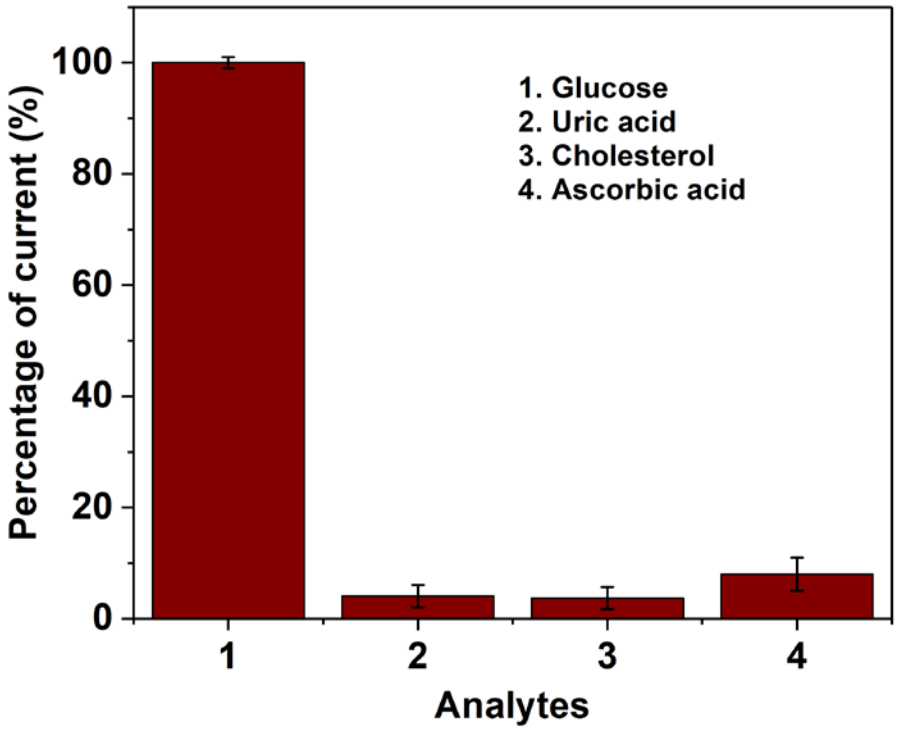

Figure 5 : Influence of common electroactive interferences with (1) glucose (2 mM), (2) Uric acid (5 mM), (3) Cholesterol (5 mM), (4) Ascorbic acid (5 mM). The working potential = 0.3 V. (n=3)

The repeatability of the measurements with bio-functionalized graphene based 3D electrode after storage was tested. Amperometric measurements were performed every day for seven days using the 3D electrodes stored at 4°C. A 5% decrease in the biosensor response was observed after 3 days and a 8% decrease after 7 days (Figure 6). The change in biosensor response was attributed due to the limited stability of the immobilized enzymes.

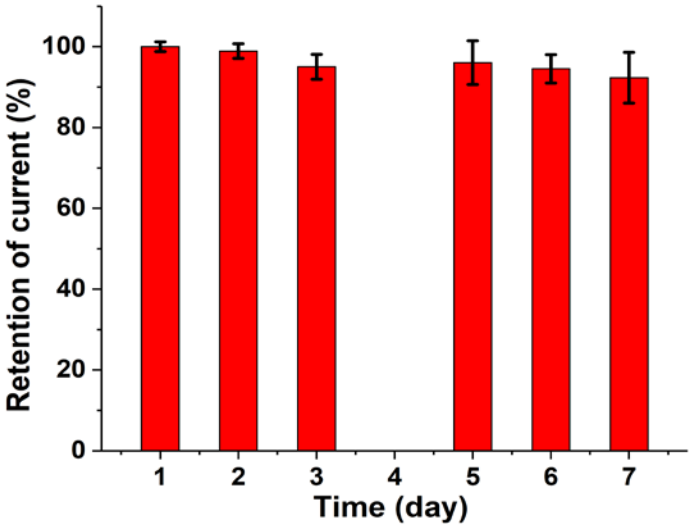

Figure 6: Response stability of 3D/RGO/GOx electrode for 7 days stored at 4 ℃.

The 3D electrode coated with RGO were further tested as a disposable sensor to evaluate the glucose level in real human blood samples. The results were compared with those obtained by a commercially available blood glucose measurement device. For evaluation of the glucose level, the human blood was added to the electrolyte (10 mM PBS, pH 7) on the 3D electrode surface and the steady state current was measured. Three individual measurements were performed for two different samples. The obtained results were in good agreement with data from the commercially available self-monitoring blood glucose device for the same samples. The RSD values for the measurements were found to be between 2 and 5. The results confirmed that the fabricated 3D electrodes functionalized with RGO can be used for the glucose level measurements in real human blood samples without any prior sample pre-treatment.

Table 1 : Real blood sample (serum) measurement

Blood sample	Conc. of blood glucose measured by our 3D sensor	Conc. of blood measured by commercial Blood Glucose Monitoring Device	RSD
Sample 1	4.51 mM	4.8 mM	3.1
Sample 2	5.89 mM	6.1 mM	4.7

Conclusion

An enzyme based electrochemical biosensor was developed with functionalized 3D carbon as working electrode. The 3D electrode provides a higher sensitivity (41 µA mM^{-1} cm^{-2}) and lower limit of detection (1.2 µM) for glucose sensing. The lower limit of detection and sensitivity of 3D electrodes when compared to 2D electrodes were 2.5 times and 4.6 times higher respectively. The developed enzymatic biosensor was highly selective and stable over time for glucose sensing. The electrodes were successfully applied for glucose detection in real blood serum. With the more sensitive 3D carbon microelectrodes, the developed sensor can be an ideal alternating platform for high sensitive electrochemical biosensors.

Acknowledgement

The authors acknowledge funding from Poul V. Andersen foundation grant and Young Investigator Program of the Villum Foundation.

References

1. Shao, Y. *et al.* Graphene based electrochemical sensors and biosensors: A review. *Electroanalysis* 22, 1027–1036 (2010).

2. Turner, A. P. F. Biosensors: sense and sensibility. *Chem. Soc. Rev.* 42, 3184–3196 (2013).

3. Bandodkar, A. J. & Wang, J. Non-invasive wearable electrochemical sensors: a review. *Trends Biotechnol.* 32, 363–371 (2014).

4. Barsan, M. M., Ghica, M. E. & Brett, C. M. A. Electrochemical sensors and biosensors based on redox polymer/carbon nanotube modified electrodes: A review. *Anal. Chim. Acta* 881, 1–23 (2015).

5. Grieshaber, D., MacKenzie, R., Vörös, J. & Reimhult, E. Electrochemical Biosensors - Sensor Principles and Architectures. *Sensors (Basel).* 8, 1400–1458 (2008).

6. Mazzocchi, R. A. Medical Sensors – Defining a Pathway to Commercialization. *ACS Sensors* acssensors.6b00553 (2016). doi:10.1021/acssensors.6b00553

7. Perreault, F., Fonseca de Faria, A. & Elimelech, M. Environmental applications of graphene-based nanomaterials. *Chem. Soc. Rev.* 44, 5861–5896 (2015).

8. Mohanty, S. P. & Koucianos, E. Biosensors: A tutorial review. *IEEE Potentials* 25, 35–40 (2006).

9. Turner, A. Biosensors: Then and now. *Trends Biotechnol.* 31, 119–120 (2013).

10. Burke, A. M. & Gorodetsky, A. A. Electrochemical sensors: Taking charge of detection. *Nat. Chem.* 4, 595–597 (2012).

11. Tiwari, J. N., Vij, V., Kemp, K. C. & Kim, K. S. Engineered carbon-nanomaterial-based electrochemical sensors for biomolecules. *ACS Nano* 10, 46–80 (2016).

12. McCreery, R. L. Advanced Carbon Electrode Materials for Molecular Electrochemistry. *Chem. Rev.* 108, 2646–2687 (2008).

13. Uslu, B. & Ozkan, S. Electroanalytical Application of Carbon Based Electrodes to the Pharmaceuticals. *Anal. Lett.* 40, 817–853 (2007).

14. S. Hemanth, C. Caviglia, L. Amato, T.A. Anhøj, A. Heiskanen, J. Emnéus, S. S. K. Pyrolytic 3D Carbon Microelectrodes for Electrochemistry. *ECS Trans.* 72, 117–124 (2016).

15. Dey, R. S., Hjuler, H. A. & Chi, Q. Approaching the theoretical capacitance of graphene through copper foam integrated three-dimensional graphene networks. *J. Mater. Chem. A* 3, 6324–6329 (2015).

16. Greiner, F. *et al.* Fabrication techniques for multiscale 3D-MEMS with vertical metal micro- and nanowire integration. *J. Micromechanics Microengineering* 23, 25018 (2013).

17. Piotter, V., Benzler, T., Gietzelt, T., Ruprecht, R. & Haußelt, J. Micro Powder Injection Molding. *Adv. Eng. Mater.* 2, 639–642 (2000).

18. Wu, S.-Y., Yang, C., Hsu, W. & Lin, L. 3D-printed microelectronics for integrated circuitry and passive wireless sensors. *Microsystems Nanoeng.* 1, 15013 (2015).

19. Hart, A. & Taylor, H. 2D and 3D growth of carbon nanotubes on substrates, from nanometre to millimetre scales. *Int. J. Nanomanuf.* X, 1–9 (2007).

20. Choi, J.-W. *et al.* 3-dimensional electrode patterning within a microfluidic channel using metal ion implantation. *Lab Chip* 10, 783 (2010).

21. Wang, C. & Madou, M. From MEMS to NEMS with carbon. *Biosens. Bioelectron.* 20, 2181–2187 (2005).

22. Martinez-Duarte, R. & Rodrigo. SU-8 Photolithography as a Toolbox for Carbon MEMS. *Micromachines* 5, 766–782 (2014).

23. Falcao, E. H. & Wudl, F. Carbon allotropes: beyond graphite and diamond. *J. Chem. Technol. Biotechnol.* 82, 524–531 (2007).

24. Amato, L. *et al.* Pyrolysed 3D-Carbon Scaffolds Induce Spontaneous Differentiation of Human Neural Stem Cells and Facilitate Real-Time Dopamine Detection. *Adv. Funct. Mater.* 24, 7042–7052 (2014).

25. Lee, J. A. *et al.* An electrochemical impedance biosensor with aptamer-modified pyrolyzed carbon electrode for label-free protein detection. *Sensors Actuators B* 129, 372–379 (2008).

26. Halder, A., Zhang, M. & Chi, Q. Graphene-Metal Oxide Hybrid Nanostructured Materials for Electrocatalytic Sensing and Sustainable Energy Storage. *Reviews in Advanced Sciences and Engineering* 5, 4–31 (2016).

27. Buzaglo, M. *et al.* Graphite-to-Graphene: Total Conversion. *Adv. Mater.* 29, 1603528 (2016).

28. Morales-Narváez, E., Baptista-Pires, L., Zamora-Gálvez, A. & Merkoçi, A. Graphene-Based Biosensors: Going Simple. *Adv. Mater.* 29, 1–7 (2016).

29. Hemanth, S., Caviglia, C. & Keller, S. S. Suspended 3D pyrolytic carbon microelectrodes for electrochemistry. *Carbon N. Y.* 121, 226–234 (2017).

30. Halder, A., Zhang, M. & Chi, Q. Electroactive and biocompatible functionalization of graphene for the development of biosensing platforms. *Biosens. Bioelectron.* 87, 764–771 (2017).

31. Chi, Q., Han, S., Halder, A., Zhu, N. & Ulstrup, J. Graphene-polymer-enzyme hybrid nanomaterials for biosensors. *EU Patent application no PCT/EP2015/076933* (2016).

Appendix A: Patents

P1. PCT/EP2016/072388 - 3D pyrolysed carbon electrodes for cell analysis
Claudia Caviglia, Letizia Amato, Suhith Hemanth and Stephan Sylvest Keller (2015)

P2. P2276EP00 - Electrode assembly for a rechargeable battery
Poul Norby, Claudia Caviglia, Suhith Hemanth and Stephan Sylvest Keller (2017)

Appendix B: Conference contributions

A. Talks

1. *Pyrolysed 3D Carbon Microelectrodes for Electrochemistry*
S.Hemanth, C.Caviglia, L. Amato, T.A. Anhøj, A.Heiskanen, J. Emnéus, and S.S. Keller at 229th Electrochemistry Society Meeting, May 29th - June 2nd (2016), San Diego, USA.

2. *2D AND 3D Pyrolytic carbon microelectrode for electrochemistry*
S.Hemanth, C.Caviglia and S.S. Keller at International Conference on Electroanalysis, June 12th - 16th (2016), Bath, UK.

3. *Microfabrication of 3D pyrolytic carbon electrodes for electrochemistry*
S.Hemanth, C.Caviglia, Y.M. Hassan, T.A. Anhøj, and S.S. Kellera at Micro and Nano Engineering, September 19th – 23rd (2016), Vienna, Austria.

4. *Ultrasensitive 3D Carbon Microelectrodes for Electrochemical Biosensing Application*
Suhith Hemanth, Arnab Halder, Claudia Caviglia, Qijin Chi, and Stephan Sylvest Keller at AMN8, February 11th – 16th (2017), Queenstown, New Zealand.

5. *Three-dimensional sensing scaffold for bone cells studies*
Claudia Caviglia, Suhith Hemanth, Yasmin Mohamed Hassan, Gaetano Panagia, and Stephan Sylvest Keller at First European / 10th German BioSensor Symposium, March 20th – 23rd (2017), Potsdam Germany.

6. *Biomaterial Microsystems for Drug Delivery and Bioelectrochemistry*
Stephan Sylvest Keller, Letizia Amato, Ritika Singh Petersen, Claudia Caviglia, Suhith Hemanth, Arto Heiskanen, Anja Boisen, Jenny Emnéus at Micro and Nano Engineering, September 21st - 24th (2015), The Hague, The Netherlands.

7. *Carbon Microelectrodes for Real Time Osteoporosis Drug Screenings*
C. Claudia, G. Panagia, S. Hemanth, Y. M. Hassan, S. S. Keller at 229th Electrochemistry Society Meeting, May 29th - June 2nd (2016), San Diego, USA.

8. *Pyrolytic carbon microelectrodes for impedance based cell sensing*
Yasmin Mohamed Hassan, Claudia Caviglia, Suhith Hemanth, David Mackenzie, Dirch Hjorth Petersen, and Stephan Sylvest Keller at 229th Electrochemistry Society Meeting, May 29th - June 2nd (2016), San Diego, USA.

9. *Optimized SU-8 pyrolysis for fabrication of pyrolytic carbon microelectrodes*
Yasmin Mohamed Hassan, Claudia Caviglia, Suhith Hemanth, David Mackenzie, Dirch Hjorth Petersen, Tommy Sonne Alstrøm,and Stephan Sylvest Keller at Micro and Nano Engineering, September 19th – 23rd (2016), Vienna, Austria.

B. Poster

1. *Pyrolysed carbon microelectrode in a self-aligning electrochemical batch system*
Suhith Hemanth, Letizia Amato, Claudia Caviglia, Jenny Emnéus and Stephan Sylvest Keller at XXIII International Symposium on Bioelectrochemistry and Bioenergetics, June 14th -18th (2015), Malmo, Sweden.

2. *Microfabrication of multi-layered 3D pyrolysed carbon electrodes*
Suhith Hemanth, Claudia Caviglia, Letizia Amato and Stephan Sylvest Keller at Micro and Nano Engineering, September 21st - 24th (2015), The Hague, The Netherlands.

3. *Microfabrication of 3D pyrolysed carbon electrodes*
Suhith Hemanth, C. Caviglia, L. Amato, T.A. Anhøj and S. S. Keller at Annual Meeting of the Danish Electrochemical Society, October 1st – 2nd (2015) Copenhagen University, Denmark.

4. *Bioengineering of solution processed graphene for the development of ultrasensitive flexible biosensing platforms*
Arnab Halder, Suhith Hemanth, Stephan Sylvest Keller, Jens Ulstrup, and Qijin Chi at PRiME 230th ECS Meeting, October 2nd -7th (2016),Honolulu, Hawaii.

5. *3D pyrolytic carbon microelectrodes for electrochemical sensing*
   Suhith Hemanth, Claudia Caviglia, Yasmin Mohamed Hassan, Jenny Emnéus and Stephan Sylvest Keller at First European / 10th German BioSensor Symposium, March 20th – 23rd (2017), Potsdam Germany.

Appendix C: Awards and Funding

1. *Poul V. Andersens Foundation grant* of 250,000 DKK (2016) jointly with Arnab Halder from DTU chemistry: A research grant to establish a new collaboration between two departments in DTU.

2. *DTU POC funding* of 100,000 DKK was awarded for commercialization of carbon microelectrodes.

3. Venture cup finalist, 2017. (It's a national startup competition, where top 4 business idea in Denmark are selected for the finals. Carbon4Bio made into finial in category GreenTech).

4. Dropsens international award finalist, 2016. (It's an international competition for the upcoming research ideas in electrochemistry. Top 3 ideas were selected for the finals)

5. *Otto-Mønsted travel grant* for attending an international conference. (2015, 2016, and 2017).

Appendix D: Business plan for Carbon4Bio

miCa (Micro carbon)

Brief introduction

A highly sensitive 3D carbon based electrochemical biosensor is developed. The proposed novel sensor has a 3D carbon microelectrodes which mimic the natural *in vivo* environment, leading to more physiologically realistic and reliable biomedical tool than currently used standard 2D electrodes. The 3D carbon technology pushes the state of the art 2D technology to a more sensitive region which will help in detecting a small concentration of the virus, bacterial or cancer cells.

Product and/or service and business model

Business concept: The highly sensitive sensor platform will be the heart of the next generation electrochemical sensors. The higher sensitivity due to the 3D nature of the carbon electrode will result in more accurate, realistic and cheap sensor.

Value proposition: This technology drives more insight to the problem and may lead to many more medical break thoughts. The 3D nature of the carbon electrode, which is the sensing component will be the first of its kind. Furthermore carbon being one of the most attractive bio-material for electrochemical measurements, 3D carbon makes an ideal electrode electrochemical sensors.

Prototype: Figure 1.A shows the prototype of the carbon microelectrode fabricated with a patented novel MEMS technology (UV photolithography and pyrolysis). Figure 1.B shows the experimental setup.

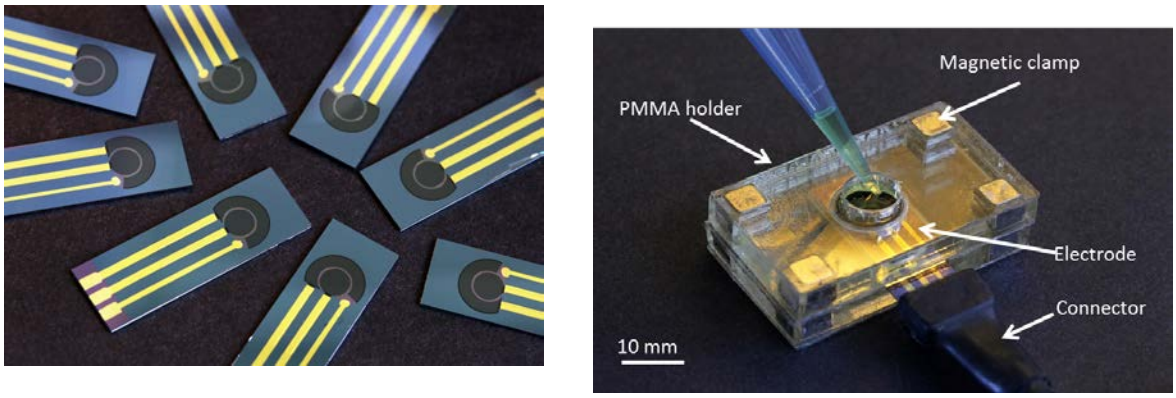

Figure 1: A : Carbon miroelectrode chips B: experimental set-up

Proof of concept: The electrochemcial detection of dopamine released by human stem cells is shown in Figure 2. The higher signal (sensitivity) for 3D cabron microelectrode is very evident, comapred to traditional 2D electrodes.

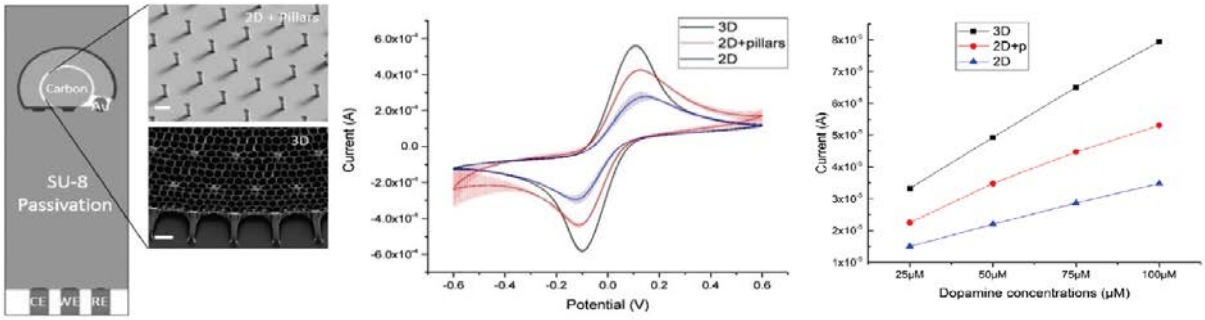

Figure 2: Left: Microelectrode chip design with three electrode configuration. SEM images of carbon micropillars (2D+pillars) and suspended grids (3D); Cyclic voltammetry with 10mM ferri-ferrocyanide redox probe (center) and dopamine detection with square wave voltammetry (right) with different electrode configurations

Business model: The basic prototype will be established in DTU, Denmark. The manufacturing of the carbon microelectrode will be outsourced to a fab-center (i.e. STMicroelectronic). The electrode will be integrated to a user friendly device, with a readout by our partner LeapCraft (Copenhagen). The end product will be sold to hospitals, clinics, labs etc (who will be out potential costumers).

Market and competition

Market and competition: The market for electrochemical sensor is 4500 M$ and rapidly increasing to 6000 M$ by 2019 according to bcc research.

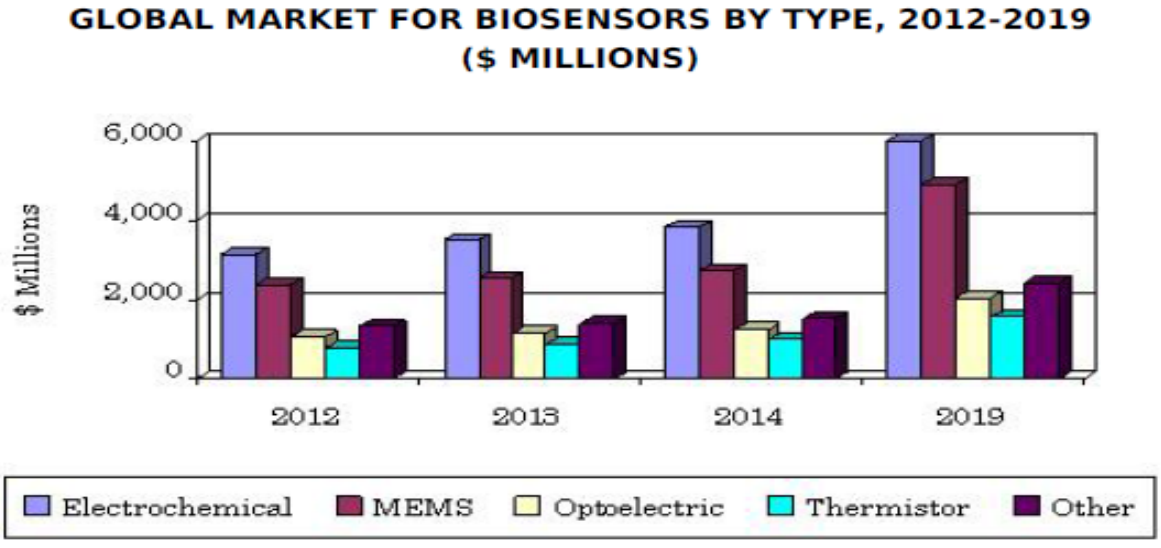

This will be pushing the technology forward. The main competitors will be the carbon electrode manufactures, like (SGL group, China and Schutz carbon electrodes Pvt Ltd, Germany). But the challenge is making the 3D carbon electrode, which miCa has mastered and has an IP protection.

Team, implementation, traction and budget

Team: The founding team consists of Suhith Hemanth (expert on Microfabrication and start up experience), serial Entrepreneur Kristofer Kis, Ast. Prof Stephan Sylvest Keller in DTU Nanotech and we will need an electrochemistry expert to start. An advisory board will be formed with will consists of experts on electrochemistry, sensor and business models. LeapCraft an interfacing and data analysis company have joined hands in this venture. Banking on the knowledge of the advisory board, LeapCraft and foundry team, a first prototype will be developed. A marking and sales guys will be hired to promote and bring in customer capital/business angels. Finally a CEO after second milestone i.e. after our first sales.

Implementation plan: There are three major milestone set for the coming 5 years

1. PoC for PD testing (until 2017) – In this phase 4 founders will work part time with the advisory board to prove the concept.
2. First Prototype and sales – A marking/sales guys will be hired to find some customer capital/business angels. One full time employer will be employed to optimize the process before outsourcing it to STMicroelectronics. With customer (Hospitals and clinics) an optimal design of diagnostic tool will be derived. And first sales will happen in 2019.
3. Deployment and expansion – After the first two sales a CEO and two full time employee will be hired to expand the sales. Also one full time employee will be hired to come up with an innovative electrochemical sensors.

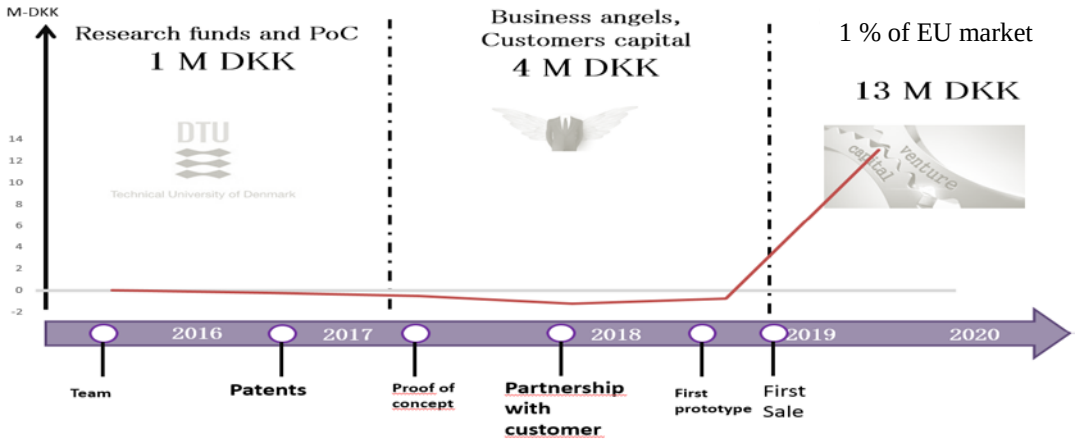

Traction: Some of the main objective achieved in this direction are:

1. Patent on the fabrication process of 3D carbon microelectrode
2. Prototype of the 3D carbon electrochemical sensor
3. Proof of concept test with chemical dopamine
4. Finished on top three in **"Dropsens International award"** and have got an **initial grant** of 350000 DKK from DTU
5. Dropsens, Spain wants to buy out 3D carbon microelectrodes (asked for 100 chips quotation)

Budget

1. 2016-2017 – 1M DKK, accumulated from research funds and PoC funds
2. 2018-2019 – 5M DKK from customer capital /Business angels
3. 2019- 20.. – 13M DKK from venture capital (At this state we expect to break even)